Durham E-Theses

Development and application of the phase-screen seismic modelling code

White, James C.

How to cite:

White, James C. (2009) *Development and application of the phase-screen seismic modelling code*, Durham theses, Durham University. Available at Durham E-Theses Online: http://etheses.dur.ac.uk/2034/

Use policy

Development and application of the phase-screen seismic modelling code

James C. White

A dissertation submitted for the degree of
Doctor of Philosophy
Durham University

Ustinov College
February 2009

3 1 MAR 2009

Software used:
This dissertation was written using LaTeX. The references and citations were produced using BibTeX. Most figures were plotted with the *Generic Mapping Tools* (GMT). The software *Gimp* was used for image conversion and manipulation. Seismic data processing and plotting was done with *Seismic Unix*.

Development and application of the phase-screen seismic modelling code

James C. White

Abstract

As a consequence of the aims of this project, this thesis is divided into two distinct sections. Initially, the computationally efficient phase-screen forward modelling technique is extended to allow investigation of non-normal ray paths. The code is developed to accommodate all diffracted and converted phases up to critical angle, building on a geometrical construction method previously developed with a narrow-angle approximation. The new approach relies upon pre-scanning the model space to assess the complexity of each screen. The propagating wavefields are then divided as a function of horizontal wavenumber, and each subset is transformed to the spatial domain separately, carrying with it angular information. This allows both locally accurate 3-D phase corrections and Zoeppritz reflection and transmission coefficients to be applied. The phase-screen code is further developed to handle simple anisotropic media. During phase-screen modelling, propagation is undertaken in the wavenumber domain where exact expressions for anisotropic phase velocities are incorporated. Extensive testing of the enhanced phase-screen technique includes simple analytical models to justify the inclusion of multiple energy alongside synthetic examples from models commonly used to test numerical modelling techniques. Additionally the code is tested with real models from a producing field in a marine sedimentary location where an exhaustive range of geophysical techniques were used to constrain the VTI parameters.

Secondly within this thesis, the narrow angle version of the phase-screen method is used to generate a comprehensive pre-stack seismic reflection dataset for our industrial partners. Current exploration within the European oil and gas community is heavily focused on regions where the targets for production are positioned beneath plateau basalts on the north west European margin. These environments produce a complex seismic response due to the scattering generated by the internal composition of the basalt flows. This study generates a large subsurface volume, derived from geological mapping projects in the Hold-with-Hope region of north east Greenland, and synthetically acquires a realistic 3-D reflection study across it. The basalt is uniquely generated as a single random volume with distinct correlation lengths in each orthogonal direction and a novel approach to determine seismic attenuation through basalts is developed. Initial results from this data set are presented after careful optimisation of the modelling code and parameters.

Declaration

This dissertation describes my original work except where acknowledgement is made in the text. It does not exceed the page limit and is not substantially the same as any work that has been, or is being submitted to any other university for any degree, diploma or any other qualification.

James C. White
March 17, 2009

Acknowledgements

Contents

List of Figures

List of Tables

Chapter 1

Introduction

1.1 Motivation

This thesis is divided into two distinct sections. Initially, the elastic and visco-elastic modelling of seismic propagation through 3D heterogeneous anisotropic media is discussed and developed. The phase-screen technique is a frequency domain method for modelling seismic propagation which alternates between the wavenumber and spatial domains as the wavefield moves forward through a series of parallel diffracting screens placed perpendicular to the primary direction of propagation. Advantages of the method include fast run-times and full waveform responses, at narrow angles of propagation, for heterogeneous media. This study involved increasing wide angle resolution and introducing propagation through anisotropic media. Additional efforts focus on developing a viscoelastic code written in c++, with dynamic memory allocated at the start of the model run.

Secondly within this thesis, as a consequence of industrial sponsorship, the narrow angle version of the phase-screen method will be used to generate a comprehensive pre-stack seismic reflection dataset for our industrial partners. Current exploration within the European oil and gas community is heavily focused on regions where the targets for production are positioned beneath plateau basalts in the north west European continental margin. These environments produce a complex seismic response due to the internal composition of the basalt flows. The study generates a large subsurface 3-D volume, derived from geological mapping projects in the Hold-with-Hope region of north east Greenland, and synthetically acquires a realistic 3-D seismic reflection survey

across it. This is the largest modelling task yet attempted with the phase-screen modelling code and the work necessitites significant code optimisation in order to make the project feasible on a university based computer cluster. These data will then be used by the project sponsors to test their sub-basalt imaging algorithms on a pre-determined model.

1.2 Approaches to seismic modelling

Seismic modelling techniques can, in general, be sub-divided into a series of classes dependant upon the method of formulation. These techniques are catagorised depending on the method they adopt to solve the wave equation and additional factors such as propagation distance, the accuracy of the solution and the size and scheme of scattering theory. Each method offers a different set of advantages and limitations meaning the required accuracy of the solution, and the time and computational-power available to deliver it, are often the key factors when deciding which method to adopt.

Wu and Aki (1988) classified the various methods and below the main sub-divisions are briefly discussed in order to correctly position the phase-screen method alongside its alternatives.

Numerical techniques are most commonly used to model the accurate full wavefield response of the subsurface. These techniques, finite difference (Kelly et al., 1976; Dablain, 1986; Levander, 1988; Robertsson et al., 1994) and finite element (Smith, 1975; Marfurt, 1984), suffer from a necessity to acquire large allocations of computer memory since they are discretised in both time and space. The schemes work by replacing derivatives with difference quotients within the wave equation and model all modes of the wavefield. The time consuming processing makes the method unsuitable for massive 3D volumes without significant optimisation and considerable computational power. Additionally the spacing of the nodal distribution must be evaluated with respect to the frequency range to avoid numerical dispersion. Falk et al. (1998) have shown some improvements with the introduction of locally variable time steps, and irregular gridding methods have also been implemented to achieve the same purpose (Opršal and Zahradník, 1999). A more promising approach, pioneered by Robertsson and Chapman (2000), addressed a chosen subsection

of the model space and determined the wavefield only within this targeted zone and a local buffering area. However, these hybrid methods are prone to unwanted artefacts at the model edges where the energy is coupled. Large scale finite element projects have not been commonly utilised within 3D seismological studies due to the extortionate run time costs.

A comparable method to finite difference schemes, the pseudo-spectral method (Kosloff and Baysal, 1982; Fornberg, 1987; Reshef et al., 1988a,b), determines the spatial derivatives using a fast Fourier transform and although the grid discretisation can be less severe than traditional finite difference models the technique still suffers from extensive run times. Spectral element methods, pioneered by Komatitsch and Tromp (1999), have also been utilised to model in regions of intricate geometries since the grid shape can be skewed, yet these methods require massive parallel computing facilities and are difficult to program.

The commonly employed ray-tracing techniques are approximate methods that result in the high frequency response of a medium (Cervený et al., 1977). In general, the zeroth order term of an asymptotic series is used to solve the wave equation in heterogeneous media, producing a response where the magnitude of the slowness equates to the magnitude of the gradient of the phase term. By numerically integrating for position and slowness at every time step along the ray the seismic response is derived. The method incorrectly handles grazing rays, caustics, diffractions and coupling effects since the technique considers only Fermat rays. However, development of asymptotic techniques produced methods valid at lower frequencies. Maslov theory (Chapman and Drummand, 1982), a ray summation approach, and Gaussian Beam theory (Popov, 1982) are transform methods which include the contribution of non-geometrical rays and are therefore accurate for modelling waveforms near caustics. WKBJ is an additional transform technique (Chapman, 1985), reliant upon a slowness integration, that is only valid in 1D media but also offers accurate modelling of non-Fermat raypaths. All these techniques are quick modelling schemes but require a continuous distribution of elastic wavefield parameters in order to accurately determine first and second order differentials in space.

The reflectivity technique (Fuchs and Müller, 1971) is a fast full waveform method limited to 1-D structure where the runtime is proportional to the number of layers. The technique, a wavenumber integration method applicable to horizontally stratified media, relies upon integration of the plane wave reflection coefficients across the entire wavenumber domain.

1.3   Phase-screen modelling technique

A thorough review of the phase-screen method is provided later in this thesis but it is important to outline where the method fits in to the overall scheme of seismic modelling. The phase-screen is a dual domain technique and is most closely linked with the pseudo-spectral method but does not require the discrete, evenly spaced grid of its more cumbersome relative. Unlike the ray tracing technique, the method can accurately determine amplitudes in caustic zones and is able handle sharp discontinuities in the sub-surface. The phase-screen approach also differs from the reflectivity technique in that it is not limited to 1-D structure. The technique, in its simplest constructions, offers order of magnitude time savings over finite difference and finite element schemes and, due to the distribution of elastic parameters, does not necessitate such large memory requirements. These advantages make the phase-screen an ideal tool for modelling both 2-D subsurfaces quickly and accurately and for undertaking 3-D modelling projects.

The principal disadvantage of most phase-screen codes is the narrow angle restriction which limits the validity of the synthetic data to simple imaging rather than more demanding analysis such as studying the amplitude vs. offset characteristics.

1.4   Sub-basalt imaging

Sub-basalt imaging remains one of the great challenges within the seismic acquisition, processing and interpretation communities. The nature of flood basalts produces a high level of heterogeneity. Highly rugose, fractured flows are separated by layers of ash and sediment meaning the basalt cannot be

considered a single homogeneous layer during both forward modelling and real data processing.

Common industrial seismic acquisition aiming to image underlying sub-basalt structure relies upon low frequency, deep towed sources aiming to reduce the effects of short wavelength scattering from small scale heterogeneities. The acquisition is generally performed over long offsets (greater than 6 km) and during processing particular attention is paid during the demultiple and velocity analysis steps. These techniques, combined with non-seismic methods, have led to an improved imaging strategy for sub-basalt targets. However, the hit-and-miss nature of the imaging procedures has left hydrocarbon companies looking for additional tools to enhance the reliability of their processing strategies. In an attempt to understand the seismic imaging issues, this study generates a complete synthetic dataset over an area greater than 200 km^2 allowing processing teams the opportunity to handle data from a known subsurface so exact error analysis can be performed. This study will deliver a complete seismic dataset covering a subsurface aperture of 27.5 km by 12 km. The other advantage is that novel acquisition geometries can be evaluated, eg. wide-angle towed-streamer (WATS), at a fraction of the cost of testing in the field.

1.5   Thesis objectives and layout

Already within this first chapter the general objectives of this study have been set out. The current industry standard seismic modelling techniques have been introduced and the positioning of the phase-screen technique within this general body of work has been identified. The specific aims of this project have also been introduced and the two pronged nature of the research project has been identified.

In chapter 2, a comprehensive examination of the development of the phase-screen technique is undertaken. The mathematically complex derivation of Wu (1994) is discussed prior to undertaking the geometrical construction method of Wild and Hudson (1998) in order to deliver analogous governing equations. Unpublished ideas from Andriatsitohaina (2004) which provided the initial concepts for some of the development ideas contained within this manuscript are reviewed next.

By following a similar geometrical construction technique to Wild and Hudson (1998) it enables the extension of the technique, in chapter 3, to wider angles of propagation without loss of accuracy. Simple models are used to confirm the accuracy of this technique.

Further extension of the method to anisotropic models is undertaken in chapter 4. Limiting velocity and density variation to vertically transverse isotropy allows additional development of the phase-screen technique for rock types characterised by Thomsen's parameters δ and ϵ (Thomsen, 1986).

Chapter 5 validates the enhanced phase-screen code against alternative numerical techniques and industry standard analytical models and solutions. The full range of the method is explored with reflection seismic data, vertical seismic profiles, source modelling and post-stack exploding reflector models being generated.

Chapter 6 sees the start of the second section of the thesis to generate a reflection seismic dataset for our industrial sponsors. Initially the thesis discusses the generation of such a model and includes a novel approach for generating sub-surface basalts. Once the model is finalised, chapter 7 focuses on the initial results of the modelling and evaluates the computational requirements of generating large seismic datasets within academic institutions.

Finally conclusions from the work will be discussed in chapter 8, where possibilities for future work will also be addressed.

Chapter 2

Principles of phase-screen modelling method

2.1   Introduction

Early work using phase-screen dual-domain propagators modelled the transmission of acoustic waves in heterogeneous media. Prior to the successful generalisation of the technique for elastic wave propagation (Wu, 1994), the approach was used to model amongst other things: atmospheric interference on starlight (Ratcliffe, 1956); scattering of radio waves (Buckley, 1975); propagation of light along fibre optic cables (Feit and Fleck, 1978); and marine acoustics (Tappart, 1977).

Initial attempts to produce an elastic phase-screen derivation were presented by Fisk and McCartor (1991). It was soon noted that there were limitations with the technique since mode conversions were handled incorrectly as the P- and S-wave system was decoupled. Noting these limitations Wu (1994) produced a full theoretical derivation where wave mode conversions are calculated as a consequence of background perturbation.

Wild and Hudson (1998) presented a complimentary elastic phase-screen derivation to Wu (1994). They approached the problem from a geometrical perspective which yielded the same set of governing equations through a much simplified derivation.

The phase-screen method models propagation across heterogenous media by decimating the model space into a series of diffracting screens positioned perpendicular to the primary direction of propagation. The modelling pro-

ceeds monochromatically, with frequencies considered discretely. For each screen the algorithm has two parts. Firstly, the background medium between two screens is approximated to a homogeneous slab for the purposes of transmission. As such, propagation reduces to a bulk phase shift by $e^{i\sqrt{k^2-k_T^2}\Delta z}$ in the transverse wavenumber domain for a slab of thickness Δz, where k_T is the transverse wavenumber and $\sqrt{k^2-k_T^2}$ is the wavenumber in the primary propagation direction, perpendicular to the screen orientation.

Secondly, a phase correction is applied as a function of position across each screen to correct for the interaction of the wavefield with a diffracting medium. The phase function, $\chi(x,y)$, is calculated from the background perturbations within the slab of interest and is applied as a spatial domain multiplication. When considered simply it corrects locally for phase errors caused by the reduction of a heterogeneous medium to a homogeneous one. It is the calculation of the phase function that provides the biggest challenge during phase-screen modelling.

2.1.1 Development of scalar wave approach – Governing equation

The fundamental principle behind the scaler phase-screen method is that it propagates a wavefield $u(x,y,z,\omega)$ from screen j to screen $j+1$ and can be stated as

$$u(x,y,z_{j+1},\omega) = \mathcal{F}^{-1}\left\{e^{i\sqrt{k^2-k_T^2}\Delta z}\mathcal{F}\left\{\chi_j(x,y)u(x,y,z_j,\omega)\right\}\right\}, \qquad (2.1)$$

where $\mathcal{F}$ represents the 2-D spatial forward Fourier transform and $\mathcal{F}^{-1}$ the inverse.

When dealing exclusively with an acoustic wavefield with no attenuation, heterogeneities affect only the phase of the wave. This means that the phase function, $\chi(x,y)$, can be expressed as $e^{i\Phi_j(x,y)}$, where $\Phi_j(x,y)$ is always real.

2.1.2 Development of elastic wave approach – Governing equations

When dealing with propagation through elastic media, conversions between P and S waves are generated during interaction with heterogeneities. Complex values of $\Phi_j(x, y)$ are required to account for the changes in both the phase and the amplitude of the wavefield and the elastic equivalent of equation 2.1 is a pair of equations,

$$
\mathbf{u}^P(x, y, z_{j+1}, \omega) = \mathcal{F}^{-1}\{e^{i\sqrt{k_P^2 - k_T^2}\Delta z}\mathcal{F}\{\chi_j^{PP}(x, y)\mathbf{u}^P(x, y, z_j, \omega) \\
+ \chi_j^{SP}(x, y)\mathbf{u}^S(x, y, z_j, \omega)\}\},
\tag{2.2}
$$

$$
\mathbf{u}^S(x, y, z_{j+1}, \omega) = \mathcal{F}^{-1}\{e^{i\sqrt{k_S^2 - k_T^2}\Delta z}\mathcal{F}\{\chi_j^{SS}(x, y)\mathbf{u}^S(x, y, z_j, \omega) \\
+ \chi_j^{PS}(x, y)\mathbf{u}^P(x, y, z_j, \omega)\}\},
\tag{2.3}
$$

where u^P and u^S represent the displacements of the P and S wavefields, k_P and k_S are the P and S wavenumbers and $\chi^{mn}(x, y)$ denote the complex phase-screen functions with m and n the incoming and outgoing wavefields respectively.

2.2 Wu's derivation of the elastic wave complex-screen approach

The derivation of the elastic complex screen for one–way elastic wave propagation by Wu (1994) is a highly complex mathematical formulation. Most readers find that the complicated reasoning results in a general lack of understanding which manifests itself in an inabilty to both see and exploit the underlying properties of the final equations.

The method can be considered in two parts, firstly Wu (1994) derives the thin slab formulation by applying the Born approximation to the linear homogeneous elastic equation of motion. Application of a parabolic small-angle approximation to the thin screen formulation equations result in the elastic complex screen formulation. This achieves significant run-time improvements over other full-waveform modelling techniques.

Over the next few sections I will briefly discuss the steps Wu (1994) undertook during his complex mathematical derivation to provide justification for the geometrical approach employed throughout the remainder of this study.

2.2.1 Developing the method

2.2.1.1 Born scattering in elastic media

The linear heterogeneous elastic equation of motion can be expressed as (Aki and Richards, 1980)

$$\rho \frac{\partial^2 u_i}{\partial t^2} - \frac{\partial}{\partial x_j} \left(c_{ijpq} \frac{\partial u_p}{\partial x_q} \right) = S_i \left(\mathbf{x}, t \right), \tag{2.4}$$

in the time-space domain, and can be recast into the temporal frequency-space domain as

$$-\omega^2 \rho u_i - \frac{\partial}{\partial x_j} \left(c_{ijpq} \frac{\partial u_p}{\partial x_q} \right) = S_i \left(\mathbf{x}, \omega \right), \tag{2.5}$$

where ρ is the density, c_{ijpq} is the 4-D elastic tensor relating the stress field to the strain, $\mathbf{x}$ is the spatial position vector and S_i is the source term which during this derivation will be considered absent (equal to zero).

The density and the elastic parameters in a perturbed medium are expressed as the sum of the background values (in a homogeneous medium) and a perturbation,

$$\rho \left(\mathbf{x} \right) = \rho_0 + \delta \rho, \tag{2.6}$$

$$c \left(\mathbf{x} \right) = c_0 + \delta c. \tag{2.7}$$

If it is assumed that the total field, $\mathbf{u}$, is split in a similar fashion, then one can suppose that this field is expressed as,

$$\mathbf{u} \left(\mathbf{x} \right) = \mathbf{u_0} \left(\mathbf{x} \right) + \mathbf{U} \left(\mathbf{x} \right), \tag{2.8}$$

where u_0 is the component representing the field in the homogeneous, unperturbed background and U is the scattered field developed as a consequence of the heterogeneity. It can also be assumed that the background field satisfies a relationship similar to equation 2.4,

$$\rho_0 \frac{\partial^2 u_{0i}}{\partial t^2} - \frac{\partial}{\partial x_j} \left(c_{0ijpq} \frac{\partial u_{0p}}{\partial x_q} \right) = 0. \tag{2.9}$$

Inserting equations 2.6 and 2.7 into equation 2.4 and expressing $\frac{\partial^2 u_i}{\partial t^2}$ as $\ddot{u}_i$ yields,

$$\rho_0 \ddot{u}_i + \delta\rho \ddot{u}_i - \frac{\partial}{\partial x_j} \left(c_{0ijpq} \frac{\partial u_p}{\partial x_q} \right) - \frac{\partial}{\partial x_j} \left(\delta c_{ijpq} \frac{\partial u_p}{\partial x_q} \right) = S_i\left(\mathbf{x}, t\right) = 0. \tag{2.10}$$

Next an additional source term $S_i'\left(\mathbf{x}, t\right)$ is defined, representing any real source term and additional sources due to perturbation in the medium and the field,

$$S_i'\left(\mathbf{x}, t\right) = S_i\left(\mathbf{x}, t\right) - \delta\rho \ddot{u}_i + \frac{\partial}{\partial x_j} \left(\delta c_{ijpq} \frac{\partial u_p}{\partial x_q} \right). \tag{2.11}$$

This can be equivalently expressed by rearranging equation 2.10 as

$$S_i'\left(\mathbf{x}, t\right) = \rho_0 \ddot{u}_i - \frac{\partial}{\partial x_j} \left(c_{0ijpq} \frac{\partial u_p}{\partial x_q} \right), \tag{2.12}$$

and taking equation 2.12 and inserting equation 2.8 results in

$$S_i'\left(x, t\right) = \rho_0 \ddot{u}_{0i} + \rho_0 \ddot{U}_i - \frac{\partial}{\partial x_j} \left(c_{0ijpq} \frac{\partial u_{0p}}{\partial x_q} \right) - \frac{\partial}{\partial x_j} \left(c_{0ijpq} \frac{\partial U_p}{\partial x_q} \right). \tag{2.13}$$

Application of equations 2.9 and 2.11 produces

$$\rho_0 \ddot{U}_i - \frac{\partial}{\partial x_j} \left(c_{0ijpq} \frac{\partial U_p}{\partial x_q} \right) = -\delta\rho \ddot{u}_i + \frac{\partial}{\partial x_j} \left(\delta c_{ijpq} \frac{\partial u_p}{\partial x_q} \right), \tag{2.14}$$

which is equivalent to equation 11 in Wild and Hudson (1998). The left hand side of equation 2.14 represents a set of sources on the unperturbed background medium. Adopting the usual notation where

$$\mathcal{L}_i\left(\mathbf{u}, c, \rho; \mathbf{x}\right) \equiv \rho \ddot{u}_i - \frac{\partial}{\partial x_j}\left(c_{ijpq}\frac{\partial u_p}{\partial x_q}\right),$$

(2.15)

the scattered field solution can be derived by multiplying the Green's function G for a homogeneous unbounded medium by the right hand side of equation 2.14 and integrating over all the individual sources,

$$U_n\left(\mathbf{x}\right) = -\sum_m \iiint_V \mathcal{L}_m\left(\mathbf{u}, \delta c, \delta\rho; \xi\right)\mathbf{G}_{mn}\left(x - \xi\right)dV\left(\xi\right).$$

(2.16)

2.2.1.2 Thin slab formulation

Wu (1994) then proceeds to divide the medium up into a series of plane slabs perpendicular to the primary direction of propagation. This simple redistribution of the model space allows for a couple of simple approximations to be introduced. Firstly, since the method is derived for one-way elastic wave propagation the incoming field for a chosen screen is simply the outgoing field from the previous screen combined with equivalent sources for any heterogeneities within the slab. From this assumption it follows that the integral is no longer global, and instead need only be performed over the chosen slab,

$$U_n\left(x', y', z'_{j+1}\right) = -\sum_m \int_x\int_y\int_{z_j}^{z_{j+1}}\mathcal{L}_m\left(\mathbf{u_0}, \delta c, \delta\rho; x, y, z\right) \times$$
$$\mathbf{G}_{mn}\left(x', y', z'_{j+1}; x, y, z\right)dxdydz.$$

(2.17)

Secondly, the Born approximation assumes that the total field, u, can be replaced by the background field, u_0, in equation 2.14. If the slabs are chosen to be thin enough for the Born approximation to be valid [1] then all the terms in the equivalent source are now known and the scattered field, U, can be calculated at the output to the slab under consideration.

The output field must also contain the background field at the outgoing face of the slab. This is calculated by propagating the background field, or

---

[1] The scattered field must be small in comparison with the incident field. In general a phase deviation of less than 1 rad should be observed from the passage of the wave through the slab (Wu, 1989)

more accurately the total field, at the input face across the slab by applying a multiplication in the transverse wavenumber domain. Wu (1994) labels the derivation up to this point as the thin slab formulation and whilst the method is accurate for a wide angular range it fails to offer significant run time advantages over other full waveform modelling techniques. The reason for this perceived failure is because the technique necessitates an integral over every transverse wavenumber on the input screen for each transverse wavenumber on the output screen. This, coupled with the need to propagate the energy across the slab at each stage, led Wu (1994) to conclude that additional approximations were required in order to render the method workable.

2.2.1.3 Deriving the complex-screen

Having noticed that the limiting factor in the derivation of the thin screen formulation was the computational complexity of the integral over the transverse spatial frequencies, Wu (1994) introduced a parabolic small angle approximation. This, simply put, reduced this integral to a convolution in the transverse wavenumber domain. Noting that a convolution in the transverse wavenumber domain could equivalently be expressed as a multiplication in the spatial domain led to construction of equations of the form shown in 2.2 and 2.3. Here the wavefield is subjected to repeated multiplications in the transverse wavenumber and spatial domains for each screen. The domain can be switched quickly using fast Fourier transforms giving the technique a run-time advantage of 2 to 3 orders of magnitude over conventional 3D finite difference methods (Wu, 1994).

Assuming a primary direction of propagation in the z-direction the elastic complex screen formulae derived by Wu (1994) are as follows,

$$\tilde{\mathbf{u}}^P\left(k_x, k_y, z_{j+1}, \omega\right) = e^{i\sqrt{k_\alpha^2 - k_T^2}\Delta z}\left\{\tilde{\mathbf{u}}^{PP}\left(k_x, k_y, z_j, \omega\right) + \tilde{\mathbf{u}}^{SP}\left(k_x, k_y, z_j, \omega\right)\right\},$$

$$(2.18)$$

$$\tilde{\mathbf{u}}^S\left(k_x, k_y, z_{j+1}, \omega\right) = e^{i\sqrt{k_\beta^2 - k_T^2}\Delta z}\left\{\tilde{\mathbf{u}}^{SS}\left(k_x, k_y, z_j, \omega\right) + \tilde{\mathbf{u}}^{PS}\left(k_x, k_y, z_j, \omega\right)\right\}, \quad (2.19)$$

where,

$$\tilde{\mathbf{u}}^{PP}\left(k_x, k_y, z_j, \omega\right) = \hat{\mathbf{k}}_\alpha \hat{\mathbf{k}}_\alpha \cdot F\left\{\chi_j^{PP}\left(x, y\right) \mathbf{u}^P\left(x, y, z_j\right)\right\}, \qquad (2.20)$$

$$\tilde{\mathbf{u}}^{SP}\left(k_x, k_y, z_j, \omega\right) = \hat{\mathbf{k}}_\alpha \hat{\mathbf{k}}_\alpha \cdot F\left\{\chi_j^{SP}\left(x, y\right) \mathbf{u}^S\left(x, y, z_j\right)\right\}, \qquad (2.21)$$

$$\tilde{\mathbf{u}}^{SS}\left(k_x, k_y, z_j, \omega\right) = \left(1 - \hat{\mathbf{k}}_\beta \hat{\mathbf{k}}_\beta\right) \cdot F\left\{\chi_j^{SS}\left(x, y\right) \mathbf{u}^S\left(x, y, z_j\right)\right\}, \qquad (2.22)$$

$$\tilde{\mathbf{u}}^{PS}\left(k_x, k_y, z_j, \omega\right) = \left(1 - \hat{\mathbf{k}}_\beta \hat{\mathbf{k}}_\beta\right) \cdot F\left\{\chi_j^{PS}\left(x, y\right) \mathbf{u}^P\left(x, y, z_j\right)\right\}, \qquad (2.23)$$

and

$$\chi_j^{PP}\left(x, y\right) = 1 - ik_\alpha \Delta z \frac{\delta\alpha}{\alpha_0}\left(x, y, z_j\right), \qquad (2.24)$$

$$\simeq e^{-ik_\alpha \Delta z \frac{\delta\alpha}{\alpha_0}\left(x, y, z_j\right)}, \qquad (2.25)$$

$$\chi_j^{SP}\left(x, y\right) = -ik_\alpha \eta^* \Delta z \left\{\frac{\delta\beta}{\beta_0}\left(x, y, z_j\right) + \left(\frac{\beta_0}{\alpha_0} - \frac{1}{2}\right)\frac{\delta\mu}{\mu_0}\left(x, y, z_j\right)\right\}, \qquad (2.26)$$

$$\chi_j^{SS}\left(x, y\right) = 1 - ik_\beta \Delta z \frac{\delta\beta}{\beta_0}\left(x, y, z_j\right), \qquad (2.27)$$

$$\simeq e^{-ik_\beta \Delta z \frac{\delta\beta}{\beta_0}\left(x, y, z_j\right)}, \qquad (2.28)$$

$$\chi_j^{PS}\left(x, y\right) = -ik_\beta \eta \Delta z \left\{\frac{\delta\beta}{\beta_0}\left(x, y, z_j\right) + \left(\frac{\beta_0}{\alpha_0} - \frac{1}{2}\right)\frac{\delta\mu}{\mu_0}\left(x, y, z_j\right)\right\}, \qquad (2.29)$$

with,

$$\eta \equiv \mathrm{sinc}\left\{\left(k_\beta - k_\alpha\right)\Delta z/2\right\} e^{-i\left(k_\beta - k_\alpha\right)\Delta z/2}, \qquad (2.30)$$

where the complex conjugate of η is η^*. Finally the unit vectors $\hat{\mathbf{k}}_\alpha$ and $\hat{\mathbf{k}}_\beta$ have components proportional to the transverse wavenumber k_T and to $\sqrt{k_\alpha^2 - k_T^2}$ for $\hat{\mathbf{k}}_\alpha$ and to $\sqrt{k_\beta^2 - k_T^2}$ for $\hat{\mathbf{k}}_\beta$.

2.3 Wild and Hudson's geometrical approach to the elastic complex screen

Wild and Hudson (1998) noted that the consequence of perturbations in the density and/or the elastic constants only influenced the spatial phase-screen function part of the modelling algorithm. The propagation step was independent of their influence meaning that the effect of heterogeneities is always considered at a fixed position (i.e. a screen). This effective repositioning of diffractors means that energy propagating at all angles through certain position, (x, y), on a screen will be affected by the perturbations equally. Yet it should be noted that the propagation across the background medium is calculated as a function of angle since position within the wavenumber domain can be considered a proxy for angle.

2.3.1 Developing the method

The initial construction required when considering the Wild and Hudson (1998) derivation is that of a perturbed slab in a background medium. The elastic parameters of the medium are evaluated at the entry point and are assumed to be constant between there and the point of exit from the slab. The background medium is represented by the P-wave velocity, α_0, the S-wave velocity, β_0, and the density, ρ_0. Since the elastic parameters (λ, μ) and density are only perturbed by small amounts the slab is represented by the P-wave velocity, $\alpha_0 + \delta\alpha$, the S-wave velocity, $\beta_0 + \delta\beta$, and the density, $\rho_0 + \delta\rho$, with respect to the unperturbed region. Figure 2.1 (a) shows how the incoming energy can be represented as a series of plane waves incident upon a plane homogeneous layer. If this mindset is pursued it leads to the constuction of figures 2.1 (b) and 2.1 (c) for an incident P- and S-wave. Considering only one-way forward propagation at this stage, energy will be scattered at both the incoming and outgoing interfaces of the slab. It is important to realise that within a coupled P- and S-wave system only SV polarisation is relevant during the derivation. S-waves polarised in the horizontal plane (into the page) form a separate, unique SH system. This study considers a single S-wave vector field, since only the SV component will convert to a P-wave at an interface and vice versa.
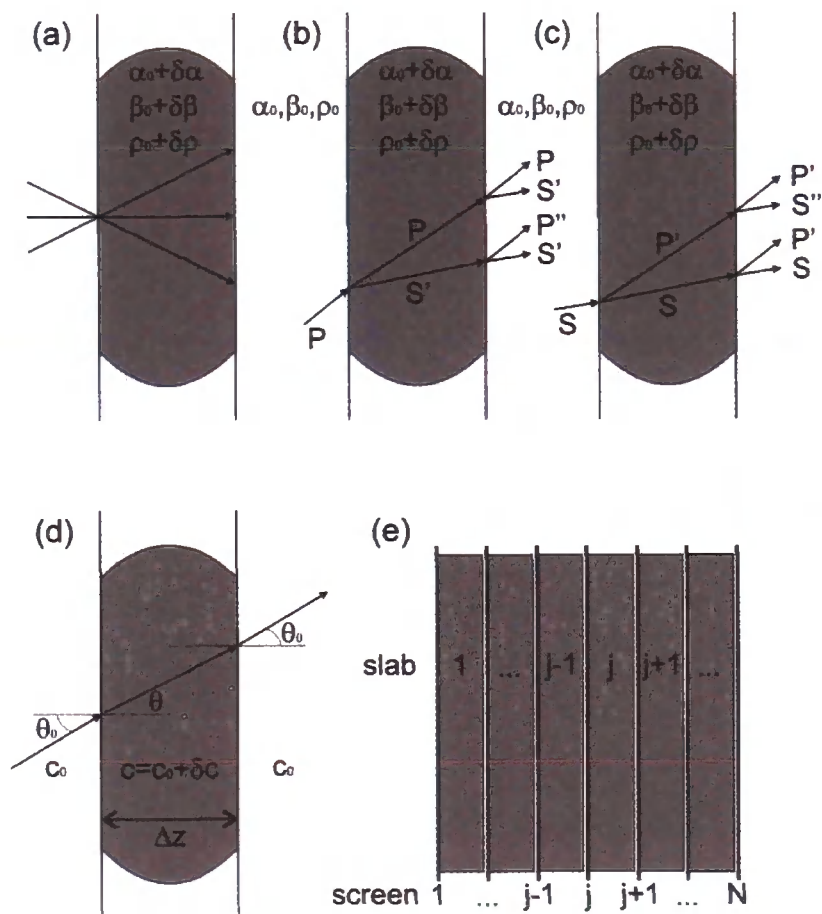
Figure 2.1: *The phase-screen method highlighting the effective repositioning of the model space to a series of screens (after Wild and Hudson (1998))*

Therefore throughout the remainder of this work the term S-wave will be used to represent the SV component of the field unless implicitly stated otherwise.

At each interface the incident ray is split into two ongoing rays (one P and one S) and each of these rays is, upon transmission at the second interface, split into two further rays. Figures 2.1 (b) and 2.1 (c) provide a graphical representation of this scattering.

The fundamental aim of the geometrical construction is to derive the multiplication factor to be applied spatially to the wavefield at the entry point of the slab that combines the effects of all the perturbations within the slab. This will then be followed by a plane wave propagation across the slab at the background velocity.

Luckily the phase-screen function multiplication can be divided into a phase effect and an amplitude effect that can be considered separately. It is

at this stage that Wild and Hudson implicitly state the assumptions that will be carried through the derivation:

1. The perturbations within the slab are small enough that they may be exclusively considered as a first order effect within the fractional perturbations;

2. They also make a first order angular approximation which will be used in the phase effect calculation.

2.3.2 Phase and amplitude considerations

2.3.2.1 Phase

Figure 2.1 (d) shows a ray crossing a perturbed slab of thickness Δz incident at an angle θ_0. If the background velocity is c_0 (which can be thought of as either a P- or S-wave velocity) and the perturbed slab has velocity $c = c_0 + \delta c$, the angular direction of propagation within the slab can be computed by Snell's law,

$$\frac{\sin \theta_0}{c_0} = \frac{\sin \theta}{c}. \tag{2.31}$$

Wild and Hudson (1998) then consider the transit times to cross the perturbed slab,

$$t = \frac{\Delta z}{c \cos \theta}, \tag{2.32}$$

and the equivalent time if the slab were unperturbed,

$$t_0 = \frac{\Delta z}{c_0 \cos \theta_0}. \tag{2.33}$$

Combining these results produces

$$t = t_0 \frac{c_0 \cos \theta_0}{c \cos \theta}. \tag{2.34}$$

They next calculate that, to first order in fractional velocity, equation 2.31, Snell's law, can be expressed as

$$\cos\theta = \cos\theta_0 \left(1 - \frac{\delta c}{c_0}\tan^2\theta_0\right),$$ (2.35)

and with this, revise equation 2.34, initially deriving

$$t = t_0 \left(1 + \frac{\delta c}{c_0}\right)^{-1} \left(1 - \frac{\delta c}{c_0}tan^2\theta_0\right)^{-1},$$ (2.36)

and then apply a first order approximation in fractional velocity to produce

$$t = t_0 \left\{1 - \frac{\delta c}{c_0}\left(1 - \tan^2\theta_0\right)\right\}.$$ (2.37)

The change in phase that ensues from a variation in transit time can be expressed as

$$\delta\phi = (t - t_0)\, c_0 k.$$ (2.38)

Combining the results from equations 2.32 and 2.37 with equation 2.38 the final phase correction is derived as

$$\delta\phi(x,y) = -k\Delta z \frac{\delta c}{c_0}(x,y)\left(\frac{1 - \tan^2\theta_0}{\cos\theta_0}\right),$$ (2.39)

where k is the background wavenumber.

2.3.2.2 Amplitude

Referring back to figures 2.1 (b) and 2.1 (c) we can use the plane wave, plane interface transmission coefficients derived by Zoeppritz (1919) to determine the amplitude of the ongoing waves at the interfaces. The Zoeppritz solutions provide exact responses, as a function of angle, for the partitioning of energy at an interface. Wild and Hudson (1998) however adopt approximations for these

solutions, firstly they continue working to first order in the fractional perturbations and later, make a small angle approximation. Aki and Richards (1980) provide the best first order approximations for the transmitted wavefields and these can be recast as

$$T^{PP} = 1 - \frac{\delta\rho}{2\rho_0} - \frac{\delta\alpha}{2\alpha_0}\left(1 - \tan^2 i\right), \qquad (2.40)$$

$$T^{SS} = 1 - \frac{\delta\rho}{2\rho_0} - \frac{\delta\beta}{2\beta_0}\left(1 - \tan^2 j\right), \qquad (2.41)$$

$$T^{PS} = -\frac{\sin i}{\cos j}\left\{\frac{\delta\beta}{\beta_0} + \frac{\delta\mu}{\mu_0}\left(\sin^2 j + \frac{\beta_0}{\alpha_0}\cos i\cos j - \frac{1}{2}\right)\right\}, \qquad (2.42)$$

$$T^{SP} = \frac{\sin j}{\cos i}\left\{\frac{\delta\beta}{\beta_0} + \frac{\delta\mu}{\mu_0}\left(\sin^2 j + \frac{\beta_0}{\alpha_0}\cos i\cos j - \frac{1}{2}\right)\right\}, \qquad (2.43)$$

where the angle i is the incident arrival angle for the P wave in the background medium and j is the equivalent angle for an incident S wave.

2.3.2.3   Deriving the phase screen complex functions

In order to utilise the phase-screen approach four complex phase-screen functions are required (a non-converted and a converted function for each of the incoming wave polarisations). Initially a small-angle approximation, taking only terms up to first order in ray angle, is applied to equation 2.39 and equations 2.40 - 2.43. This produces the small-angle, weak-scattering phase-shift correction,

$$\delta\phi\left(x,y\right) = -k\Delta z\frac{\delta c}{c_0}\left(x,y\right), \qquad (2.44)$$

and the small-angle, weak-scattering amplitude corrections,

$$T^{PP} = 1 - \frac{\delta\rho}{2\rho_0} - \frac{\delta\alpha}{2\alpha_0}, \qquad (2.45)$$

$$T^{SS} = 1 - \frac{\delta\rho}{2\rho_0} - \frac{\delta\beta}{2\beta_0}, \qquad (2.46)$$

$$T^{PS} = -\sin i \left\{ \frac{\delta\beta}{\beta_0} + \frac{\delta\mu}{\mu_0} \left(\frac{\beta_0}{\alpha_0} - \frac{1}{2} \right) \right\}, \qquad (2.47)$$

$$T^{SP} = \sin j \left\{ \frac{\delta\beta}{\beta_0} + \frac{\delta\mu}{\mu_0} \left(\frac{\beta_0}{\alpha_0} - \frac{1}{2} \right) \right\}. \qquad (2.48)$$

Referring back to figure 2.1 (b) it can be seen that the outgoing non-converted P wavefield comprises the rays labelled both P and P″. Considering these ray paths separately, we first evaluate the ray labelled P. The phase-screen function is constructed, starting with $T^{PP+}\hat{T}^{PP-}e^{i\delta\phi_\alpha}$. Since the media on either side of the perturbed slab are the same, the transmission coefficients will be identical except that the sign of the fractional perturbations will be switched. Firstly, it is noted that computing $T^{PP+}T^{PP-}$ and applying the weak scattering approximation will give unity since all first order terms vanish. Secondly, the phase correction part of the function, calculated using equation 2.44, will be amended to $e^{i\delta\phi_\alpha}$ for P-wave forward scattering. If we now consider the ray P″, the phase screen function will be derived from $T^{PS+}T^{SP-}e^{i\delta\phi_\beta}$. However, when notice is taken of equations 2.47 and 2.48 it is easily seen that the resultant function will be at least second order in fractional perturbations so the entire term can be neglected. Therefore the wavefield derived after transformation to the wavenumber domain, prior to propagation, will be calculated, to first order, as

$$\tilde{\mathbf{u}}^{PP} \left(k_x, k_y, z_j, \omega \right) = \hat{\mathbf{k}}_\alpha \hat{\mathbf{k}}_\alpha \cdot \mathcal{F} \left\{ e^{ik_\alpha \Delta z \delta\alpha/\alpha_0} \mathbf{u}^P \left(x, y, z_j, \omega \right) \right\}, \qquad (2.49)$$

where the $\hat{\mathbf{k}}_\alpha \hat{\mathbf{k}}_\alpha$ factor is added to ensure the correct polarisation.

The P- to S-wave converted field is constructed in a similar way, again attention is drawn to figure 2.1 (b), where the relevant rays are both labelled S′ and it is noted that both routes will contain terms of first-order fractional perturbations. An additional consideration at this stage is that the S′ wavefields will be summed with the non-converted S wavefield prior to the propagation step and as such the component that crosses the medium as a P wave will require an additional correcting term $e^{i(k_\alpha - k_\beta)\Delta z}$ which allows for the difference

between the P and S wave background velocity to first order. Therefore, the ratio of scattered to incident energy for the P-to-S converted wavefield is given by

$$A^{PS} = T^{PS+}T^{SS-}e^{i\delta\phi_\beta} + e^{i\left(k_\alpha - k_\beta\right)\Delta z}T^{PP+}T^{PS-}e^{i\delta\phi_\alpha}, \qquad (2.50)$$

and when the correct terms for the amplitude transmission coefficients (equations 2.45 to 2.48) are applied this reduces to

$$A^{PS} = -\sin i \left(1 - e^{i\left(k_\alpha - k_\beta\right)\Delta z}\right) \left(\frac{\delta\beta}{\beta_0} + \frac{\delta\mu}{\mu_0}\left(\frac{\beta_0}{\alpha_0} - \frac{1}{2}\right)\right), \qquad (2.51)$$

once the second order terms have been neglected. In this case the polarisation of the scattered S wave is orthogonal to the scattered unit wave vector $\hat{\mathbf{k}}_\beta$ so we construct a vector in the required direction from the incident P ray through

$$\left(1 - \hat{\mathbf{k}}_\beta\hat{\mathbf{k}}_\beta\right) \cdot \tilde{\mathbf{u}}^P. \qquad (2.52)$$

Since we have now defined the component of $\tilde{\mathbf{u}}^P$ orthogonal to $\hat{\mathbf{k}}_\beta$ we have a vector in the correct direction, but with the wrong magnitude. We can express the angle between $\tilde{\mathbf{u}}^P$ and $\hat{\mathbf{k}}_\beta$ as $i - j$ giving the magnitude of the vector expressed in equation 2.52 as

$$\left(\sin i \cos j - \cos i \sin j\right) \left|\tilde{\mathbf{u}}^P\right|, \qquad (2.53)$$

and to first order in i and j this becomes

$$\left(1 - \frac{\beta_0}{\alpha_0}\right) \sin i \left|\tilde{\mathbf{u}}^P\right|. \qquad (2.54)$$

Finally a vector is constructed in the direction of 2.52 which varies in magnitude from $\left|\tilde{\mathbf{u}}^P\right|$ by the forward scattering ratio expressed in 2.51

$$
\begin{aligned}
\tilde{\mathbf{u}}^{PS}\left(k_x, k_y, z_j, \omega\right) = {}& \left(1 - \hat{\mathbf{k}}_\beta \hat{\mathbf{k}}_\beta\right) \cdot \mathcal{F}\Bigg\{ \left(1 - e^{i\left(k_\alpha - k_\beta\right)\Delta z}\right) \\
& \times \left(\frac{\partial \beta}{\beta_0} + \frac{\partial \mu}{\mu_0}\left(\frac{\beta_0}{\alpha_0} - \frac{1}{2}\right)\right) \\
& \times \left(1 - \frac{\beta_0}{\alpha_0}\right)^{-1} \mathbf{u}^P\left(x, y, z_j, \omega\right) \Bigg\}.
\end{aligned}
\tag{2.55}
$$

Following identical principles the S-to-S and the S-to-P phase-screen forward scattering functions are calculated. The S-to-S function equivalent to 2.49 is

$$
\tilde{\mathbf{u}}^{SS}\left(k_x, k_y, z_j, \omega\right) = \left(1 - \hat{\mathbf{k}}_\beta \hat{\mathbf{k}}_\beta\right) \cdot \mathcal{F}\left\{ e^{ik_\beta \Delta z \partial \beta / \beta_0} \mathbf{u}^{SS}\left(x, y, z_j, \omega\right) \right\},
\tag{2.56}
$$

whilst S-to-P function (equivalent to 2.55) is

$$
\begin{aligned}
\tilde{\mathbf{u}}^{SP}\left(k_x, k_y, z_j, \omega\right) = {}& \left(\hat{\mathbf{k}}_\alpha \hat{\mathbf{k}}_\alpha\right) \cdot \mathcal{F}\Bigg\{ \left(1 - e^{1\left(k_\beta - k_\alpha\right)\Delta z}\right) \\
& \times \left(\frac{\partial \beta}{\beta_0} + \frac{\partial \mu}{\mu_0}\left(\frac{\beta_0}{\alpha_0} - \frac{1}{2}\right)\right) \\
& \times \left(\frac{\alpha_0}{\beta_0} - 1\right)^{-1} \mathbf{u}^P\left(x, y, z_j, \omega\right) \Bigg\}.
\end{aligned}
\tag{2.57}
$$

2.3.2.4 Formulating a forward modelling tool

The derivation of the elastic complex screen presented thus far is a useful tool for calculating the propagation through a single weakly scattering medium at small-angle. It should be made clear that the results presented above provide the response from a single perturbed region within a background medium. In order for the method to develop into a useful forward modelling tool, capable of performing in more realistic environments, additional steps are required.

The necessary progression is to consider the model not as a series of slabs, but rather as a series of screens (or interfaces). In this set-up, shown in figure 2.1 (e) it is not necessary to calculate the scattering effects at both the input and output faces of the slab during a single calculation. Using the wavefield at the

output of one screen, j, as the input to the next, $j + 1$, the amplitude corrections can be determined as a consequence of the reflection and transmission effects between the two local rock types, as is the case for any interface.

The phase effect, the shift in the wavenumber domain from one screen to the next, is now undertaken at the average velocity of the screen meaning the spatial phase correction and is no longer calculated with respect to a background medium. It is instead determined with respect to the difference between the local (x, y, z) P- or S-wave velocity and the average velocity for the time taken to cover the region between the two screens.

This approach also offers the advantage of removing the $e^{i(k_\beta - k_\alpha)\Delta z}$ component of the phase-screen function in equations 2.55 and 2.57 since the propagation of P- and S-wave energy can be combined at the output of the interface. As such, the energy will be propagated at the correct P- or S-wave velocity without the need for this correction.

2.3.2.5 Inclusion of backscattered energy

Once the model space is considered as a series of diffracting screens rather than as a sequence of interfaces the next logical development is the inclusion of backscattered energy. The initial attempts to produce a fully elastic two-way complex screen technique used the Born approximation and a small angle approximation to calculate the reflections (Xie and Wu, 1995). They built upon the work of Wu and Huang (1995) who had previously published an acoustic phase-screen technique that incorporated backscattered energy. This approach, based on the de Wolf approximation provides the template for storing and propagating the reflected energy that will be used in this study. The approach Wild and Hudson (1998) rely upon involves reversibly backpropagating the reflected components of the wavefield alongside the forward propagation and will be unsuitable for the additional developments discussed in this thesis.

The starting point for the extension to backpropagation comes from the calculation of the first order Zoeppritz solutions for the backscattered energy. If these are considered only to first order in angle they can be expressed as (analogous to equations 2.45 - 2.48)

$$R^{PP} = \frac{\delta\rho}{2\rho_0} + \frac{\delta\alpha}{2\alpha_0}, \tag{2.58}$$

$$R^{SS} = -\frac{\delta\rho}{2\rho_0} - \frac{\delta\beta}{2\beta_0}, \tag{2.59}$$

$$R^{PS} = -\sin i \left(\left(\frac{1}{2} + \frac{\beta_0}{\alpha_0} \right) \frac{\delta\rho}{\rho_0} + 2\frac{\beta_0}{\alpha_0}\frac{\delta\beta}{\beta_0} \right), \tag{2.60}$$

$$R^{SP} = -\sin j \left(\left(\frac{1}{2} + \frac{\beta_0}{\alpha_0} \right) \frac{\delta\rho}{\rho_0} + 2\frac{\beta_0}{\alpha_0}\frac{\delta\beta}{\beta_0} \right). \tag{2.61}$$

Since the model is now divided into a series of perpendicular screens it is straightforward to think of the reflection as coming from the interface between two differing media (if the media are the same, the entire wavefield will propagate as expected). With the non-converted and converted P wavefields combined prior to the propagation (and the same for the S-wavefields) and with the phase shift and inverse transforms applied, phase-screen functions for the eight different energy partitions ($T^{PP}, T^{PS}, T^{SP}, T^{SS}, R^{PP}, R^{PS}, R^{SP}, R^{SS}$) can be utilised.

The forward propagating fields will continue on through the model, whereas the backscattered energy is left behind on the topside of each interface. The two reflected P fields (P-to-P and S-to-P) can be combined, as can the two reflected S fields (S-to-S and P-to-S) and, in the approach adopted throughout this project, stored locally for each screen. Once the forward propagating field has successfuly passed through the entire model-space then the reverse propagation is initiated. Starting on the topside of the lowest screen the fields are propagated in a manner identical to the forward propagation algorithm. Yet prior to the phase propagation step any additional reflected energy is added to the wavefield at each screen.

The validity of the elastic phase-screen algorithm has been justified previously. Wu (1994) showed that accuracy of the forward propagation whilst Wild and Hudson (1998) showed the reliability of extending the idea to two-way propagation (albeit using a different algorithm, but the same principles).

2.4   Andriatsitohaina's general angular approach

Andriatsitohaina (2004) first proposed the wide angle phase-screen technique based upon a geometrical construction during the work on his unpublished thesis. The suggestion being that if a screen were composed of N nodes then by dividing the wavefield into N separate wavefields and transforming each individually angular information could be carried from the wavenumber domain into the spatial domain. This method is similar to the problematic thin screen formulation of Wu (1994). Andriatsitohaina (2004) proposed a filtering and decomposition technique that although computationally expensive provides the basis for the methods developed in this thesis.

The method proceeds as follows for a single screen in a 2D model, with a wavefield $\tilde{u}_j(\omega, \mathbf{k})$ in the wavenumber domain:

- Since the modelling is performed monochromatically it allows the determination of the slowness at each node from the transverse wavenumber $p = \frac{k_T}{\omega}$ when in this domain.

- The mean slowness, μ_G, and the standard deviation, σ_G, of the distibution are calculated for each node. The mean is simply the slowness value at each position since there will be a filter at every node and $\sigma_G = \sqrt{\frac{1}{(N-1)} \sum_{i=0}^{N-1} [p - \mu_G]}$.

- For every node a Gaussian filter $P(p)$ is built, and the wavefield is weighted with this filter, $\tilde{\tilde{u}}_j(\omega, \mathbf{k}) = P(p)\tilde{u}_j(\omega, \mathbf{k})$. This requires storage of N filtered wavefields all consisting of N nodes.

- The wavefield $\tilde{\tilde{u}}_j(\omega, \mathbf{k})$ is decomposed to $\tilde{\tilde{u}}_x(\omega, \mathbf{k})$ and $\tilde{\tilde{u}}_z(\omega, \mathbf{k})$ using the relationships $\tilde{u}_x = \tilde{u} \sin\theta$ and $\tilde{u}_z = \tilde{u} \cos\theta$ where θ is the take-off angle.

- Application of an inverse FFT to $\tilde{\tilde{u}}_x(\omega, \mathbf{k})$ and $\tilde{\tilde{u}}_z(\omega, \mathbf{k})$ determines $\tilde{\tilde{u}}_x(\omega, \mathbf{x})$ and $\tilde{\tilde{u}}_z(\omega, \mathbf{x})$.

- The angle of propagation is calculated from $\sin\theta = \frac{\tilde{\tilde{u}}_x(\omega, \mathbf{x})}{\tilde{u}_j(\omega, \mathbf{k})}$ and it is noted that $p = \frac{\sin\theta}{v}$.

- The angular information is then used to determine the reflection and transmission coefficients since the rock types are known spatially. These

are applied to each of the N filtered wavefields at each of the N spatial positions.

2.4.1 Assessment of shortcomings

Previous versions of the phase-screen code have found numerous applications within the hydrocarbon industry and the traditional narrow angle version of the code works adequately when modelling target interfaces at depth. The run time advantages the method enjoys over other full waveform techniques have usually made up for the lack of accuracy at wide angles. The wide angle phase-screen technique based upon a geometrical construction proposed by Andriatsitohaina (2004) offered a method to overcome some of these problems but is a cumbersome technique that fails to solve many of the problems adequately.

In regions with lateral velocity variations the phase correction is applied as a 1D function and therefore deals with all arrivals the same regardless of direction. This leads to an increase in the error of the phase correction in regions of lateral velocity variation as a function of angle, a problem noted in the original phase-screen construction.

An additional problem with previous phase-screen modelling codes is that only isotropic rock types can be accurately modelled. In narrow angle versions of the code this is not a problem since the velocity variation with dip will be negligible in almost all cases. However, when considering a wider angular range this velocity variation will cause changes not only in the travel times of arrivals but also in the reflection and transmission of energy.

The main issue with the unpublished work of Andriatsitohaina (2004) is that the method lacks clarity and necessitates splitting each screen of N nodes into $N \times N$ nodes once all the filtered wavefields have been created. Additional storage, and run time, issues are created when each of the filtered wavefields are decomposed in to 2 or 3, for 2D and 3D modelling respectively, additional wavefields. This overcomplicated mechanism then requires the inverse Fourier transformation of all the filtered and decomposed wavefields in order to calculate the angle of propagation and apply the correct partitioning of energy calculations.

Another short coming, a consequence of the previous coding preferences of phase-screen modellers, is the decision to write the code in c. This results in a lack of portability when compared to the class structure available to $c++$ coding. In order to allow a user to determine the level of complexity required whilst modelling, it would be advantageous to write the code in a language that offers the maximum potential for development.

2.5   Source modelling

In realistic modelling environments a spherical wave originating from a point source is required. However, in reality it is difficult to model spherical or cylindrical waves. The approach adopted during this study is to express a spherical wave as the superposition of plane waves. This approach is taken from Aki and Richards (1980) and follows the subsequent argument.

Start with the inhomogeneous wave equation with a point source at the origin,

$$\frac{\partial^2 \phi}{\partial t^2} - c^2 \Delta^2 \phi = 4\pi \delta\left(\mathbf{x}\right) f\left(t\right), \tag{2.62}$$

and a source function with time dependence $f\left(t\right) = c^2 e^{i\omega t}$. The solution (Aki and Richards, 1980) for the potential function, ϕ, is

$$\phi\left(\mathbf{x}, t\right) = \frac{1}{R} e^{i\omega\left(\frac{R}{c} - t\right)}, \tag{2.63}$$

where $R = \sqrt{x^2 + y^2 + z^2}$. Aki and Richards (1980) note that equation 2.62 can also be solved using Fourier transform techniques and derive, for a spherical wave propagating from the origin at speed c,

$$\phi\left(\mathbf{x}, t\right) = \frac{e^{-i\omega t}}{2\pi^2} \int \int_{-\infty}^{\infty} \int \frac{e^{i\mathbf{k}\cdot\mathbf{x}}}{k^2 - \frac{\omega^2}{c^2}} dk_x dk_y dk_z. \tag{2.64}$$

Performing an integration in k_z, and following some complex mathematical arguments, the final decomposition reduces to the Weyl integral, with the integration performed over the horizontal wavenumbers,

$$\frac{1}{R}e^{i\omega\left(\frac{R}{c}\right)} = \frac{1}{2\pi} \int_{-\infty}^{\infty} \int_{-\infty}^{\infty} \frac{1}{k_z} e^{i(k_x x + k_y y + k_z |z|)} dk_x dk_y. \tag{2.65}$$

This result is immediately applicable to the phase screen method where the source is constructed in the horizontal wavenumber domain.

2.6 Seismic attenuation

Generally, during interpretation and modelling of seismic data, wavefield attenuation is expressed as the effective quality factor, Q_{eff}. In order to realistically model the response of the subsurface it is necessary to include a mechanism to simulate attenuation. The method adopted in this study is to individually assign each rock type an effective Q for P- and S-wave energy respectively. Assuming that Q_{eff} is independent of frequency over the limited spectral bandwidth used during seismic studies (Sams et al., 1997), the amplitude, $A(x)$, can be determined from the original amplitude, A_0, by

$$A(x) = A_0 e^{\frac{-\pi f z}{v Q_{eff}}}, \tag{2.66}$$

if a zero phase non-causal filter is applied.

2.7 Review of phase screen method development

The mathematically demanding elastic complex screen method developed by Wu (1994) provides the foundations for all future developments using phase-screen type modelling. Wild and Hudson (1998) revisited this work, extracting the fundamental principles behind the equations and expressing these using a geometrical construction technique that opened the method up to the geophysics community. This allowed less mathematically minded seismic modellers another tool with which to tackle the problem of wave propagation in complex rock volumes.

Wild and Hudson (1998) also developed a back-scattering algorithm analogous to the forward-scattering approach that allowed the technique to be

implemented for reflection seismology. This step-forward moved the technique under the radars of the hydrocarbon industry who saw an opportunity to utilise a relatively fast full waveform technique without the computational costs associated with finite difference and pseudo-spectral methods. However, the limitations of the method meant that it was unsuitable for some applications where investigation of non-normal raypaths is desired. Andriatsitohaina (2004) postulated ideas to develop a wide angle method based upon the same geometrical principles. Suggesting a split wavefield approach which provided a greater angular clarity, he failed to account for non-normal corrections in laterally varying media. His technique was also limited since the larger the model the greater the number of wavefield subsets, as the scheme necessitates separate wavefields for each node across a screen. This meant that the method proved unsuitable for any large 2D models and prohibitative for 3D modelling. As such, any additional developments must attempt to limit the effects on the overall run time of the modelling. If this fundamental advantage were lost the phase-screen technique would suffer in comparison with the numerical, number crunching techniques often employed for seismic modelling.

The desirable next steps forward were to create a fully functionable phase-screen code that correctly modelled non-normal raypaths but which had a control over run time. Additionally, a non-isotropic code would be most advantageous since many subsurface packages are intrinsically anisotropic. If these developments were applied the final logical step would be to use the phase-screen technique on a large scale industry problem assessing a real modern day problem in complex heterogeneous media.

Chapter 3

Phase screen development - angular effects

3.1 Development Aims

The aim of developing a phase-screen code that has the capacity to deal with an increased angular range, and can model amplitudes correctly at non-normal incidence is the primary driving force behind this section of the project. The work builds upon the efforts of Andriatsitohaina (2004) but produces a more robust and mathematically rigorous solution. The unpublished ideas of Andriatsitohaina (2004) described in section 2.4 still have a 1D phase correction for the variation between average and local velocity, and have no control on run time issues

3.2 Wide-angle development

3.2.1 Building upon the geometrical construction

In the Wild and Hudson (1998) derivation of the spatial domain correction they make two approximations. First, taking an average background velocity c_0 and a local phase velocity c the perturbation described in equation 2.7 is assumed. A weak scattering approximation is also applied to Snell's Law in equation 2.35. This approximation is applicable in regions without significant lateral velocity variations. Second, Wild and Hudson (1998) make a small–angle approximation reducing the phase correction, $\delta\phi = (t - t_0)\,\omega$, from equation 2.39 to equation 2.44.

This simplification is required in previous versions of the phase-screen modelling code because the phase correction is applied spatially as a 1-D vertical approximation, regardless of propagation direction. This is a consequence of the domain transform technique deployed during modelling. Since the entire wavefield is transformed from the wavenumber domain in a single step, the angular signature is removed from the data. The correction is calculated from the difference between the local velocity and the average layer velocity.

To remove this simplification, angular information is required for equation 2.39. This study develops an approach to enable conservation of angular information between wavenumber and spatial domains in order to allow calculation of exact phase corrections. This allows determination of correct travel times for non-normal offsets in regions of weak lateral heterogeneity. The method developed divides the wavefield in the wavenumber domain into a series of subsets, then transforms each subset of the wavefield individually allowing slowness information to be preserved, and therefore the angle of propagation is retained. The angular phase correction, equation 2.39, can now be applied on a node-by-node basis.

The wavefield is best divided into a series of Gaussian windows centered at regular intervals across the wavenumber domain grid; the mean value of the window is then used to determine the slowness of the subset. This slowness is then available for calculating the reflection and transmission coefficients as a function of angle. The partitioning of energy as a consequence of the horizontal wavenumber gives the enhanced technique an immediate advantage over the previous versions of the code and drops out of the geometrical construction method developed by Wild and Hudson (1998).

3.2.2 Construction of variable sized Gaussian subsets

Depending on the complexity of the model space, the number of wavefield subsets is varied. If the wavefield is divided into i subsets, then the jth subset, centred at k_j will be calculated by applying equation 3.1 or equation 3.2 across the whole wavenumber space.

$$MULT_j = \frac{1}{\sqrt{2\pi}} \frac{1}{\sigma_{k_x}} e^{-(k_j-k)^2/2\sigma_{k_x}^2} \qquad (3.1)$$

for 2D modelling, and

$$MULT_j = \frac{1}{2\pi} \frac{1}{\sqrt{\sigma_{k_x}^2 + \sigma_{k_y}^2}} e^{-\left(k_{x_j} - k_x\right)^2 / 2\sigma_{k_x}^2} e^{-\left(k_{y_j} - k_y\right)^2 / 2\sigma_{k_y}^2}, \quad (3.2)$$

during 3D modelling, where the standard deviation, σ, is equal to the spacing of the Gaussian means in the subscripted direction.

Figure 3.1 (a) shows the distribution of 21 Gaussians subsets on a 2D model whilst figure 3.1 (b) shows how the total energy of the wavefield is preserved across the entire wavenumber space, except approaching the positive and negative Nyquist wavenumbers where the amount of energy lost is proportional to the number of Gaussian subsets created. This also shows that the Gaussian windowed Fourier basis is no longer orthogonal and therefore results in some redundancy.

The splitting of the wavefield is possible with alternative distributions, (e.g. cosine), but the Gaussian window was chosen in this study because of the benefits it offers with Fourier transform methods; and because it provides a simple and robust approach when altering the window spacing on a screen-by-screen basis.

The capability to vary the number of Gaussian subsets ensures that a control on run time is developed but energy is not lost as a consequence. The number, and spacing, of Gaussian subsets can be constructed differently in x and y, if required, giving even greater user control.

3.2.3 Single point transforms

Greater angular accuracy can be achieved if the number of Gaussian subsets is increased. In the limit of this argument there is a Gaussian window centered on every node, but with a finite value (Gaussian tails) at every node across the grid as in Andriatsitohaina (2004). This means that for larger grids the time taken to calculate the required number of Fourier transforms is prohibitive. Instead of dividing the wavefield into Gaussian subsets in this limit this study proposes to transform the data on a node-by-node basis with
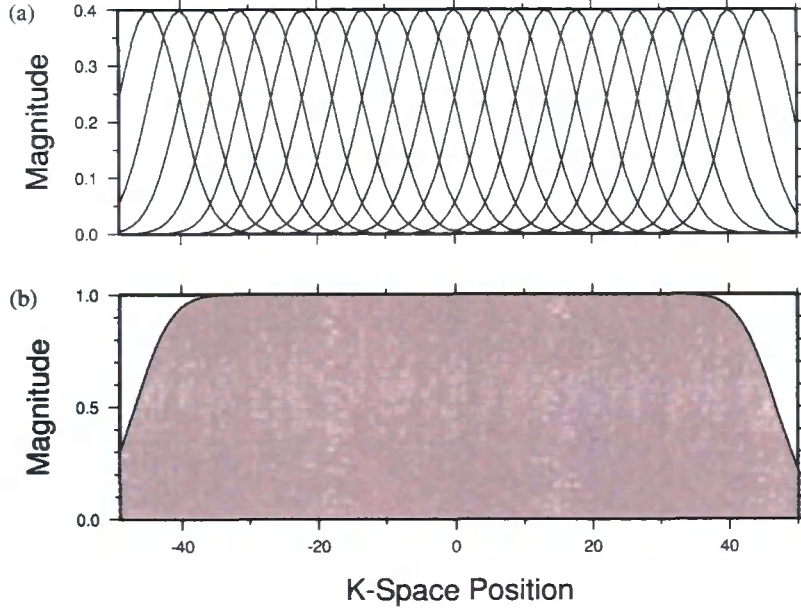
Figure 3.1: *Distribution of 21 Gaussian subsets on a 2D, 100 node screen in the wavenumber domain. (a) The spacing and position of the distributions; (b) the summation of the Gaussian subsets, showing loss of energy only at wavenumbers close to the Nyquist limit, where the wavefield is already damped to reduce Gibbs phenomena.*

$$A = \sqrt{Re\left(u\left(k_x, k_y, \omega\right)\right)^2 + Im\left(u\left(k_x, k_y, \omega\right)\right)^2}, \tag{3.3}$$

and

$$\phi = tan^{-1}\frac{Im\left(u\left(k_x, k_y, \omega\right)\right)}{Re\left(u\left(k_x, k_y, \omega\right)\right)}, \tag{3.4}$$

allowing the calculation of the spatial wavefield $u\left(x, y, \omega\right)$ from the wavefield in the wavenumber domain $u\left(k_x, k_y, \omega\right)$ by

$$u\left(x, y, \omega\right) = Ae^{-i\left(k_x x + k_y y + \phi\right)}. \tag{3.5}$$

Exact angular information is now available, because the angle of incidence can be calculated from

$$sin\theta = \frac{k_T c_0}{\omega}. \tag{3.6}$$

It is also necessary to implicitly state that this scheme, both the single point and Gaussian subsets transforms techniques, do not require the decomposition of the wavefield into additional orthogonal distributions for each subset as in section 2.4. The method of determining the slowness, and therefore the angle of propagation, in equation 3.6 is applicable to both these schemes since the distribution is built in horizontal wavenumber (k_x, k_y) space.

3.2.4 Amplitude Correction

The exact expressions for plane-wave reflection and transmission amplitude coefficients at a plane interface were derived by Zoeppritz (1919). They provide solutions for all mode conversions experienced at a change of acoustic impedence. Previous phase-screen codes have relied upon the normal incidence approximations to determine the partitioning of energy at an interface (Wild and Hudson, 1998; Wild et al., 2000). However removal of the small-angle approximation determines that it is inappropriate to use these simplified equations for reflection and transmission and that the amplitude correction must be calculated as a function of angle.

3.2.4.1 Justification of method

This study adopts the approach of Sheriff and Geldert (1995), calculating systems to define interfaces between two elastic media; an elastic media and a fluid; and two fluid media. The solutions are exact in the regions where the assumptions implicit in their derivation are valid. Realistically however, it is unlikely that plane interfaces will be encountered in many modelling environments. It should be noted that the improved phase-screen technique is still an approximate full elastic-waveform method, but that by applying the Zoeppritz solutions they offer a significant improvement on previous phase-

screen procedures, which adopted a zero offset approximation, for calculating energy partitioning.

Since this study follows a method derived from the geometrical derivation employed by Wild and Hudson (1998) and removes some of the inherent approximations, it is essential that the reflection and transmission coefficeints are determined rigorously to provide a more accurate technique to model reflection seismics.

3.2.4.2 Deriving the exact solution - Zoeppritz

The partitioning of energy at an interface was first described by Knott (1899), but he expressed the problem, and solutions, in terms of potential functions. Zoeppritz (1919) expressed the corresponding equations in terms of amplitudes and by applying conservation of both normal and tangential displacement and stress a system of 4 boundary condition equations are derived. In this study the solutions to these 4 simultaneous equations are solved using a lower-upper decomposition technique (Press et al., 2002) for a range of angles between normal incidence and critical angle. A look-up table is created for every interface encountered and the values stored for future use. Application of locally exact reflection and transmission coefficients results in four outgoing wavefields (T_{pp}, R_{pp}, T_{ps}, and R_{ps}) for each incoming P-wave subset, these are then summed over the entire angular range to compute the corrected wavefields from each screen.

It should be reiterated that the reflection and transmission coefficients are also determined for the S-wave energy and all solutions are calculaed by assuming a locally plane interface between two distinct rock types at the spatial node of the interface. Therefore even with a variation in rock properties across the screen, the exact coefficients are applied as a function of wavenumber with no approximations required.

Table 3.1 shows the rock parameters of two solids and a fluid. Reflection and transmission coefficients are calculated for all mode conversions for P- and S-wave arrivals for an interface between the two solids with the wavefield incident from solid A, and between solid A and the fluid to determine that the method of calculating energy partitioning can correctly handle both solid and fluid interfaces. Figure 3.2 shows the results of these tests from the phase-

screen modelling code in comparison with the standard results available from the CREWES Zoeppritz applet (University of Calgary, 2005).

Scenario A	$V_{p\downarrow}\ (ms^{-1})$	$V_{s\downarrow}\ (ms^{-1})$	$\rho\ (kgm^{-3})$	δ	ϵ
Solid A	2000.0	1250.0	1800.0	0.0	0.0
Solid B	2500.0	1500.0	2000.0	0.0	0.0
Fluid	1500.0	0.0	1000.0	0.0	0.0

Table 3.1: *Elastic parameters for media used in reflection and transmission coefficient calculations*
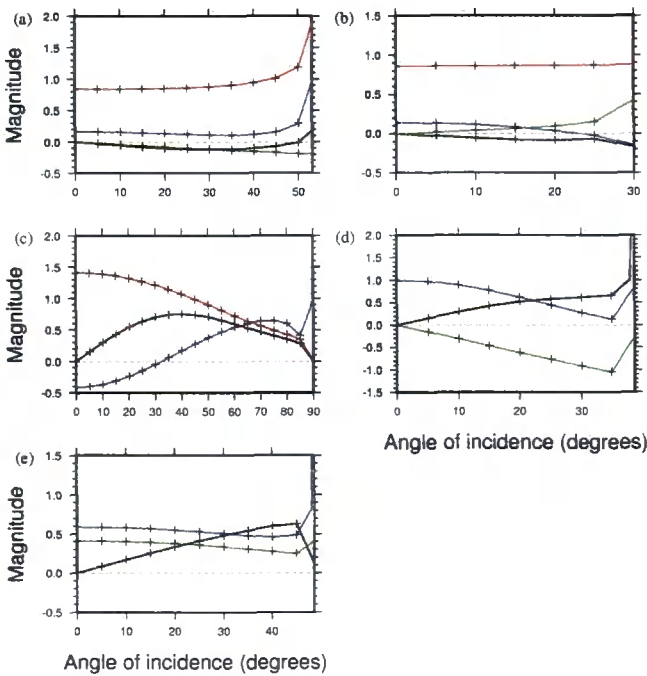
Figure 3.2: *Solutions for the reflection and transmission coefficients for an interface between: (a) solid A and solid B with an incident P-wave; (b) solid A and solid B with an incident S-wave; (c) solid A and fluid with incident P-wave; (d) solid A and fluid with incident S-wave; and (e) fluid and solid A with incident P-wave, with crosses representing results from the phase-screen code, and lines results from the CREWES Zoeppritz applet. The colours represent: red - non-converted transmission; blue - non-converted reflection; green - converted transmission; and black - converted reflection.*

3.2.5 Deriving a complexity coefficient

Different subsurface scenarios require a different distribution of Gaussian subsets and two complimentary examples are included below: both model the reflection from a planer interface between a salt layer and an overlying sediment. The first example (scenario A) results in a P-P reflection coefficient that

remains relatively constant prior to deviation as it appproaches critical angle. The second example (scenario B) results in a steadily varying P-P reflection coefficient where a polarity inversion is encountered as the angle of incidence increases. Tables 3.2 and 3.3 show the rock parameters for both cases whilst figures 3.3 (a) and 3.3 (b) display the reflection coefficient as a function of angle for scenario A and B respectively. In both examples a flat-topped Ricker wavelet with peak frequencies between 5 and 30 Hz is used as the source which is positioned on the top surface of the model.

Scenario A	$V_{p\downarrow}\,(ms^{-1})$	$V_{s\downarrow}\,(ms^{-1})$	$\rho\,(kgm^{-3})$	δ	ϵ
Sediment	2600.0	1500.0	2200.0	0.0	0.0
Salt	4480.0	2590.0	2100.0	0.0	0.0

Table 3.2: *Elastic parameters for rock types used in scenario A numerical example*

Scenario B	$V_{p\downarrow}\,(ms^{-1})$	$V_{s\downarrow}\,(ms^{-1})$	$\rho\,(kgm^{-3})$	δ	ϵ
Sediment	3000.0	2000.0	3300.0	0.0	0.0
Salt	4480.0	2590.0	2100.0	0.0	0.0

Table 3.3: *Elastic parameters for rock types used in scenario B numerical example*
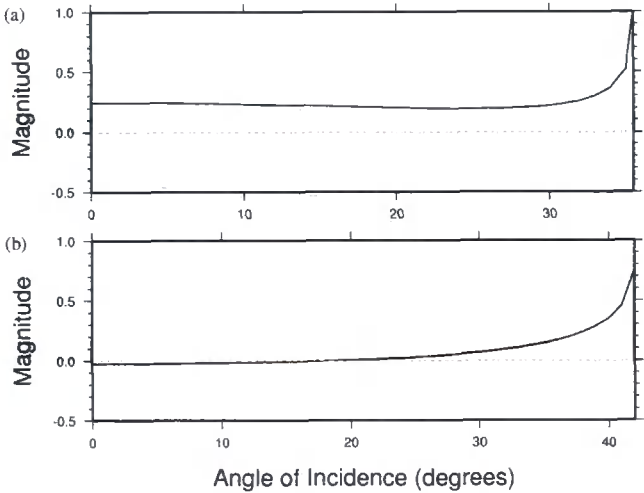
Figure 3.3: *P-P reflection coefficiants as a function of angle between normal incidence and critical angle for (a) scenario A, and (b) scenario B*

The sediment-salt interface is positioned beneath 400 m of sediment, with receivers stationed on the surface at 10 m intervals on an 11 screen, 2D model
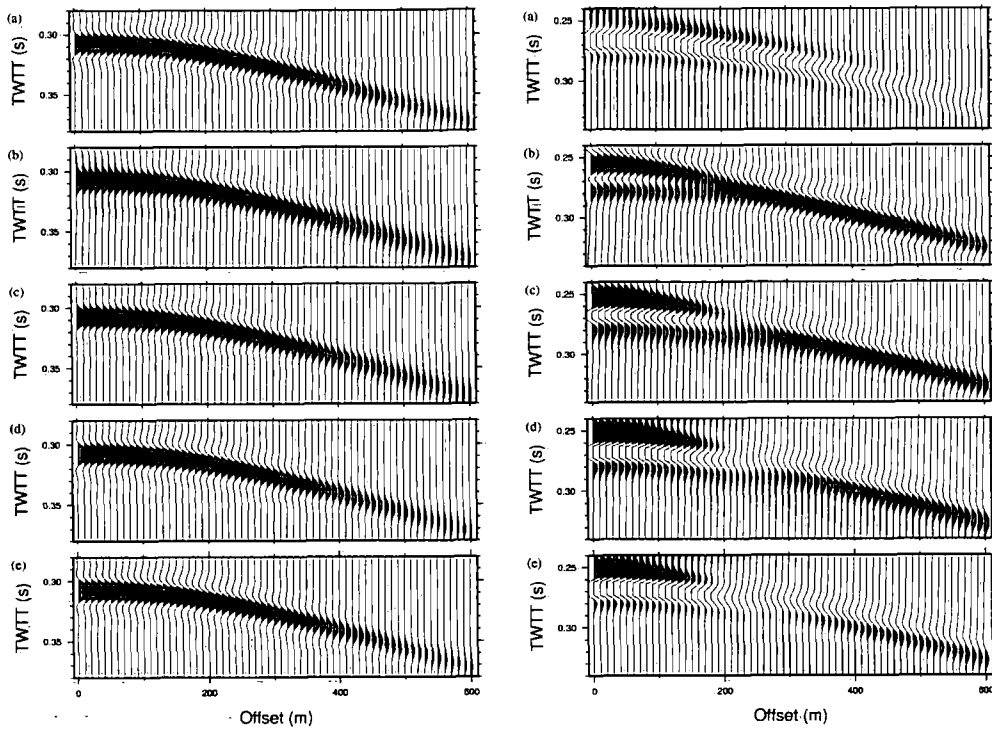
(a) Synthetic seismic responses for P-P reflection from scenario A

(b) Synthetic seismic responses for P-P reflection from scenario B

Figure 3.4: *Reflected non-converted P-wave responses with, at each screen: (a) a single global transform of the wavefield; (b) wavefield divided into 9 subsets with each transformed separately; (c) wavefield divided into 99 subsets; (d) wavefield divided into 199 subsets; and (e) wavefield transformed on a node-by-node basis.*

space with 200 nodes per screen spaced every 10 m. Initially the forward models are run with a single global transform for each screen, then the number of Gaussians per screen are increased, and finally, the nodes are transformed individually. Figures 3.4(a) and 3.4(b) show the results for the single transform; for 9, 99 and 199 Gaussian wavefield subsets; and for individual node-by-node transforms for scenarios A and B respectively.

Scenario A produces comparable responses for all cases since the energy is partitioned almost identically regardless of propagation angle. Scenario B shows how adopting an angle-dependent phase-screen approach offers insights into the variation of amplitude with offset. The single global transform

approach, figures 3.4(a)(a) and 3.4(b)(a) use the normal angle reflection coefficient to partition all of the energy, independent of angle, and therefore produce a negative polarity arrival at all receivers for scenario B. Figure 3.4(b) shows that increasing the number of wavefield subsets increases the accuracy of the response in scenario B. The polarity inversion is expected at an offset of ~ 260 m and it should be noted that the response from 199 Gaussian subset transforms and from individual node-by-node transforms is virtually identical.

This result is a direct consequence of the advances made over the previous pages, and is the exact kind of scenario where previous versions of the phase-screen code would have given spurious results. The travel time and amplitude with offset signature of the results derived from the enhanced phase-screen method would match the shot gathers acquired in a real seismic shoot over a comparable subsurface. This would enable additional conclusions to be drawn from the data as to the nature of the interface, see section 3.3.4, and these advantages are further tested in chapter 5.

In order to determine the number of Gaussian subsets required for a specific screen a trade-off between several issues needs to be deliberated. The primary concern is run-time since the Fourier transforms account for a significant proportion of the computational requirement but traded off against this is the desire for increased accuracy that new developments allow. This study proposes two methods for dividing the wavefield into subsets: firstly a global number of subsets is forced upon the modelling, which is influenced by user experience, the lateral extent of the model and the expected velocity contrasts within the subsurface volume. The second, more rigorous technique is to assess the range of the PP reflection coefficient between normal incidence and 75% of the critical angle. If the maximum variation encountered at each interface is determined then the number of Gaussians can be weighted accordingly; optimising the result and the run time. The main problem with this approach is that it only investigates the range of the PP reflection coefficient, but it is a quantitative procedure for subdividing the wavefield.

3.2.5.1   Approaching the critical angle

Since the aim of this study is to generate synthetic shot gathers for raypaths in the pre-critical energy domain it presents the problem: what to do with the post-critical energy generated during modelling?

It is necessary to consider the reflected and transmitted energies seperately due to the different nature of the wavefields. The obvious solution is to set the post-critical reflection coefficient to 1.0 to mirror real world acquisition. However, if the reflection coefficient is small at narrow angles, the tails of the Gaussian subsets in the pre-critical domain produce a finite value across the entire wavenumber domain and artefacts of this post-critical reflection can overlay the true response. This is especially applicable in regions where the reflection coefficient undertakes a polarity inversion as a function of angle.

The post-critical transmitted evanescent energy presents a completely different problem. By defining k_z as an imaginary number it is possible to construct an identical argument to the pre-critical system if the propagation is also defined by an imaginary angle of energy transfer. The problem that arises is that this evanescent energy only becomes real if the velocity of the subsurface reduces at depth. This scenario, although plausible, is not usually encountered and the added computational expense of storing the rapidly decaying evanescent energy means that this study discounts all post-critical transmission.

In summary the transmitted wavefields are normally damped between 80% and 100% of the critical angle by a multiplication factor between 1 and 0.0001, whilst the reflected wavefields are, by default, treated the same way but can be altered to a constant post-critical value of 1.0 if the user requires. Most commonly a Gaussian taper that smoothly mutes the energy is applied as the horizontal wavenumber approaches either the critical angle, or the Nyquist value, in an effort to reduce wraparound energy or ringing, which are common consequences of dual domain methods.

Since this project involves only pre-critical energy the best option is to remove all post-critical effects enabling the conclusions drawn from the modelling to fit the specifications of the project.

3.2.5.2   Introduction of multiple energy

The derivation of the elastic complex screen by Wu (1994) was based upon
the one-way wave equation. The plausibility of expanding the technique to
include back-scattered energy was verified by Wild and Hudson (1998) using
the geometrical construction derivation. In a system with distinct layers and
interfaces where the angle of propagation is implicit within the modelling of
the data this study seeks to prove that the inclusion of multiple reflected energy
is a realistic next step.

The scheme to introduce this multiple energy is a progression of the tech-
nique adopted previously to enable the phase-screen method to model two-
way propagation. The primaries only data is generated from a single forward
run through consecutive screens followed by single backward propagation
through the screens. If the coding is set-up to store the reflected energy gen-
erated at every screen during both forward and backward propagation then by
using the energy reflected from the top surface as a subsequent source and
adding the reflected energy to the propagating wavefield as each screen is
passed, the only limit on the number of multiples captured in the modelling is
the number of runs through the model that are undertaken. As such, generat-
ing additional orders of multiples has a linear effect on run time. It is important
to remember that the phase-screen technique is based on an approximation to
the wave equation and the inclusion of multiples is an attempt to more accu-
rately model the expected response of a subsurface volume by pushing the limit
of these approximations. Accepting the assumption that only one scatterer is
encountered between nodes on consecutive screens this study attempts to show
that several passes of multiple can be accurately modelled using a geometrical
phase-screen construction.

Table 3.4 shows the elastic parameters of three layers that make up a 1D
subsurface. With the source placed midway across a 2000 m 2D model, the
receivers are positioned every 10 m across the top surface and the modelling
is performed with a source wavelet, constructed using the Nucleus Marine
Source Modelling application fired from a single Bolt gun with 150 cu. in.
volumetric capacity and a pressure of 2000 psi. The source is placed at 1 m
depth and source ghosts are not generated.

Thickness (m)	$V_{p\downarrow}\ (ms^{-1})$	$V_{s\downarrow}\ (ms^{-1})$	$\rho\ (kgm^{-3})$	δ	ϵ
500	1500.0	0.0	1000.0	0.0	0.0
1000	2000.0	1250.0	1700.0	0.0	0.0
∞	3000.0	1850.0	2000.0	0.0	0.0

Table 3.4: *Elastic parameters for rock types used in multiple pass example*

The modelling is run to generate a primaries only shot gather, a four pass multiple shot gather and a four pass multiple shot gather with a damped free surface to demonstrate that the intra-bed multiples are also correctly modelled. Figure 3.5 shows the primary shot gather with every 10th receiver in the positive offset direction included. Figure 3.6 shows the complete four multiple pass shot gather from the phase-screen alongside the response from a reflectivity modelling code, the theory of which is briefly discussed in section 5.3, and includes all posible multiple routes. Figure 3.7 shows the same shot gather after removal of the free-surface multiples and relevant arrivals are displayed on all figures.
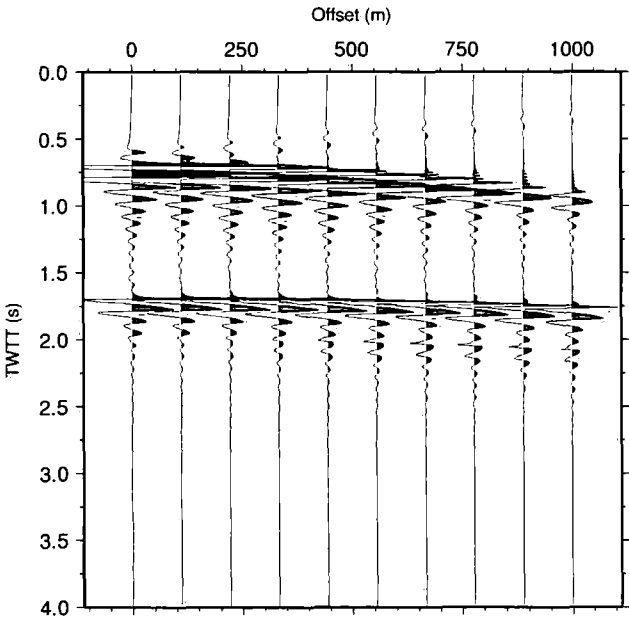
Figure 3.5: *Primary only shot gather from phase-screen modelling to three layer model shown in table 3.4*
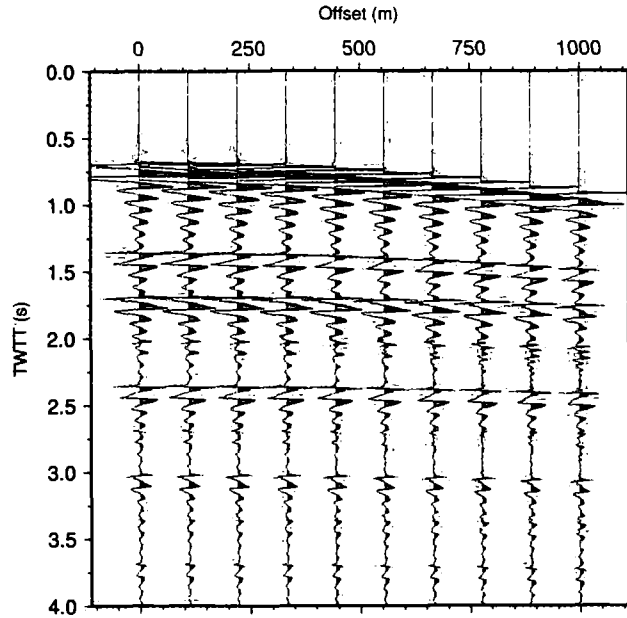
Figure 3.6: *Primary and multiple (up to third order) arrivals from phase screen (red) and entire wavefield response from reflectivity modelling (black)*

Figure 3.5 clearly shows the two distinct primary arrivals, whilst figure 3.6 contains a significantly more complicated wavefield. The variation in amplitude of the first arrival in figure 3.6 is not a modelling error, merely a consequence of the source aperture used in the phase-screen code and it can be seen that not only do the travel times of the multiple (and primary) arrivals agree, but there is also agreement in amplitude and form of the arrivals.

Figure 3.7 shows a simpler response with continued agreement of the primaries and two noticable multiples, one caused by a double reverberation in the second layer as a P-wave, and the other by a double reverberation in the second layer, once as a P-wave and once as an S-wave. These two arrivals are captured with both modelling techniques with excellent agreement.

3.3 Sloping interfaces

Screens are positioned perpendicular to the primary direction of propagation (the z-axis) during phase-screen modelling, although it is unlikely that interfaces in real-earth models will be either planer or aligned with this geometry.
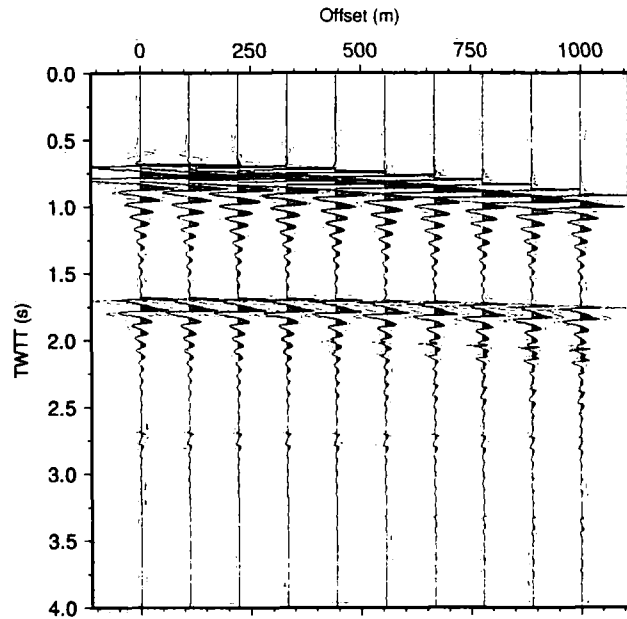
Figure 3.7: *Primary and multiple (up to third order excluding free surface) arrivals from phase screen (red) and entire wavefield response (excluding free surface) from reflectivity modelling (black)*

The direction of energy propagation derived from splitting the wavefield is relative to the screen orientation, meaning, unless a correction to account for local slope is introduced, the computational effort of producing exact arrival angles will be wasted. This would lead to incorrect partitioning of energy at an interface, although the phase correction would suffer no such error. Consequently, this study develops an approach that ascertains the local slope of an interface in 3-D.

3.3.1 Tracking an interface

In terms of the the computational cost, the optimum time to determine the local slope is during the input of the model. Interfaces are tracked between adjacent nodes, in x and y, over a pre-determined number of screens. This range can be set by the user, but a default of ±5 screens is usually sufficient to capture slopes of less than 80°.

If the user specifies that the local slope should be included in the energy partitioning calculations then it is assumed that this local slope is planer at an
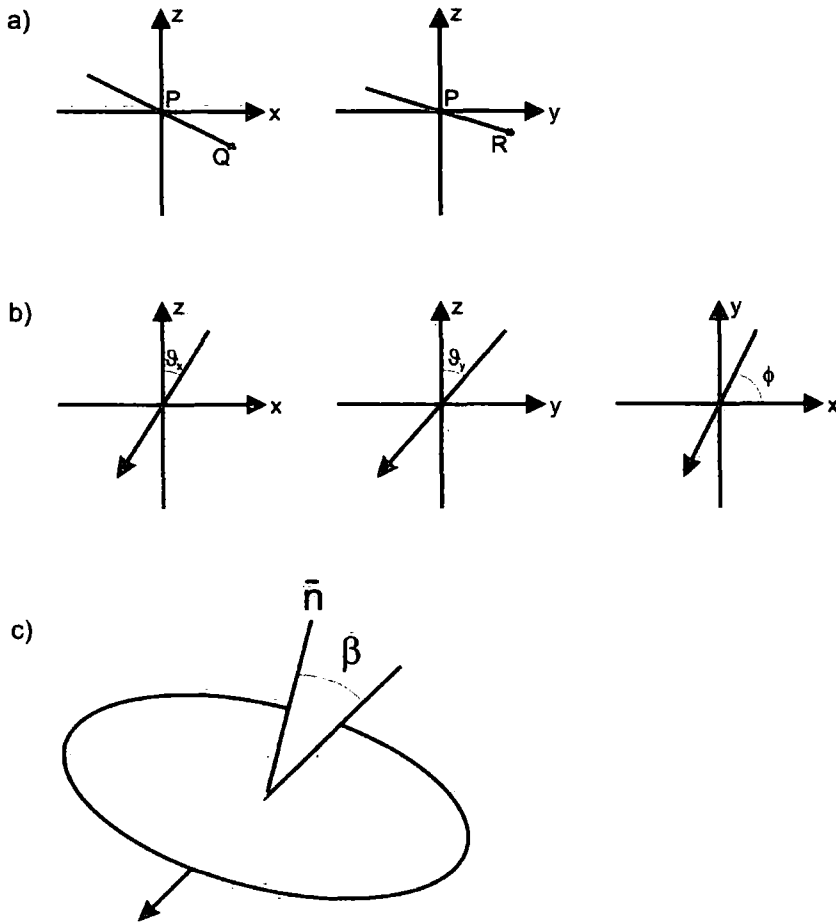
Figure 3.8: *The steps to calculate the local angle of incidence for a dipping reflector. a) the local slope is difined as two perpendicular vectors, b) the incoming angle of propagation is defined relative to the grid orientation; and c) the true incidence angle is determined as the angle between the normal to the local slope and the direction of energy propagation*

individual node of a screen. Figure 3.8 a) shows two lines, **PQ** and **PR**, that sit upon this plane, the equations for which can be easily determined if the node is temporarily repositioned to $P = (0, 0, 0)$. The normal to the plane, n, is calculated from

$$n = PQ \times PR. \qquad (3.7)$$

Figure 3.8 b) shows the phase angle of the incoming wavefield and the azimuth of propagation. The angle required in the partitioning calculation, β, is between the vector normal to the slope, n, and the incoming raypath, m,

where m (shown in figure 3.8 c) as the arrowed line) transects both P and a point where $z = 1$ and

$$x = \tan(\theta \cos \phi), \tag{3.8}$$

$$y = \tan(\theta \sin \phi). \tag{3.9}$$

This enables the calculation of β, shown in figure 3.8 c), from the identity,

$$\mathbf{m} \cdot \mathbf{n} = |m||n| \cos \beta. \tag{3.10}$$

3.3.2 Superposition theory

Calculating the local slope on the interface, and applying this in conjunction with the angular information determined as a consequence of splitting the wavefield ensures that the correct amount of energy is transmitted at each screen. Since the phase-screen modelling technique splits the model space into parallel screens perpendicular to the primary direction of propagation, in effect the propagation between screens is a conservation of horizontal slowness. This principle, Snell's Law, ensures the correct angle of propagation after energy partitioning, whilst the reflection and transmission coefficients ensure the correct amount of energy. The nature of this set up means that the direction of propagation after interaction with an interface is calculated without considering the orientation of the interface. This results in reflected and transmitted wavefields that have the correct amplitude characteristics, but that are not necessarily going in the right direction. Travel time errors in reflected signals from regions with dipping reflectors are a consequence of the geometrical construction method.

This study proposes, through a series of simple tests a method to overcome these shortcomings. The technique adopted is to look at the screen spacing in regions containing sloping interfaces and rely upon the principle of superposition to provide the correct travel times and angular resolution. In the limit

of this argument, with an unlimited number of screens, the reflection from the staircase would mirror the true response of a slope. Figure 3.9 shows the reflected P-wave arrivals from three different sloping interfaces built with four different screen spacings. The rocktypes used have identical P- and S-wave velocities, $2000.0\ ms^{-1}$ and $1250.0\ ms^{-1}$ respectively, but have differing densities of $1500.0\ kgm^{-3}$ for the upper layer and $2500.0\ kgm^{-3}$ for the lower layer. Each 2D model is built on a grid of 100 nodes at 10 m lateral spacing with a free surface source positioned at $x = 500$ m. The source signature is a flat-topped Ricker wavelet with peak frequencies between 10.0 and $30.0\ Hz$. In all the examples the interface is hinged at a depth of 300 m at $x = 0\ m$, and deepens with increasing x with a gradient of: 1 in 8 in the examples shown in figures 3.9 (a)-(d) ; 1 in 4 in the examples shown in figures 3.9 (e)-(h): and 1 in 2 in the examples shown in figure 3.9 (i)-(l). The screen spacings are: 5 m in the examples shown in figures 3.9 (a), (e) and (i); 10 m in the examples shown in figures 3.9 (b), (f) and (j); 20 m in the examples shown in figures 3.9 (c), (g) and (k); an 40 m in the examples shown in figures 3.9 (d), (h) and (l).
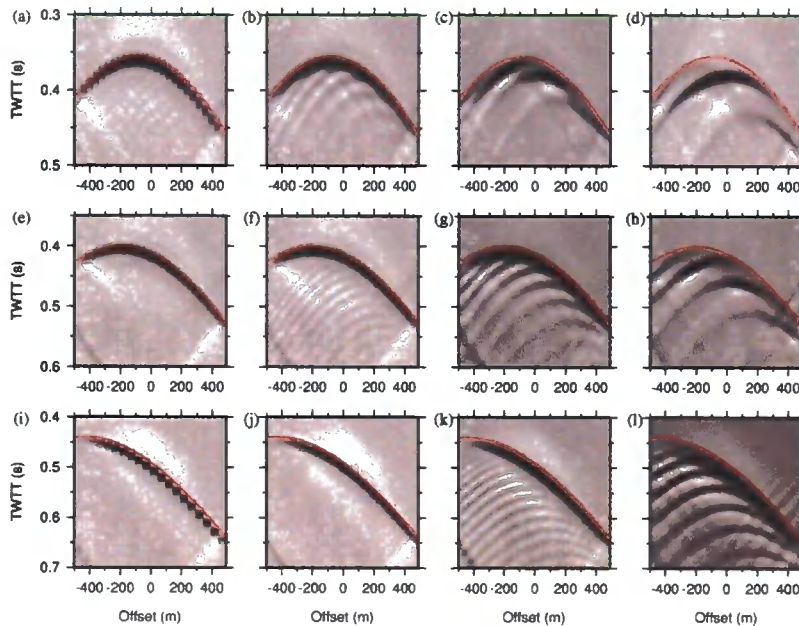
Figure 3.9: *Comparison between the exact travel times (red line) and phase-screen reflections (variable density traces) for a range of screen spacings (5 m in (a), (e) and (i); 10 m in (b), (f) and (j); 20 m in (c), (g) and (k) and; 40 m in (d), (h) and (l)) and inclined reflectors (1 in 8 in (a), (b), (c) and (d); 1 in 4 in (e), (f), (g) and (h) and; 1 in 2 in (i),)j), (k) and (l))*

The responses for the shallowest dip, figures 3.9 (a)-(d), show that a screen spacing of >10 m is insufficient to capture the correct travel time, or a coherent reflected arrival. This is mirrored in the conclusions drawn from figures 3.9 (e)-(h) and figures 3.9 (i)-(l) for the other inclined reflectors. Considering an average peak frequency of $20.0\ Hz$ and using the upper layer velocity, a seismic wavelength, λ, of 75 m is computed. The threshold for vertical resolution between two beds in seismic acquisition and interpretation is $\lambda/4$ (Sheriff and Geldert, 1995) which in this case is 18.75 m. Therefore, this study has shown that as a general rule, in order to apply the principle of superposition to phase-screen modelling for inclined reflectors the screen sampling must be less than a quarter of the dominant wavelength.

3.3.3   K-space corrections

An additional method for correcting the angle of propagation after energy partitioning at a dipping interface has been investigated during this study. The method, which eventually proved unworkable, is included for completeness. The general scheme is a follow on from the Gaussian subset method derived for solving the angular energy partitioning problem but involves dealing with the spatial domain wavefield. Since spatially the local slope is already calculated and the energy has already been partitioned, by splitting the wavefield and transforming the subsets separately it is possible to carry the information pertaining to slope into the horizontal wavenumber domain. The consequence of the slope is that the energy will be incorrectly positioned within this domain which can be considered a proxy for angle. Unfortunately the k-shift correction is not linear across the domain so a simple repositioning of the energy en masse is not feasible. Attempts to reposition the energy using a constant k-shift and also by interpolating the corrected wavefield did not yield the desired results but are still open to investigation. Since N transforms are required to preserve local slope information for an N node screen the increase in run-time means that application of the superposition method is a more feasible approach for handling dipping interfaces during phase-screen modelling.

3.3.4 AVO Effects

The variation in the amplitude of reflection as a function of offset has become a key factor for interpretation of seismic data (Castagna and Backus, 1993). Inversion of the energy partitioning with angle allows numerous subsurface conclusions to be tested whist the integration of successful AVO techniques with borehole data, traditional seismic reflection processing, rock physics studies and reservoir engineering projects are now commonplace in industrial interpretation companies. The use of AVO analysis as a lithology identifier is now well-known (Castagna and Backus, 1993) and the link between AVO signatures and the presence of hydrocarbons have led to much interest, and monitoring during 4D seismic studies.

The enhanced phase-screen allows a realistic correlation between the lithologies and the amplitudes of modelled arrivals giving a more complete picture of the subsurface. However, tuning effects, not modelled with phase-screen due to screen separation can, in real data, give apparent AVO effects that will not be seen in the final shot gathers and the plane wave representation of the source wavefield can also generate some spurious effects.

3.3.4.1 Hydrocarbon indicators

Replacing water wet sand with the equivalent hydrogen charged sand can produce a significant variation in the amplitude of the reflected arrival at all offsets. In chapter 5 this phenomenon is investigated using the Marmousi2 model (Martin, 2004) where the reflections from the top and bottom of hydrocarbon charged sands are isolated with both phase-screen, finite difference and energy partitioning modelling.

The most pronounced indication of the presence of hydrocarbons is a bright spot caused by a significant increase in reflection coefficient at a range of angles caused by the emplacement of gas/oil at the expense of water (Brown, 1991). However, particularly with limestones, the opposite effect can be seen and a dim spot can often be an indication of hydrocarbons. Additionally, variation in the reflection amplitude as a function of offset is a common oil indicator yet, it should be noted, gas charged sands cause variation in the P-wave anomaly only. The enhanced phase-screen technique, whilst still an

approximate method for handling wavefield propagation now provides a realistic response as a function of angle and the AVO effects generated during modelling can be aligned with the lithology of the subsurface.

3.3.5 Causal seismic attenuation

In section 2.6 the method required to implement a zero phase Q filter was described, however in more realistic models a causal filter may be required. This study produces a method for specifying the Q filter used for attenuation. Initially an input wavelet, with a predetermined quality factor, Q_{std}, and a known sampling rate and total length, t_{std}, is created, transformed to the spectral domain and the phase, ϕ_{std}, is saved as a function of frequency ready for analysis during the phase-screen modelling.

As before, each rock type is assigned a rock specific Q_{eff} for P- and S-wave propagation and the local travel time through a screen, t_{act}, is calculated from the screen thickness and the local velocity. The amplitude, Amp, of the filter is determined from equation 2.66 but now the phase of the filter is no longer set to zero. The phase is weighted by

$$\phi_{freq} = \phi_{std} \frac{Q_{std}}{t_{std}} \frac{t_{act}}{Q_{eff}}, \tag{3.11}$$

allowing the correct Q filter to be determined from the original wavelet by

$$Real_{freq} = Amp \times \cos \phi_{freq}, \tag{3.12}$$

$$Im_{freq} = Amp \times \sin \phi_{freq}, \tag{3.13}$$

for any value of Q_{eff}.

3.4   Review

A new phase-screen method, based upon the geometrical construction principle, to model seismic reflection acquisition with all arrivals up to critical

angle has been presented in this chapter. The code has been developed in $c++$, in order to provide an optimised, portable and easily extendable scheme. The advantages and limitations of previous phase-screen and elastic complex screen techniques have been reviewed and this study has proposed a method to split the wavefield in a way that aims to optimise the trade off between run time and accuracy. This approach relies upon creating a series of wavefield subsets that when considered together contain the entire useful pre-critical wavefield. By transforming these subsets separately it is possible to transfer information pertaining to direction of propagation into the spatial domain where it can be used in energy partitioning calculations.

The implementation of a new method to determine local slope of an interface has also been put forward. This additional input into reflection and transmission coefficient functions ensures that these factors are still determined accurately in regions of local dip. Furthermore, this chapter also contained simple demonstations to prove that the new code correctly calculated the energy partitioning coefficients during forward modelling in order to illustrate how variations in amplitude as a function of offset can be modelled with the enhanced phase-screen code.

The introduction of multiple energy has also been considered during this chapter. This further advantage may be seen to be stretching the limits of the phase-screen technique yet examples have been used to show the merits of this development when modelling offshore synthetic data. In these regions multiples, particularly those relating to additional legs within the water column, offer serious challenges to the oil and gas industry and their inclusion is expected during modelling studies.

Ideas that correct the angle of propagation in regions with dipping beds have been discussed during this development chapter. Application of the principle of superposition has been proven to accurately model the arrivals from a dipping interface if careful consideration is given to the screen spacing once the source wavelet has been identified. A supplementary approach based on the wavefield splitting method to carry angular information has also been postulated. The method proved to be unworkable at this time but was included for completeness.

Causal seismic attenuation has been correctly included in the phase-screen modelling to account for more realistic means of energy loss. This enables the user to generate an attenuating wavelet that can be scaled to any Q value and applied throughout the model space. This enhancement is tested in chapter 5.

These developments have ensured that the enhanced phase-screen technique is a viable option when considering generating synthetic seismograms in regions of complex structure where amplitude analysis of the reflected arrivals is expected. Additional testing of the new algorithm, in more realistic environments, is undertaken in chapter 5.

Chapter 4

Phase screen development - anisotropic modelling

4.1 Development Aims

In the work by Wu (1994), Wu and Huang (1995) and Wild and Hudson (1998), media are assumed to be isotropic. However it is widely reported (Levin, 1979; Thomsen, 1986; Tsvankin and Thomsen, 1994) that during exploration, varying degrees and orientations of anisotropy are encountered. Anisotropy is, by definition, the variation of a physical property with direction. In seismic exploration, anisotropy is used to refer to a change in the magnitude of the velocity vector with direction of propagation or polarisation.

The primary aim in this part of the study is to produce a phase-screen modelling code that can quickly and accurately model the response from propagation through an anisotropic medium. In keeping with the previous development work, this new code should have the capacity to produce full waveform responses from elastic subsurfaces composed of both isotropic and anisotropic media.

It is also essential that any anisotropic phase-screen code has the capacity to model not only exact travel time responses but also has the accuracy to enable AVO analysis from an anisotropic subsurface.

4.2 Vertically Transverse Isotropy

The most commonly considered anisotropic orientation is Vertically Transverse Isotropy (VTI), also referred to as polar anisotropy. This can represent both

truly anisotropic rocks, such as a cracked medium with the preferred crack orientation aligned horizontally, or more frequently, isotropic or anisotropic deposits layered over distances smaller than or comparable to seismic wavelengths. When seismic waves propagate through such a medium they act to average out the physical properties of the beds creating an equivalent medium that behaves as if it were truly anisotropic. In VTI media the symmetry axis is vertical and therefore perpendicular to both the bedding and, for modelling, the screen orientation, see figure 4.1. Velocity varies as a function of dip, with the horizontal plane behaving isotropically since there is no azimuthal variation in velocity.
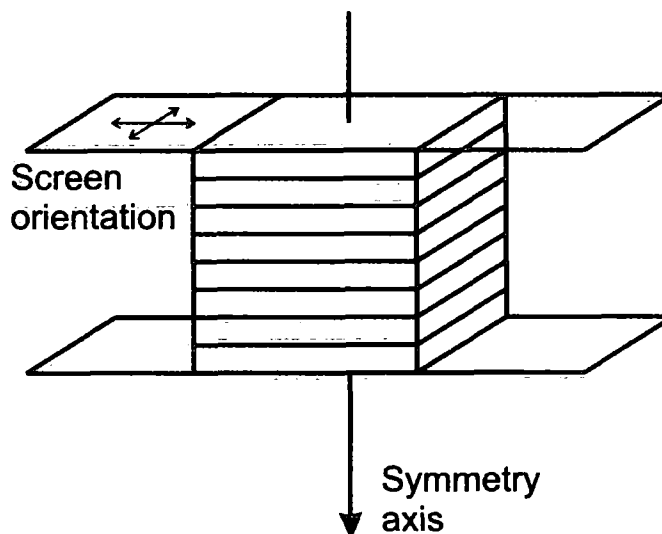
Figure 4.1: *The orientation of the symmetry plane for VTI media is parallel to the primary direction of propagation and perpendicular to the local screen orientation*

The primary benefit of a VTI orientation when approaching from a phase-screen modelling problem perspective is that the P- and S-waves still form a coupled system. Since the incident P- or S-wave are restricted to a 2D plane and there is no azimuthal variation in velocity, all vertical planes can be considered equivalent. This results in particle motion exclusive to a 2D plane with no excitation of the additional orthogonal component. The phase-screen technique lends itself to modelling propagation through VTI media. If the energy can be partitioned correctly at an interface and exact phase velocities can be calculated then the phase-screen method can be extended to model VTI media.

4.3   Real world examples

This study aims to generate an approach to the type of anisotropy encountered in sedimentary basins. The bedding within these environments can itself account for the appearance of anisotropy but the primary cause is usually considered to be shale beds within the sequence. The shales have an anisotropic microstructure which can generate significant velocity variations as a function of propagation direction. As such, in most sedimentary sequences there will be a degree of anisotropy (Brune et al., 1995) making any development of the phase-screen code applicable globally.

4.4   Velocities in VTI media

For an elastic medium the wave propagation is described using the stiffness tensor C_{ijkl}. C_{ijkl} describes how each component of stress σ_{ij} is linearly proportional to each component of strain ϵ_{ij} (Nye, 1957) and is expressed through Hookes Law,

$$\sigma_{ij} = \sum_{k=1}^{3} \sum_{l=1}^{3} C_{ijkl} \epsilon_{ij}, \quad i, j = 1, 2, 3, \tag{4.1}$$

which when combined with Newton's second Law of motion,

$$\rho \frac{\partial^2 u}{\partial t^2} = \sum_{j=1}^{3} \frac{\partial \sigma_{ij}}{\partial x_j}, \quad i, j = 1, 2, 3, \tag{4.2}$$

yields the 3-D wave equation for anisotropic media. Following the lead of (Thomsen, 1986) and noting the symmetry of both stress, $\sigma_{ij} = \sigma_{ji}$, and strain, $\epsilon_{ij} = \epsilon_{ji}$, the 3x3x3x3 tensor can be replaced with a 6x6 matrix $C_{\alpha\beta}$ following the Voigt scheme.

$$
\begin{array}{ccccccc}
ij \text{ or } kl: & 11 & 22 & 33 & 32 = 23 & 31 = 13 & 21 = 12. \\
\downarrow & \downarrow & \downarrow & \downarrow & \downarrow & \downarrow & \downarrow \\
\alpha & \beta & 1 & 2 & 3 & 4 & 5 & 6
\end{array}
\tag{4.3}
$$

There are now 21 independent parameters but by taking note of symmetries within the anisotropy it is possible to reduce this number. For VTI media the

system can be described by five independent coefficients meaning the elastic modulus matrix has the form

$$\begin{vmatrix} C_{11} & (C_{11} - 2C_{66}) & C_{13} & & & \\ & C_{11} & C_{13} & & & \\ & & C_{33} & & & \\ & & & C_{55} & & \\ & & & & C_{55} & \\ & & & & & C_{66} \end{vmatrix}. \tag{4.4}$$

Plugging this back in to the wave equation in order to derive the phase velocities results in three independent solutions polarised in orthogonal directions (Daley and Hron, 1977) which represent the P, SV and SH solutions. The P and SV phase velocity functions take the form,

$$2V_P^2 = A_{33} + A_{55} + (A_{11} - A_{33})Y + Q, \tag{4.5}$$

$$2V_S^2 = A_{33} + A_{55} + (A_{11} - A_{33})Y - Q, \tag{4.6}$$

where,

$$\begin{aligned} Y &= sin^2\theta, \\ Q &= \{(A_{33} - A_{55})^2 + 2A_1Y + A_2Y^2\}^{1/2}, \\ A_1 &= 2(A_{13} + A_{55})^2 - (A_{33} + A_{55})(A_{11} + A_{33} - 2A_{55}), \\ A_2 &= (A_{11} + A_{33} - 2A_{55})^2 - 4(A_{13} + A_{55})^2. \end{aligned}$$

In keeping with Daley and Hron (1977), $A_{\alpha\beta}$ corresponds to the elastic coefficient $C_{\alpha\beta}$ divided by the medium density and θ is the angle between the z-axis and the direction of wavefront normal propagation.

Following the arguments from Tsvankin (1996) it can be seen that using the components of the elastic modulus matrix, $C_{\alpha\beta}$, offers little understanding as to the nature of the anisotropy. This means that it is very difficult to consider the angular variation in velocity by analysing the coefficients alone as none of the parameters particularly pertain to small or large offsets. It is for this reason

that the Thomsen parameters (Thomsen, 1986) are generally used to describe VTI media in conjunction with the vertical P- and S-wave velocities ($V_{P\downarrow}$ and $V_{S\downarrow}$ repectively),

$$V_{P\downarrow} = \sqrt{\frac{C_{33}}{\rho}}, \tag{4.7}$$

$$V_{S\downarrow} = \sqrt{\frac{C_{55}}{\rho}}, \tag{4.8}$$

$$\delta = \frac{(C_{13} + C_{55})^2 - (C_{33} + C_{55})^2}{2C_{33}(C_{33} - C_{55})}, \tag{4.9}$$

$$\epsilon = \frac{C_{11} - C_{33}}{2C_{33}}. \tag{4.10}$$

The parameters δ and ϵ are chosen such that they reduce to zero for isotropic media and provide a tangible understanding of the anisotropy. ϵ, often referred to as the P-wave anisotropy, gives a measure of the fractional difference between the vertical and horizontal P-wave velocity whilst δ offers an insight into the rate of change of P-wave velocity at propagation angles close to the vertical. The special case when $\delta = \epsilon$ results in an elliptically anisotropic media.

Equations 4.5 and 4.6 represent the P- and S-wave phase velocities, and are generally written (White, 1983) as

$$\begin{aligned}
2\rho V_P^2(\theta) =& C_{55} + C_{11}\sin^2\theta + C_{33}\cos^2\theta \\
& + \{[(c_{11} - C_{55})^2\sin^2\theta - (C_{33} - C_{55})\cos^2\theta]^2 \\
& + 4(C_{13} + C_{44})^2\sin^2\theta\cos^2\theta\}^{1/2},
\end{aligned} \tag{4.11}$$

and

$$\begin{aligned}
2\rho V_S^2(\theta) =& C_{55} + C_{11}\sin^2\theta + C_{33}\cos^2\theta \\
& - \{[(c_{11} - C_{55})^2\sin^2\theta - (C_{33} - C_{55})\cos^2\theta]^2 \\
& + 4(C_{13} + C_{44})^2\sin^2\theta\cos^2\theta\}^{1/2}.
\end{aligned} \tag{4.12}$$

Following the approach of Tsvankin (1996) and dividing through by the squared P-wave vertical velocity and replacing the Voigt coefficients with the Thomsen parameters δ and ϵ the following expressions for the P- and S-wave phase velocities are developed,

$$\frac{v_P^2(\theta)}{V_{P\downarrow}^2} = 1 + \epsilon \sin^2 \theta - f(1 - \sqrt{s_\theta})/2, \tag{4.13}$$

$$\frac{v_S^2(\theta)}{V_{P\downarrow}^2} = 1 + \epsilon \sin^2 \theta - f(1 + \sqrt{s_\theta})/2, \tag{4.14}$$

where

$$f = 1 - \frac{\beta_0^2}{\alpha_0^2}, \tag{4.15}$$

and

$$s_\theta = 1 + \frac{4 \sin^2 \theta}{f}(2\delta \cos^2 \theta - \epsilon \cos(2\theta)) + \frac{4\epsilon^2 \sin^4 \theta}{f^2}. \tag{4.16}$$

During phase-screen modelling the propagation is undertaken in the wavenumber domain; in order to maximise the technique, equations 4.13 to 4.16 are recast as functions of horizontal wavenumber following an argument similar to Baan and Kendall (2002). This produces phase velocities that are immediately applicable to the phase-screen technique. Additional application of Snell's Law and further rearranging yields,

$$v_p^2(k_x) = \frac{\alpha_0^2(2 - f + 2(\delta f - \epsilon)\frac{k_x^2}{\omega^2}\alpha_0^2 + f\sqrt{s_p})}{2 - 4\epsilon\frac{k_x^2}{\omega^2}\alpha_0^2 - 4f(\epsilon - \delta)\frac{k_x^4}{\omega^4}\alpha_0^4}, \tag{4.17}$$

and

$$v_s^2(k_x) = \frac{\alpha_0^2(2 - f + 2(\delta f - \epsilon)\frac{k_x^2}{\omega^2}\alpha_0^2 - f\sqrt{s_p})}{2 - 4\epsilon\frac{k_x^2}{\omega^2}\alpha_0^2 - 4f(\epsilon - \delta)\frac{k_x^4}{\omega^4}\alpha_0^4}, \tag{4.18}$$

where

$$s_p = 1 + 4(\frac{2\delta - \epsilon}{f} - \delta)\frac{k_x^2}{\omega^2}\alpha_0^2$$

$$+ 8(\frac{\delta^2}{2} + \delta - \epsilon + \frac{\epsilon - \delta - \delta\epsilon}{f} + \frac{\epsilon^2}{2f^2})\frac{k_x^4}{\omega^4}\alpha_0^4. \tag{4.19}$$

Except in the symmetry planes, the phase and group velocities vary in both magnitude and direction. Figure 4.2 shows the distinction between the two, where the phase velocity $v(\theta)$ describes the rate of advance of the wavefront along $k(\theta)$, whilst the ray velocity measures the speed of energy propagation.
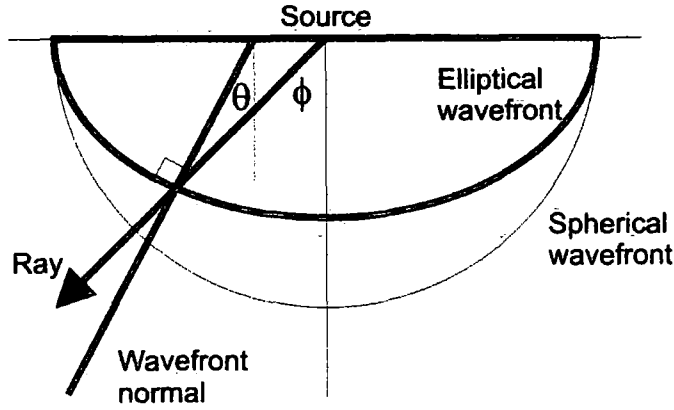
Figure 4.2: *Schematic to clarify the phase and group angles (after Thomsen (1986))*

In isotropic and any general anisotropic media $k_x = k(\theta)\sin\theta$ and $k_z = k(\theta)\cos\theta$ which gives the scaler magnitude of $k(\theta) = \sqrt{k_x^2 + k_z^2} = \omega/v(\theta)$. The group angle, ϕ, is determined as (Berryman, 1979)

$$tan(\phi(\theta)) = \frac{\partial(kv)}{\partial k_x} / \frac{\partial(kv)}{\partial k_z}$$

$$= (v\sin\theta + \frac{dv}{d\theta}\cos\theta)/(v\cos\theta - \frac{dv}{d\theta}\sin\theta) \tag{4.20}$$

$$= (\tan\theta + \frac{1}{v}\frac{dv}{d\theta})/(1 - \frac{\tan\theta}{v}\frac{dv}{d\theta}),$$

whilst the group velocity, V, is

$$V(\phi(\theta)) = \sqrt{v^2(\theta) + (\frac{dv}{d\theta})^2}. \tag{4.21}$$

Using this relationship, the group velocity surface can be determined to verify the correct phase velocities as a function of slowness. Using the SV phase velocity distribution the group velocity surface shown in figure 4.3 is derived. This is plotted with the same result calculated by Baan and Kendall (2002) and shows excellent agreement.
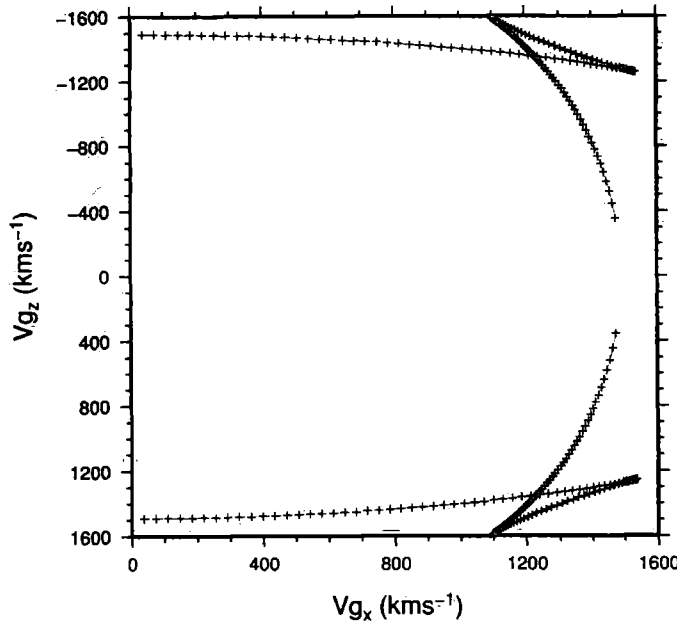
Figure 4.3: *Group velocity surface for shale B from numerical examples with crosses derived from enhanced anisotropic phase-screen calculations and red lines from Baan and Kendall (2002)*

4.4.1 Testing the travel times through simple VTI media using the phase-screen method

Initial tests through simple anisotropic media are required to confirm that the approach produces the correct travel times for arrivals. To test the travel times the results presented by Baan and Kendall (2002) are recreated using theVTI modified, enhanced phase-screen technique. This test, from White and Hobbs (2007), generates the moveout curves associated with reflected arrivals from 1 km thick packages of shale overlying an isotropic layer ($\alpha = 4000\ ms^{-1}$, $\beta = 2000\ ms^{-1}$, $\rho = 2500\ kgm^{-1}$). Additionally the traveltimes from the multilayer model of Baan and Kendall (2002) are recreated for a model composed of an isotropic layer ($\alpha = 2000\ ms^{-1}$, $\beta = 1000\ ms^{-1}$, $\rho = 2000\ kgm^{-1}$), a package

Shale	$V_{p\downarrow}\ (ms^{-1})$	$V_{s\downarrow}\ (ms^{-1})$	$\rho\ (kgm^{-3})$	δ	ϵ
Shale A	3368.0	1829.0	2500.0	-0.035	0.110
Shale B	3048.0	1490.0	2420.0	-0.050	0.255

Table 4.1: *The rock parameters for shales A and B used in anisotropic modelling tests*

of shale B, then two more isotropic layers ($\alpha = 4000\ ms^{-1}$, $\beta = 2000\ ms^{-1}$, $\rho = 2500\ kgm^{-1}$ and $\alpha = 6000\ ms^{-1}$, $\beta = 3500\ ms^{-1}$, $\rho = 3000\ kgm^{-1}$). Each layer is 1 km thick and table 4.1 shows the elastic parameters of the shales used (from Thomsen (1986)).

Sources are deployed on the top surface of the model and figure 4.4 shows the moveout curves for the single layer examples with receivers positioned on the surface at intervals of 30 m on a 4 screen, 2D model space composed of 200 nodes per screen. The node spacing is of 10 m. Figure 4.5 shows the moveout curves for the 17 screen multilayer example with the same source, receiver and node set-up. In this figure only the anisotropic moveout curves for the VTI layers from Baan and Kendall (2002) are shown.

4.5 Anisotropic reflection coefficients

The effects of anisotropic media are generally well understood when variations in travel time are considered. It is a reasonably simple concept to grasp that when there are variations in velocity as a function of direction (or slowness) the time taken to cover equal distances will vary. It is this variation in travel time that leads geoscientists to draw conclusions that the subsurface contains anisotropic deposits. However it is not only the velocities that vary within anisotropic media. Reflection and transmission of energy is also altered and the Zoeppritz solutions that apply in homogeneous, isotropic media are no longer suitable to calculate energy partitioning. With AVO being an important industrial challenge it is essential that exact solutions are derived so that we are able to quickly and accurately forward model arrivals with correct amplitudes.

4.5.1 Solid-Solid interface

The solutions for reflection and transmission coefficients in anisotropic solids were initially calculated by Daley and Hron (1977). Their work, derived from
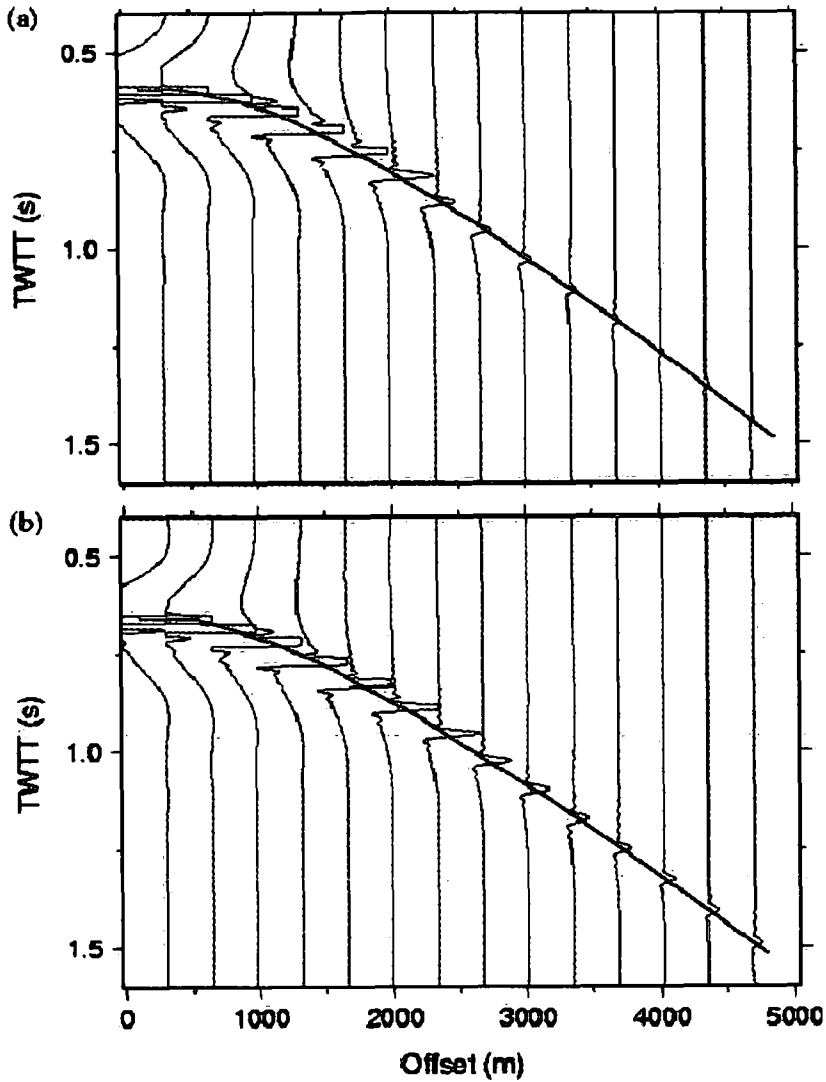
Figure 4.4: *Moveout curves for reflected arrivals through 1 km of shale package. Traces, phase-screen modelling code; line, Baan and Kendall (2002). (a) Propagation through shale A; (b) propagation through shale B*

the zero-order approximation of asymptotic theory, provided results for partitioning at an interface between two anisotropic solids and, an anisotropic solid and a free surface (vacuum).

The solutions derived by Daley and Hron (1977) are calculated as functions both of phase angle and the elastic modulus matrix ($C_{\alpha\beta}$), and, as such, are not immediately applicable to the project. Graebner (1992) published plane wave, particle amplitude reflection and transmission coefficients for two transversely isotropic solids in welded contact and for a fluid overlying a transversely isotropic solid all with vertical symmetry axes. These solutions are calculated
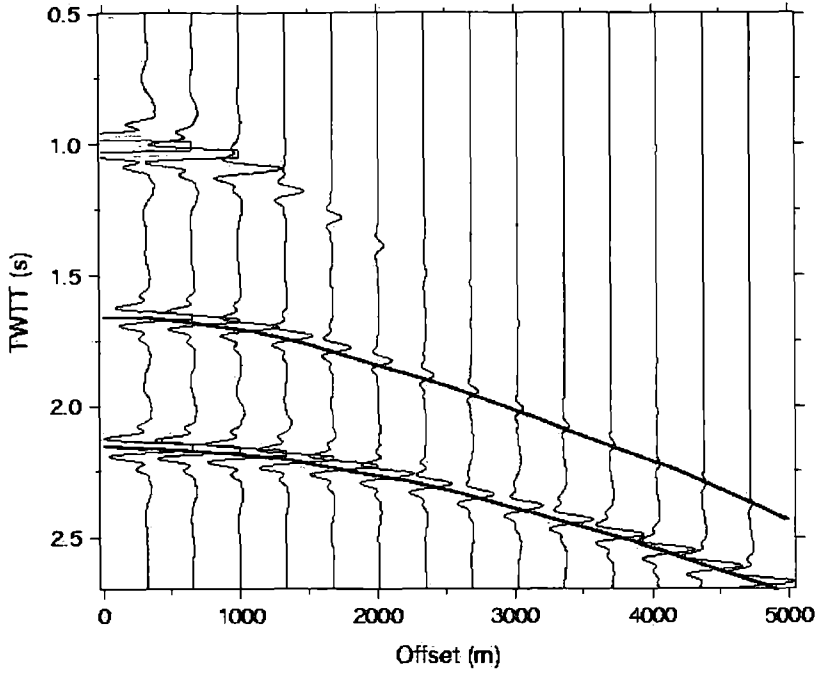
Figure 4.5: *Moveout curves for reflected arrivals from 4-layer anisotropic model. Traces, phase-screen modelling code; line, Baan and Kendall (2002).*

as a function of slowness, p_x, and can be more readily used in a phase-screen forward modelling construction

If propagation is considered only in the xz-plane it can be assumed that the motion is independent of y given the indifference to azimuth of a VTI medium. As such, equation 4.1 separates into a pair a coupled equations where the P and SV system is defined as White (1983),

$$\left(\begin{array}{cc} C_{11}\frac{\partial^2}{\partial x^2} + C_{55}\frac{\partial^2}{\partial z^2} - \rho\frac{\partial^2}{\partial t^2} & (C_{13}+C_{55})\frac{\partial^2}{\partial x \partial z} \\ (C_{13}+C_{55})\frac{\partial^2}{\partial x \partial z} & C_{33}\frac{\partial^2}{\partial z^2} + C_{55}\frac{\partial^2}{\partial x^2} - \rho\frac{\partial^2}{\partial t^2} \end{array} \right) \left(\begin{array}{c} u_x \\ u_z \end{array} \right) = \left(\begin{array}{c} 0 \\ 0 \end{array} \right). \quad (4.22)$$

Assuming a plane wave particle displacement

$$u = (l, 0, m) U e^{i\omega(px+qz-t)}, \quad (4.23)$$

where

$$\sqrt{m^2 + l^2} = 1,$$

substituting equation 4.23 into equation 4.22 results in,

$$det \begin{vmatrix} C_{11}p^2 + C_{55}q^2 - \rho & (C_{13} + C_{55})pq \\ (C_{13} + C_{55})pq & C_{33}q^2 + C_{55}p^2 - \rho \end{vmatrix} = 0. \qquad (4.24)$$

Expanding the determinant to give a quadratic in q^2, the roots of which are the vertical phase slownesses of the P- and S-waves, the eigenvalues q_α and q_β respectively,

$$q_\alpha = \frac{1}{\sqrt{2}}(\Gamma - \sqrt{\Gamma^2 - \Xi})^{1/2}, \qquad (4.25)$$

$$q_\beta = \frac{1}{\sqrt{2}}(\Gamma + \sqrt{\Gamma^2 - \Xi})^{1/2}, \qquad (4.26)$$

where

$$\Gamma = \frac{\rho}{C_{13}} + \frac{\rho}{C_{55}} - \left(\frac{C_{11}}{C_{55}} + \frac{C_{55}}{C_{33}} - \frac{(C_{13} + C_{55})^2}{C_{33}C_{55}}\right)p^2, \qquad (4.27)$$

and (noting the error in Graebner (1992)),

$$\Xi = 4\left\{\frac{C_{11}}{C_{33}}p^4 - \left(\frac{C_{11}}{C_{33}C_{55}}\rho + \frac{\rho}{C_{33}}\right)p^2 + \frac{\rho^2}{C_{33}C_{55}}\right\}. \qquad (4.28)$$

In order to ascertain the eigenvectors for each eigenvalue the following system must be solved,

$$\begin{pmatrix} C_{11}p^2 + C_{55}q_i^2 - \rho & (C_{13} + C_{55})pq_i \\ (C_{13} + C_{55})pq_i & C_{33}q_i^2 + C_{55}p^2 - \rho \end{pmatrix} \begin{pmatrix} \epsilon_i \\ \delta_i \end{pmatrix} = \begin{pmatrix} 0 \\ 0 \end{pmatrix}, \qquad (4.29)$$

with

$$\begin{pmatrix} \epsilon_i \\ \delta_i \end{pmatrix} = \begin{pmatrix} l_\alpha \\ m_\alpha \end{pmatrix} \text{ and } q_i = q_\alpha$$

for the P wave and

$$\begin{pmatrix} \epsilon_i \\ \delta_i \end{pmatrix} = \begin{pmatrix} l_\beta \\ m_\beta \end{pmatrix} \text{ and } q_i = q_\beta$$

for the S wave. The resulting P eigenvectors are given by

$$
\begin{aligned}
l_\alpha &= \left(\frac{A_{33}q_\alpha^2 + A_{55}p^2 - 1}{(A_{11}p^2 + A_{55}q_\alpha^2 - 1) + (A_{33}q_\alpha^2 + A_{55}p^2 - 1)} \right)^{1/2}, \\
m_\alpha &= \left(\frac{A_{11}p^2 + A_{55}q_\alpha^2 - 1}{(A_{11}p^2 + A_{55}q_\alpha^2 - 1) + (A_{33}q_\alpha^2 + A_{55}p^2 - 1)} \right)^{1/2},
\end{aligned}
\tag{4.30}
$$

and the S eigenvectors are given by

$$
\begin{aligned}
l_\beta &= \left(\frac{A_{11}p^2 + A_{55}q_\beta^2 - 1}{(A_{11}p^2 + A_{55}q_\beta^2 - 1) + (A_{33}q_\beta^2 + A_{55}p^2 - 1)} \right)^{1/2}, \\
m_\beta &= \left(\frac{A_{33}q_\beta^2 + A_{55}p^2 - 1}{(A_{11}p^2 + A_{55}q_\beta^2 - 1) + (A_{33}q_\beta^2 + A_{55}p^2 - 1)} \right)^{1/2}.
\end{aligned}
\tag{4.31}
$$

As with the case for isotropic interfaces there is continuity of the displacements u_x and u_z and of the stressses σ_{xz} and σ_{zz} at a boundary. Applying the calculated eigenvectors to derive both the up and down propagating P and S wave displacements. Labelling the upper rock type $\rightarrow$ 1 and the lower rock type $\rightarrow$ 2 it is possible to construct the following system (Graebner, 1992) for a P wave incident from above,

$$
\begin{pmatrix}
-l_{\alpha2} & l_{\alpha1} & -m_{\beta2} & m_{\beta1} \\
m_{\alpha2} & m_{\alpha1} & -l_{\beta2} & -l\beta1 \\
a_2 & a_1 & b_2 & b_1 \\
-c_2 & c_1 & -d_2 & d_1
\end{pmatrix}
\begin{pmatrix}
T_{PP} \\
R_{PP} \\
T_{PS} \\
R_{PS}
\end{pmatrix}
=
\begin{pmatrix}
-l_{\alpha1} \\
m_{\alpha1} \\
a_1 \\
-c_1
\end{pmatrix},
\tag{4.32}
$$

where

$$
\begin{aligned}
a_1 &= C_{55-1}(q_{\alpha1}l_{\alpha1} + pm_{\alpha1}), \\
b_1 &= C_{55-1}(q_{\beta1}m_{\beta1} - pl_{\beta1}), \\
c_1 &= pl_{\alpha1}C_{13-1} + q_{\alpha1}m_{\alpha1}C_{33-1}, \\
d_1 &= pm_{\beta1}C_{13-1} - q_{\beta1}l_{\beta1}C_{33-1}, \\
a_2 &= C_{55-2}(q_{\alpha2}l_{\alpha2} + pm_{\alpha2}), \\
b_2 &= C_{55-2}(q_{\beta2}m_{\beta2} - pl_{\beta2}), \\
c_2 &= pl_{\alpha2}C_{13-2} + q_{\alpha2}m_{\alpha2}C_{33-2}, \\
d_2 &= pm_{\beta2}C_{13-2} - q_{\beta2}l_{\beta2}C_{33-2},
\end{aligned}
$$

and the additional system for an incident S wave from above,

$$\begin{pmatrix} -l_{\alpha 2} & l_{\alpha 1} & -m_{\beta 2} & m_{\beta 1} \\ m_{\alpha 2} & m_{\alpha 1} & -l_{\beta 2} & -l\beta 1 \\ a_2 & a_1 & b_2 & b_1 \\ -c_2 & c_1 & -d_2 & d_1 \end{pmatrix} \begin{pmatrix} T_{SP} \\ R_{SP} \\ T_{SS} \\ R_{SS} \end{pmatrix} = \begin{pmatrix} -m_{\beta 1} \\ -l_{\beta 1} \\ b_1 \\ -d_1 \end{pmatrix}. \tag{4.33}$$

If we have to calculate the alternate problem of a P or S wave incident from below, all that is required is the exchanging of the subscripts 1 and 2 and equations 4.32 and 4.33 are still applicable.

4.5.2 Fluid-Solid interface

Graebner (1992) also produced the solutions for the reflection and transmission coefficients for a fluid overlying a VTI solid. The fluid upper layer is denoted by the subscript $\rightarrow 1$, whilst the lower VTI layer is denoted by the subscript $\rightarrow 2$. In this scenario there must be continuity of the vertical displacement and the stress component σ_{zz}, whilst the stress component σ_{xz} must vanish.

In the isotropic fluid layer there is no S wave propagation and the vertical slowness is simply

$$q_{\alpha 1} = \sqrt{\frac{1}{\alpha_1^2} - p_2}, \tag{4.34}$$

which results in the eigenvectors

$$\begin{aligned} l_{\alpha 1} &= \sin \theta_{\alpha 1}, \\ m_{\alpha 1} &= \cos \theta_{\alpha 1}. \end{aligned} \tag{4.35}$$

Solving this system once again produces a matrix solution, for a P-wave incident from above (the fluid),

$$\begin{pmatrix} -l_{\beta 2} & m_{\alpha 2} & m_{\alpha 1} \\ d_2 & c_2 & -\rho \alpha_1^2 (p l_{\alpha 1} + q_{\alpha 1} m_{\alpha 1}) \\ b_2/C_{55-2} & a_2/C_{55-2} & 0 \end{pmatrix} \begin{pmatrix} T_{PP} \\ R_{PP} \\ T_{PS} \end{pmatrix}$$
$$= \begin{pmatrix} m_{\alpha 1} \\ -\rho \alpha_1^2 (p l_{\alpha 1} + q_{\alpha 1} m_{\alpha 1}) \\ 0 \end{pmatrix}, \tag{4.36}$$

whilst for a P-wave incident from below,

$$
\begin{pmatrix}
-l_{\beta 2} & m_{\alpha 1} & m_{\alpha 2} \\
-d_2 & -\rho\alpha_1^2(pl_{\alpha 1} + q_{\alpha 1}m_{\alpha 1}) & -c_2 \\
b_2/C_{55-2} & 0 & a_2/C_{55-2}
\end{pmatrix}
\begin{pmatrix}
T_{PP} \\
R_{PP} \\
R_{PS}
\end{pmatrix}
$$
$$
= \begin{pmatrix}
m_{\alpha 2} \\
-c_2 \\
a_2/C_{55-2}
\end{pmatrix},
\tag{4.37}
$$

and finally for an S wave incident from below,

$$
\begin{pmatrix}
-l_{\beta 2} & m_{\alpha 1} & m_{\alpha 2} \\
-d_2 & -\rho\alpha_1^2(pl_{\alpha 1} + q_{\alpha 1}m_{\alpha 1}) & -c_2 \\
b_2/C_{55-2} & 0 & a_2/C_{55-2}
\end{pmatrix}
\begin{pmatrix}
T_{SP} \\
R_{SP} \\
R_{SS}
\end{pmatrix}
$$
$$
= \begin{pmatrix}
-l_{\beta 2} \\
-d_2 \\
b_2/C_{55-2}
\end{pmatrix}.
\tag{4.38}
$$

The case of a fluid-fluid boundary is entirely isotropic so is not modified from the previous isotropic derivation.

4.5.3 Testing the coefficients

Now the systems for each type of interface have been constructed they can be solved, as before, using a lower-upper (LU) decomposition scheme (Press et al., 2002). Since Daley and Hron (1979) produced the earliest set of standard results for reflection and transmission coefficients as a function of angle between two VTI media numerous authors (White, 1982; Wright, 1987; Yang, 2003) have published work giving further examples of exact solutions that can be used to benchmark new codes. Alongside this research there is also a considerable amount of published work concerning approximations for reflection and transmission coefficients in simple anisotropic settings. Thomsen (1998) discusses the development of these approximations for VTI media, whilst Blangy (1994) offers up an excellent overview of the topic. Since this study focuses on forward modelling and great care is taken to provide the most accurate velocities and angles in VTI media it is essential that exact coefficients are determined. As such an ideal benchmark is that of Yang (2003).

	$V_{p\downarrow}\ (ms^{-1})$	$V_{s\downarrow}\ (ms^{-1})$	$\rho\ (kgm^{-3})$	δ	ϵ
Upper Layer	2500.0	1250.0	1400.0	0.20	0.20
Lower Layer	4000.0	2000.0	2000.0	0.00	0.00

Table 4.2: *Elastic parameters for the rock types used to calculate anisotropic reflection coefficient data for figure 4.6 a)*

	$V_{p\downarrow}\ (ms^{-1})$	$V_{s\downarrow}\ (ms^{-1})$	$\rho\ (kgm^{-3})$	δ	ϵ
Upper Layer	6000.0	3000.0	2500.0	0.20	0.20
Lower Layer	3000.0	1500.0	2000.0	0.00	0.00

Table 4.3: *Elastic parameters for the rock types used to calculate anisotropic reflection coefficient data for figure 4.6 b)*

Tables 4.2 and 4.3 display the elastic parameters for the layers either side of a planer interface.

Solving the solid-solid energy partitioning systems (equations 4.32 and 4.33) using the elastic parameters in tables 4.2 and 4.3, the results for the reflected energy as a function of angle of incidence are plotted alongside those of Yang (2003) in figure 4.6.
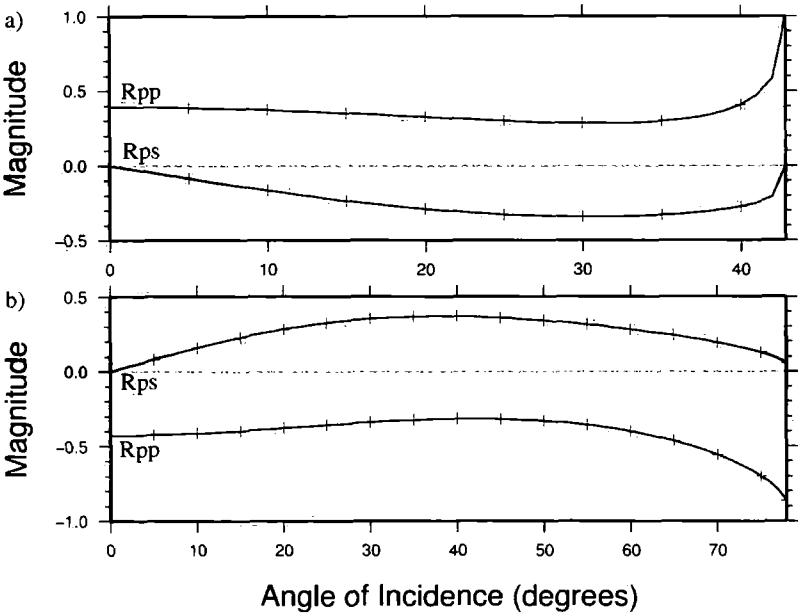
Figure 4.6: *Examples of reflection coefficients for a VTI to isotropic interface. Lines – results from the phase screen code; crosses – results from Yang (2003). a) For the case defined by table 4.2; b) for the case defind by table 4.3*

It should also be noted that equations 4.32 and 4.33 reduce to the isotropic system exactly if the anisotropic parameters are negligible. As such, the code is developed using the anisotropic reflection and transmission system. In this case isotropic rock types are considered as anisotropic with parameters δ and ϵ equal to 0.00001.

4.6   Review of developments

This study has taken the developments described in chapter 3 and further modified the enhanced phase-screen method to enable propagation through simple anisotropic media. By calculating phase velocities as a function of horizontal wavenumber exact travel times in VTI media are determined. These have been verified against published, peer-reviewed, results and used to determine local group velocities. It is also noted that the anisotropic propagation can be utilised in the narrow angle phase-screen code if only near normal travel times are required. This scheme will generate shot gathers in runtimes orders of magnitude quicker than comparable finite difference approaches. However, in order to ensure accurate pre-critical wavefield solutions this study tailors the partitioning of energy calculations for VTI specific interfaces. This ensures that the AVO conclusions drawn from the seismic modelling are applicable for comparison with real data. Further testing of the enhanced anisotropic phase-screen technique is undertaken in chapter 5. A manual for the enhanced phase-screen code is included in appendix C and the code is available from the author (jame3@bgs.ac.uk).

Chapter 5

Seismic applications and method verification

5.1 Testing a seismic forward modelling code

Following the development of an elastic seismic modelling tool, in this case the enhanced anisotropic phase-screen method, it is essential to test that the new code functions as expected. In order to verify the modelling, the creation of a series of tests with specific measurable objectives is necessary. In order to confirm that the enhanced phase-screen method correctly handles both simple and complex sub-surface structure this chapter generates a series of models enabling comparisons between the phase-screen code, theoretical solutions and alternative modelling techniques. This chapter aims to test the enhanced phase-screen code against a series of isotropic and anisotropic subsurface models in order to verify the accuracy of the solutions.

The first test is the generation of a VSP dataset over a 1-D subsurface model that displays a velocity and density trend comparable with a marine sedimentary basin. This test is designed to assess the accuracy of travel times and amplitudes in simple models, to verify the visco-elastic nature of the modelling and to further justify the modelling of multiple energy by comparing arrivals with theoretical solutions.

Next, the reflectivity method (Müller, 1985) is used to generate complimentary solutions to the enhanced phase-screen scheme allowing the full waveform solutions at wide angles to be checked. The method also allows the verification of wide angle multiple energy and enables the inclusion of anisotropic rock-

types. Ray tracing (Červený et al., 1977) is used to validate the modelling across a low velocity zone whilst testing 3-D travel times and amplitudes through lithological interfaces and for point diffractors. A salt wedge model is utilised to ensure the enhanced phase-screen method satisfies the principles of travel time and amplitude reciprocity whilst providing a complex, high velocity structure for modelling.

Finite difference modelling is used to model in realistic rapidly varying structures that are well known to the seismic modelling community. The acoustic French model (French, 1974) is initially employed, then the elastic Marmousi2 model (Martin, 2004) is used to generate wide-angle waveform solutions in realistic acquisition scenarios. The Marmousi2 model is also used to verify the modelling of AVO signatures by isolating reflections from potential hydrocarbon traps.

Finally a well constrained anisotropic 3-D model from a producing field in a marine sedimentary location is utilised to determine isotropic and anistropic migration operators. A quantitative assessment of the errors associated with ignoring anisotropy in these environments is derived.

5.2 Generation of synthetic VSP

The vertical seismic profile (VSP) is a common tool in seismic acquisition in regions where borehole exploration has previously been undertaken. Recording data at depth gives an instant tie-in between the seismic response and the rocktype since it provides a ground truth that can be interpreted across the seismic volume. In this study the exact velocities at depth are already known but generation of VSP data will allow the enhanced phase-screen code to more realistically mimic the range of seismic acquisition in the field. The VSP is also an ideal scenario to test the attenuation of seismic data by analysing the spectrum of the arrivals within the subsurface volume. The phase-screen code can generate both plane and spherical wave sources which enable the tests to be conducted with and without consideration of geometrical spreading.

A 1-D model is built containing seven rocktypes, whose elastic parameters are shown in table 5.1, generating the P-wave, S-wave and density profiles shown in figure 5.1. The effective Q values shown in this model are chosen

to mimic a real subsurface environment (Hobbs, R.W., pers. comm.) and the modelling is run with and without attenuation in order to compare the spectral response.

Rock type	$V_{p\downarrow}\,(ms^{-1})$	$V_{s\downarrow}\,(ms^{-1})$	$\rho\,(kgm^{-3})$	$1/Q_p$	$1/Q_s$
1	1480.0	0.0	1000.0	0.0	0.0
2	2000.0	1155.0	2100.0	0.0100	0.00330
3	2500.0	1433.0	2200.0	0.0100	0.0330
4	3000.0	1732.0	2300.0	0.0125	0.0350
5	3500.0	2021.0	2400.0	0.0125	0.0350
6	4000.0	2309.0	2500.0	0.0100	0.0330
7	4500.0	2598.0	2600.0	0.0312	0.0500

Table 5.1: *Elastic parameters for media used in generation of synthetic VSP*
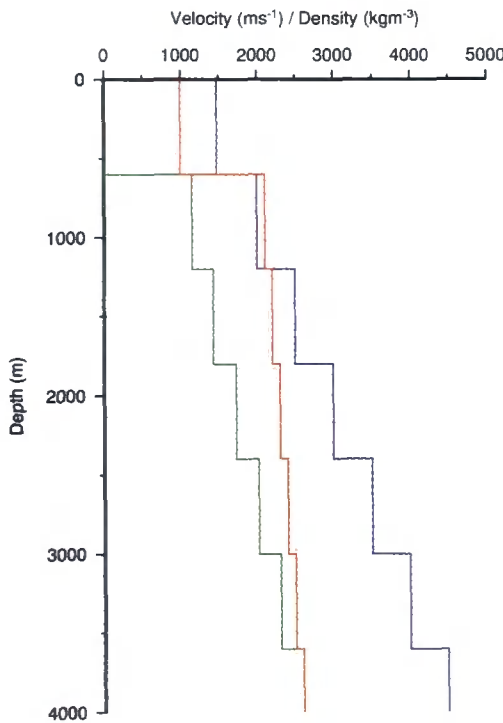
Figure 5.1: *Velocity and density structure of the VSP model as a function of depth: P-wave velocity - blue; S-wave velocity - green; and density - brown*

Receivers are placed every $100\,m$ in a 'borehole' positioned at the centre of a 3-D volume of lateral extent $1960 \times 760\,m$ with a near surface plane wave Ricker source of peak frequency $20\,Hz$. Primary-only modelling results are shown in figure 5.2 where (a) is modelled with no Q attenuation and (b) uses the Q values

in table 5.1. Both figures have been clipped identically to enable comparison between the attenuated and non-attenuated model runs. Table 5.2 presents a summary of both the theoretical and modelled travel times and expected amplitudes for significant arrivals from the wavefield in a non-attenuating subsurface.
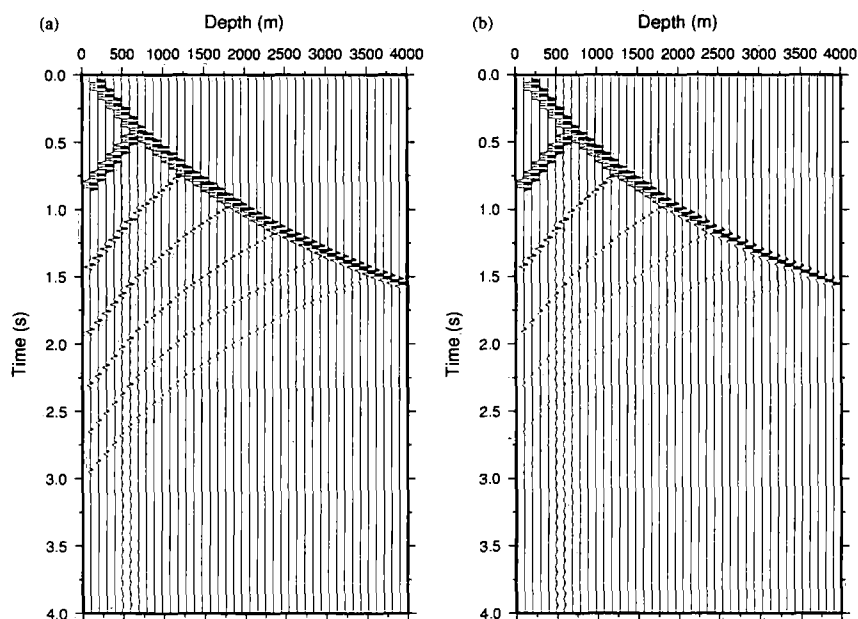
Figure 5.2: *Direct and reflected arrivals from VSP model shown in figure 5.1 with (a) from a non-attenuating subsurface and (b) from an attenuating version of the same model. Reflections from each of the interfaces are clearly observed with the relative amplitudes reduced in the attenuating volume*

The first arrivals at depths 400 m and 3800 m are isolated in order to undertake attenuation analysis in both attenuating and non-attenuating sub-surfaces. Transforming these wavelets into the frequency domain, and undertaking spectral ratio analysis it is possible to determine an effective Q for the region between the two depths. In the non-attenuating environment Q is expected to be infinite, with an effective Q of 99 expected in the attenuating volume. Figure 5.3 shows the spectral ratio results for both models with best fit gradients displayed on $ln\,(A_{38}/A_5)$ vs frequency plots.

Using an identical model the modelling is repeated with three orders of multiple included. Figure 5.4 displays the results of this modelling with and

Depth (m)	Arrival Route	Travel time (s)		Amplitude	
		Theoretical	Modelled	Theoretical	Modelled
400	D	0.2703	0.2703	1	1
1000	T	0.6054	0.6054	0.5211	0.4939
1600	TT	0.8653	0.8654	0.4513	0.4068
2200	TTT	1.1272	1.1273	0.4003	0.3505
2800	TTTT	1.2597	1.2597	0.3611	0.3095
3400	TTTTT	1.4167	1.4168	0.3297	0.2709
4000	TTTTTT	1.5557	1.5557	0.3039	0.2461
400	R	0.5405	0.5406	0.4788	0.4750
1000	TR	0.8054	0.8055	0.0698	0.0653
1600	TTR	1.0254	1.0254	0.0509	0.0456
2200	TTTR	1.2121	1.2122	0.0392	0.0347
2800	TTTTR	1.3740	1.3741	0.0314	0.0258
3400	TTTTTR	1.5168	1.5168	0.0258	0.0213

Table 5.2: *Comparison of theoretical and modelled travel times and expected amplitudes from VSP model without attenuation. The arrival routes are constructed with reference to each interface encountered where: D - direct arrival; T - transmission at interface; and R - reflection at interface. Therefore TTTRT would describe a reflection at the fourth interface followed by transmission through the third interface*
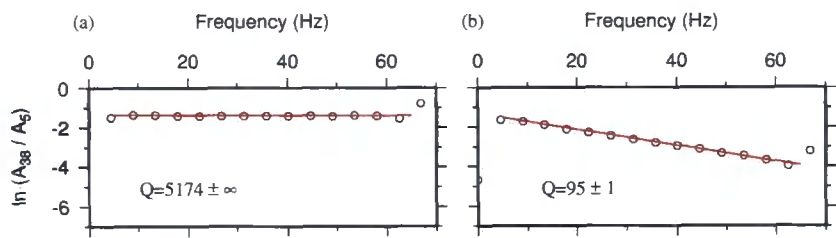
Figure 5.3: *Spectral analysis results for the VSP through attenuating and non-attenuating subsurfaces*

without attenuation whilst table 5.3 presents analytical and modelled travel times and amplitudes of significant arrivals in the non-attenuating case.

The results show the accuracy of the phase-screen modelling method in elastic and visco-elastic environments for direct, reflected and multiple arrivals. The Q attenuation has produced excellent agreement between the theoretical and modelled values, whilst small discrepancies are noticed with the amplitudes of the arrivals. However these errors can be explained as a consequence of the muting functions employed during the modelling and the accuracy of the result is not unduly affected whereas turning off the muting would create
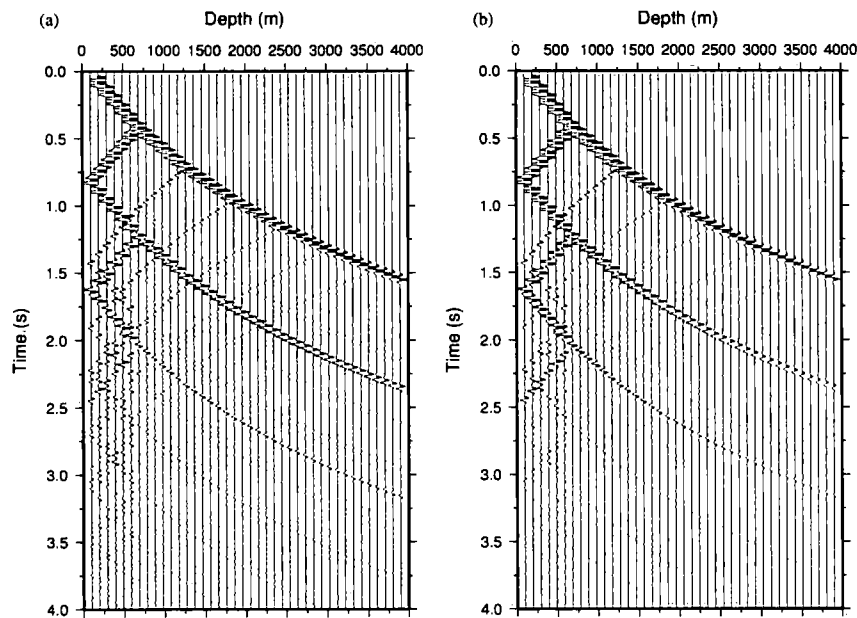
Figure 5.4: *The entire wavefield generated from three passes through the VSP model with (a) produced from a non-attenuating subsurface and (b) from the attenuating version. The generation of peg-leg multiple is clearly observed within the wavefield with parallel sets of arrivals corresponding to reverberations within a single bed. All arrivals displayed here are P-waves since a plane wave source is used.*

Depth (m)	Arrival Route	Travel time (s)		Amplitude	
		Theoretical	Modelled	Theoretical	Modelled
400	RR	1.0811	1.0810	0.4783	0.4334
400	RRRR	1.8919	1.8920	0.2228	0.1811
1000	TRR	1.2054	1.2054	0.03344	0.0291
1600	RRTT	1.6762	1.6763	0.2158	0.1754
2200	RRTTTTRT	2.3657	2.3656	0.016490	0.0131
3400	RRTTTTTR	2.3276	2.3275	0.01235	0.0092

Table 5.3: *Comparison of theoretical and modelled travel times and expected amplitudes with multiple energy included from VSP model without attenuation. The arrival routes are constructed in the same manner as for table 5.1*

numerous wrap-around events in the wavefield. For completeness, it is also necessary to state that, the phase-screen technique deals only with the components of the wavefield described in chapters 3 and 4 and makes no attempt to replicate coupling effects between the wavefield and the borehole or to model the tube waves within the borehole.

Replacing the plane wave source with a point source positioned coincident to the borehole on the top surface allows geometric spreading to be tested. The seven-layer model is replaced by a single homogeneous layer with elastic parameters equivalent to rock type 2 in table 5.1. Measurements of the amplitude of the forward propagating direct arrival at depths of 800 m and 1600 m are compared with theoretical amplitudes for a non-attenuating medium with results shown in table 5.4. The table shows the results for VSPs modelled on both a 2-D plane and a 3-D volume where amplitudes are expected to drop off proportional to $1/r$ and $1/r^2$ respectively and are scaled by the value recorded at depth of 400 m. Figure 5.5 displays this amplitude drop-off for the 2-D model without any gain applied.

Depth (m)	2-D Amplitude		3-D Amplitude	
	Theoretical	Modelled	Theoretical	Modelled
400	1	1	1	1
800	0.5	0.5922	0.25	0.3313
1600	0.25	0.320	0.0625	0.08696

Table 5.4: *Comparison of theoretical and modelled amplitudes from a homogeneous VSP in order to test geometrical spreading*

Table 5.4 shows that although the reduction in amplitude expected from geometrical spreading is not exactly accounted for, the accuracy achieved is within realistic limitations of the technique. This overestimation is again a consequence of the mute functions employed during modelling, particularly those in the wavenumber domain. Removing this muting results in a significant improvement but k-space wrap-around must be tolerated.

5.3 Validation against reflectivity method

The Reflectivity method is a wavenumber integration technique applicable to horizontally stratified media. The plane wave reflection coefficient is integrated across the entire wavenumber domain, equivalent to an integration across a range of incidence angles. The method was initially developed (Fuchs, 1968; Fuchs and Müller, 1971) to simulate propagation across a layered medium without a free-surface and was later expanded (Kennett, 1983) to model a layered half–space with a source positioned at an arbitary depth. Mallick and
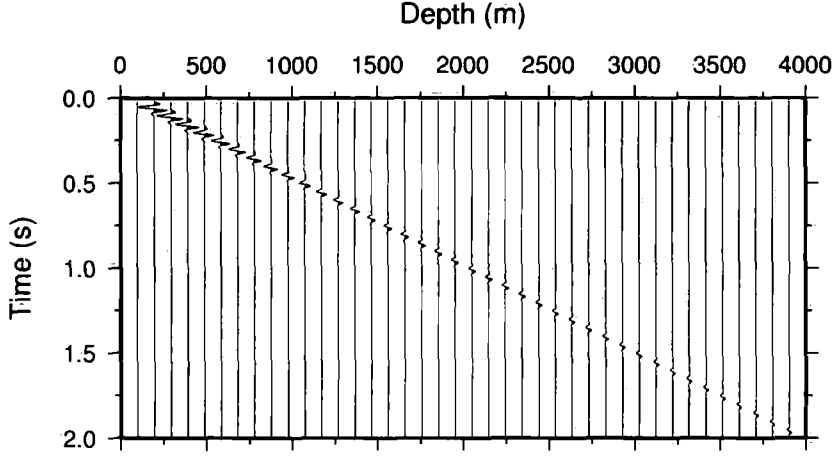
Figure 5.5: *Amplitude drop-off due to geometrical spreading in a homogeneous non-attenuating volume recorded on a VSP with a P-wave point source positioned on the top surface coincident with the first receiver*

Frazer (1987) offers a comprehensive guide for generating a reflectivity code whilst Müller (1985) provides an excellent tutorial which is summarised below.

The reflectivity technique is best described as a matrix method designed to solve the problem of the response of $n - 1$ homogeneous layers between two half spaces. Ignoring the time dependence $e^{i\omega t}$ the displacement potentials in layer j for the P-SV case are (following a similar notation to Müller (1985))

$$\phi_j = e^{-ik_x x} \left(A_j e^{-ik_{zj}^P(z-z_j)} - B_j e^{-ik_{zj}^P(z-z_j)} \right), \qquad (5.1)$$

$$\psi_j = e^{-ik_x x} \left(C_j e^{-ik_{zj}^S(z-z_j)} - D_j e^{-ik_{zj}^S(z-z_j)} \right), \qquad (5.2)$$

for $j = 0, 1, ..., n$ where the first terms correspond to the upgoing wavefield and the second terms to the downgoing wavefield. The reflectivities at the top of layer j can be defined from the amplitude ratios

$$
\begin{aligned}
PP_j^{TOP} &= \frac{B_j}{A_j}, & PS_j^{TOP} &= \frac{D_j}{A_j}, \\
SP_j^{TOP} &= \frac{B_j}{C_j}, & SS_j^{TOP} &= \frac{D_j}{C_j},
\end{aligned}
\qquad (5.3)
$$

and the combined reflectivity results can be expresed in a matrix,

$$\mathbf{MT_j} = \begin{pmatrix} PP_j^{TOP} & SP_j^{TOP} \\ PS_j^{TOP} & SS_j^{TOP} \end{pmatrix}. \tag{5.4}$$

The ratios at the bottom of layer j can be similarly expressed,

$$PP_j^{BOT} = \frac{B_j e^{+ik_{zj}^P d_j}}{A_j e^{-ik_{zj}^P d_j}} = PP_j^{TOP} e^{+2ik_{zj}^P d_j},$$
$$PS_j^{BOT} = \frac{D_j e^{+ik_{zj}^S d_j}}{A_j e^{-ik_{zj}^P d_j}} = PS_j^{TOP} e^{+i\left(k_{zj}^P + k_{zj}^S\right)d_j}, \tag{5.5}$$

and

$$\mathbf{MT_j} = \begin{pmatrix} PP_j^{BOT} & SP_j^{BOT} \\ PS_j^{BOT} & SS_j^{BOT} \end{pmatrix}. \tag{5.6}$$

This allows the relationship between the top and bottom of layer j to be defined as

$$\mathbf{MT_j} = \mathbf{E_j MB_j E_j}, \tag{5.7}$$

where the phase matrix is simply

$$\mathbf{E_j} = \begin{pmatrix} e^{-ik_{zj}^P d_j} & 0 \\ 0 & e^{-ik_{zj}^S d_j} \end{pmatrix}. \tag{5.8}$$

The next step is to calculate the relationship between the bottom of layer j, $\mathbf{MB_j}$ and the top of layer $j + 1$, $\mathbf{MT_{j+1}}$. Once again expressing the amplitudes as functions of the reflectivities and defining matrices of reflection and transmission coefficients for an interface at $z = z_{j+1}$ as

$$\mathbf{R_{j+1}^{d,u}} = \begin{pmatrix} R_{pp}^{d,u} & R_{sp}^{d,u} \\ R_{ps}^{d,u} & R_{ss}^{d,u} \end{pmatrix}, \tag{5.9}$$

$$\mathbf{T_{j+1}^{d,u}} = \begin{pmatrix} T_{pp}^{d,u} & T_{sp}^{d,u} \\ T_{ps}^{d,u} & T_{ss}^{d,u} \end{pmatrix}, \tag{5.10}$$

the required relationship is

$$\mathbf{MB_j} = \mathbf{R^d_{j+1}} + \mathbf{T^u_{j+1}} \left[\mathbf{I} + \mathbf{MT_{j+1}R^u_{i+1}}\right]^{-1} \mathbf{MT_{i+1}T^d_{i+1}}. \tag{5.11}$$

Reflectivity modelling then uses recursive applications of equations 5.7 and 5.11 to determine the overall reflectivity matrix

$$\mathbf{RR^d} = \left(\begin{array}{cc} RR^d_{pp} & RR^d_{sp} \\ RR^d_{ps} & RR^d_{ss} \end{array} \right), \tag{5.12}$$

starting at $j = n - 1$. This algorithm is stable at all slownesses and frequencies and similar equations to equation 5.12 can be calculated for transmission, and for incidence from the lower half-space.

The code used to verify the phase-screen results is the Nucleus 1D reflectivity package from PGS Research where the reflection and transmission matrices for a stack of homogeneous layers are calculated with this recursive algorithm derived by Kennett (1983). This method generates all possible interactions including converted phases, interbed and peg-leg multiples and surface related multiples. Multiplication with a source function and application of an inverse Fourier transform produces a traditional time-offset seismic profile.

The advantage of reflectivity modelling is the frequency dependent effects of thin layers are generated during modelling.

5.3.1   Building a layered half–space

Table 5.5 shows the elastic parameters of the 5 layer model.

Thickness (m)	$V_{p\downarrow}\ (ms^{-1})$	$V_{s\downarrow}\ (ms^{-1})$	$\rho\ (kgm^{-3})$	δ	ϵ	$1/Q_p$	$1/Q_s$
500	1480.0	0.0	1000.0	0.0	0.0	0.0	0.0
200	1500.0	200.0	1500.0	0.0	0.0	0.0	0.0
300	1750.0	500.0	1600.0	0.0	0.0	0.0	0.0
500	2100.0	1100.0	1900.0	0.0	0.0	0.0	0.0
∞	2700.0	1275.0	2200.0	0.0	0.0	0.0	0.0

Table 5.5: *The rock parameters for the 5 layer stratified media used for comparison between the enhanced phase-screen and reflectivity methods*

This model aims to replicate the near surface often found during streamer acquisition. The source wavelet, constructed using the Nucleus Marine Source Modelling application is fired from a single Bolt gun with 150 cu. in. volumetric capacity and a pressure of 2000 psi at 6 m depth. Receivers are towed at 8 m and source, receiver and source and receiver ghosts are modelled during the acquisition with the source coincident to the first receiver and the receiver array positioned with offsets up to 1000 m.

Figure 5.6 shows the results of the modelling at an evenly spaced range of offsets. The results show an excellent correlation between the two methods with no obvious errors for concern. The reflectivity modelling was performed with all internal and surface multiples whilst the phase-screen was modelled with three passes, giving three orders of multiple.
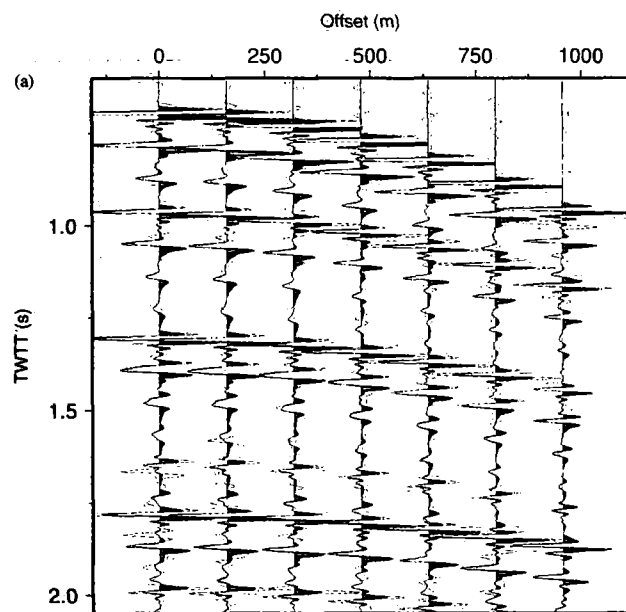
Figure 5.6: *Seismic gather for 5 layer stratified media. The red traces show the response from the wide-angle phase screen code and the underlying black traces are the results from the Nucleus reflectivity package.*

The reflectivity method can also be used to benchmark the wide-angle phase-screen technique in anisotropic environments. If layer four in the previous model is assumed to display vertical transverse anistropy then both the

phase-screen and the reflectivity methods can handle the new subsurface. Table 5.7 shows the revised model and the acquisition parameters are left unchanged.

Thickness (m)	$V_{p\downarrow}$ (ms^{-1})	$V_{s\downarrow}$ (ms^{-1})	ρ (kgm^{-3})	δ	ϵ	$1/Q_p$	$1/Q_s$
500	1480.0	0.0	1000.0	0.0	0.0	0.0	0.0
200	1500.0	200.0	1500.0	0.0	0.0	0.0	0.0
300	1750.0	500.0	1600.0	0.0	0.0	0.0	0.0
500	2100.0	1100.0	1900.0	-0.05	0.3	0.0	0.0
∞	2700.0	1275.0	2200.0	0.0	0.0	0.0	0.0

Table 5.6: *The rock parameters for the 5 layer stratified media including anisotropy used for comparison between the enhanced phase-screen and reflectivity methods*

Figure 5.7 compares the isotropic and anisotropic versions of the phase-screen code. A small difference in travel time is noted on the fourth reflected arrival, but the primary difference is with the amplitude of the third reflection as a function of angle. Figure 5.8 compares the anisotropic phase-screen response with that from the reflectivity code and the expected amplitudes map accurately between the two methods.
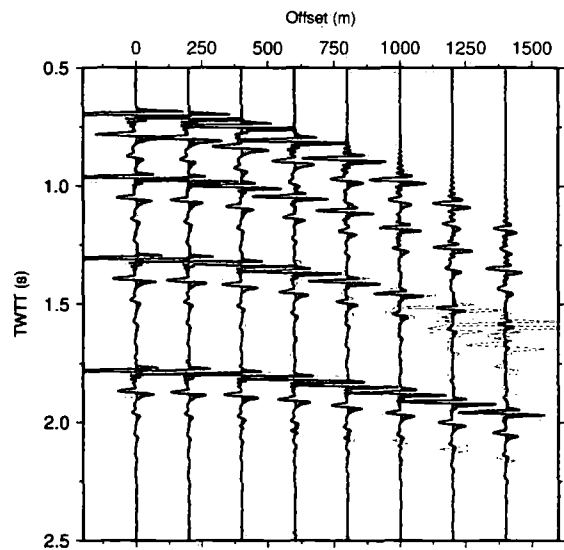
Figure 5.7: *Comparison of isotropic and anisotropic phase-screen methods in anisotropic media. The red traces show the anisotropic modelling whilst the black traces are generated with the isotropic version of the phase-screen code.*

5.4 Modelling across a low velocity zone for validation against the ray tracing technique

The aim of this section of the study is two-fold. Primarily, the objective is to provide evidence that travel paths and amplitudes are accurately modelled through 3-D volumes where velocity and density profiles normally associated with compaction are not seen. The model used in this example has a low velocity layer from which the polarity of the arrivals from the top surface of the unit will be reversed. Secondly, the model also contains an off-axis diffractor that generates an additional arrival across the receiver array. The extent of the model is 5000 m in x, and 1000 m in y, with the diffractor placed at a depth of 1750 m under $x, y = 2500, 500$ m. The source and receiver reside in the 2-D plane $y = 600$ m, with the shot fired at $x = 2800$ m. The source wavelet is generated with Nucleus Marine Source Modelling software from PGS Research and replicates a Sodora P400 watergun (400 cu.in. and 2000 p.s.i.) at 5 m depth whilst the receiver array is towed at 6 m depth and contains 141 receivers with a group spacing of 20 m.
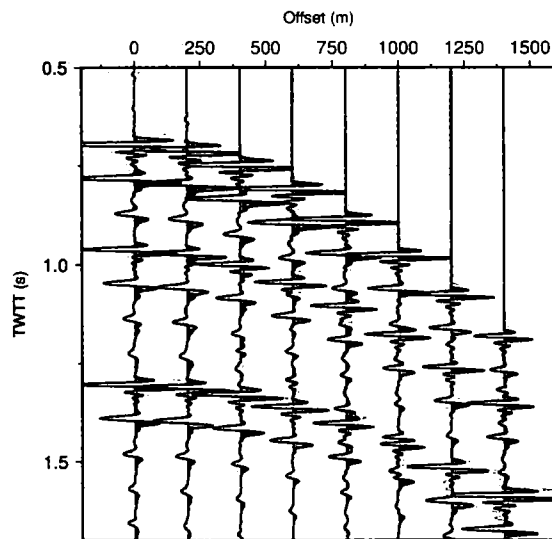
Figure 5.8: *Comparison between reflectivity (black traces) and phase screen (red traces) methods in anisotropic media. Particular attention is drawn to the amplitudes of the third reflection. The variation in amplitude of the near surface reflections is a consequence of the source tapering employed in the phase-screen modelling and is not a product of the method.*

Thickness (m)	$V_{p\downarrow}\ (ms^{-1})$	$V_{s\downarrow}\ (ms^{-1})$	$\rho\ (kgm^{-3})$
500	1480.0	0.0	1000.0
500	2000.0	1200.0	1750.0
250	1750.0	1000.0	1500.0
1000	3000.0	1900.0	2400.0
∞	3600.0	2000.0	2700.0

Table 5.7: *The rock parameters for the 3-D ray tracing example*

The ray paths from the Nucleaus 3-D seismic ray tracing code are shown in figure 5.9. The primary only wavefield is generated in order to better constrain the noted arrivals. The diffractions are generated differently by the two modelling techniques, with an independent arrival of arbitary strength being derived for the ray tracing. This arrival which is equivalent to an additional source at depth, time shifted to account for the propagation to the diffractor, is not derived as a consequence of the ray tracing through the model since simple ray tracing methods fail to accurately account for diffractions. Instead the final result can be thought of as a summation of two wavefields which, between them both, generate the expected arrivals. In the phase-screen code the diffraction is derived by generating a small region of high-velocity, high-density material of thickness less than 1/8th of the shortest modelled wavelength and of lateral extent less than the horizontal Fresnel zone at the depth of the diffractor.

Figure 5.10 shows the response of the phase-screen modelling alongside the shot gather from the 3-D ray tracing and agreement between the two methods is excellent. The difference in the amplitude of the arrival from the diffractor is a consequence of the varying methods adopted by the modelling codes and the phase-screen solution can be considered the more accurate since it is generated from the incident wavefield on the diffracting region. Since it is impossible to correlate the diffracted arrival by eye, figure 5.11 shows this section of the wavefield with a gain applied to the phase-screen response in order to generate a comparable amplitude from the diffractor.
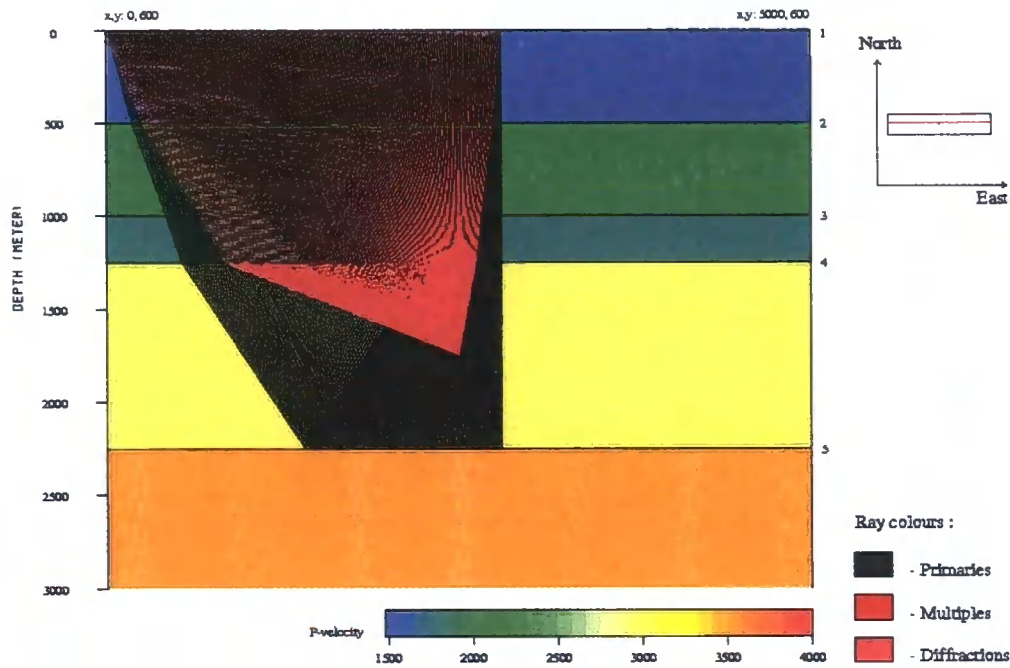
Figure 5.9: *Modelled raypaths for the ray tracing study including arrivals from the off-axis diffractor (after screen shot from PGS Nucleaus 3-D seismic ray tracing.*
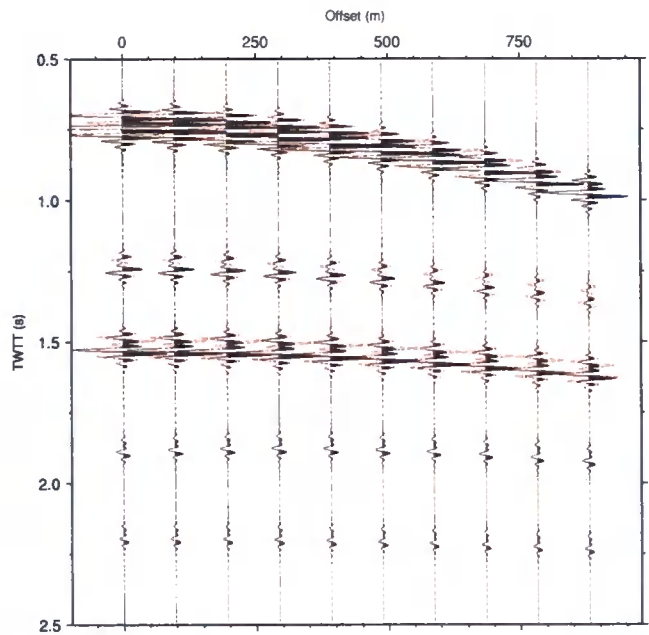
Figure 5.10: *Seismic shot gather for comparison between phase-screen method (red traces) and ray tracing technique (black traces).*
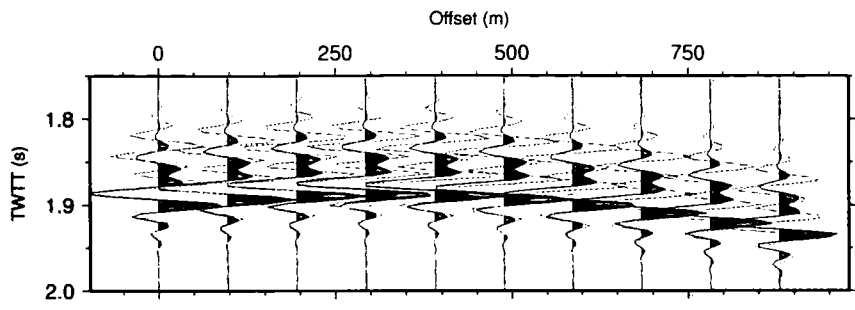
Figure 5.11: *Sub-section of seismic shot gather for comparison between phase-screen method (red traces) and ray tracing technique (black traces).*

5.5 Investigating reciprocity

Reciprocity is one of the fundamental tenets of seismic theory and confirming that forward modelling codes obey this principle is a necessary test for any commercial code. The expected results are well known within the modelling community but can still confuse investigators (Muerdter et al., 2001) when observations and results seem to contradict the expected outcomes. The aim of this section is to construct a model that confirms that travel times and amplitudes are equivalent for symmetric ray paths shot up or down dip when switching source and receiver positions. The model generated for this test is inspired by the model of Muerdter et al. (2001) where a water layer overlays a thick homogeneous unit within which sits an intruded salt wedge of high velocity. Beneath the homogeneous layer sits an infinite half space composed of a higher velocity unit, figure 5.12 shows the model whose elastic properties are shown in table 5.8. Attenuation and anisotropy are not considered in this example.

Rock	$V_{p\downarrow}\,(ms^{-1})$	$V_{s\downarrow}\,(ms^{-1})$	$\rho\,(kgm^{-3})$
1 – Water (Blue)	1500.0	0.0	1000.0
2 – Sediment (Green)	2400.0	1200.0	1800.
3 – Salt	4450.0	2590.0	2100.0
4 – Sediment (Brown)	3000.0	1800.0	2000.0

Table 5.8: *The rock parameters for the reciprocity tests through a salt wedge*
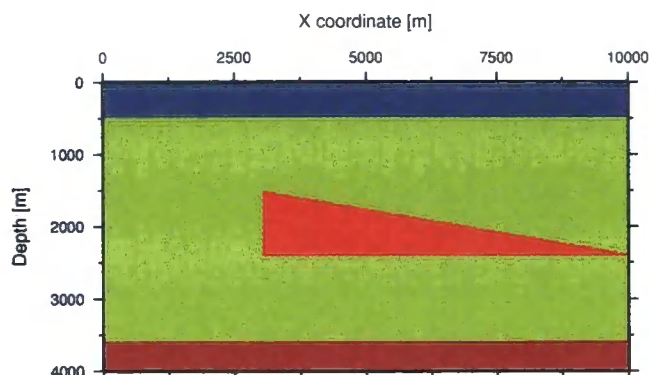
Figure 5.12: *Salt wedge model generated to confirm principle of reciprocity with enhanced phase-screen technique*

Considering rays shot down-dip (left to right) that reflect off the interface at $3600\ m$, enter the salt body through the flat base and continue up to the surface the enhanced phase-screen method will endeavor to determine the true angle of incidence and apply exact reflection and transmission coefficients at any interfaces, even in regions of local slope. The screen separation through the vertical extent of the salt body was $20\ m$ and with a $20\ Hz$ Ricker employed as the source wavelet a quarter of the dominant wavelength will be greater than the screen spacing and the principle of superposition will ensure that the angle of propagation is correctly determined.

Plotting the travel times of down-dip and up-dip ray paths as red circles and blue crosses respectively the reciprocity of travel times can be confirmed in figure 5.13. Adopting the same symbols but measuring amplitudes instead an equivalent plot, figure 5.14 demonstrates that the enhanced phase-screen technique obeys the principle of reciprocity. Small errors in the amplitudes of arrivals are noted with this technique and are a consequence of the modelling mutes but to within the errors expected in seismic data these small discrepancies can be neglected.

5.6   Validation against finite difference

The finite-difference method is the most rigorous scheme regularly employed by industry and academia to solve the wave equation (Etgen and OBrien, 2007)
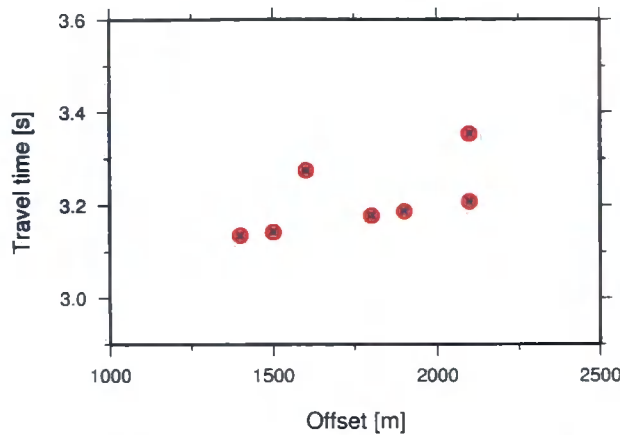
Figure 5.13: *Up- and down-dip travel times through the salt wedge model demonstrating the equivalence of symmetrical ray paths*
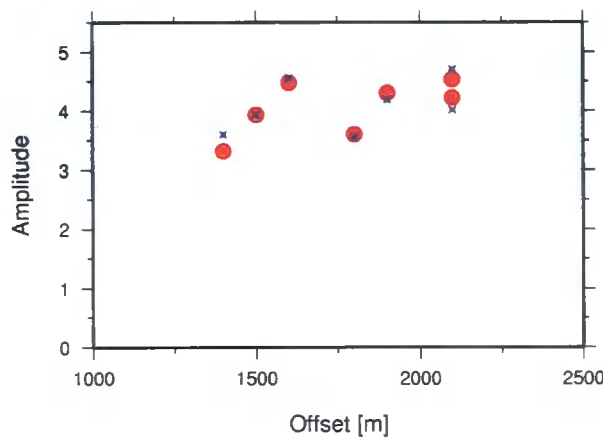
Figure 5.14: *Up- and down-dip amplitudes through the salt wedge model demonstrating the equivalence of symmetrical ray paths*

and tackles the problem by replacing derivatives with difference quotients. By considering a function, $f(x)$, defined at regular equal intervals, Δx, and developing the Taylor Series for the points $f(x_{i+1})$ and $f(x_{i-1})$ from $f(x)$ enables calculation of the forward, reverse and central differences,

$$\frac{\partial f}{\partial x} = \frac{1}{\Delta x}(f_{i+1} - f_i) + \Theta(\Delta x), \tag{5.13}$$

$$\frac{\partial f}{\partial x} = \frac{1}{\Delta x}(f_i - f_{i-1}) + \Theta(\Delta x), \tag{5.14}$$

and

$$\frac{\partial f}{\partial x} = \frac{1}{2\Delta x}\left(f_{i+1} - f_{i-1}\right) + \Theta\left(\Delta x^2\right)^2,\tag{5.15}$$

where $\Theta\left(\Delta x\right)$ is the error in the approximation. Analogously, higher-order finite difference approximations can be determined, by applying equation 5.15 at $f\left(i + \Delta x/2\right)$ and $f\left(i - \Delta x/2\right)$ for the second derivative central difference approximation,

$$\frac{\partial^2 f}{\partial x^2} = \frac{1}{\left(\Delta x\right)^2}\left(f_{i+1} - 2f_i + f_{i-1}\right) + \Theta\left(\Delta x\right)^2.\tag{5.16}$$

Assuming the sampling is fine enough the expresssions 5.13 – 5.16 are sufficiently accurate to describe the required derivatives.

Finite difference techniques are most commonly used to determine solutions to the acoustic wave equation,

$$\frac{\partial^2 u}{\partial t^2} = v^2\left(x\right)\frac{\partial^2 u}{\partial x^2},\tag{5.17}$$

where a second order in time (evaluated using a forward difference) and space (evaluated using a central difference) time-marching finite difference solution would be

$$\begin{aligned}u\left(x, t + \Delta t\right) = v^2\left(x\right)\frac{\Delta t^2}{\Delta x^2}\left[u\left(x + \Delta x, t\right) - 2u\left(x, t\right) + u\left(x - \Delta x, t\right)\right]\\ + 2u\left(x, t\right) - u\left(x, t - \Delta t\right),\end{aligned}\tag{5.18}$$

allowing the wavefield at t_{-1} and t to derive the entire wavefield at t_{+1}. Solutions to more complex variants of the wave equation are generated following the same principles.
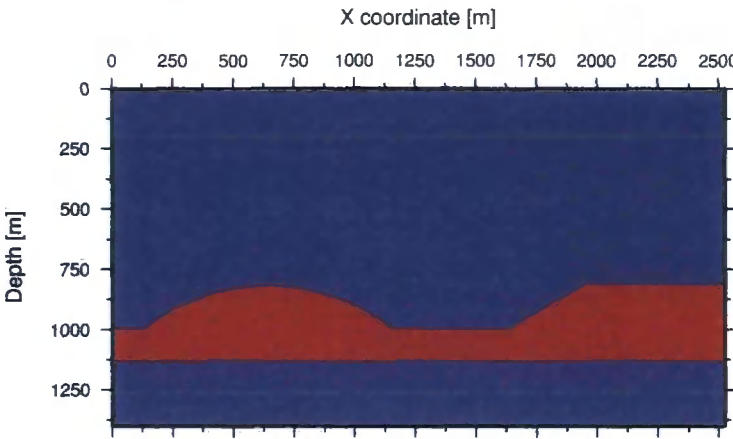
Figure 5.15: *The 2-D French model comprised of two rocktypes generating a ridge and fault interface*

5.7   French 2D model

Sub-surface models demonstrating rapidly varying lateral structural changes were used to test migration algorithms by French (1974). The models generated in this paper are regularly used to test how seismic forward modelling algorithms respond to structural changes. French (1974) produced both 2- and 3-D models and, for the purposes of this study, the 2-D model will be used to test the wide angle phase-screen code. The model is designed to replicate a seismic profile over two subsurface features: a rounded ridge and a normal fault. Figure 5.15 shows the model comprised of 2 distinct rocktypes whose parameters are displayed in table 5.9. The top interface contains the topography whilst the lower interface, with an acoustic impedence increase, is flat across the entire region of interest.

Rock	$V_{p\downarrow}\,(ms^{-1})$	$V_{s\downarrow}\,(ms^{-1})$	$\rho\,(kgm^{-3})$	δ	ϵ
Rock A	3600.0	2080.0	2200.0	0.0	0.0
Rock B	2880.0	1664.0	2200.0	0.0	0.0

Table 5.9: *The rock parameters for the 2-D French model*

Initially acoustic modelling will be performed for comparison with Pro-Max's second order finite difference scheme. The technique, based upon Kelly et al. (1976) is a simple acoustic finite difference method.

Two shots are modelled for comparison with a split spread of top surface receivers out to ± 625 m. The source function is a Gaussian with a peak frequency of 20 Hz and is located at (a) $x = 1245$ m, and (b) $x = 1800$ m. Figures 5.16 and 5.17 show the responses from both the wide-angle acoustic phase-screen technique and the second order acoustic finite difference method. The arrival times and amplitude characteristics are consistent in both examples.

5.8 Marmousi2 model

The original Marmousi data set (Versteeg, 1994) has been utilised extensively in the geophysics community (Zhu and Lines, 1998; Alkhalifah, 2000) as a synthetic 2-D sub-surface example to test finite difference modelling codes. This original model is acoustic and contains complex structure and subtle velocity variations. Martin (2004) expanded the original Marmousi model, creating a larger version specifically designed for AVO analysis. Since the AVO response is dependent upon deriving exact reflection and transmission coefficients de-
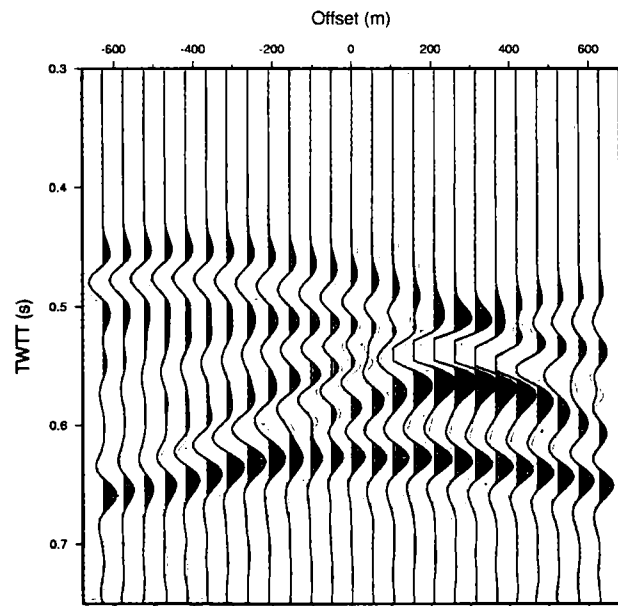
Figure 5.16: *Comparison between acoustic finite difference (black traces) and phase screen (red traces) methods over the French model with source positioned at* $x = 1245$ *m.*
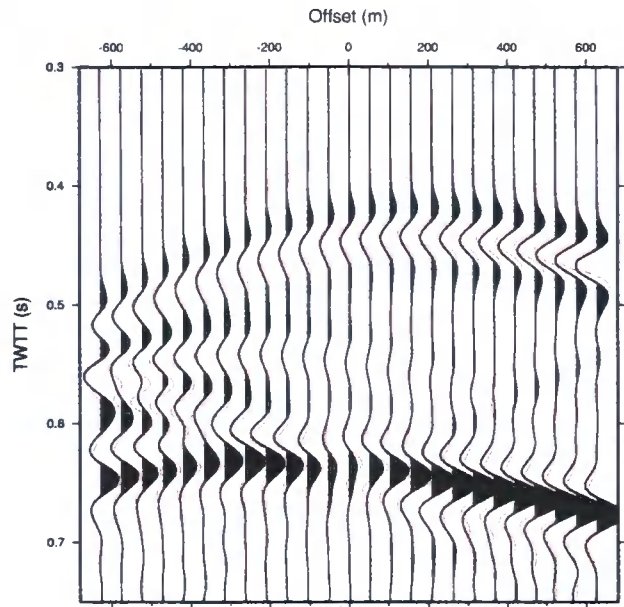
Figure 5.17: *Comparison between acoustic finite difference (black traces) and phase screen (red traces) methods over the French model with source positioned at* $x = 1800$ *m.*

veloping an elastic model was essential. This 'next generation' model was named Marmousi2.

The complete Marmousi2 model now contains a deep-water layer placing the waterbottom at 450 m. There are also several thin transition layers displaying characteristics comparable with soft tertiary sediments beneath this top surface. This gives a realistic comparison with deep water acquisition and offers a better coupling opportunity. The P-wave velocity model is shown in figure 5.18 with no vertical exageration.
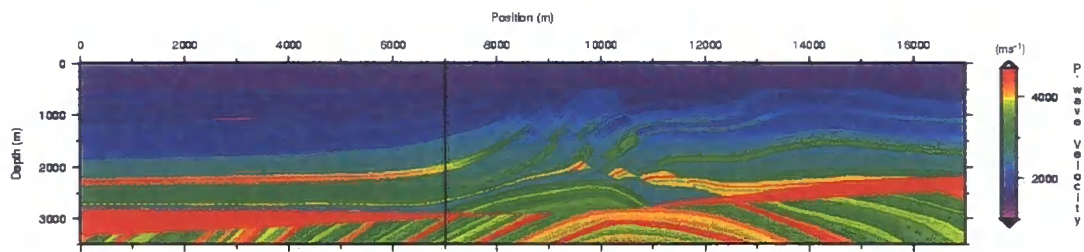
Figure 5.18: *The complete Marmousi2 P-wave velocity model*

The area of interest within this study is the section between $0 \, m$ and 7000 m, part of the expanded section where there is less structural complexity and a general flattening of the sedimentary horizons. Table 5.10 gives details of the scale of the reduced model and the parameterisation for phase-screen modelling. The lateral spacing was increased to $15 \, m$ and the screen spacing was set at $5 \, m$ in order to maintain the structural complexity of the model and capture the thinner units. Typically the sedimentary layers have thicknesses ranging from 20–$100 \, m$ and this directly influences the screen spacing used during phase-screen modelling. Detailed P- and S-wave velocity and density plots for the region of interest are displayed in figure 5.19.
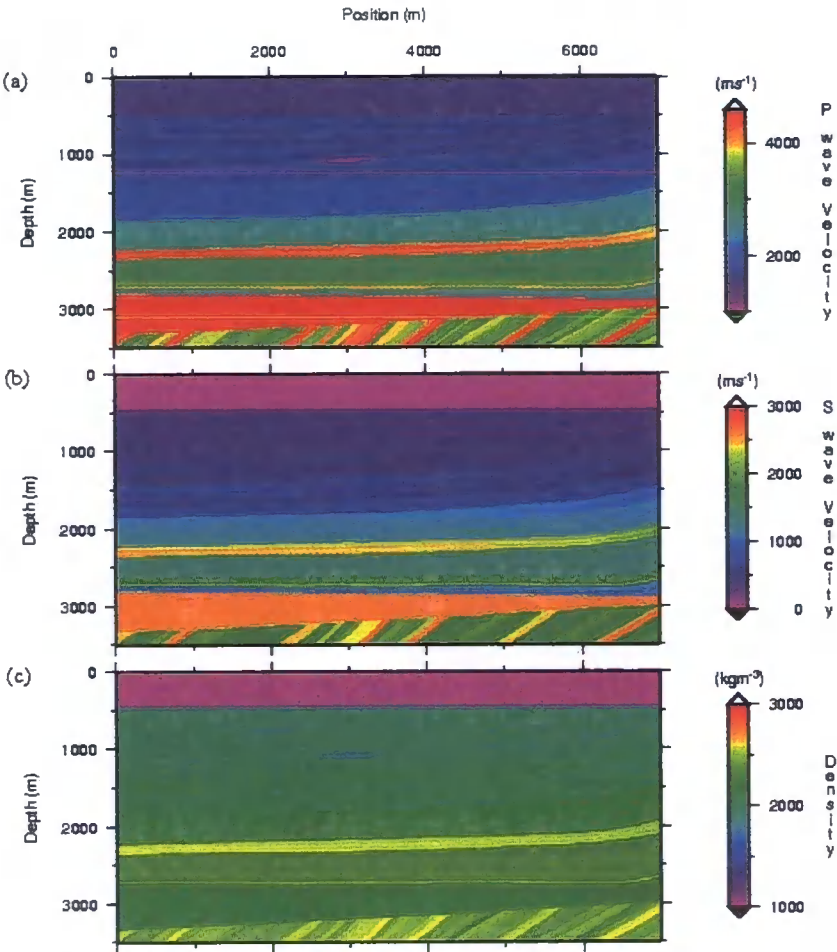
Figure 5.19: *The reduced Marmousi2 model utilised in this study showing (a) the P-wave velocity profile; (b) the S-wave velocity profile; and (c) the density profile.*

	Full Marmousi2	Zone of interest
Start position X(m)	0.00	0.00
End position X(m)	17.00	7.00
Depth(m)	3.50	2.25
Total screens	X	701
Total rock types	X	521

Table 5.10: *Summary of parameterisation of reduced Marmousi2 model*

The sediments themselves are based upon geology from the North Quenguela Trough in the Quanza Basin of Angola. Martin (2004) assigns lithologies to the rocktypes using the following criteria:

- The salt and water layers from the original model are preserved.

- The first two layers (transitional layers) are shale, and possess properties consistent with soft modern sediments.

- All layers containing hydrocarbons must be sand.

- All other layers are either sand or shale, with the majority being shale. The sand layers were picked out by assuming that sands are typically less dense then shale.

The aim of this part of the study is two-fold, firstly to replicate synthetic streamer data generated by Martin (2004) using an elastic finite difference approach at a node spacing of 1.25 m, and secondly to investigate the AVO response of a hydrocarbon trap within the extended section of the Marmousi2 model.

5.8.1 Comparison with elastic finite difference

The finite difference modelling used for comparison with the enhanced phase-screen code was produced by Martin (2004), used a large bandwidth source and generated all possible multiple paths. A reference shot at $x = 6100$ m was replicated with a comparable source signature and acquisition geometry in order to test the phase-screen code against a seismic model in common usage. During processing multiple energy was removed from the shot data allowing

comparison with both primary only and full wavefield modelling from the phase-screen code.

Figure 5.20 (a) shows the multiple pass enhanced phase-screen code against an elastically modelled finite difference response which includes all internal reflections. The agreement is excellent with the only noticeable regions of error at wide angles for the upper reflections where the phase-screen code has been muted to avoid unwanted wrap-around energy. Martin (2004) then performs a standard processing flow with surface related multiple attenuation in order to isolate the primary wavefield and figure 5.20 (b) shows this overlain by the phase-screen single pass wavefield. Again there is a high degree of correlation in terms of travel time, polarity, and amplitude of the arrivals.

The primary hydrocarbon trap introduced into the Marmousi2 model is buried at a depth of $\approx 1000\ m$ at a position 3000 m from the left edge of the model and can be clearly seen in figure 5.19. The water-wet sand is substituted with a hydrogen-charged sand containing a gas deposit which results in a significant reduction in the P-wave velocity and the density, but only a minor variation in the S-wave velocity. The expected upshot of this substitution is a very bright spot with large amplitudes at all offsets and a moderate increase in amplitude with increasing offset. Modelling the expected variation in amplitude for an interface between a gas charged sand overlain by a shale at comparable depths reveals the expected response from the top and bottom of the trap and is shown in figure 5.21.

The average thickness of the the hydrocarbon trap under investigation is 38 m with a maximum vertical extent of 45 m. As such, the phase-screen model has $\sim$seven screens covering the thickness of the trap. Four shots were synthetically acquired in order to test the AVO response of the model. The first, at $x = 3030$ m, has zero offset from the target and additional shots are fired at intervals of 260 m with increasing x. The modelling was undertaken with both the old and the enhanced versions of the phase-screen code and figure 5.22 displays the cdp gathers at $x = 3030\ m$ for each of these model runs after a normal moveout correction has been applied. The maximum relevant source-receiver offset of 1560 m is approaching the point where offset equals depth.
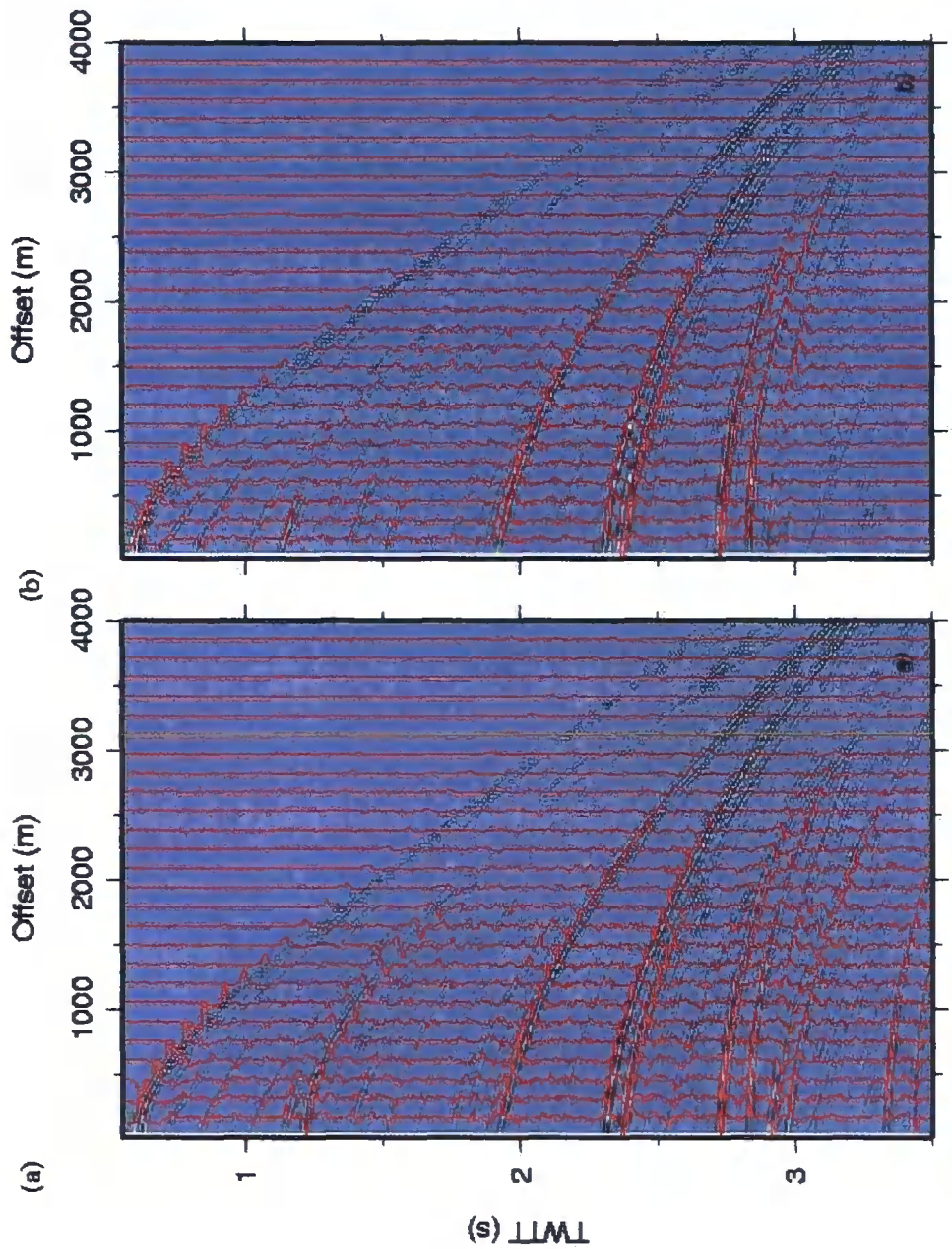
Figure 5.20: *Comparison between enhanced phase-screen and elastic finite difference methods for streamer data over the Marmousi2 model. In each case the red traces are the phase-screen response and (a) shows the entire synthetic response whilst, (b) contains only the primary wavefield (after Martin (2004)).*
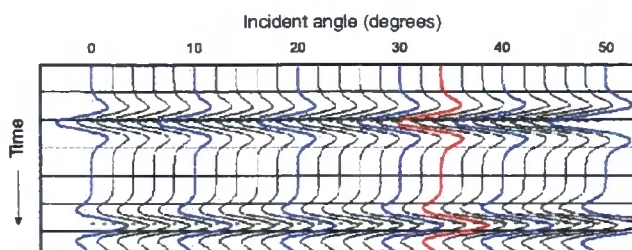
Figure 5.21: *The expected AVO characteristics from a hydrocarbon trap in Marmousi2 model where the red line indicates offset=depth and the first response in time is from the top of the trap and the second response is from the bottom, after Martin (2004)*
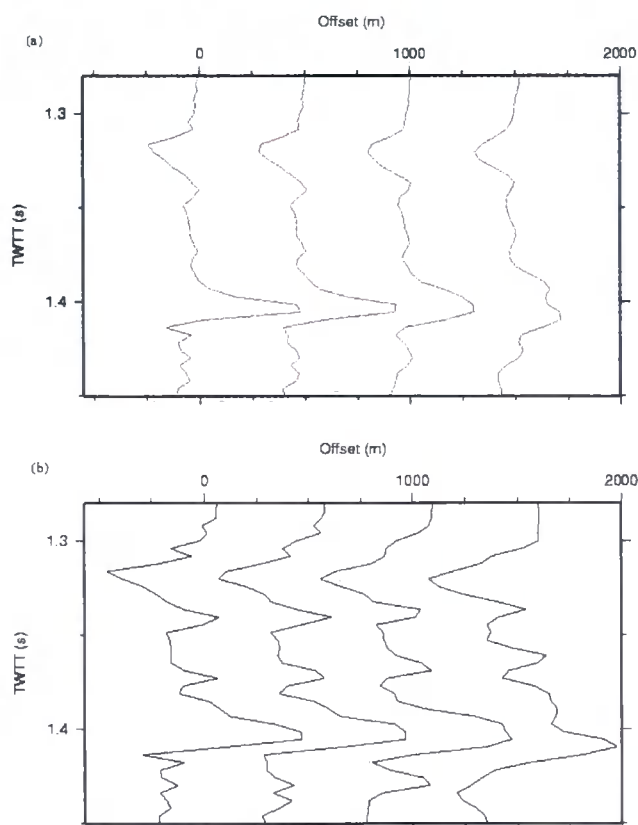
Figure 5.22: *AVO analysis from the (a) old and (b) enhanced phase-screen methods for a hydrocarbon trap in Marmousi2 model. The variation in amplitude with the enhanced phase-screen code more realistically approximates the expected response from the trap and provides agreement with the calculated response of figure 5.21.*

The expected bright spots at both the top and the bottom of the hydrocarbon are clearly seen in both versions of the phase-screen, but it is apparent, and expected, that only the enhanced phase-screen code manages to correctly

replicate the moderate increase in amplitude with offset. In most modelling assignments the screen spacing would be considerably sparser than those chosen for this experiment meaning worse results could be expected if this modelling were undertaken as part of a larger modelling assignment.

5.8.2 Justification for using the enhanced phase-screen method for AVO analysis

The results shown in this chapter, supported by the conclusions in White and Hobbs (2007), have clearly demonstrated that the enhanced phase-screen method has the capacity to model variations in the amplitude of arrivals as a function of offset. The technique accurately captures the subtleties of the energy partitioning but is still an approximate technique for modelling seismic reflection and should be considered as such. The results demonstrate that the accuracy is sufficient to make assumptions, based on the reflected wavefield, in reasonably complex subsurface scenarios. The method generates a plane-wave, planer-interface solution to the problem yet, can run considerably faster than finite difference methods on comparable models. As such the enhanced phase-screen technique is a useful addition to the community of seismic wave modelling techniques that aim to produce more than simple travel time arrival curves.

5.9 Modelling in an anisotropic marine sedimentary location

This part of the study involves generating synthetic seismic data using associated velocity and anisotropy models. The region under investigation is a producing field in a marine sedimentary location where an exhaustive range of geophysical techniques were used to constrain the VTI parameters since surface seismic data is unable to do this if considered independently. An integrated approach (Bear et al., 2003) that incorporated sonic logs, vertical and offset checkshots alongside horizon constraints were used to feed an anisotropic PSDM velocity analysis algorithm that produced VTI parameters that are a true representation of geology whilst giving correct move-out and travel times for

shot gathers. The technique produces an improved positioning of reflectors in relation to isotropic PSDM. The method uses well logs to constrain the vertical velocity, then, by isolating the small to mid offset seismic data at the well locations, δ is derived. δ is then extrapolated/interpolated across the subsurface volume using a user controlled interpolation method forced by the local geology. Finally η is picked from the far offset seismic data at a limited number of positions and interpolated to all locations. This allows the calculation of ϵ from

$$\eta = \frac{\epsilon - \delta}{1 + 2\delta}.$$

(5.19)

The velocity structure follows the expected compaction trends seen in marine sedimentary basins, however, the anisotropy shows a strong correlation with structure providing evidence that the primary control on anisotropy is lithology. A cross-section from the region of the model used in this study is shown in figure 5.23 where the velocity, the local vertical velocity gradient, and the anisotropic parameters δ and ϵ are displayed. It is apparant that a smooth velocity structure has been derived from the anisotropic velocity analysis. There are no sharp acoustic impedence contrasts that would generate a correlated reflection on a seismic shot record. Since the elastic parameters are used in the pre-stack migration of data, this study aims to generate two migration operators equivalent to a point source at depth. These operators will both be generated from a position $x = 5.5\ km$, $z = 5.5\ km$ using 3-D phase-screen modelling but one will calculate the operator isotropically whilst the second will use the VTI parameters to generate a more accurate response.

Adopting a 25 Hz Ricker wavelet as the source signature, and recording a 7 km receiver array split equally across the source position, the migration operators were determined. Figure 5.24 shows the two responses which, due to the lack of lateral heterogeneity in the region of interest, are reasonably symmetrical. This approximate 1-D nature of the sub-surface is normally required in order to realistically approximate the lithology to a VTI media. As expected, the difference at zero-offset is negligible since the model is described
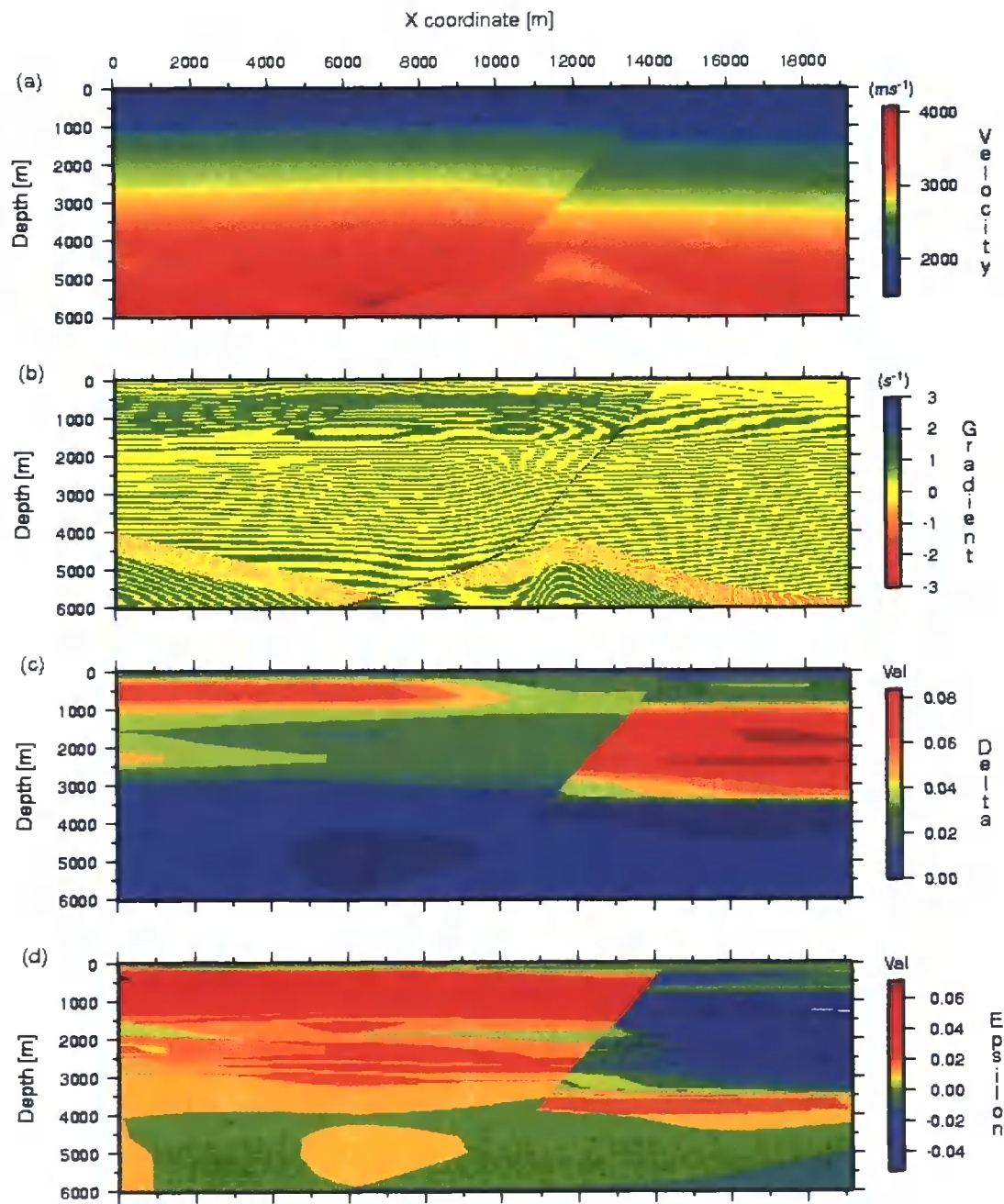
Figure 5.23: *Cross-sections from anisotropic marine sedimentary location showing (a) P-wave velocity, (b) vertical velocity gradient, and the anisotropic parameters (c) δ and (d) ϵ*

as a function of vertical velocity, however the error in the operator increases with offset.
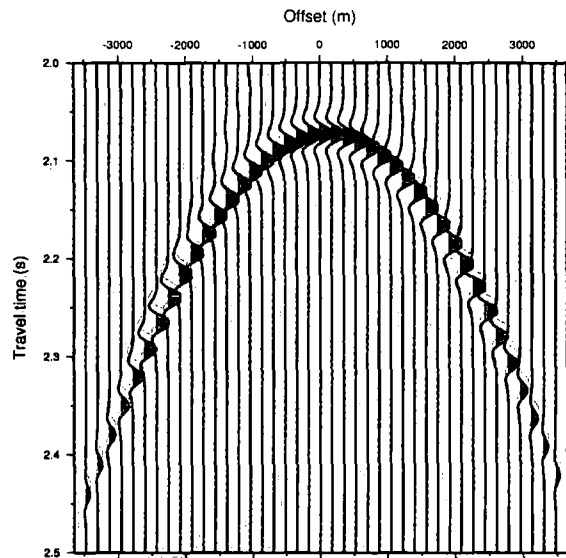
Figure 5.24: *Isotropic and anisotropic migration operators from 5.5 km depth where the red traces display the isotropic response and the black traces display the true anistropic migration operator.*

Considering this error in terms of building a velocity profile on the assumption that the sub-surface were isotropic would result in a normal moveout velocity of 2770 ms^{-1} for the anisotropic example created with the enhanced phase-screen. The true stacking velocity should be 2830 ms^{-1} resulting in an approximate error of 60 ms^{-1}, which in turn, would lead to a depth error of ~ 250 m on the two-way travel path for a reflector at 5.5 km. This kind of significant error provides a perfect example of why anisotropic parameterisation must be considered in simple sedimentary basins.

5.10   Remarks

In this chapter the enhanced phase-screen method has been successfully tested against forward modelling techniques normally used to generate synthetic seismic data. The results show that the code has the capacity to handle complex

sub-surface structures and generate accurate full waveform reponses for the pre-critical wavefield.

The anisotropic version of the code has been verified against simple geological models and used to quatitatively assess the errors associated with assuming isotropy in sedimentary basins.

Chapter 6

The Hold-with-Hope project

6.1 Hold-with-Hope - Rationale

The Hold-with-Hope project is funded as a direct consequence of the bidding
process for blocks within the Faroese economic zone of control. Extensive
interest from hydrocarbon exploration and production companies for access to
possible reserves has been fuelled by the successful exploitation of producing
fields eg. Foinavon, Clair, on the UK side of the Faroe-UK border. Unfor-
tunately, the Faroese region of control contains an extensive basalt sequence
within the underlying sedimentary succession. Figure 6.1 shows the Faroe-
UK region highlighting the international border whilst the edge of the basalt is
displayed with a brown line. The orange line is the position, east of which, the
basalt sequence is greater than one kilometer thick. The small region without
basalt, WNW of the Foinaven field, has been drilled with no success and the
limitations of imaging seismically beneath the basalt initially cooled interest in
exploration within the region. However, once the Rosebank field, discovered
by Chevron under less than 1 km of basalt, was found to be profitable it acceler-
ated interest in the potential of Faroese blocks. Wisely the Faroese government,
noting that a lack of seismic visibility of the underlying sediments would ham-
per the value of it's reserves, insisted that research grants must form part of
any block bidding process. Imaging under basalts reveals very little about the
structure of the sedimentary succession (Lemers and Carmichael, 1999) using
traditional acquisition techniques, and developing a tailored approach is the
key to better understanding the local geology. This study forms part of the
integrated technique.
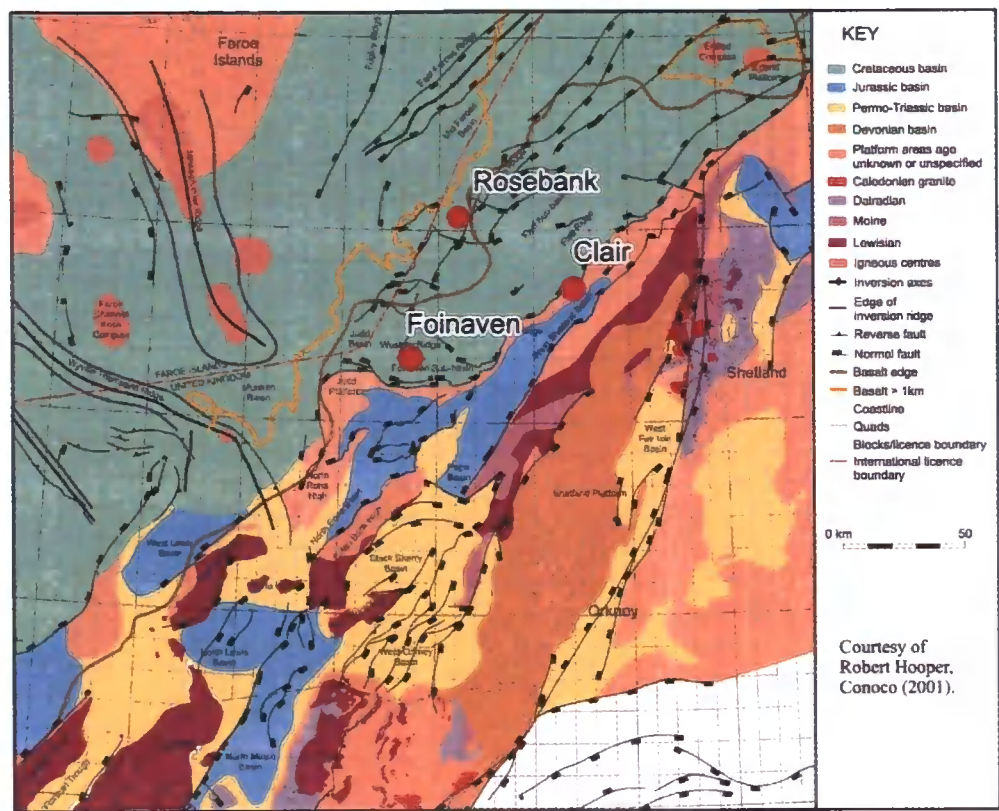
Figure 6.1: *The Faroe-Shetland trough. The extent of the basalt and the border between UK and Faroese waters are displayed alongside producing fields in the area.*

In order to seismically image sub-basalt structure most projects have attempted to either alter the data acquisition methods in an effort to enhance the sub-basalt response or, modify the seismic data processing techniques to amplify the wavefield produced beneath the basalt. This study approaches the problem from a different perspective and attempts to build a realistic geological model, which when populated with accurate elastic rock parameters can be used to produce synthetic narrow angle towed streamer (NATS) data. Once processed these data will give clues to the industrial sponsors looking to enhance their techniques for seeing beneath basalts at a fraction of the cost of acquiring the real data.

6.2   Hold-with-Hope - Project aims

The Hold-with-Hope project has the primary aim to investigate the possibility of seismically imaging sedimentary structure beneath plateau basalts. Due to

the general uncertainty in undertaking seismic exploration beneath basaltic lavas (Maresh and White, 2005), the project will endeavour to ascertain the potential for resolving seismic data acquired in these environments. The chosen study area is northern Hold-with-Hope (Lat. $73.75°$, Long. $-21.083°$) in north east Greenland where uplifted sediments provide field examples analogous to the volcanic margins of north-west Europe and also contain a faulted block structure similar to those found in the north European margin. Figure 6.2 shows the Norway Greenland Sea region of north western Europe prior to the onset of sea floor spreading with the region of interest positioned close to the spreading axis.

Geologists from the Cambridge Arctic Shelf Programme (CASP) have been working in the Hold-with-Hope region since 1995 and have produced extensive 1:25000 maps (figure 6.3), whilst concurrently collating the biostratigraphy and sedimentology of the succession. A thorough review of the CASP fieldwork is provided in Pickles and Whitham (1999) but for the benefit of the reader a brief summary of the rift history of the basin and an outline of the primary lithostratigraphic units follows. Once the regional stratigraphy is laid out, the method of construction for the 3-D model will be discussed and direct similarities between the Hold-with-Hope succession and similar hydrocarbon producing basins will be highlighted.

The model will be constructed over a $35\ km \times 15\ km$ region with a suprabasalt succession added to provide an appropriate analogue for the Faroe-Shetland basin. The model will be placed into the existing cartesian coordinate system employed by CASP, therefore the model range will sit between $x = 668800 - 703800\ m$ and $y = 8202850 - 8217850\ m$.

6.3   Method for developing regional model

The geological map of northern Hold-with-Hope (figure 6.3) has been created by pooling the mapping work undertaken by CASP geologists E.J-P. Blanc, S.R.A. Keely, C.S. Pickles, S.P. Price, D.P. Strogen and A.G. Whitham between the period 1995 and 2002. Creation of regional cross sections have led to an improved understanding of the geological evolution of the region.
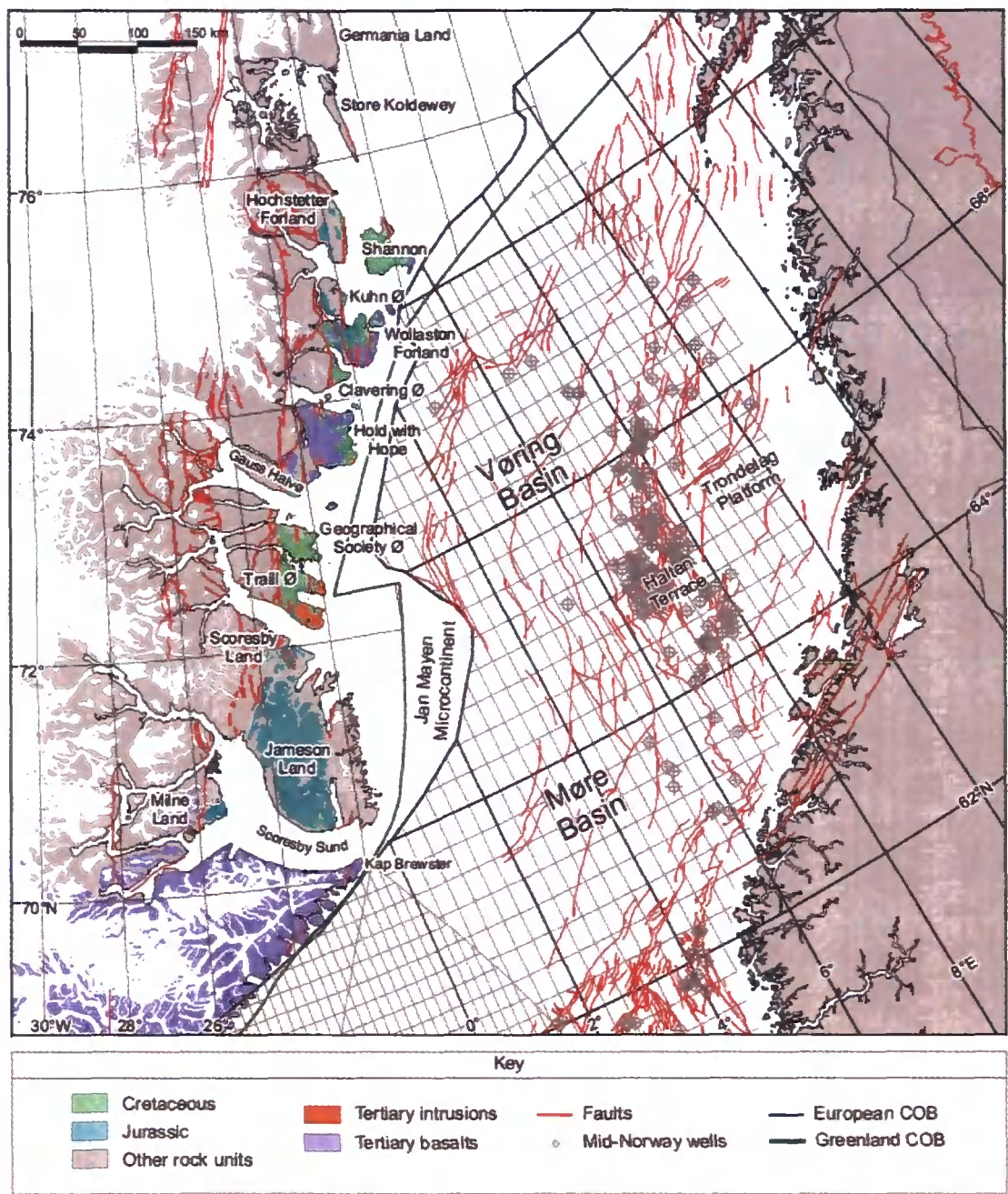
Figure 6.2: *Norway Greenland Sea region prior to the onset of seafloor spreading. The Hold-with-Hope region, in North East Greenland, is labelled, after (Sinclair, 2006).*

Quaternary	Rogelv member	Wordie Creek
Basaltic intrusions	Diener Bjerg member	Heledal Fm
Paleocene basalts	Gulelv member	Carboniferous
Tertiary sediments	Vandekloft member	
Foedalen member	Wordie Creek conglomerates	
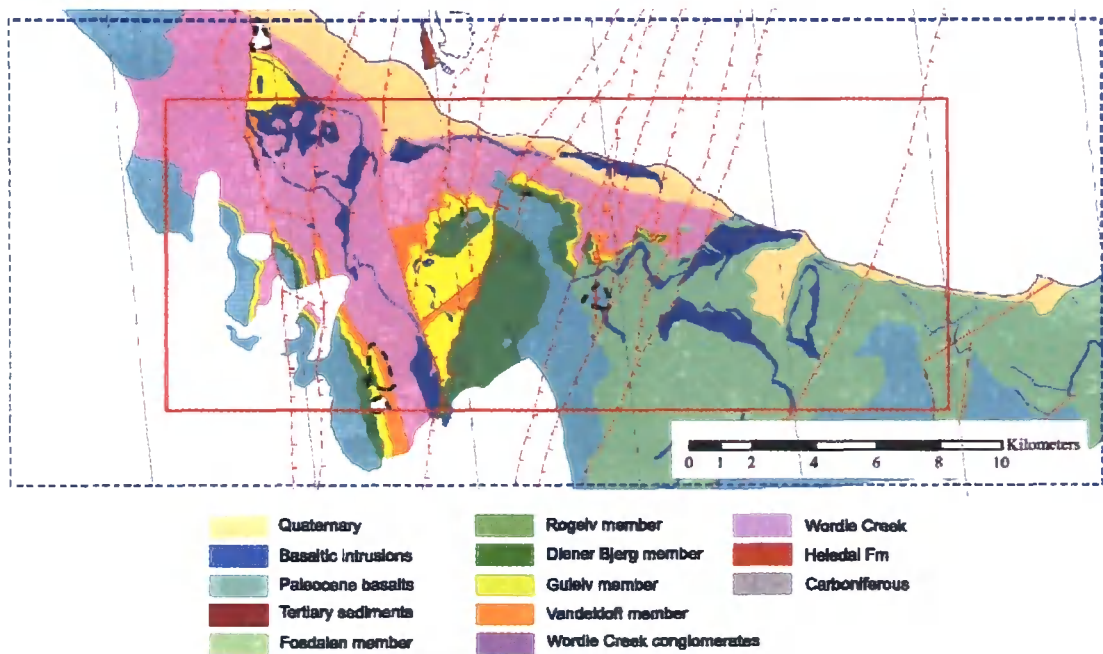
Figure 6.3: *Geological map of the Hold-with-Hope region with the 35 x 15 km region of interest shown within the dashed blue line, adapted from (Sinclair, 2006) after (Pickles and Whitham, 1999). The thin red lines indicate normal faults and the corresponding key highlights the formations present in the region.*

The Hold-with-Hope succession is made up from sedimentary strata ranging in age from Carboniferous to Tertiary. These sediments are overlain by Paleocene basalts of age 58.7 ± 1.4 Ma to 56.7 ± 0.7 Ma (Upton et al., 1995) and the entire succession is intruded by tertiary basaltic sills. N-S and NE-SW trending normal faults provide the general structure of the region with the beds dipping up to 20° eastward within the fault blocks.

The sequence has been defined with 12 principal lithostratigraphic units for the purposes of constructing the model. Figure 6.4 shows the final CASP lithostratigraphy for the Hold-with-Hope model area with the supra-basalt succession included.

The oldest, and deepest, rocks in the region are migmatites and metasediments which make up the crystalline basement (Koch and Haller, 1971). Permian fluvial conglomerates with occasional Permian shales, carbonates and evaporates directly overlay the basement across almost the entire region. It should be noted the older Carboniferous sediments outcrop sparsely (Sinclair, 2006) but are not included in the model. Sitting comfortably on the conglomer-
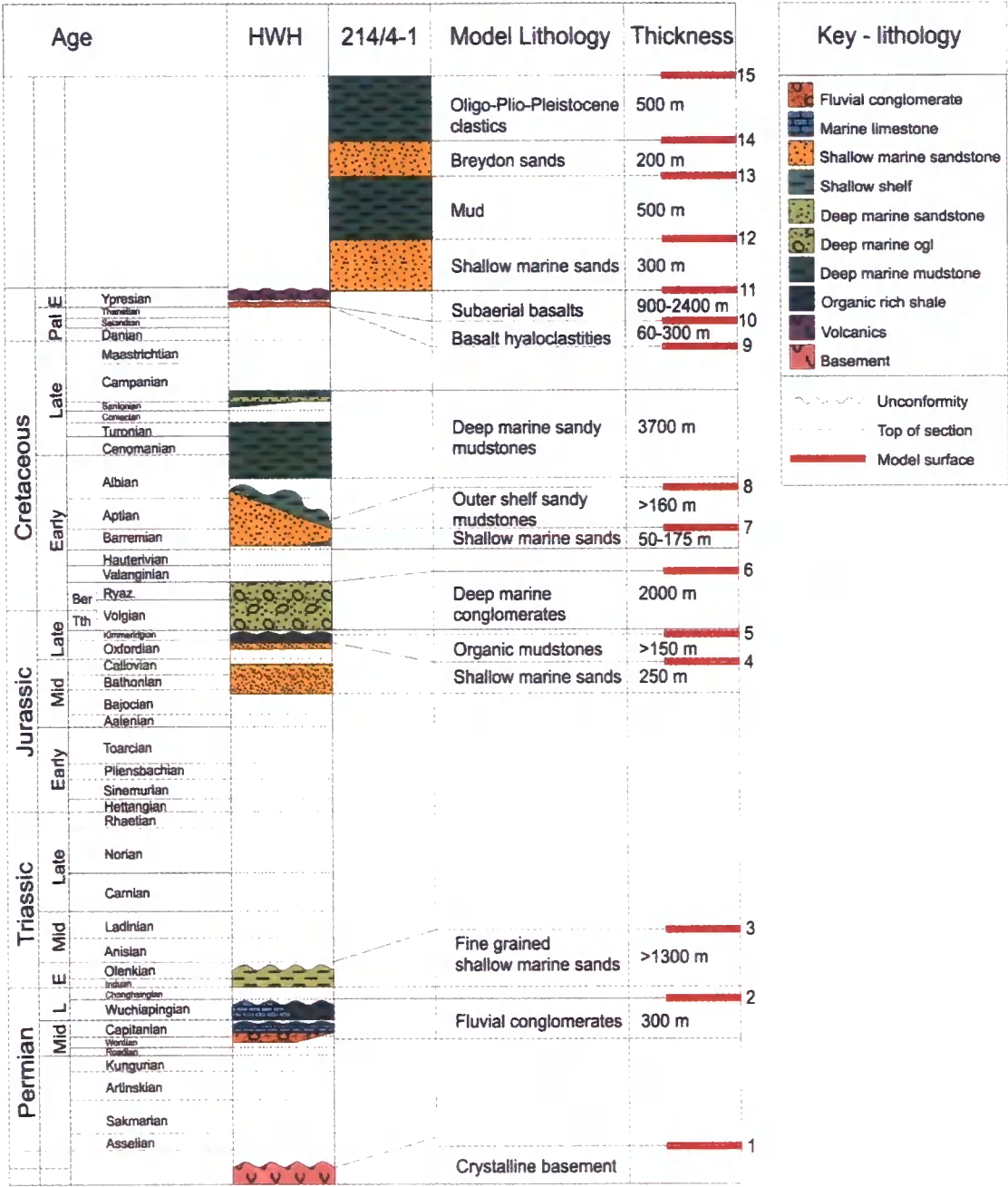
Figure 6.4: *The Hold-with-Hope region lithostratigraphy, after (Sinclair, 2006). The table summarises the modelled interfaces and details the bed thicknesses within the model*

ates are late Permian mudstones and carbonates (Stemmerrik et al., 1993) which form a single unit with early Triassic sandstones and mudstones of the Wordie Creek formation (Sinclair, 2006).

An angular unconformity separates the early Triassic sediment from the overlying Mid-Jurassic shallow marine sandstones deposited between the Bajocian and Oxfordian (Kelly et al., 1998). These deeper units are continuous across the entire model space whereas the overlying late-Jurassic mudstones have suffered post-depositional erosion and are absent in many of the fault blocks. Sitting on top of these units are late Jurassic-early Cretaceous conglomerates which can approach 2 km thickness in the hangingwalls of the fault blocks.

Early Cretaceous sandstones overly the late Jurassic-early Cretaceous conglomerates unconformably, which reflects fault block rotation in response to Volgian-Volanginian rifting. This unit is a possible potential reservoir with medium-to-coarse grained shallow marine sandstones.

Early Cretaceous shallow marine mudstones succeed the sandstones and are themselves succeeded by very fine grained early-late Cretaceous deep marine mudstones of thicknesses in excess of 1 km.

Sitting unconformably atop the Cretaceous sequence are Tertiary sediments which are not more than 20 m thick anywhere within the study area, and as such, for the purpose of model building are ignored. However, this layer marks the start of the flatter, laterally continuous units that dominate the near surface. The majority of the Tertiary succession are plateau basalts from the early Eocene overlaying a zone of basaltic hyaloclastites formed as a result of the basalt flows coming in to contact with water. The thickness of the hyaloclastite increases from east to west across the modelled region.

The basalt intrusions within the region tend to be laterally extensive and were emplaced during the Eocene. The supra basalt succession is added to provide similarity with the Faroe-Shetland basin and is based on the sequence in well 214/4 − 1. These beds are continuous and flat across the entire model space and are not cut by any of the regional normal faulting.

6.4 Regional rifting history

The northern Hold-with-Hope region has an interesting rift history that is reviewed in detail in Price and Whitham (1997). In summary, the sequence provides little evidence of the pre-Jurassic rifting that characterises the rift history of other parts of north east Greenland yet the angular unconformities underlying the Permian and the Jurassic suggest Carboniferous and Triassic rifting respectively. The region can be characterised by N-S and NE-SW trending normal faults with beds dipping $\sim 20°$ to the WSW. Within the region of interest there are three major fault blocks with fault separation of the order of ~ 20 km. Movement along these larger faults, which results in modern day displacements of over 1 km, and in the case of the Fosdalen fault over 5 km, appears to have begun during the Volgian-Valangian extension in the late Jurasssic-early Cretaceous (Whitham and Pickles, 2000).

In the late Barremian further fault block rotation occurred characterised by sedimentary gravity flow deposits (Whitham and Pickles, 2000). Additional rifting in the Mid-Albian caused the generation of shorter wavelength faulting within the existing fault blocks leading to considerably closer spaced blocks. Whitham and Pickles (2000) describe the development of an unconformity between the Barremian-mid Albion and the Mid-Albian-Late Santonian which is truncated by these normal faults allowing accurate dating for this episode of faulting.

The Cretaceous is noticeable for reactivation along existing fault planes yet as Whitham and Pickles (2000) comment, it is difficult to accurately age this reactivation due to the lack of exposure of the Cretaceous succession. The onset of seafloor spreading between the north-western European margin and Greenland occurred in the Tertiary and is the final phase of rifting. During this period there is evidence for formation of new faults and also reactivation of some, but not all, of the previous faults.

6.5 Suitability of the sub-basaltic succession as a sediment reservoir

The primary target for hydrocarbon exploration within the sub-basaltic sediments would be the Jurassic and the early Cretaceous sandstones. The petrography of these units is presented in Whitham and Hyden (1996). They conclude that the units are generally coarse sands displaying significant cross-bedding. The porosity and permeability results also provide positive potential hydrocarbon reservoirs within the shallow marine deposits. However, the deep marine sandstones units within the early-late Cretaceous are poorly connected and very thin so would most likely be a non-viable hydrocarbon reservoir.

6.6 The initial 3D ArcGIS model

Using the data collected during the geological mapping of the region, the bedding planes of the surfaces were estimated for each of the units. The units were divided by the following surfaces:

1. Top basement

2. Top Permian

3. Top Triassic

4. Top Jurassic sandstones

5. Top Jurassic mudstones

6. Top Valanginian

7. Top Early Cretaceous sands

8. Top Early Cretaceous shallow marine mudstones

9. Top Late Cretaceous deep marine sandy mudstones

10. Top Basalt hyaloclastites

11. Top Basalt

12. Marine sandstones

13. Muds

14. Breydon sands

15. Oligo- Plio- Pleistocene sands

All surfaces, except 7 and 8, were taken as parallel to the bedding and as such define beds of constant thickness. Surfaces 7 and 8 display a general thinning from west to east in some blocks which is a result of the depositional environment and not a product of erosion.

The strike, dip and position of all of the fault planes were extracted from field measurements and are used as the primary control on the lateral bed continuity. Figure 6.5 shows the 21 regional faults that were used in the model building. These faults define 22 regions (fault blocks), shown in figure 6.6, within the model space. The surfaces were then generated via a series of ArcGIS steps by Stewart Sinclair at CASP and are displayed alongside the fault surface, the sills and the complete structure in figure 6.7. Final surfaces and sills were then extracted as x,y,z files and made available for modelling.
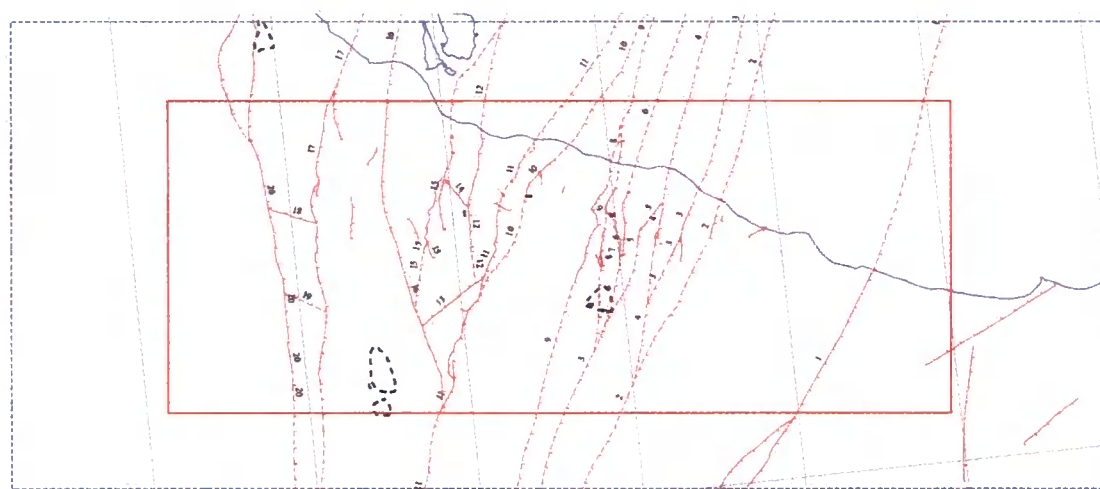
Figure 6.5: *The region modelled during the Hold-with-Hope project within the dashed blue line. The map shows the 21 faults mapped in the project (after Sinclair (2006)).*
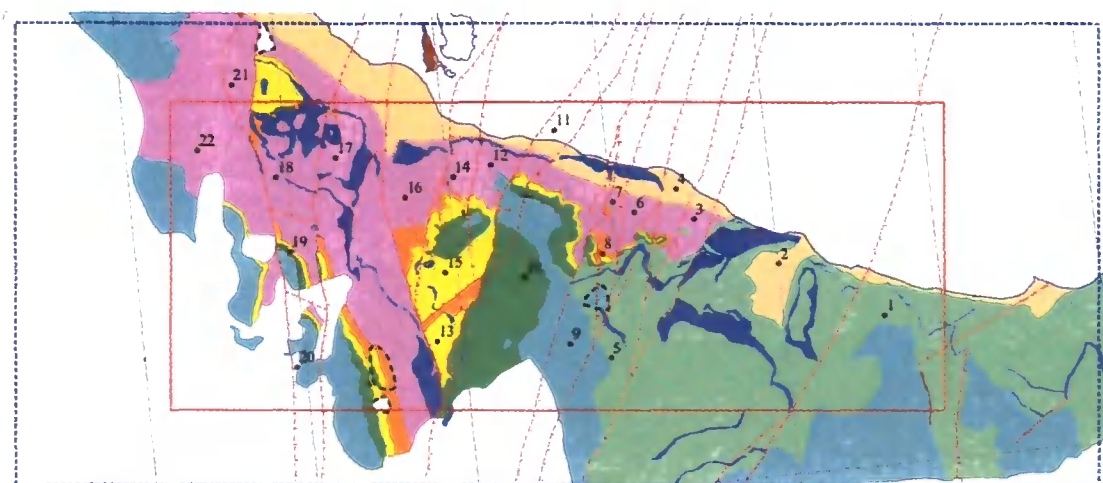
Figure 6.6: *The region modelled during the Hold-with-Hope project within the dashed blue line. The map shows the 22 defined fault blocks within the region (after Sinclair (2006)).*

6.7   Populating the model with rock properties

The model is defined as a series of surfaces, each of which covers the entire lateral extent of the model where each surface corresponds to the top of a unit. The model space has been constructed so that there is no crossbedding between the units so if a unit is absent, its top surface is given the same value as the unit below. The intrusions are a series of top and bottom surfaces which can pinch out anywhere within the model space. Now that the model can be defined as a series of surfaces, each representing the top surface of a lithostratigraphic unit it is necessary to assign distinct, and accurate rock properties to the individual rock types. The basalt is assigned differently in order to replicate the flow structure and will be discussed in section 6.9.

The assignment of rock parameters to specific lithostratigraphic units was undertaken at a sponsors meeting. Data from wells situated off the northwest European margin were studied to find units comparable with those in the Hold-with-Hope model. P-wave velocity and density values were assigned and in some cases S-wave velocity profiles were also measured within the well. Where this were not the case, a suitable empirical relationship to convert P-wave velocity to S-wave velocity was employed on a rock type by rock type basis. The depth of burial was taken into consideration during the assignment of elastic parameters to ensure consistancy with the Faroe-Shetland basin. Fig-

(a) 3-D faults displayed with the top basalt surface
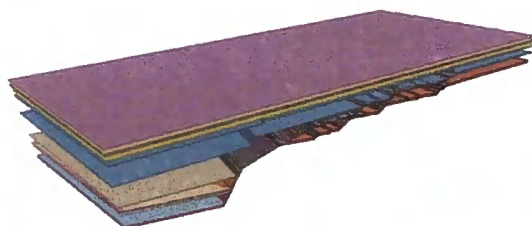
(b) 3-D surfaces from basement to the sea-bed
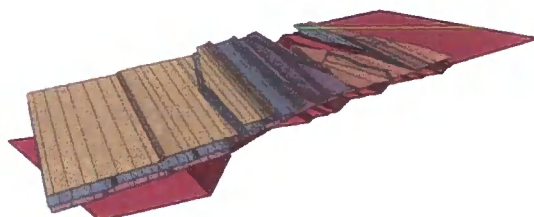
(c) 3-D sills displayed in relation to the basement

(d) 3-D structure of the model prior to the rotation that ensured a flat sea-bed

Figure 6.7: *The 3-D faults, surfaces and sills that make up the Hold-with-Hope model.*

ure 6.8 shows the log used to determine the elastic parameters of the sills within the model. The sonic log displays little variation over the unit and results in a P-wave velocity of 6096.0 ms^{-1}. Additional logs, used to determine elastic parameters for parts of the succession, are included in appendix A.
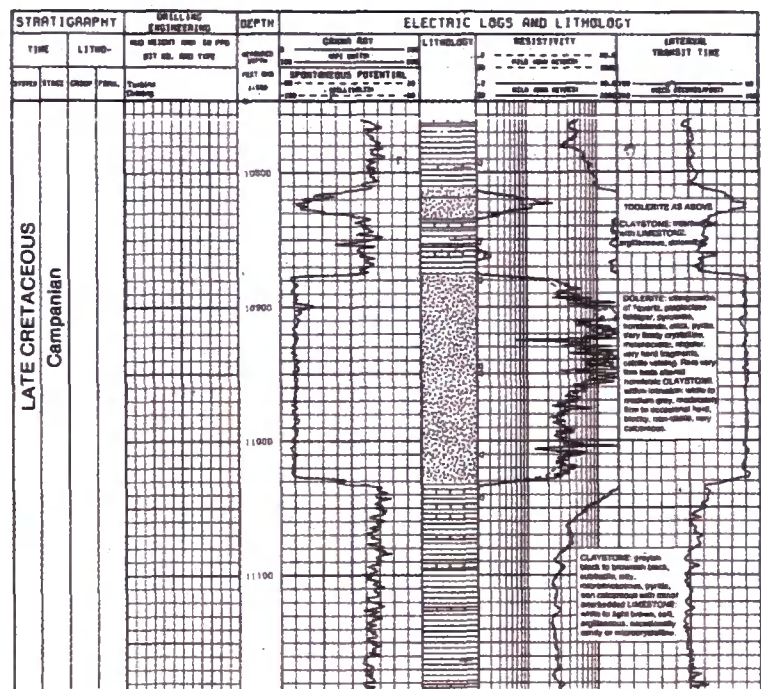
Figure 6.8: *Well log record 205-10-2b used to determine the elastic parameterisation of the sills within the Hold-with-Hope model volume*

6.7.1 Suitability of assigned rock properties

Once the initial rock properties had been assigned, the P- and S-wave velocities were plotted as a function of density and compared with the Nafe-Drake curve ((Ludwig et al., 1970) after (Nafe and Drake, 1957)). The Nafe-Drake curve summarises the general relationship between rock parameters in commonly occurring sedimentary, metamorphic and igneous rocks. Figure 6.9(a) shows the rock parameters initially chosen from the well data. It is clear that at high and low velocities the values do not correspond with the expected trend. The Nafe-Drake curve is known to mis-represent certain rocks (Jones, 1999), but for the sedimentary succession under investigation it should provide an accurate representation of the rock physics. After careful consideration the values were reassigned by keeping the P-wave velocity and adjusting the density. The

(a) Well log measurements   (b) Recalibrated values
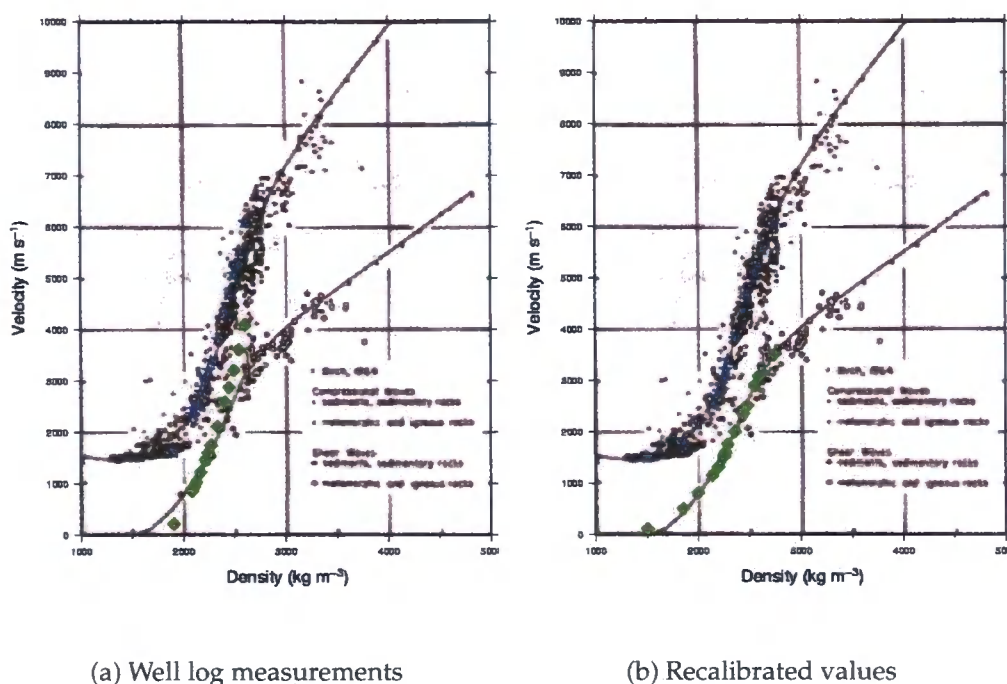
Figure 6.9: *The original Nafe-Drake curve from Ludwig et al. (1970) after Nafe and Drake (1957), superimposed with (a) the well log velocity vs density picks, and (b) the recalibrated velocity vs density picks. The P-wave and S-wave values are shown in blue and green respectively.*

revised density was used to scale the S-wave velocity and a plot of the recalibrated values is shown in figure 6.9(b). A summary of the final rock parameters for each of the units is shown in table 6.1.

6.8   Generating the phase-screen input model

The final task in constructing the sub-surface model was to create a format suitable for phase-screen modelling. The phase-screen technique requires a model space defined as a series of nodes, equally spaced laterally, where the rock type is specified at each nodal point. An accompanying input file provides details of the number of nodes per screen (in x and y) and the number and spacing of the screens. The approach adopted to populate the model is a top down conversion where the phase-screen model space is first constructed with

its minimum screen spacing, in this case 20 m. Each screen is realised with the final nodal distribution, 20 m × 20 m, and starting from the top of the model the entire 3D cube is first populated with the upper-most layer, the water column. Next the top Oligo- Plio- Pleisocene surface is inputted and all points beneath this surface are populated with the rock identifier for a Oligo- Plio- Pleisocene medium. Since there is no cross-bedding, this approach allows each surface to be taken in turn and the model is built up until the crystalline basement is in place.

The intruded sills are input last of all and both top and bottom surfaces are required. The nodes between the upper and lower surface at each position are filled with the sill specific rock identifier and the approach continues laterally across the entire grid. This method gives the option of creating models without intrusions which will tend to represent large acoustic impedence contrasts and, as such, give bright reflections in the seismic record.

Once the entire model space is populated the next task is to assess the possibility of reducing the number of screens. In homogeneous media the number of screens required is considerably less than that required for complex structure. Throughout this study, it was decided that the maximum screen spacing would be 200 m to help control wrap-around problems. Where identical adjacent screens are encountered, they are combined to minimise the computational requirement. Figures 6.10 (a) and (b) show the final models, with and without sills respectively, for a 2D profile through the centre of the model (at $y = 7.5$ km) with an homogeneous basalt used for this unit.

6.9   How random was that?? - a basalt

The assignation of rock properties to the model has previously assumed that the rocktypes are, for modelling purposes, homogeneous. As such, single values of P- and S-wave velocities and density are deemed appropriate for each medium. This approach, although crude, was suitable for the majority of the rocktypes encountered since the variation in elastic parameters across a single unit was expected to be small. During the allocation of velocities and densities, average values were extracted from well records and pleasingly displayed very little long wavelength variation over bed thicknesses comparable to those in

Unit	$V_{p\downarrow}\ (ms^{-1})$	$V_{s\downarrow}\ (ms^{-1})$	$\rho\ (kgm^{-3})$	δ	ϵ
Water	1480.0	0.0	1000.0	0.0	0.0
Oligo- Plio- Pleisocene sands	1500.0	110.0	1500.0	0.0	0.0
Breydon sands	1800.0	500.0	1850.0	0.0	0.0
Muds	2150.0	800.0	2000.0	0.0	0.0
Marine sandstone	2771.0	1310.0	2200.0	0.0	0.0
Basalt	X	X	X	0.0	0.0
Basalt Hyaloclastite	3810.0	2000.0	2360.0	0.0	0.0
Late Cretaceous deep marine mudstones	3387.0	1747.0	2290.0	0.0	0.0
Early Cretaceous shallow marine mudstones	2540.0	1150.0	2140.0	0.0	0.0
Early Cretaceous sands	3048.0	1520.0	2250.0	0.0	0.0
Valanginian	5542.0	3150.0	2630.0	0.0	0.0
Jurassic mudstones	2771.0	1310.0	2200.0	0.0	0.0
Jurassic sandstones	3208.0	1593.0	2270.0	0.0	0.0
Triassic	4689.0	2500.0	2480.0	0.0	0.0
Permian	4354.0	2900.0	2440.0	0.0	0.0
Basement	5080.0	2900.0	2550.0	0.0	0.0
Intruded sills	6096.0	3500.0	2740.0	0.0	0.0

Table 6.1: *Elastic rock parameters for the lithostratagrphic units comprising the Hold-with-Hope model.*

the Hold-with-Hope model. This study takes the approach that assigning an average value, which is tied into the Nafe-Drake curve, is an appropriate method for selecting parameters. Basalts however, pose an altogether different problem.

In this model, thick basalts, extruded during continental break up, cover an earlier sedimentary basin to be investigated for hydrocarbon potential. The nature of these plateau basalts means that it is difficult to image both the sub- and intra-basalt architecture. This problem is a result of several factors intrinsically linked to basaltic lava flows: the basalt flows are heterogeneous both in terms of internal structure (Martini and Bean, 2002a,b) and interfaces between separate flows are highly rugose. These highly irregular properties both produce significant effects during both real and synthetic wave propagation (Maresh et al., 2006).

Significant velocity variations occur within the basaltic sequence. These are caused by; intra flow variablity in both composition and structure, and
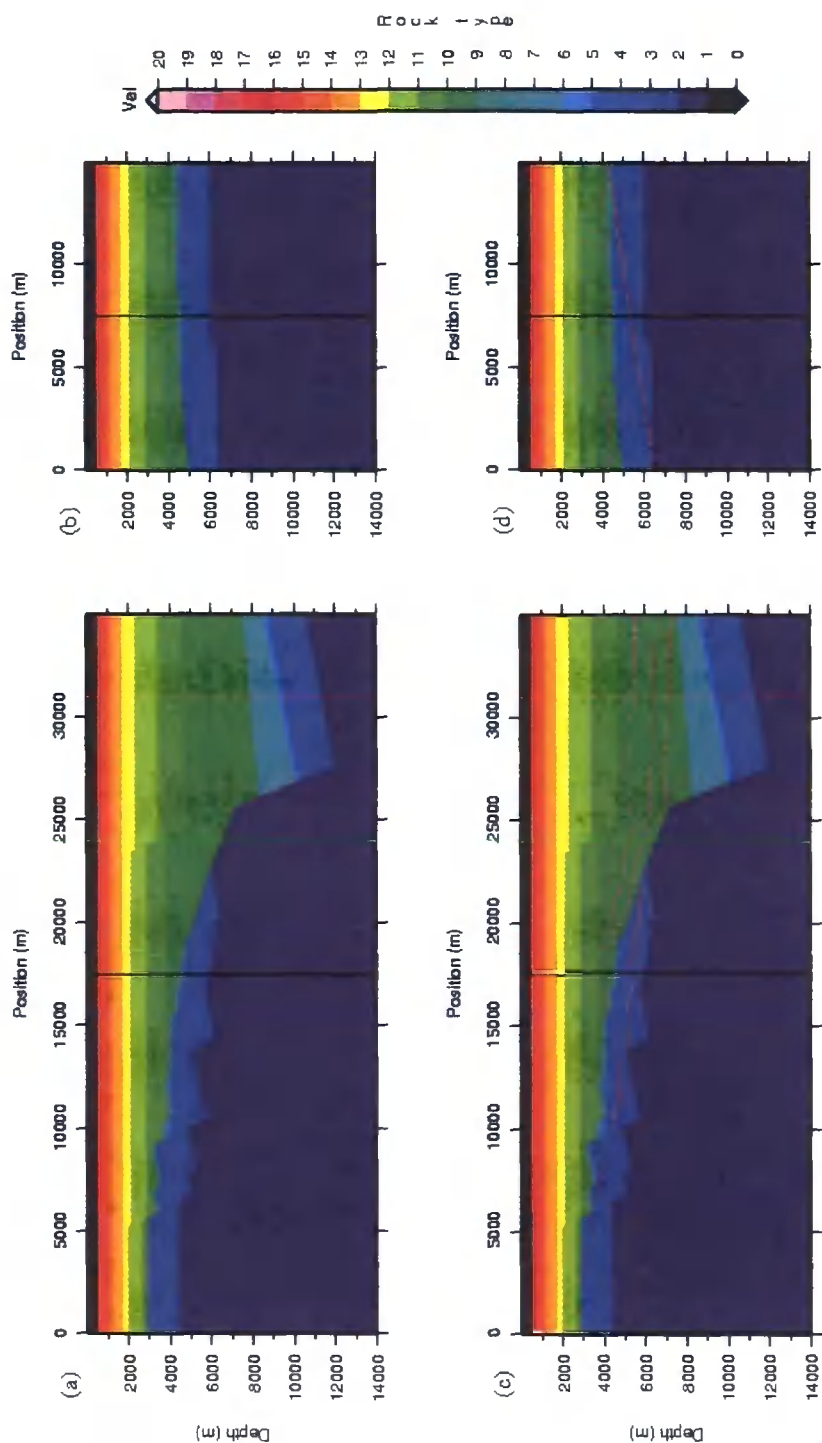
Figure 6.10: *Cross sections from the original Hold-with-Hope model constructed via a top down approach. The solid vertical lines show where the along and cross flow sections cross-cut each other. (a) and (b) show the model without sills whilst (c) and (d) show the sections with the sills included.*

are accentuated by effects related to rates of cooling; and on a larger scale by layering of flows, sediments, sills and hyaloclastites. These effects give rise to high impedence contrasts within the single 'basalt' layer, causing extensive scattering within the medium. It is also important to point out that the high impedence contrast at the top (and conversely at the bottom) of the basalt pile produces a mechanism where a substantial portion of the downgoing energy never makes it into the basalt sequence.

In order to offer more than a passing insight into the problems of acquisition and processing of data in basalt rich environments it was necessary to produce accurate 2-D and 3-D synthetic data which contains the same pitfalls and problems that are seen on real data from comparable locations.

The model space within this study was agreed between the partners early in the project and it was decided that the top and bottom interfaces of the basalt would not contain irregular topography. This is partially because of the screen spacing chosen during the modelling prohibits small scale irregularity and also because significant work has previously looked at the problems caused by rough surfaces (Maresh et al., 2006). Therefore, in this study, the heterogeneity will be exclusively expressed within the basalt flow sequence.

6.9.1   Building a random sequence to best represent a basalt

Considerable work has been undertaken mapping the lateral extent of individual basalt flows within sequences of tabular basalts. These studies reveal elongated fingers of basalt that extend in a proximal to distral direction, see figure 6.11. The flows are generated from a central feed with extensive sheet lobes formed off this axis.

As a general rule, the length of these flows in this primary direction are an order of magnitude greater than the width of the flow (Jerram, D.A., personal communication, 2007). Self et al. (1998) describe the emplacement of basaltic pahoehoe flows generated by inflation and these are responsible for the majority of the large basaltic lava flow provinces in the world and will be used as the basis for the basalt construction in this study. The basalt unit is created by the repeated layering of flood lava eruptions over geologically short time spans (0.5 – 60 MY). The model shown in figure 6.12 (a) is equally applicable to small

scale sheet lobes, $< 1\ m$ thick, as it is to lateral extensive, $> 100\ m$ thick, lobes. Since some basalt flows extend beyond $100\ km$ this model is applicable on a large scale, yet Thomson (2005) mapped basalt lobe structures on a kilometer scale from interpreted 3-D seismic data and concluded that the elongated flows were seen at all scale lengths. Figure 6.12 (b) shows the simplified cross section of the subsurface at the position marked by the yellow circle in figure 6.12 (a). The lobes themselves are generally described as P- or S-type pahoehoe, with the more common P-type considered here having a denser interior with vesicular exterior edges. Figure 6.12 (c) shows how the velocity varies within a single lobe and also how the jointing is influenced by the regions of high vesicularity.

Pahoehoe flows are common in regions of mid-ocean ridge volcanism (Iceland), mid-plate hotspot volcanism (Hawaii) and in areas of crustal extension (Western United States) and provide an excellent analogy for what this work aims to replicate. A reasonable estimate of the average flow length in an environment comparable to north east Greenland is $5\ km$, giving an average flow width of $0.5\ km$ which is a suitable value for modelling with the phase-screen code.

These lobes are made up of a high velocity central core surrounded by low velocity crusts at the top and bottom of the flow. The thickness of the flows can vary massively (Self et al., 1998) so the priority is to accurately map the velocity distribution within the flow sequence and use this to populate the basalt volume. In order to calculate a realistic velocity structure, and assess the average flow thickness within an equivalent basalt, it is necessary to evaluate well log records that penetrate through basalt.
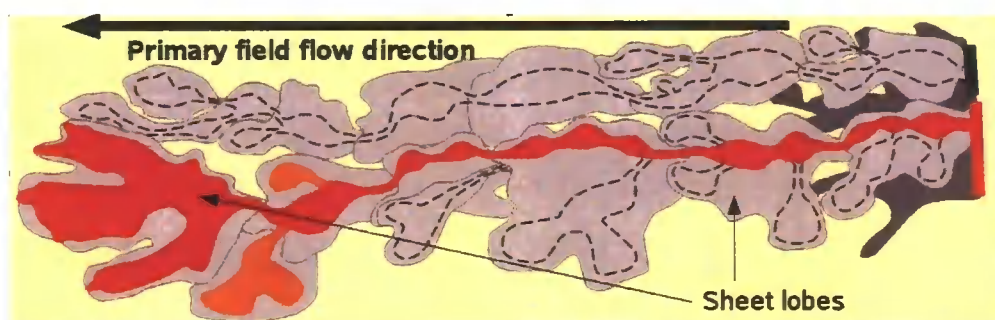
Figure 6.11: *Individual lava flow showing the elongated nature of the individual basalt lobes (after Thordarson, 2006).*
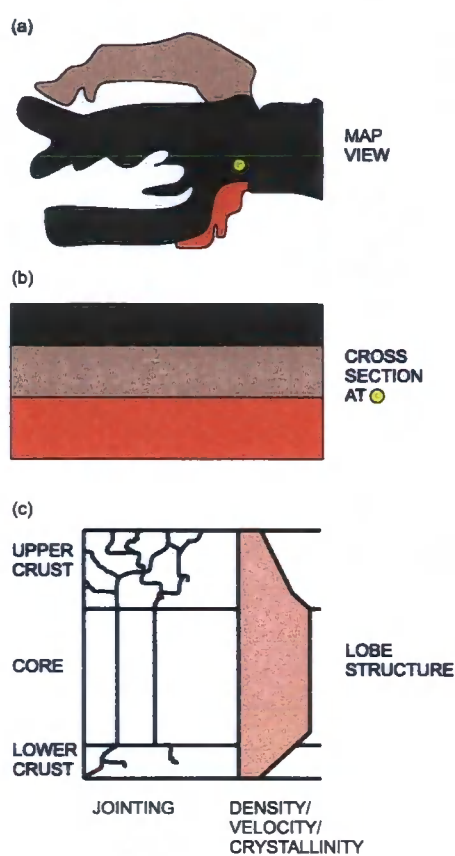
Figure 6.12: *Structure of individual pahoehoe sheet basalt lobes (after Self et al. (1998)). (a)*
The final structure after a period of lobe emplacements gives a cross section (b) containing
several distinct lobe structures. The individual lobe structures, shown in (c), are characterised
by a dense, high velocity core with less crystalline, highly jointed crusts that display significant
vesicularity.

For this study well 164/07-1, drilled through the Rockall Trough of north-
west Scotland, was available for analysis. This record has previously been
classified as an particularly heterogeneous basalt section typical of extrusions
found on the Atlantic margin (Maresh et al., 2006). Figure 6.13 (a) shows the
P-wave velocity record as a function of vertical travel time, whilst figure 6.13
(b) focuses on the basalt sequence within the log. The distribution of velocities
within the basaltic flow sequence is summarised by the histogram in figure 6.13
(c).

The velocity distribution within the well log cannot be fitted to a Gaussian
distribution. This study will fit the basalt velocity variation as a log normal
distribution with the long tail skewed to slower velocities.
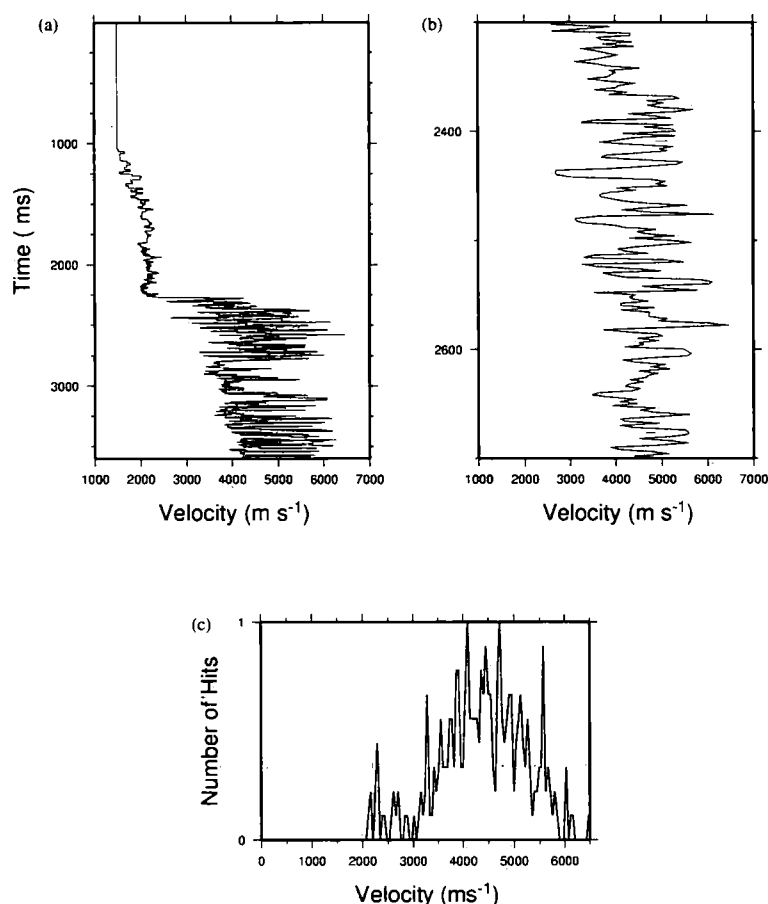
Figure 6.13: *A summary of well 164/07-1 in the northern Rockall Trough showing (a) the entire velocity record as a function of travel time, (b) a subsection of the well log showing the variation in velocity throught the basalt and, (c) a normalised histogram showing the variation in velocity through the basalt.*

Seismic modelling studies have used random velocity models to approximate small scale heterogeneity for approximately two decades. Stochastic realisations of velocity distributions are generally built in one of two ways. The first (Frankel and Clayton, 1986), is to create a random distribution in the spatial domain and, after transforming to wavenumber space, force the distribution to the required power spectrum and then transform back for the desired spatial distribution. The second, and more common technique (Frenje, 2000) is to compute the desired power spectrum in the wavenumber domain and randomly assign the phase with a uniform distribution between 0 and 2π. Setting the amplitude of the DC value to zero will ensure a zero mean, whilst the random phase will produce a Gaussian velocity distribution when

Medium	Autocorrelation function	Power Spectrum
Gaussian	$C\left(r\right) = \sigma^2 e^{-\frac{r^2}{a^2}}$	$P\left(k\right) = \sigma^2 a^3 \sqrt{\pi^3} e^{-\frac{k^2 a^2}{4}}$
Exponential	$C\left(r\right) = \sigma^2 e^{-\frac{r}{a}}$	$P\left(k\right) = \dfrac{\sigma^2 \left(2\sqrt{\pi}a\right)^n \Gamma\left(\frac{1}{2}+\frac{n}{2}\right)}{\Gamma\left(\frac{1}{2}\right)\left(1+k^2 a^2\right)^{\frac{1}{2}+\frac{n}{2}}}$
von Kàrmàn	$C\left(r\right) = \dfrac{\sigma^2 2^{1-v}}{\Gamma(v)}\left(\frac{r}{a}\right)^v K_v\left(\frac{r}{a}\right)$	$P\left(k\right) = \dfrac{\sigma^2 \left(2\sqrt{\pi}a\right)^n \Gamma\left(v+\frac{n}{2}\right)}{\Gamma(v)\left(1+k^2 a^2\right)^{v+\frac{n}{2}}}$

Table 6.2: *The autocorrelation functions and their respective n-dimensional power spectrums for the three commonly used categories of random media. Here, r is the spatial lag, a is the correlation length of the random media and k is the wavenumber, where in the 3D case* $k = \sqrt{k_x^2 + k_y^2 + k_z^2}$ *and* k_x, k_y *and* k_z *are the wavenumber components in the three cartesian directions.* K_v *is the modified Bessel function of the second kind of order v where v is the Hurst number and finally,* Γ *is the gamma function. In order to produce random models with variation in correlation length as a function of direction (Ikelle et al., 1993), define three correlation lengths* a_x, a_y *and* a_z *where* $a = \sqrt{a_x^2 + a_y^2 + a_z^2}$ *and replace* $k^2 a^2$ *with* $k_x^2 a_x^2 + k_y^2 a_y^2 + k_z^2 a_z^2$

the spectrum is Fourier transformed into the spatial domain. During this study, this second method for producing random media will be used.

The power spectrum in the wavenumber domain is commonly derived, via a Fourier transform, from one of three spatial autocorrelation functions: Gaussian, exponential and self-similar (or von-Kàrmàn). The autocorrelation functions and their respective power spectrums are summarised in table 6.2. In general, the Gaussian correlation function produces very little short wavelength variability and is unsuitable for this work. The von-Kàrmàn autocorrelation function produces a self similar medium with a considerable short wavelength component that makes it a suitable choice to model basalt flows. The exponential autocorrelation function is a specific subset of the von-Kàrmàn distribution where the Hurst number is equal to 0.5.

The seismic modelling undertaken during this study is unlike most of the work that has previously used random models to approximate inhomogeneous media. Here the aim is to replicate velocity variation on scales between 10 m and 10 km and simulate distinct flow structures whereas a substantial amount of the previous literature concerns large scale mantle models on scale lengths of 10's to 100's of kilometers (Baig et al., 2003; Angus, 2005).

Martini et al. (2005) conducted a previous study that attempted to model basaltic flows as a random medium. This project also investigated the possibility of creating a 3D volume in order to ascertain the possibility of imaging

beneath basalts. Martini et al. (2005) noted that due to the compositional variability of both the individual flows and the overall flow structure it was inappropriate to model the basalt as a homogeneous media. Whilst they do not provide the exact details of the method used to populate their random basalt, Martini et al. (2005) state that the correlation length in y is 5 times that in x, whilst the correlation length in z is effectively infinite. It appears that they then averaged the bed thickness to 100 m. The basalt model itself was built up of smaller volumes (Hobbs, R.W., personal communication, 2007) which were then fitted together to produce the final model. It also appears from the vertical slices of the model that they chose their proximal to distral direction in a way that was not consistant with the expected local structure in the Faroe-Shetland trough, where flow direction would be along the dip direction into the basin. In this study it was essential that the basalt was populated as a single volume where the characteristic length scales of the flows agreed with the published literature and the velocity distribution replicated a real tabular basalt. One possible explanation for the decision of Martini et al. (2005) not to construct the basalt as a single volume is computational power. The code used to generate the 3D volume for this study was written in C++, with the Fourier transforms once again determined using FFTW, and is included in appendix B. This allows larger models to be constructed than possible with similar methods in MATLAB.

The plan within this study was to follow the approach of Frenje (2000) when building a random velocity distribution. In order to produce a model space larger than the required volume of basalt, a region of 1750 nodes by 750 nodes by 150 nodes was created. With a spatial sampling of 20 m this creates a volume of $1.6 \times 10^6 km^3$. A log-normal distribution is described by

$$f(v) = \frac{1}{\sqrt{2\pi}\sigma_{tmp}\left(\frac{\sigma}{C_v} - v\right)} e^{-\frac{\left(ln\left(\frac{\sigma}{C_v} - v\right) - \bar{v}_{tmp}\right)^2}{2\sigma_{tmp}^2}}, \qquad (6.1)$$

where

$$\sigma_{tmp} = \sqrt{ln\left(C_v^2 + 1\right)}, \qquad (6.2)$$

$$\bar{v}_{tmp} = ln\left(\frac{\sigma}{C_v}\right) - \frac{1}{2}ln\left(C_v^2 + 1\right).$$ (6.3)

The skewness of the distribution is determined through the parameter C_v, where the bigger the value the more skewed the resulting sequence. σ is the standard deviation and the distribution has a zero mean. If a classical Gaussian distribution is derived with standard deviation σ_{tmp} then this can be transformed to the desired log-normal distribution using the relationship,

$$v_{ln} = \frac{\sigma}{C_v} - e^{v_{gauss} + \bar{v}_{tmp}}.$$ (6.4)

Figure 6.14 (a) and (b) show slices from the initial random basalt derived with a Gaussian velocity distribution shown in figure 6.14 (c) with correlation lengths $a_x = 5000m$, $a_y = 500m$ and $a_z = 50m$ and Hurst number $v = 0.25$. Slices from the transformed distribution are shown in figures 6.14 (d) and (e) calculated with $C_v = 0.28$ and $\sigma = 200$. The transformed velocity distribution is shown in figure 6.14 (f).

To check the result has the correct variability in the vertical direction, well log 164/07-1 is isolated and, sampling at a rate comparable to seismic recording, the mean is removed in order to determine the autocorrelation function of the record as a function of z. Once this autocorrelation function has been determined, transforming this to the wavenumber domain reveals the power spectrum of the log. A vertical record can be taken through the new random basalt and an autocorrelation and power spectrum determined. Figure 6.15 shows the autocorrelation and power specrum of both the real log data and the synthetic random basalt and it is easily seen that these have an excellent agreement with the loss of high value wavenumber information due to the sampling rate of the synthetic model.

Since the model space derived for this study is larger than the required basalt volume it can be easily inserted into the model. Following the same technique as before the top basalt surface is identified and the random flow realisation is used to fill the model from the top down until the base of the
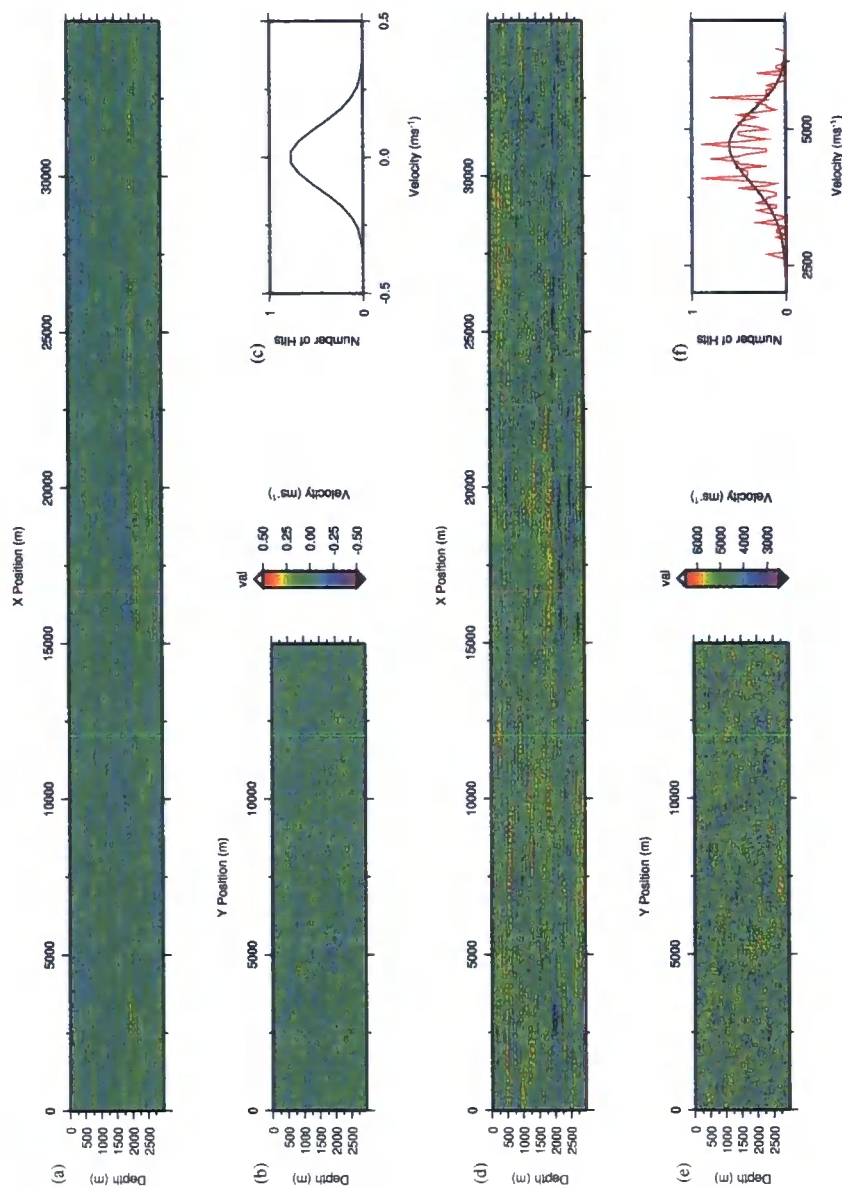
Figure 6.14: *The derived random basalt model showing a slice of the original realisation at (a) y=200 m, and (b) x=200 m calculated with the normal velocity distribution shown in (c). (d) and (e) show the same slices in the final basalt realisation after the velocity distribution (f) has been skewed to a fit log normal curve with $Cv = 0.28$. The velocity distribution from well 164/07-1 is included in figure (f) for completeness.*
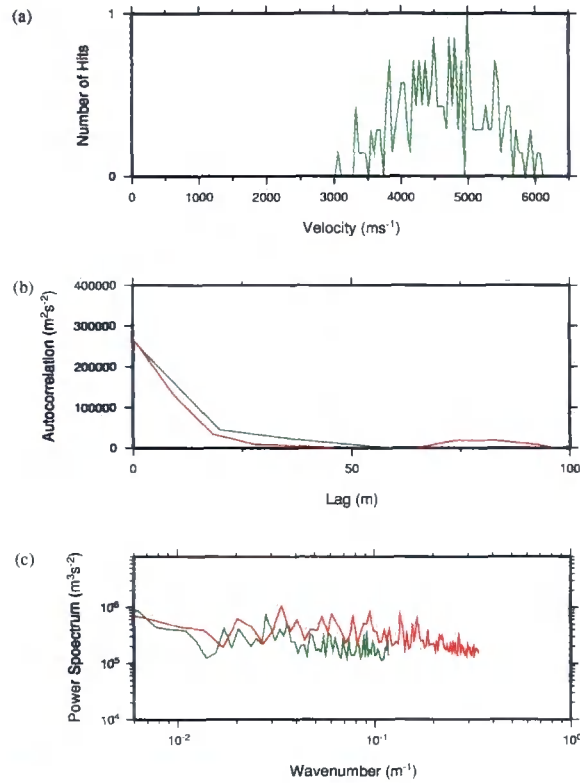
Figure 6.15: *(a) The velocity distribution for a vertical log through the random basalt. The autocorrelation function (acf) of this record (green) is compared with the acf of the real well log 164/07-1 (red) in (b) whilst the power spectrums of both logs are calculated and displayed in (c).*

random basalt is reached. Once this occurs the method continues as before with the next layer filling the model space from the base basalt downwards.

Figure 6.16 (a)-(d) show slices from the final Hold-with-Hope model at positions $y = 12720\ m$ for (a) and (c) and $x = 33520\ m$ for (b) and (d). (a) and (b) show the rock type identifiers and the colour palette used is dominated by the basalt that is represented by 100 different rock types whereas the rest of the model is comprised of only 20 rock types. (c) and (d) show the actual velocity distribution through the model. Since the basalt is derived as a P-wave velocity model, the S-wave velocity is calculated as

$$v_s = \frac{v_p}{\sqrt{3}},$$ (6.5)

and the density, in kgm^{-3}, is determined using the empirical realtionship,
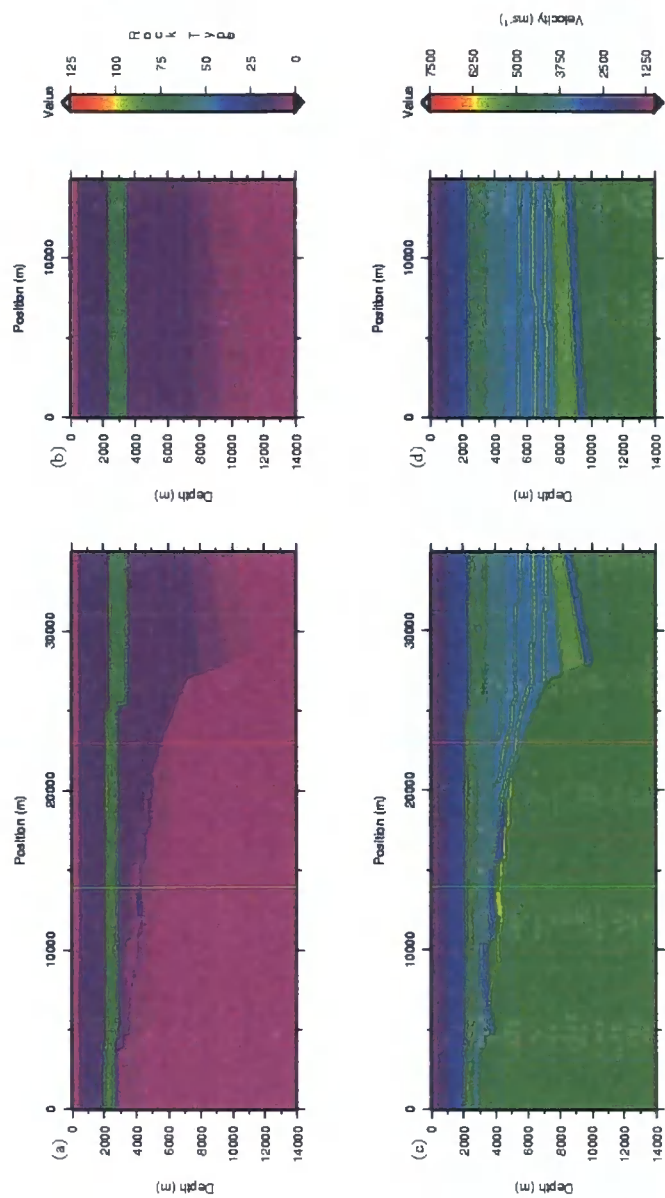
Figure 6.16: *Slices from the final Hold-with-Hope model displaying cross sections at $y = 12720$ m in (a) and (c) and at $x = 33520$ m in (b) and (d). Figures (a) and (b) show the construction in terms of distinct rock types whilst (c) and (d) show the model as a function of P-wave velocity.*

$$\rho = 1700.0 + 0.2 v_p, \tag{6.6}$$

from Sheriff and Geldert (1995).

6.10   Coordinate system for the Hold-with-Hope model

The Hold-with Hope modelled generated so far has been set in a 35×15 km area based at the origin. This does not coincide with the coordinate system used by CASP and the model is transformed into their reference frame. The origin is shifted to $x = 668800$, $y = 8202850$ m with the same 35000 m and 15000 m extent in x and y respectively.

6.11   Attenuation and spectral response through basalts

Even after generating a statistically accurate basaltic medium, realistic spacing of the screens during phase-screen modelling still necessitates the creation of an equivalent media philosophy when dealing with the basalt sequence. Since the model spacing is larger than the internal lobe structures often seen within flood basalts, see figure 6.12, it is necessary to state that the exact nature of the seismic signature will never be captured and a best approximation is sought. The method adopted in this study is a novel technique where the results provide a best effort in terms of both the complexity of the model and the run time of the simulation. One of the prerequisites for the industrial partners involved in this project was to ensure that the spectral characteristics of the synthetic data matched those found in real data. This is particularly important in sub-basalt imaging as the important reflections tend to be rich in low frequencies.

This problem of imaging intra- and sub-basalt interfaces has long been a major headache for the hydrocarbon industry and general practice involves acquisition with powerful low frequency (< 25 Hz) sources (Gallagher and Dromgoole, 2007). This approach is undertaken because basalts display a low effective Q and, as such, can be considered high frequency sponges. Further development using wave-localization theory (Baan et al., 2007) which considers frequency dependent scattering to optimise the reflected response is not undertaken in this study. Table 6.3 displays results from previous studies to determine the effective Q value for basalt (Maresh et al., 2006; Shaw et al., 2008; Christie et al., 2006; Rutledge and Winkler, 1989) and although these display a

range of values each project has concluded the basalt is a highly attenuating medium.

Investigation	Year	North Alantic Region	Effective Q
Maresh, White, Hobbs and Smallwood	2006	Northern Rockall Trough, N Atlantic Margin	15-35
Shaw, Worthington, White, Anderson and Petersen	2008	Glyvursnes, Streymoy, Faroe Islands	10-45
Christie, Gollifer and Cowper	2006	Lopra, Suduroy, Faroe Islands	35
Rutledge and Winkler	1989	Vøring Plateau, Norwegian Sea	40

Table 6.3: *Summary of effective Q values form studies of the the North Atlantic*

The values in table 6.3 catalogue effective Q, Q_{eff}, which is often misinterpreted as the intrinsic quality factor, Q_{int}. However, for basalts Q_{int} is higher, with most experiments reporting a value greater than 100 (Rutledge and Winkler, 1989) and some suggesting values between 200-600 (Gordon and Davis, 1968; Brennan and Stacey, 1977). Additionally, high pressure work by Wepfer and Christensen (1990) ensuring cracks were sealed during analysis derived a Q_{int} of approximately 100. The primary issue to extract from these results is that the effective Q values derived from transmission through a basalt pile appear to be significantly different from the expected intrinsic Q values. Maresh et al. (2006) investigated the possible mechanisms for this discrepancy using a vertical seismic profile (VSP) from well 164/07 − 1 in the Rockhall Trough, the position of which is shown in figure 6.17(a). A seismic profile from the same location is shown in figure 6.17(b), interpretation of which revealed a basalt with 60-70 separate flows of average thickness 20 m.

Maresh et al. (2006) analysed the VSP data, concentrating only on the direct downgoing first arrivals which were separated from the other components of the wavefield with a seven-point median filter. Spectral ratio analysis derived a Q_{eff} of 25 ± 2 for the basalt in this region. Given the discrepancy between this result and the previously published values of Q_{int} for basalts, Maresh et al. (2006) concluded that the primary mechanism of attenuation must be scattering. Equation 6.7 expresses how the Q_{eff} is a combination of Q_{int} and scattering attenuation, Q_{scatt},

(a) Location of well 164/07-1

(b) Seismic at well 164/07-1

(c) Sampling of the basalt

(d) Spectral analysis
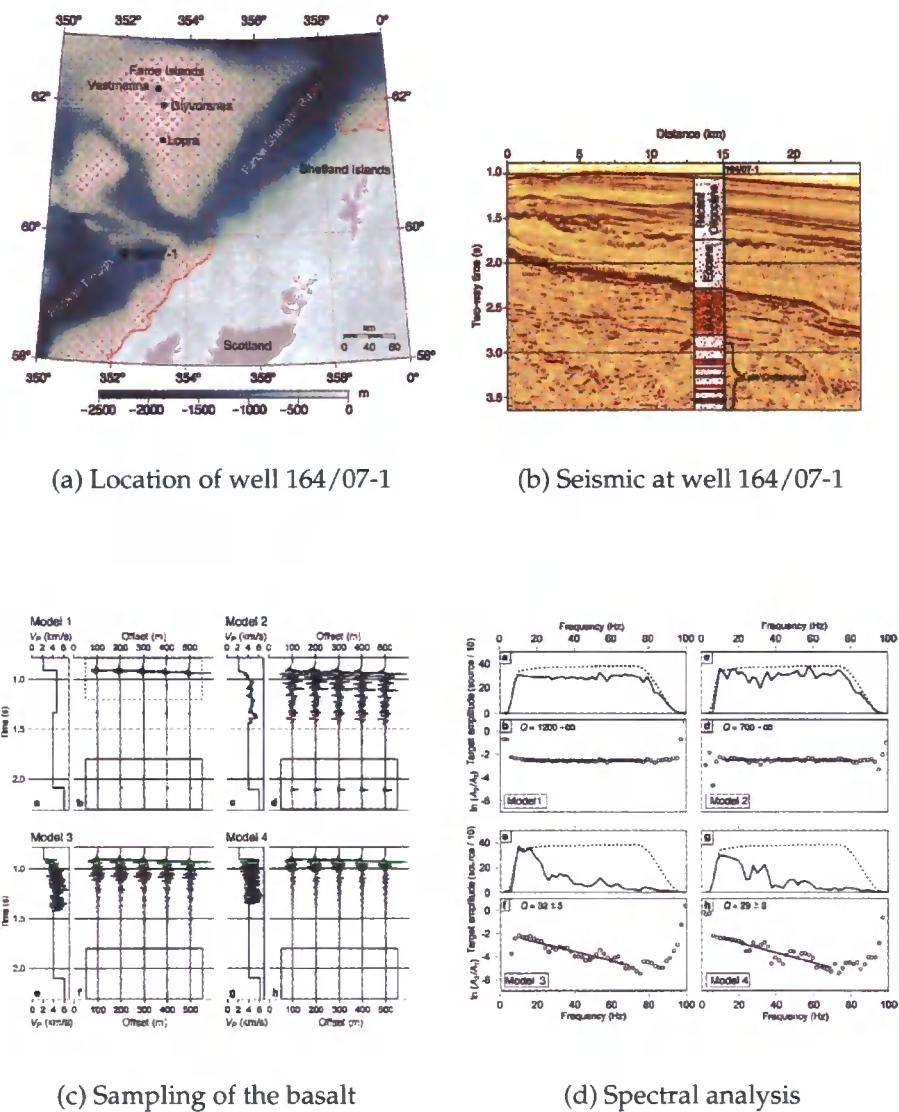
Figure 6.17: *Well 164/07-1 (After Maresh et al. (2006))*

$$\frac{1}{Q_{eff}} = \frac{1}{Q_{int}} + \frac{1}{Q_{scatt}}. \tag{6.7}$$

In order to investigate the effects of scattering Maresh et al. (2006) created a 1-D subsurface model with a homogeneous sediment overlying a basalt flow sequence derived from the basalt structure found in the Roughall Trough. Underlying the basalt was a low velocity layer which formed the upper interface of the target reflector with an increase to basement velocities below. Creating

4 variations of the same model: model 1 (figure 6.17(c)-a) was the reference model with a homogeneous basalt; model 2 (figure 6.17(c)-c) had the basalt sampled at 15 m intervals; model 3 (figure 6.17(c)-e) had the basalt sampled at 3 m spacing; and model 4 (figure 6.17(c)-g) had the basalt sampled at 1 m spacing Maresh et al. (2006) generated four synthetic VSPs. Modelling with reflectivity code they created synthetic seismograms with and without the target reflector. Subtracting the seismogram without the target reflector from the one with, this reflection was isolated and the spectral content could be compared with that of the top-basalt reflection. Figures 6.17(d)-a), -c), -e) and -g) show the source wavelet spectra (dashed line) and the target wavelet spectra (solid line) for each of the four models, whilst figures 6.17(d)-b), -d), -f) and -h) show the calculation of q_{eff} using the spectral ratio technique. What is apparent is that the homogeneous and sparsely sampled basalts show no Q_{scatt} effects whilst the finely sampled basalts produce a Q_{eff} comparable with observed values from the field. Here the sampling rates are significantly smaller than those used in the phase-screen modelling. This gives rise to the hypothesis that only modelling with a complete set of internal reverberations using a finely sampled model captures the scattering effects that lead to effective attenuation. The construction of the model in this study does not meet these criteria requiring a different, and novel, approach.

The problem of propagation through thinly layered media has been investigated on numerous occasions (O'Doherty and Anstey, 1971; Schoenberger and Levin, 1974, 1978) and the major conclusion of this work is that during transmission type experiments the intrinsic attenuation is normally overestimated. This is because the high frequencies are removed from the transmitted wavefield as a consequence of the layering. Schoenberger and Levin (1974) compared the spectral content of synthetic data with and without the inclusion of multiple energy and concluded that the deciding factor for the loss of high frequencies on the transmitted wavefield was the inclusion of internal multiples.

Studies of the earth's reflection coefficient series have determined that the reflectivity series is blue, this relates to an increasing amplitude spectrum with frequency and can be attributed to consecutive reflection coefficients having

opposite sign. This 'blueing' of the spectrum, especially in regions where the impedence contrasts are large such as with intra-basalt reflections, causes the low frequency short-period multiples to reinforce the transmitted signal through constructive interference. The high frequencies are not lost within the scatterer, rather they are reflected back towards the surface and are normally missed in the reflected signal. Conventional seismic reflection processing and interpretation studies generally isolate distinct deep reflectors which correspond to travel paths with long transmission legs through the scattering media. The consequence of this action is the allocation of low Q values for the scattering zone where the method of attenuation is rarely considered. Mateeva (2003) points out that investigation of different parts of the wavefield would result in a different conclusion and the separation of intrinsic Q and scattering effects could be quantified.

Whilst the energy transmitted through a thinly layered medium, i.e. a basalt, will display a lower than expected Q_{eff}, intra basalt reflections will, as a consequence, behave oppositely. They will be rich in higher frequencies causing an underestimate of the intrinsic attenuation. Therefore in reflection studies it is essential to understand the component of the wavefield under investigation whilst undertaking spectral studies. Previous studies generally fail to attribute the absorption to different mechanisms and simply produce a single Q value which they conclude may include a component due to scattering (Clark et al., 2000).

6.11.1 Composing a novel approach to the problem of attenuation in thinly layered media

Initially the velocity profile from within the basalt sequence of well $164/07 - 1$ in the Rockhall Trough was recast as a reflection coefficient series plotted as a function of time, see figure 6.18 (a). Transforming this series into the frequency domain and plotting the power spectrum, figure 6.18 (b), reveals an increasing amplitude spectrum with frequency and the conclusion that the reflection coefficient series is blue.

This blue spectrum supports the assumption that the variation between Q_{eff} and Q_{int} is a result of the constructive interference patterns generated
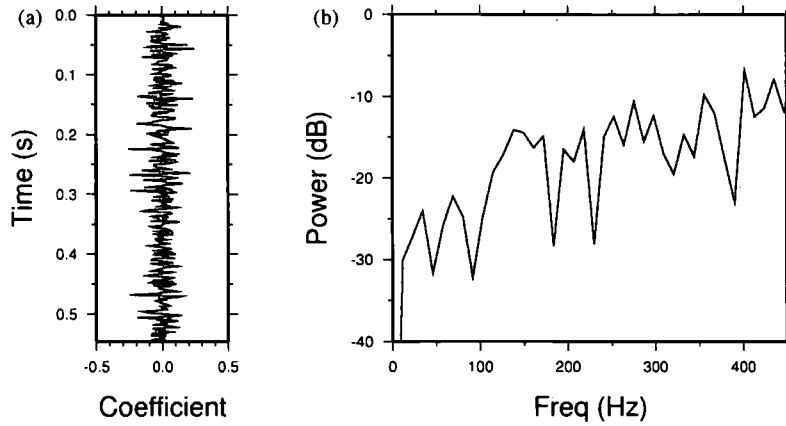
Figure 6.18: *The normal reflection coefficient series plotted as (a) a function of time for the basalt sequence from well 164/07 − 1 in the Rockhall Trough. Taking the Fourier transform of this time series (b) reveals the spectrum to be blue*

by the low frequency component of the wavefield. It is necessary that the transmitted energy passing through the highly scattering region displays the correct spectral signature but a solution that aims to approximate the real scattering effects that take place is desirable. The approach adopted in this study is to consider each screen of the model as a series of scatterers where internal reverberations would generate the effects seen in previous work. In order to replicate this model the entire scattering medium is given its true Q_{int}, for the case of basalt ~ 100, and the wavefield is propagated across an individual screen as before. At the end of each screen the reflection and transmission coefficients are derived for the relevent rock types that make up the interface and the reflected field is stored as before. The transmitted wavefield is then additionally attenuated by a further Q filter (in the manner described in section 3.3.5) which results in the desired Q_{eff}, determined with equation 6.7. The energy removed from the forward propagating wavefield, $Rem.re$ and $Rem.im$, is then reflected, and subjected to a random phaseshift that repositions it somewhere in the previous screen, as shown in equations 6.8–6.10. It is then added into the reflected wavefield generated in the energy partitioning equations,

$$HighFreqRef.re = Rem.re \times \cos\left(Diff\right) - Rem.im \times \sin\left(Diff\right), \qquad (6.8)$$

$$HighFreqRef.im = Rem.re \times \sin{(Diff)} + Rem.im \times \cos{(Diff)}, \qquad (6.9)$$

where

$$Diff = Rand\,(-1, 1)\,\omega \frac{ds}{v_{local}}, \qquad (6.10)$$

and ds is the thickness of the previous screen, v_{local} is the local P- or S-wave velocity and $Rand\,(-1, 1)$ is a random number between -1 and 1 generated at runtime giving a spatially random phaseshift.

This technique ensures that an accurate intrinsic attenuation is applied, and that the transmitted wave has the correct spectral signature whilst also ensuring that the high frequency component of the wavefield is preferentially back-scattered as is expected from previous studies of this phenomena. Finally, it is also important to point out that this method of capturing the attenuation signature of thinly layered media is applicable to both new and old formulations of the phase-screen technique. The method makes no reference to the angle of propagation as the application of the random phase-shift renders this unnecessary.

6.11.2 Testing the seismic attenuation characteristics in thinly layered media

In order to test this method, a simple realisation of a basalt pile is constructed. The model, derived from only 12 distinct rock types, is shown in figure 6.19 and is composed of 3 homogeneous units (rock types 0, 1 and 2) and a basalt flow sequence 940 m thick constructed from 9 separate lithologies. The elastic parameters for the rock types are shown in table 6.4 where Q_{int} values are displayed.

In order to produce an effective Q of ~ 30, a scattering Q of 40 was used for the basalt. Initially the aim of the modelling was to test the transmission effects and the spectrum of the target reflector at 2000 m was compared with the reflection from the top basalt. The modelling was performed twice: firstly,
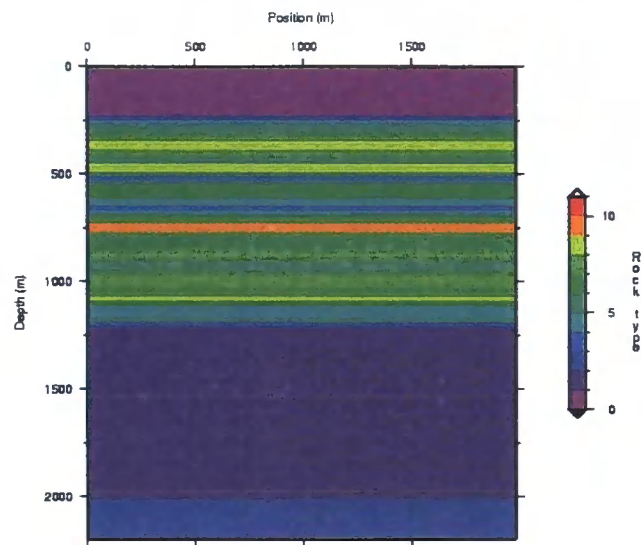
Figure 6.19: *Schematic of the rock types in the simple basalt model*

Rock type	$V_{p\downarrow}\,(ms^{-1})$	$V_{s\downarrow}\,(ms^{-1})$	$\rho\,(kgm^{-3})$	Q_p	Q_s
0	2000.0	1250.0	1500.0	0.0	0.0
1	3000.0	1750.0	2500.0	0.0	0.0
2	5000.0	2850.0	3500.0	0.0	0.0
3	2200.0	1350.0	1600.0	0.01	0.01
4	2400.0	1450.0	1700.0	0.01	0.01
5	2600.0	1550.0	1800.0	0.01	0.01
6	2800.0	1650.0	1900.0	0.01	0.01
7	3000.0	1750.0	2000.0	0.01	0.01
8	3200.0	1850.0	2100.0	0.01	0.01
9	3400.0	1950.0	2200.0	0.01	0.01
10	3600.0	2050.0	2300.0	0.01	0.01
11	3800.0	2150.0	2400.0	0.01	0.01

Table 6.4: *Elastic rock parameters for the simple basalt model used to verify the novel method of applying attenuation in thinly layered media*

with the preferential high frequency reflections and separate Q_{int} and Q_{scatt}; and secondly, with a single Q_{eff} of 29 which should give comparable results. A plane wave source was adopted to negate the effects of geometrical spreading.

Figure 6.20 shows the results of the two methods which produce virtually identical spectral responses proving that the new method for applying attenuation in thinly layered media correctly calculates the effect on the transmitted wavefield.
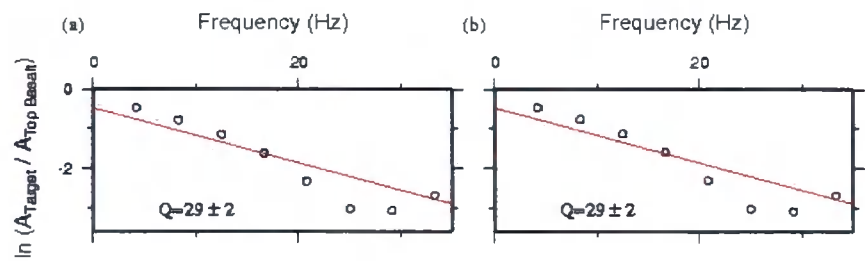
Figure 6.20: *Spectral ratio results for target reflector at base of simple basalt model where (a) plots the response derived with the old method if determining attenuation ($Q_{eff} = 29$) and (b) shows the response with the new approach to modelling attenuation in thinly layered media ($Q_{int} = 100$, $Q_{scatt} = 40$)*

Next an attempt was made to study the reflected waveform from the first interface within the basalt where the consequence of successive transmissions would be least apparent. Generating the top basalt reflection by running only the first five screens of the model and then repeating the modelling for six screens. By subtracting the five screen result from the six screen result isolates the reflected arrivals from screen six. Performing this investigation with both the old and new methods of achieving the required Q_{eff}, the different methods produced significantly different results. Figure 6.21 shows the spectral ratio results for (a) the old method and (b) the new method. The Q_{eff} computed from the new approach yields a higher value meaning less attenuation of the high frequencies as expected from the theory.

In order to verify that this result is not anomolous the test was repeated with the reflection from the interface between screens 35 and 36 and again for the reflection generated between screens 37 and 38. Arrivals from this deep in the basalt will have undertaken 1720 and 1800 m of transmission through the basalt with only a single reflection event boosting the high frequencies. As
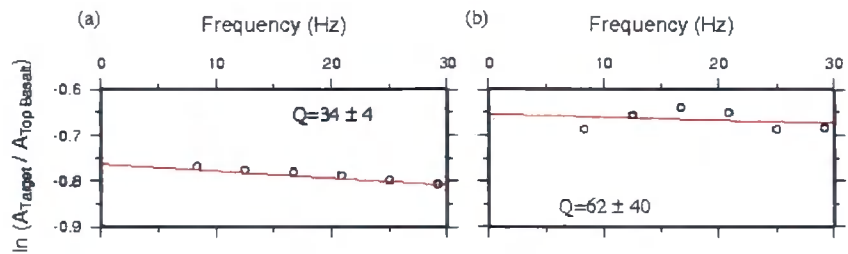
Figure 6.21: *Spectral ratio results for intra basalt reflector near top of simple basalt model where (a) plots the response derived with the old method if determining attenuation and (b) shows the response with the new approach to modelling attenuation in thinly layered media*

such, it is expected that the spectral ratio results will show a Q value similar to that expected solely from transmission. Figure 6.22 shows the results for (a) interface at screen 35 and (b) interface at screen 36 and this expected scenario plays out with a Q_{eff} of 31 clearly demonstrating why this effect is difficult to spot in real data. Clearly most of the energy that gets deep into the scatterer has already suffered a large amount of high frequency attenuation and the small boost is often negligible.
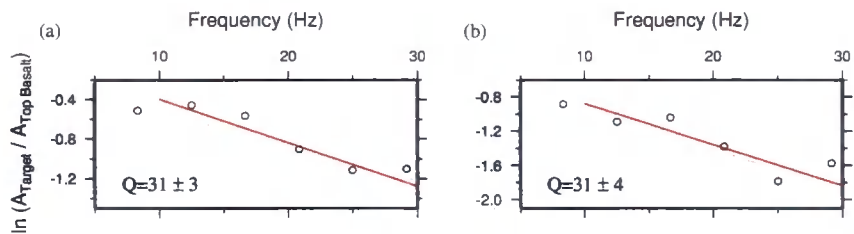
Figure 6.22: *Spectral ratio results for intra basalt reflectors within simple basalt model. Both results are derived with the new method for calculating attenuation in thinly layered media and produce comparable results since transmission effects have dominated the spectral content.*

Finally, it is possible to exclusively image the additional high frequency reflections from the thinly layered scattering medium, figure 6.23 (a). The amplitudes are clipped at one 23rd of the clip value of the complete reflected package, shown in figure 6.23 (b), where this additional high frequency energy is not detectable to the eye, though spectral ratio analysis of the data is sensitive to this modification.
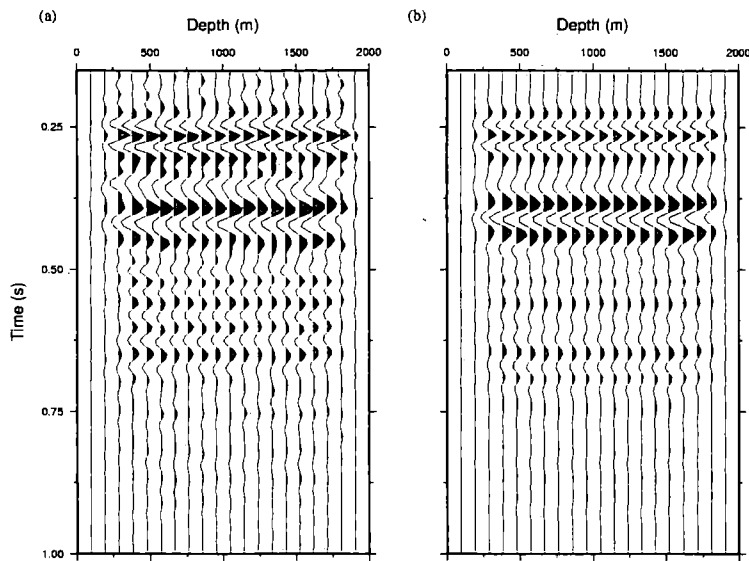
Figure 6.23: *Reflected wavefield from the basalt sequence within the simple basalt model where (a) displays only the high frequency additional energy generated as a consequence of the new approach to determining attenuation in thinly layered media. (b) displays the complete wavefield including all intra-basalt reflections and the high frequency component is not noticable by eye since (a) is clipped at one 23rd of the value of (b).*

6.11.3 Problems with wraparound energy

In order to model data to a reasonable offset whilst maintaining realistic run-times the source is placed close to the edge of the model space to maximise efficiency. Unfortunately since the method is a dual domain technique this produces substantial wrap-around from the reflected wavefield. This is a considerable nuisance since this rogue energy can interfere with the tails of the reflections that are required during demultiple processing steps.

Figure 6.24 (a) shows a typical 2-D shot gather (with source positioned at x=696300, y=8210350) from a swathe through the centre of the Hold-with-Hope model. This figure shows significant wraparound energy and figure 6.24 (b) focuses on the regions in which this most noticeably obscures the true reflected wavefield. This unwanted energy is difficult to remove during processing without also removing some of the reflected wavefield. Initial approaches focused on damping away the energy during modelling by increasing the muting at the

edge of the model space. This proved inappropriate since the source, and the short-offset receivers, were then positioned in the extended muting band.
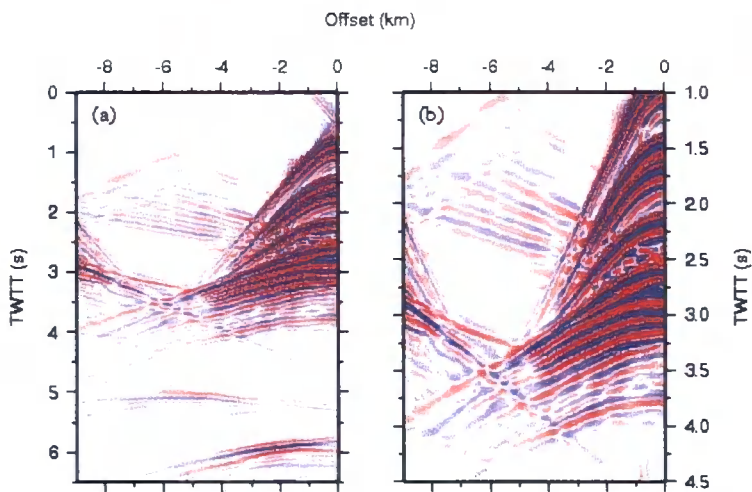
Figure 6.24: *Raw shot gather with source at x=696300, y=8210350 from phase-screen code. (a) shows the first 6.5 s of the t-x record and (b) a subsection of the record between 1 and 4.5 s with the most problematic wraparound energy highlighted.*

The solution proposed in this study uses the model geometry and is demonstrated using 2-D modelling. The technique takes advantage of the fact the interfaces above the basalt are flat across the entire model space and the top basalt surface is comprised of three flat surfaces, shown in figure 6.25 with the modelled 2-D plane highlighted. It is the wraparound energy developed from these upper interfaces that interferes most strongly with the deeper reflections and, as such, becomes the primary target for removal.
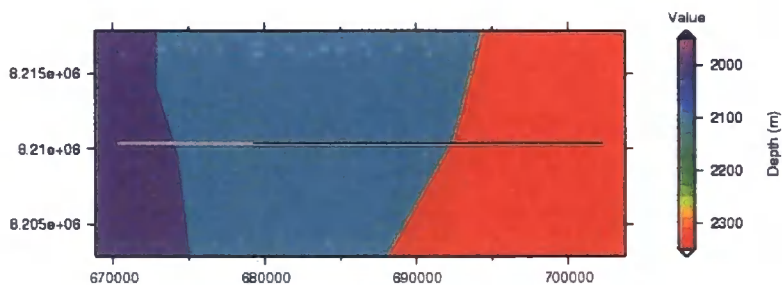
Figure 6.25: *The depth to top basalt across the Hold-with-Hope model. The top basalt surface is made up of three flat sections that deepen to the east. The black line highlights the range of the source and the underlying grey line displays the extent of the receivers.*

A reduced Hold-with-Hope model is created with the same node spacing but encompassing only the screens down to and including the top basalt. Additional shots with identical source and receiver geometries are modelled on this reduced model. The first has the same lateral extent whilst the second has double the aperture in x and y. The wraparound energy is caused by the source being positioned close to the edge of the model space so with a much larger model the wraparound occurs later in the record and has a significantly reduced amplitude. The receivers should record the same signal from the true subsurface meaning the only difference between equivalent receivers is a consequence of wraparound effects. Calculating the difference between coincident receivers will isolate the unwanted energy. Once this has been removed from the original shot gathers, the wraparound energy generated as a consequence of the top five interfaces is removed.
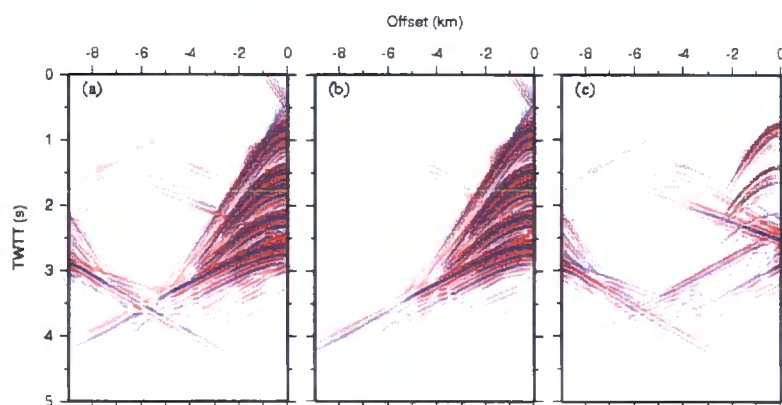
Figure 6.26: *Shot gathers from the reduced Hold-with-Hope model with (a) equivalent lateral extent to original geometry, and (b) double the model lateral extent. (c) the difference between (a) and (b) highlighting the wraparound energy generated as a consequence of the flat upper layers.*

Figure 6.26 shows a shot gathers from, (a) the reduced-depth Hold-with-Hope model and, (b) from the laterally extensive reduced-depth model, for the same shot and receiver configuration as in figure 6.24. The difference between these plots, figure 6.26 (c), is the wraparound energy. Subtracting this from the shot record shown in figure 6.24 gives the corrected wavefield, figure 6.27 (a). Figure 6.27 (b) shows the primary region of interest, equivalent to 6.24 (b), and the improvement is noticable with the cross-cutting wraparound noise removed.
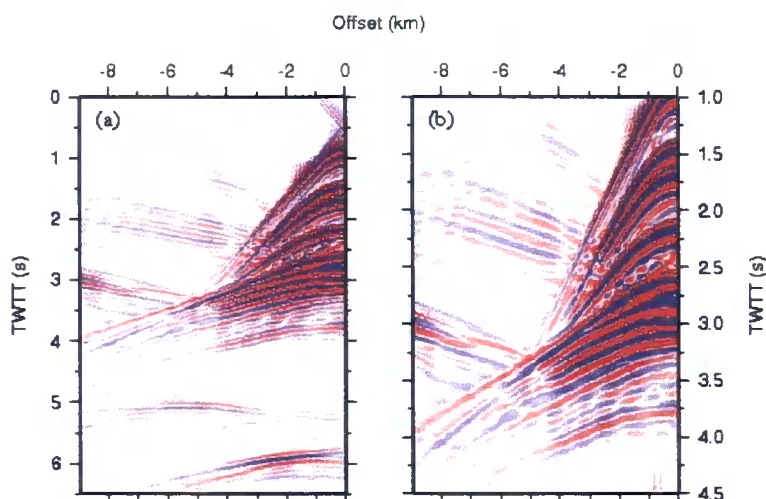
Figure 6.27: *Corrected shot gather from x=696300, y=8210350 with the wrap-around energy removed. (a) shows the first 6.5 s of the t-x record and (b) a subsection of the record between 1 and 4.5 s with the most problematic wraparound energy removed.*

Figure 6.25 shows how shots are only required across two distinct basalt depths, as one step is small, so the calculation of two difference plots is sufficient to correct the majority of the modelled energy to a good first approximation. Figure 6.28 (a) shows an additional shot gather (source position x=700000, y=8210350) above the same depth to top basalt, whilst figure 6.28 (b) shows this shot gather corrected with the energy displayed in figure 6.26 (c). This simple technique produces significant improvements.

6.11.4   Seismic source

The source wavelet used during the Hold-with-Hope modelling project is comparable with sources used in industrial acquisition and was generated in conjunction with Chevron to maximise the frequency content over a bandwidth between 5 and 20 Hz. The optimisation was undertaken by testing numerous air gun array wavelets at a range of source and receiver array depths in order to produce maximum energy within the low frequency spectrum. Pulse shaping with sea-surface ghosts was considered during the optimisation. Initially, the source wavelet was generated at a sampling rate of 0.5 ms, and is shown in figure 6.29 (a) with its respective frequency spectrum displayed in figure 6.29 (b). The modelling during the Hold-with-Hope project requires a wavelet
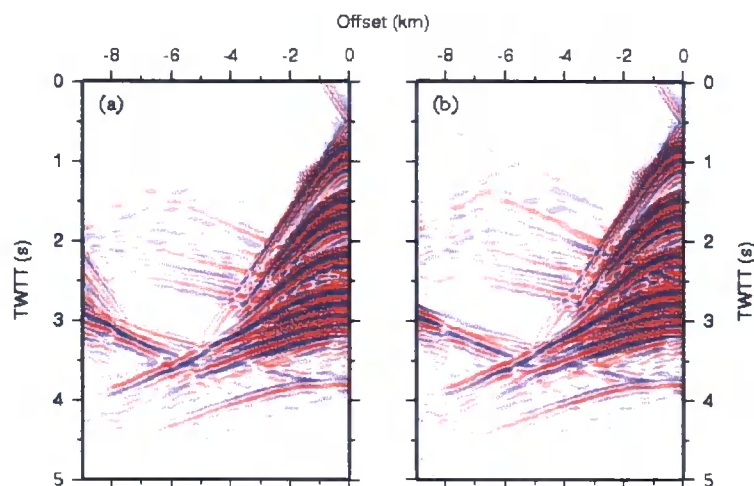
Figure 6.28: *Corrected shot gather from x=700000, y=8210350 with the wrap-around energy removed. (a) shows the uncorrected version and (b) the same shot gather with the most problematic wraparound energy removed.*

sampled at 8 ms and the resampled wavelet is shown in figure 6.30 (a). To ensure suitable anti-aliasing steps were taken prior to modelling this wavelet was created by low-pass filtering the original wavelet with roll-off between 35 and 45 Hz and then resampling using Seismic Unix (Cohen and Stockwell, 2003).

A source depth of 12 m produced a normal incidence lag of 0.0162 s and a notch in the frequency spectrum at 61.7 Hz. The receivers were towed deeper than generally expected (Gallagher and Dromgoole, 2007) at 28 m generating a frequency notch at 26.5 Hz and a normal incidence lag of 0.0378 s. The source and receiver ghost has a lag of 0.0541 s.

Figure 6.31 (a) shows the reflected sea-bed arrival generated from phase-screen modelling, shifted 0.67 s, with the different components of the wavelet highlighted whilst figure 6.31 (b) displays the frequency spectrum of this arrival. For comparison, figures 6.31 (c) and (d) show the original over-sampled wavelet manipulted with Seismic Unix (Cohen and Stockwell, 2003) to produce the equivalent effects at normal incidence, without consideration of attenuation or geometrical spreading. It can be seen that the limitations imposed by the longer sampling interval have shaped the pulse but the frequency content within the range of interest is comparable.
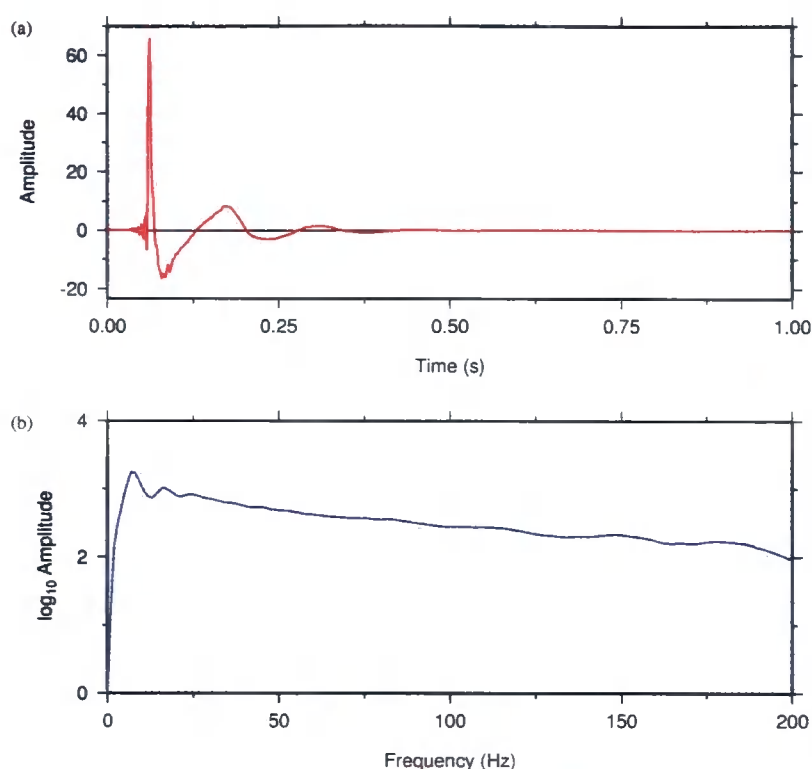
Figure 6.29: *(a) Source wavelet and (b) frequency spectrum of the original Hold-with-Hope wavelet sampled at* $0.5\ ms$

6.11.5   Seismic interpolation of synthetic data

The computational run-time for the 2-D and 3-D modelling performed during this study is directly proportional to the number of shots generated. In order to provide the largest possible dataset for the industrial partners a proposal to increase the shot spacing and interpolate the missing shots was put forward. This idea allowed for a substantially larger area to be investigated within the Hold-with-Hope model and also offered the opportunity for a large scale interpolation project on synthetic data. The interpolation will be performed using the ProMAX3D seismic data processing software with the aim of interpolating three out of every four shots. This means that the regular 1201 shot traverse can be reduced to 301 shots. This interpolated shot spacing will reduce the trace offset from $160\ m$ to $40\ m$ in the cdp domain which will allow improved processing of data which would previously have suffered spatial aliasing. F-X domain interpolation (Spitz, 1991) relies upon the continuity of events in
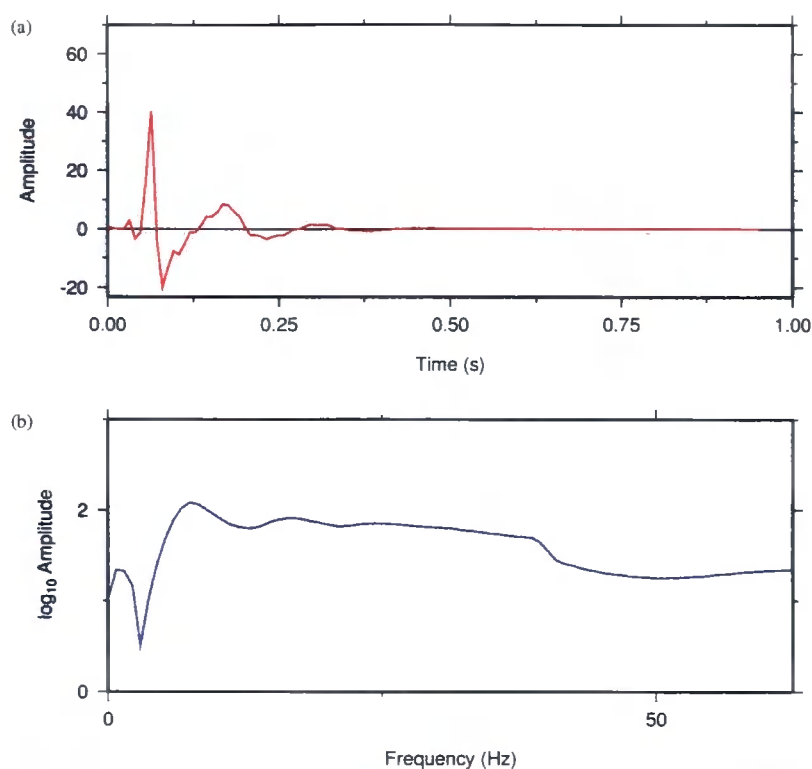
Figure 6.30: *(a) Resampled source wavelet for Hold-with-Hope project recorded at a rate of 8 ms and (b) its frequency spectrum*

the f-x domain and using the sparse modelled traces as an input the missing traces can be interpolated as the output of a linear system. Application of this interpolation technique is beneficial in this study since it maintains the frequency content of the original data leading to no loss of vertical resolution. Large scale interpolation of synthetic data is not usually undertaken but has significant run-time advantages over forward modelling. It is also analogous to the techniques employed in industry.

One significant problem in interpolating traces from real data is the component of source generated noise that masks the coherent subsurface signal. However since the data in this study is interpolated from synthetic, noise-free traces; as long as ample traces are used for the interpolation and an adequate range of slopes are investigated the method should produce excellent results.

The primary option when interpolating traces is the choice of interpolation domain. Most interpolation is performed in the cdp domain and initial investigations for this study followed this path, however, results were disappointing.
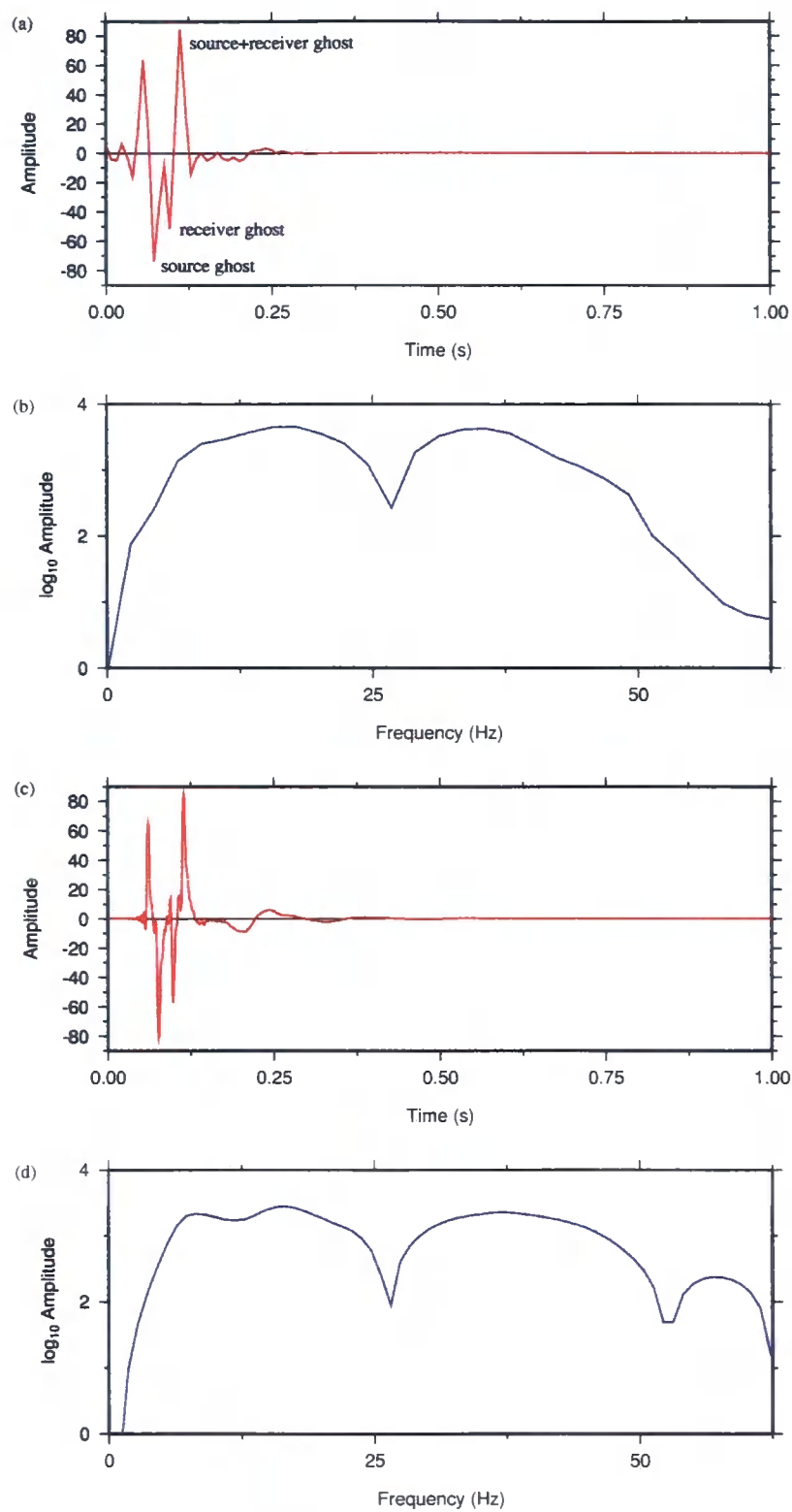
Figure 6.31: *Sea-bed reflection from Hold-with-Hope modelling highlighting the different components of the wavelet in (a) the time domain and (b) the frequency domain*

Figure 6.32 shows a 2-D inline stacking diagram which replicates the source and receiver geometry of the Hold-with-Hope project. With a shot interval, ΔX_s, of 80 m, and a receiver spacing, ΔX_r, of 20 m the distance between cmp gathers, ΔX_y, is 10 m with a trace separation, $2\Delta X_h$, of 160 m. In the common receiver gather, trace separation is 80 m and the reflection point moves 40 m between traces, whereas in a common offset gather the reflection point separation between traces is 80 m. As such, by interpolating in the cdp domain the algorithm has to work considerably harder to produce results. Further tests revealed that the common offset domain provided traces with the least variation from modelled traces and interpolation of data during the project will be undertaken in this domain.
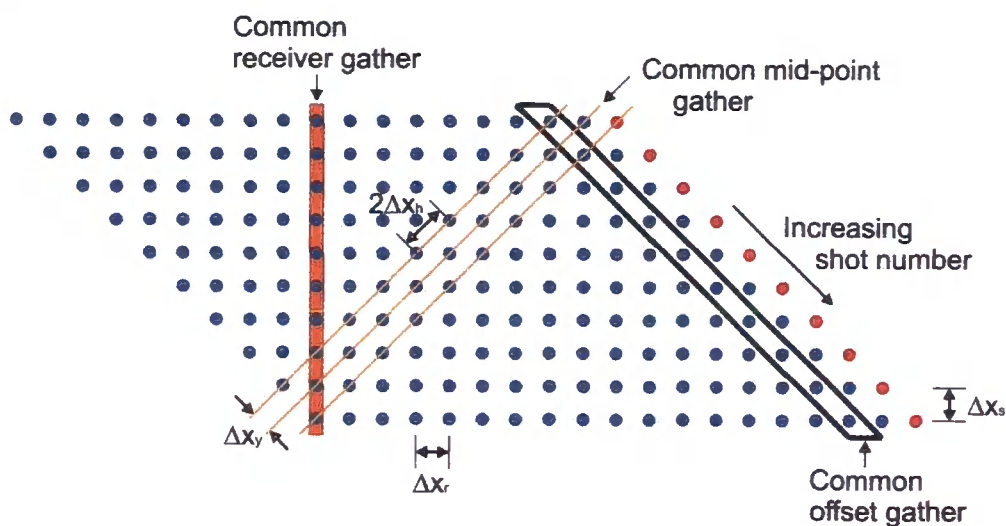
Figure 6.32: *A 2D inline stacking diagram displaying* 10 *consecutive shots and the first* 18 *receiver channels. Examples of common offset, common receiver and common mid-point gathers are shown.*

Initially the investigation of the interpolation steps will be undertaken with 2-D data prior to the 3-D interpolation study required for the final data-set shown in chatper 7. This is a reasonable assumption since the interpolation will be performed on individual receiver arrays which can be considered as a 2-D plane of data.

Figure 6.33 (a)-(e) show five consecutive shots gathers (starting at x=699300, y=8210350) with a 20 m shot spacing modelled using the phase-screen code. The receiver spacing of 20 m ensures that the water wave only aliases at $\sim$ 38

Hz. Figure 6.33 (f)-(j) shows the f-k plot for each of the shot gathers where the Nyquist wavenumber is $0.025 \ m^{-1}$.
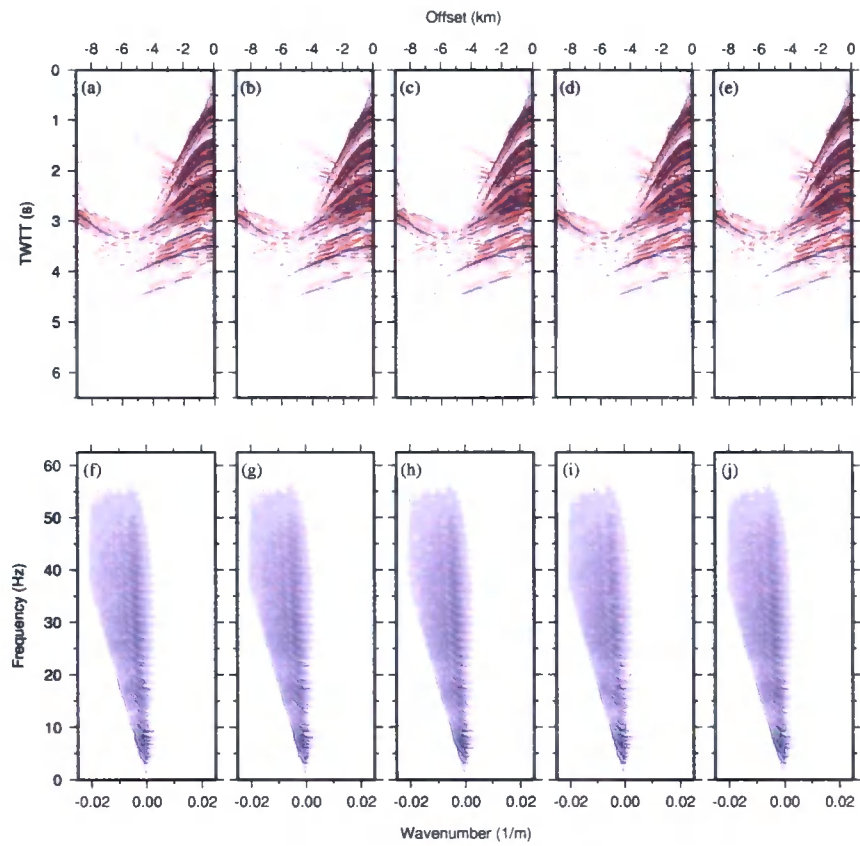
Figure 6.33: *Five phase-screen shot gathers modelled at the final shot and receiver spacing. Data is displayed in the t-x domain in (a)-(e), and in the f-k domain in (f)-(j).*

Sorting the shot gathers into the cdp domain results in a trace spacing of $40 \ m$. Figure 6.34 (a) and (c) show a cdp gather at position $x = 679300$ and its f-k plot respectively. The energy is wrapped around the f-k domain but doesn't interfere with the desired part of the spectrum. If only every fourth shot is modelled, as is planned in the final modelling routines giving a shot spacing of $80 \ m$, the cdp gather at 679300 has a trace spacing of $160 \ m$ and the f-k plot is severely aliassed. This would present numerous processing difficulties where the application of spatial filters are used. Figure 6.34 (b) and (d) show the reduced shooting cdp and its respective f-k plot.

The f-x interpolation is applied twice within the processing flow. It initially allows a cdp domain trace spacing of $80 \ m$ to be recaptured then these traces
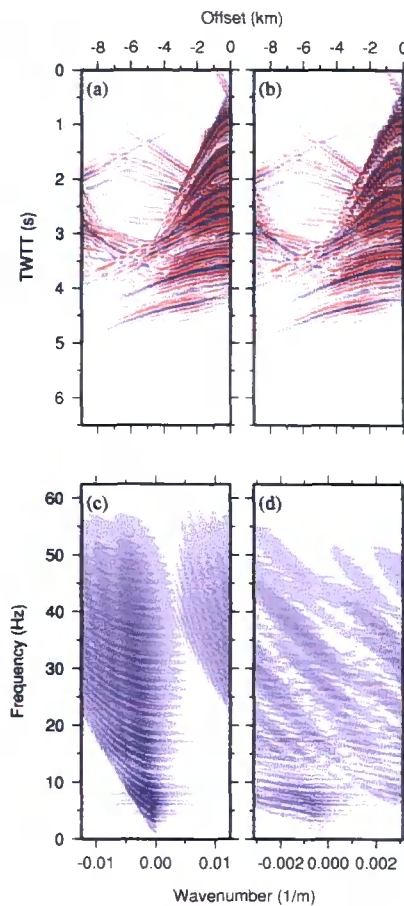
Figure 6.34: *Phase-screen cdp gather modelled at (a) and (c) the final shot and receiver spacing and (b) and (d) at the reduced shot spacing proposed for the Hold-with-Hope project.*

are used, alongside the original modelled data, to derive the missing traces that give the 40 m trace separation during the second interpolation step. Figure 6.35 (a) and (d) show the t-x and f-k plots for the cdp gather at $x = 679300$ derived exclusively from the modelled data with the final shot and receiver spacing. Figure 6.35 (b) and (e) show the comparable plots for data interpolated from a shot spacing of 80 m at the same position. The difference at $> 50\ Hz$ is a consequence of the interpolation algorithm being set to operate over the frequency range 0.5 to 50 Hz. The plots shown in figure 6.35 (c) and (f) are the difference plots between the modelled and interpolated t-x and f-k plots shown to the same scale. There is an obvious, and expected, difference at high frequency on the f-k plot whilst the t-x plot reveals an excellent match.

There are some minor short offset discrepancies which are a consequence of the missing high frequency energy in the interpolated plots.
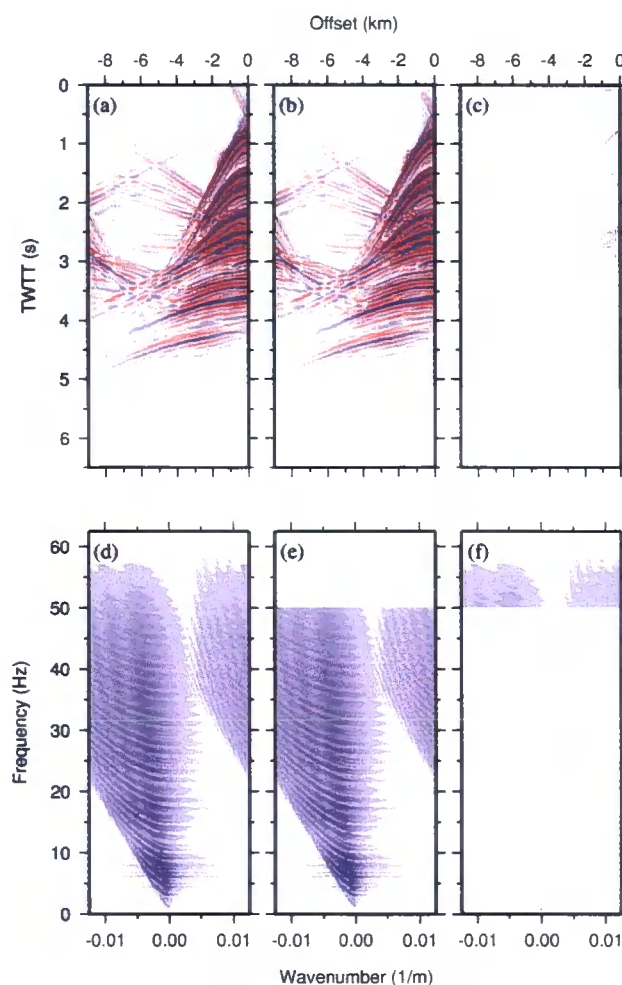
Figure 6.35: *Equivalent t-x and f-k cdp gathers from: phase-screen modelling at the final shot and receiver spacing in (a) and (d); two f-x interpolation steps after phase-screen modelling at the reduced shot spacing proposed for the Hold-with-Hope project in (b) and (e) and; the difference between the modelled and interpolated data in(c) and (f)*

Figure 6.36 shows the corresponding interpolated shot gathers to figure 6.33: (a) and (e) are original modelled shots; (c) is a first pass interpolated shot gather: whilst (b) and (d) are second pass interpolated shots. Once again the only significant difference is at high frequency where the shot gathers are modified by the algorithm which is eqivalent to a high cut filter.
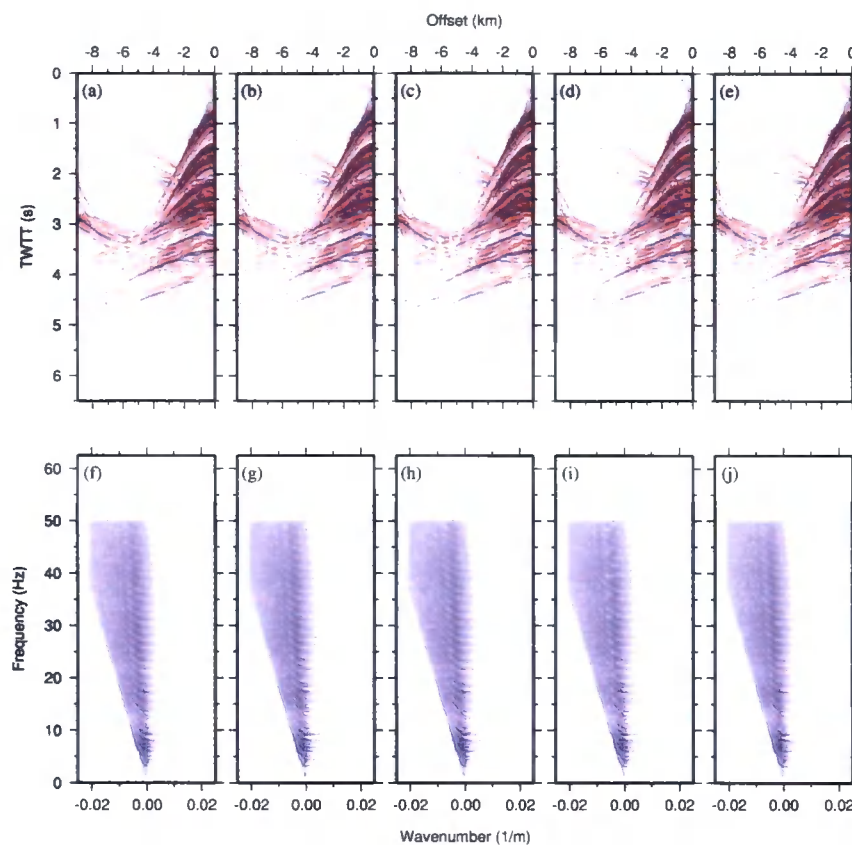
Figure 6.36: *Five interpolated shot gathers recreating the final shot and receiver spacing. Data is displayed in the t-x domain in (a)-(e), and in the f-k domain in (f)-(j).*

Finally, figure 6.37 shows a zoomed image of the same single shot in the t-x domain derived in (a) by phase-screen modelling and in (b) by interpolation. The accuracy of the interpolation method has proven to faithfully replicate the modelled data and agreement was reached with the industrial partners to proceed with modelling at a sparser shot spacing and generate the missing shots through processing. The interpolation will proceed in the common offset domain and will be responsible for generating $3/4$ of the shot records.

6.11.6   Setting the model size

Once a decision was made to model the narrow angle acquisition with $6 \times 7\,km$ receiver arrays spaced at $100\,m$ laterally, the active model size for the modelling was set to approximately $9000\,m \times 1500\,m$. Initial modelling on the $20\,m$ grid
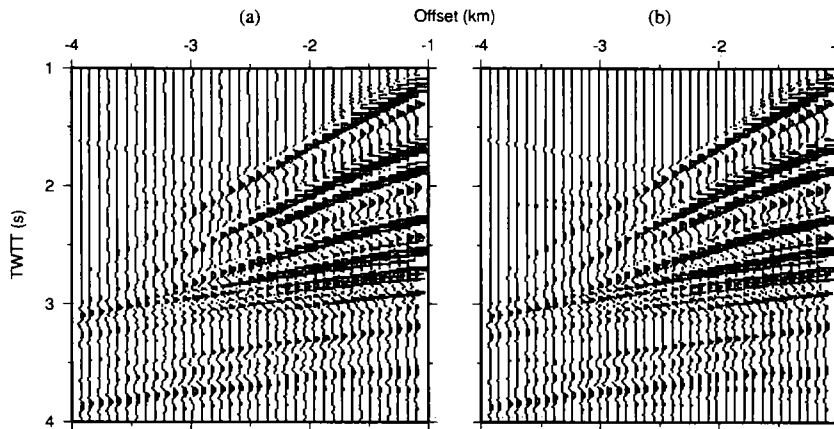
Figure 6.37: *Modelled and interpolated shot gather*

was undertaken with 446 × 74 nodes and the run time was considerably longer than anticipated. A study was undertaken to determine the transform times for a range of grid sizes available for use with 20 m node spacing. Initially 1-D transforms were tested over a range suitable for a 40 m grid where figure 6.38 (a) shows transforms for a range in y between 1000 m and 2540 m and (b) shows transforms for a range in x between 8000 m and 10000 m. It is immediately obvious that the gridsize is highly influential in the time taken to transform the data and there appears to be three trends within these plots where the longest time per transform can be an order of magnitude greater than the minimum, well-chosen transform.

This variability in transform time is again seen in the 2-D transforms for 40 m and 20 m grids and is displayed in figures 6.38 (c) and (d) respectively. These 'tartan' results show that a correctly chosen model size will result in an optimised run time that can be greater than one order of magnitude quicker than a poorly chosen 2-D grid.

Making use of freeware from Valgrind and Kcachegrind it is possible to generate the relative time spent undertaking each function within a modelling code. The Fourier transforms are the single largest part of the narrow-angle phase-screen code, taking 27.2% of the run-time in the Hold-with-Hope 2-D examples. By picking a model size that ignores optimisation the overall run-
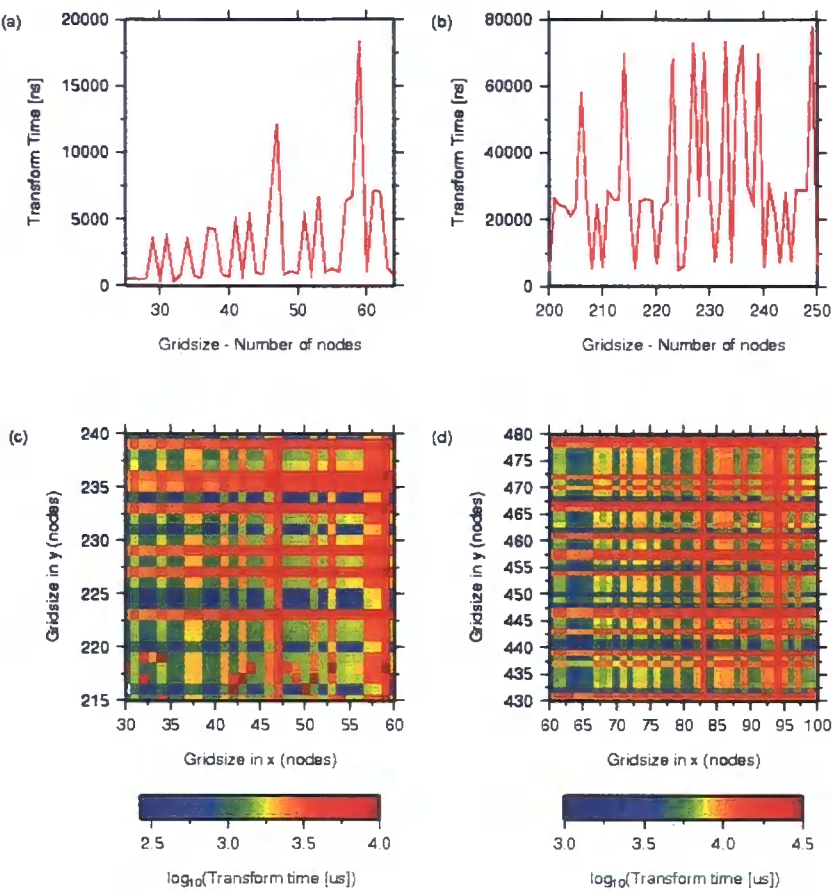
Figure 6.38: *Individual Fourier transform times for varying grid sizes where (a) and (b) show the times for 1-D transforms sized for a 40 m grid whilst (c) and (d) shows the 2-D transform times for a range of 40 m grid sizes and 20 m grid sizes respectively*

time can increase significantly. The chosen grid size for the $20\ m$ 3-Dmodel grid is shown in table 6.5

Node spacing (m)	Nodes	Size of model (m)
20	448×72	8940×1420

Table 6.5: *Node distribution and model size for the 20 m and 40 m grids of the Hold-with-Hope project*

6.12 Discussion

In this section the rationale for the Hold-with-Hope project has been explained, and the reasoning behind the use of the narrow-angle phase-screen code has

been put forward. A justification of why uplifted lithology in north east Greenland make a viable proxy for the buried, basalt covered sediments found in the hydrocarbon exploration regions of north west Europe has been included. Following this the geological history of the region was highlighted to isolate the beds within the succession that would be of interest as potential reservoir rocks.

This study then described the building of a large subsurface model suitable for generating synthetic seismic data and explained how the elastic parameters were chosen to ensure consistancy with those in the Faroe-Shetland trough. The developement of a method to better produce synthetic plateau basalt piles was postulated, and the method was shown the generate statistically accurate velocity distributions and mimic the flow correlation lengths seen in the real world. Additionally, the attenuation effects due to basalt flows have been reviewed and a novel technique to replicate this attenuation, whilst still maintaining an equivalent media philosophy, has been put forward and tested. This method produces small, but measureable effects.

A simple, but effective, system for removing the near surface wraparound energy often seen in dual-domain modelling schemes has been developed and employed. This technique has improved the resolution of the shot records but has come at a significant cost in terms of computational run time and set-up.

This study has also ensured a realistic source wavelet for sub-basalt investigation has been generated. The frequency content of the wavelet is optimised in the spectral region of interest and ensures maximum energy at key low frequencies.

A study of the best methods for seismic interpolation on synthetic data has been undertaken using 2-D data modelled with the phase-screen code. This work concluded that the use of f-x interpolation procedures in the common offset domain generated the optimal results. It was also noted that when utilising fast Fourier transforms in seismic modelling codes, the choice of grid size can have a significant effect on the run time of the modelling. A poor chosen grid can result in model runs that take orders of magnitude longer than almost equivalently sized grids.

This work has ensured that the project is now ready to generate an accurate 3-D synthetic seismic dataset over the Hold-with-Hope model.

Chapter 7

Hold-with-Hope results

7.1 Introduction

During conventional marine seismic acquisition, in addition to the primary investigative procedures, other methods of subsurface illumination are usually undertaken (Greenroyd et al., 2007). As well as presenting the initial seismic reflection results, this study intends to produce a range of synthetic geophysical measurements derived from the Hold-with-Hope model. This collection of data will offer a unique geophysical dataset for processing and interpretation. Alongside seismic reflection modelling, a VSP through the centre of the Hold-with-Hope subsurface will be derived, gravity data will be produced across the model and exploding reflector plots analagous to the expected final stacked sections will be made. These methods would provide the opportunity for integrated inversion techniques to be adopted in order to better constrain the sub-surface. Thought was also given to generating synthetic magnetic and magneto-telluric data for this purpose, but since the results of these studies would be entirely dependent on the user-defined parameterisation of the specific lithological units within the Hold-with-Hope model there seemed no compelling reason to compute this data. The range of data produced should enable comparisons to be drawn between the different processing methods employed by the industrial partners.
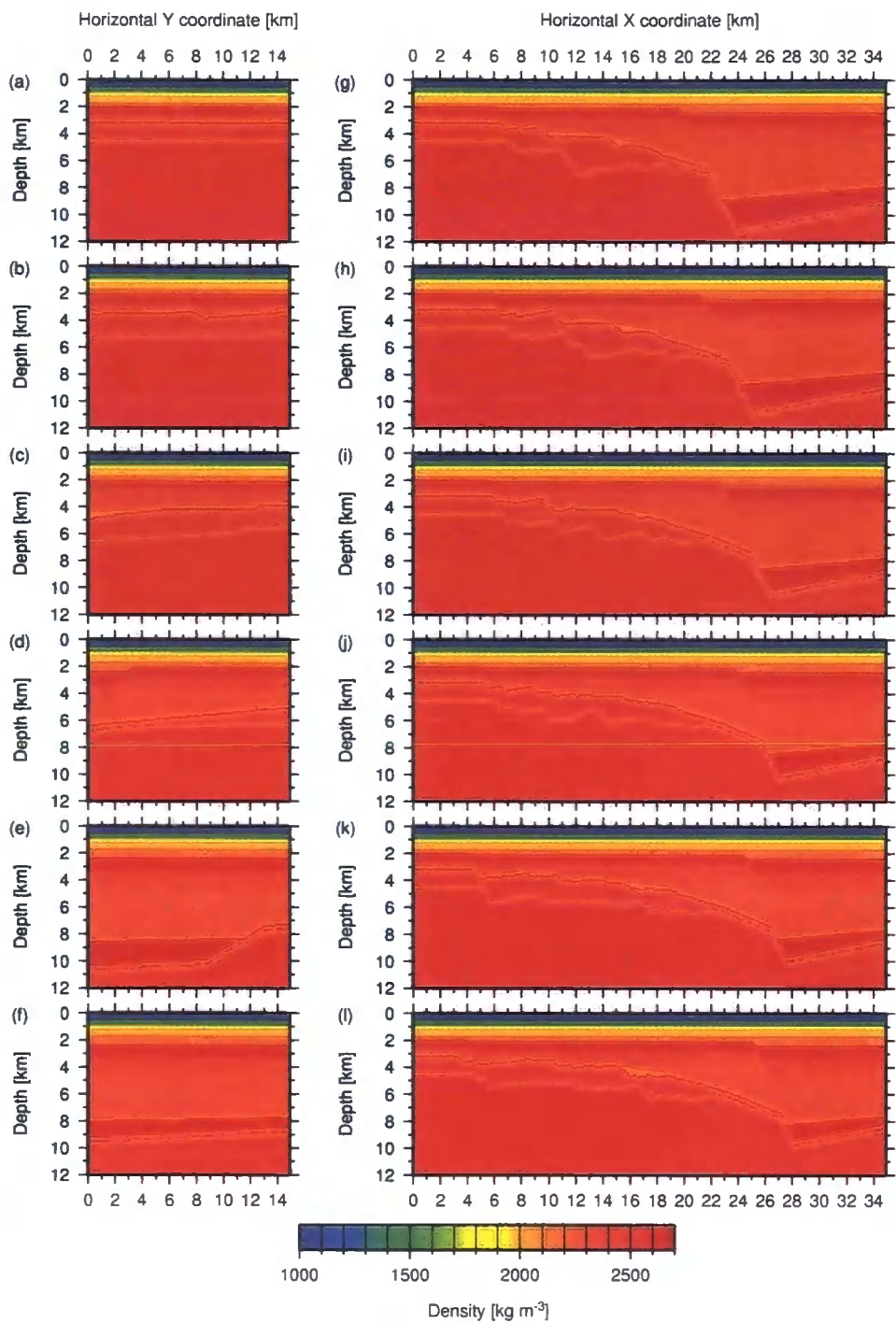
Figure 7.1: *Density cross sections from the Hold-with-Hope model. (a)–(f) show cross-flow plots at $x = 671800, 677800, 683800, 689800, 695800$ and 701800 m respectively whilst (g)–(l) show along-flow plots for $y = 8203850, 8206350, 8208850, 8211350, 8213850$ and 8216350 m respectively.*

7.2   Gravity modelling

Gravity modelling is generally inplemented with polygon–based, constant–density, modelling algorithms (Talwini, 1985) yet the parameterisation of the subsurface for seismic modelling is discretised on a regular grid. Recent increases in computational speed and memory storage have enabled gravity modelling algorithms which sample the subsurface on a considerably finer scale to be fully implemented across large 3-D models. Trinks and Hobbs (2005) proposed a technique for 2-D and 3-D sub-surface structures where heterogeneity was described on a regular grid of constant density cubes an order of magnitude smaller than previous kilometer scale sampling (Bear et al., 1995). The technique lends itself to modification to handle phase-screen seismic models since the density volumes can be generated from sub-surface interfaces, during derivation of the phase-screen input files, to create a finely sampled rock parameter grid ideal for this approach to gravity modelling. This study resamples the phase-screen 3-D model to a coarser grid size of 100 m^3 in order to reduce run-time whilst still providing the required accuracy.

Figure 7.1 shows regularly spaced density cross-sections in both x and y from the Hold-with-Hope model constructed from cubes of edge length 100 m. The flat upper layers seen across the entire model will not produce a gravity anomaly meaning that the modelled response for the Hold-with-Hope volume will be an indication of the lower (> 2 km deep) structure. The method described by Trinks and Hobbs (2005) requires infinite padding of the chosen model space so changes in the density distribution outside the model boundaries will be ignored. The sedimentary succession shows the expected compaction driven increase in density, and therefore velocity, with depth. However, the notable exception are the anomalously high density Valanginian deep marine conglomerates which disrupt this compaction trend. Appendix A.3 shows the log from well 206/4-1 which shows the sonic record for a comparable deep marine conglomerate justifying this high velocity and density unit. The assumption being that the conglomerate is a highly cemented quartzite rich package.

Table 7.1 summarises the different analytical expressions used to determine the overall response on the model. The method uses the gravity response of

Position of cell	Modelled response	Analytical expression
Internal cube (3D)	Sphere	$\Delta g = G\rho z \Delta z \Delta y \Delta z a$
Cube at vertical side (3D)	Semi-infinite horizontal rod	$\Delta g = Gz\Delta y \Delta z b$
Cube at vertical corner (3D)	Semi-semi-infinite sheet	$\Delta g = G\rho \Delta z c$
Internal cell (2D)	Infinite horizontal rod	$\Delta g = 2G\rho \Delta x \Delta z d$
Cell at vertical edge (2D)	Semi-infinite sheet	$\Delta g = 2G\rho \Delta z e$

Table 7.1: *The expressions for the gravity effects used in the summation across the entire model space. The total gravity response at an individual station is the total of each cells contribution.* Δx, Δy *and* Δz *are the dimensions of the cell whilst* x, y *and* z *are the distances between the station and the cell centre,* ρ *is the density of the grid and* G *is the gravitational constant. For a rod perpendicular to the x-axis, the* x *and* y *change places in the expression for a semi-infinite rod and* $a = (x^2 + y^2 + z^2)^{-\frac{3}{2}}$,

$b = (x^2 + z^2)^{-1} \left[1 - \frac{y}{\sqrt{x^2+y^2+z^2}} \right]$, $c = \frac{\pi}{2} - tan^{-1}\frac{x}{z} - tan^{-1}\frac{y}{z} + tan^{-1}\frac{y}{z}\frac{x}{\sqrt{x^2+y^2+z^2}}$,

$d = \left(z \left(1 + \frac{x^2}{z^2} \right) \right)^{-1}$ *and* $e = \left(\frac{\pi}{2} + tan^{-1}\frac{x}{z} \right)$

simple volumes to replace the approximate nature of the grid. The difference between the anomaly caused by the true mass distribution of the grid nodes and that of the modelled response is negligible if the integration is performed over a large number of cells which are small in comparison to the cell–station distance (Trinks and Hobbs, 2005). The position of the cell within the modelled volume determines which analytical expression is used since the outer cells must be infinitely padded to generate a realistic response.

Figure 7.2 shows 2-D gravity profiles across the Hold-with-Hope model recorded at stations positioned at regular intervals on the top surface. The swathes are coincident with the density cross sections shown in figure 7.1. In order to leave only the anomaly, the mean value of the computed response is subtracted from the data prior to plotting. The red and dashed blue lines in figure 7.2 show the response from: the entire 3-D model; and from the exclusive consideration of the 2-D plane respectively. This is intended to highlight the fact that since gravity models are normally approximated from 2-D profiles small discrepancies can occur from off axis density changes, however in re-
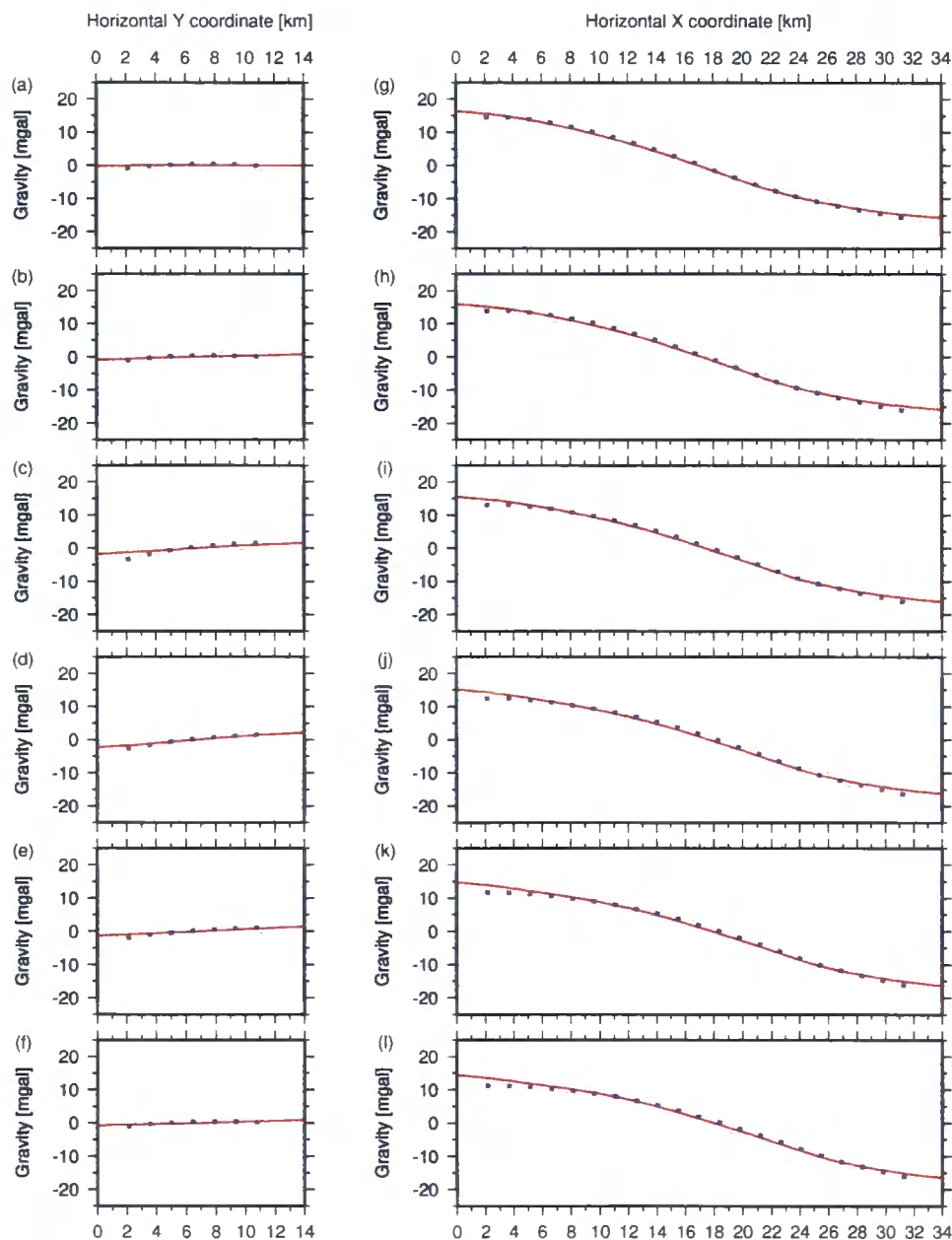
Figure 7.2: *2-D gravity profiles across the Hold-with-Hope model. (a)–(f) shows plots at* $x = 671800, 677800, 683800, 689800, 695800$ *and* 701800 *m respectively whilst (g)–(l) shows plots for* $y = 8203850, 8206350, 8208850, 8211350, 8213850$ *and* 8216350 *m respectively.*

gions where the lateral variation is minimal, figure 7.2 (g)–(l), the difference is negligible and a 2-D approximation is sufficient.

The complete 3-D gravity anomaly recorded over the entire Hold-with-Hope volume is shown in figure 7.3. The anomaly high is, as expected, over the region where the high density basement is closest to the seabed and the anomaly low sits beyond the foot wall of the large extensional fault. The variation in the position of this fault can easily be inferred from the gravity data, and the extension of the faulting zone as the function in y can be concluded from the reduction in the rate of change of the gravity profile. Since the aim of the gravity modelling is to reveal details of the gross structure of the subsurface in order to back up the seismic modelling, it is possible to assess the throw of the major Fosdalen fault using equation 7.1, the slab formula (Kearey et al., 2002),

$$Anomaly = 2\pi G\rho t \times 10^5 \tag{7.1}$$

where G is the Gravitational Constant, ρ is the density contrast, t is the slab thickness and anomaly is determined in $mgal$. Taking the anomaly as 20 $mgal$ and an average density contrast of 100 kgm^{-3} gives a fault offset of $\sim$ 4.7 km which compares well with the true value of 5.5 km.

However, gravity modelling fails to reveal any of the subtleties of the model since the effect of each, and every, position is included in the derived response at a single receiver resulting in an unconstrained solution. It is also necessary to point out that in the region of interest, the Faroe-Shetland trough, the gravity anomaly recorded is strongly influenced by the variation in crustal thickness (Richardson et al., 1998) and this long wavelength effect should be accounted for if comparisons are made between the gravity data from this study and real Bougier corrected data from the Faroes.

7.3 Seismic acquisition parameters

In order to adequately model the mid-offset reflections required for the demultiple processing steps used by our industrial partners it was decided for this study that the narrow-azimuth towed streamer (NATS) acquisition would be
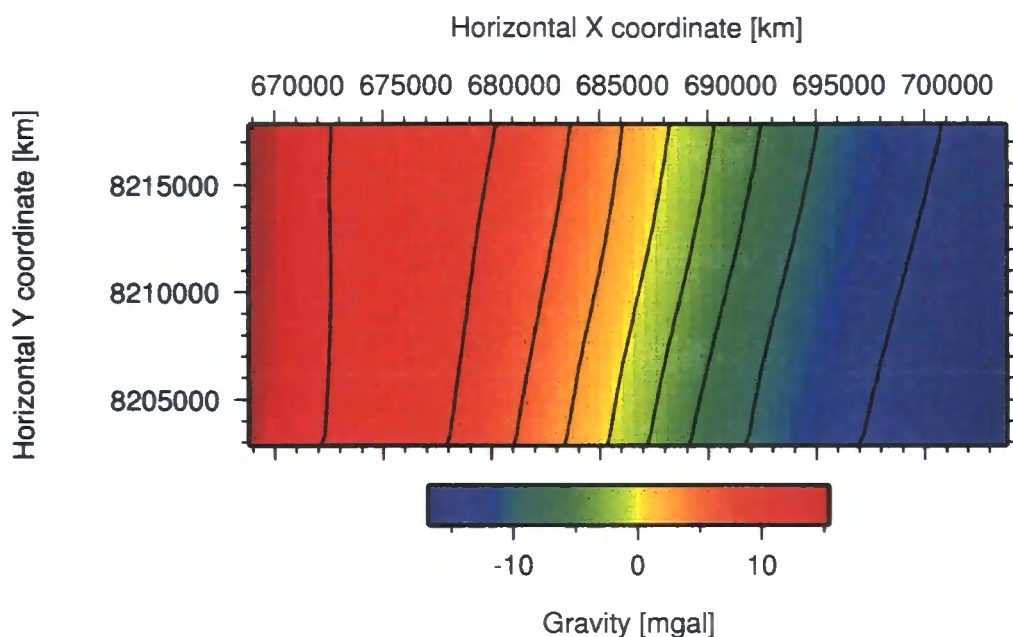
Figure 7.3: *3-D gravity response across the Hold-with-Hope model recorded at 69×29 stations evenly spaced acoss the surface*

run with six $7\ km$ streamers spaced at $100\ m$. Figure 7.4 shows a cartoon of the source and streamer geometry where within each of these streamer arrays the receiver spacing was $20\ m$ requiring 350 synthetic receivers to give a maximum offset of $6980\ m$. A shot spacing of $20\ m$ was interpolated from modelled shots fired every $80\ m$. All modelling was performed on a grid with $20\ m$ node spacing in both x and y and gave a sub-surface common reflection point spacing of $10\ m$ in x and $50\ m$ in y. The chosen acquisition parameters mean that individual swathes produce all the traces for each cdp position illuminated during the ship's traverse enabling swathe records to be considered separately as a complete data-set. Unfortunately no zero-offset data were derived during the Hold-with-Hope modelling, and more problematically none of the acquisition was performed with the source and receivers in a coincident 2-D plane. This proved to be a considerable problem since the trace spacing in the common shot domain was non-linear and required additional out of plane source positions to compute zero-offset shots required during processing. In order to cover the required subsurface aperture, 40 passes spaced at $300\ m$, were modelled with the first swathe at $y = 8204490$. The first of 301 shots was fired at $x = 677800$,
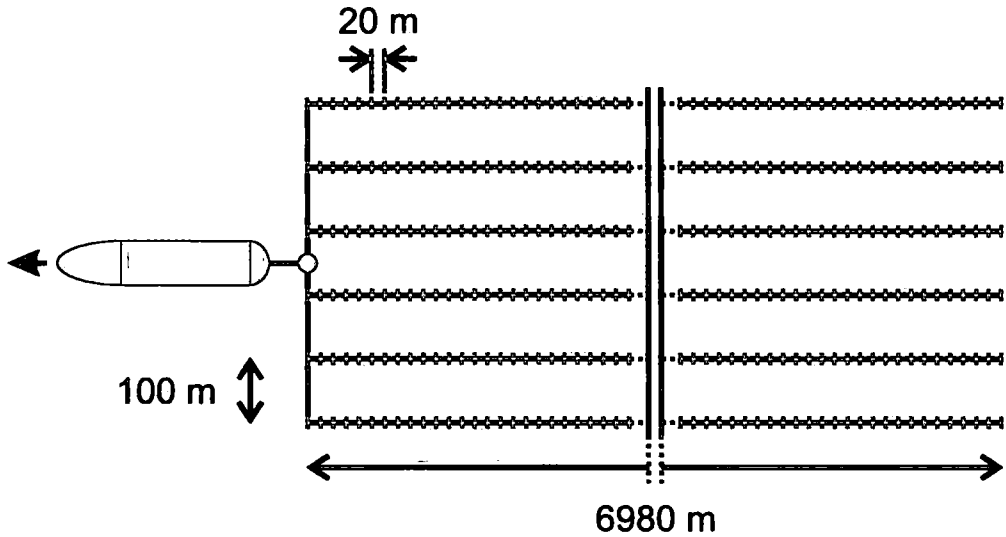
Figure 7.4: *Cartoon of the streamer geometry. The source position is shown by the pink circle and the green dashes correspond to the receiver positions. Receiver arrays are separated by 100 m laterally and the source moves 20 m between shots in the final interpolated record.*

resulting in an interpolated swathe record of 1201 shot gathers, with the final shot positioned at $x = 701800$. The final data-set contained 48040 shots resulting in over 1×10^8 trace records [1]. The computational requirements for creating this data-set are discussed in section 7.10.

Figure 7.5 shows, in blue, a plan view of the lateral extent of the model area. In grey the subsurface coverage is displayed whilst the ship's traverses, shown in red, respond to a westerly path. The remainder of this chapter focuses on presenting results from the shot swathe at $y = 8208690$ in order to provide a cohesive set of conclusions. The aim is to produce stacked sections with both the single and multiple pass data-sets and compare the clarity with the original model and with the exploding reflector simulation. These conclusions will point to the predicted success of imaging the sub-basalt structure within the Hold-with-Hope model.

7.4   Exploding reflector modelling: a stacked section

Exploding reflector modelling enables the generation of a complete subsurface response analagous to a fully processed stacked section derived from point source shot gathers. Calculating the reflection coefficients spatially throughout

---

[1] 40 swathes × 1201 shots × 6 arrays × 350 receivers = 10884000 traces
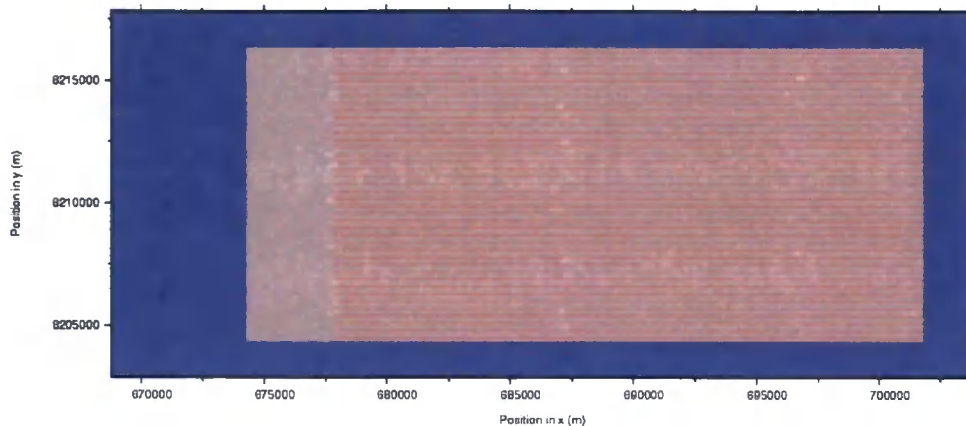
Figure 7.5: *Plan view of acquisition region in Hold-with Hope project. Blue zone - lateral model extent; grey zone - subsurface illumination aperture; and red lines - ship lines during acquisition*

the model then adopting a plane P-wave source and passing it through the model picking up the reflected energy allows an equivalent final stack to be created. This stack provides correct travel times and approximate near normal amplitudes whilst the attenuation of the wavefield is computed since the modelling is performed visco-elastically.

This study provides an exploding reflector 3-D stack across the entire model which is ideal for quality control of the processed sections as it offers an idea as to the best possible result achievable from the data. Figure 7.6 shows an unmigrated exploding reflector section down a single swathe at $y = 8208690$ where the primary interfaces have been labelled in relation to the interfaces described in table 6.1. The source wavelet has not been collapsed and maintains the same signature in order to enable estimates of the degeneration of the wavelet. The primary near-surface interfaces are clearly visible down to the top basalt, whilst the intra-basalt lobe structure can be observed since reverberations are absent. All the interfaces down to the top basalt show a positive impedance contrast, as expected from compaction, and are easily distinguishable in the primaries-only exploding reflector section. However, it is apparent from the section that the first sea-bed multiple will arrive coincident to the top Breydon sands reflection. The sub-basalt reflectors are visibly lower-frequency than those from the near-surface but the general sub-basalt structure can be concluded. As expected the high acoustic impedance contrasts at the sills are the most noticable sub-
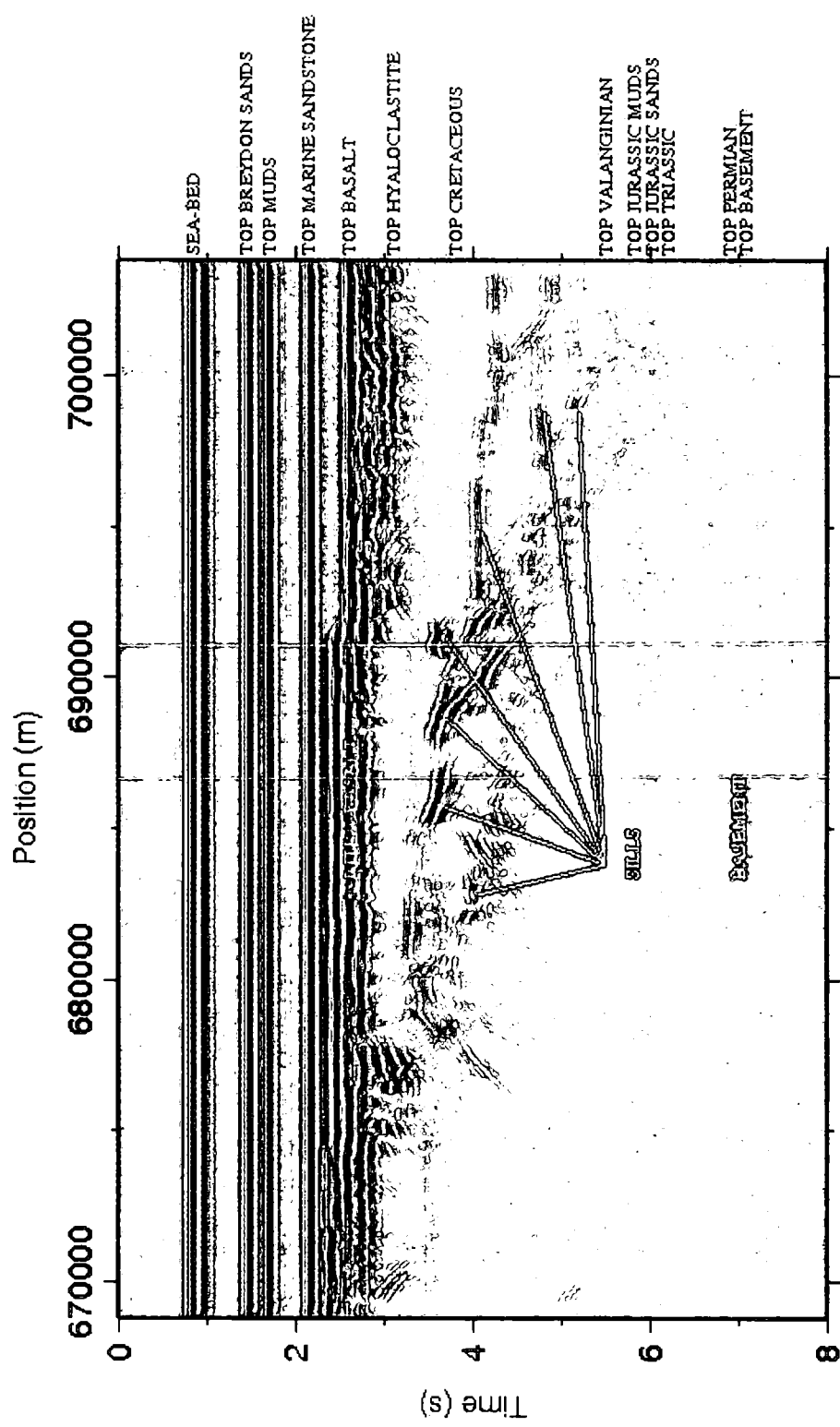
Figure 7.6: *Exploding reflector profile through Hold-with-Hope model at* $y = 8208690$. *The labels (in blue) are positioned just above the interface to which they relate. The red labels describe a package of reflectors and are overly the section to which they refer.*

basalt reflections and in some regions overlay the expected response of the sedimentary structure. Migrating the exploding reflector stack would result in a perfectly optimised section where the numerous diffraction tails seen in the plot would be collapsed back to the position of origin. However, the lithological interfaces have sufficient correlation to be interpretable, enabling specific targets to be pin-pointed, and any migration will be left for the processed shot gathers. The aim whilst processing the point source data is to achieve a stack comparable in clarity to figure 7.6. Yet, since this plot is derived from a single pass through the data the effects of multiple energy on the wavefield will be absent enabling the imaging to be focused without sea-surface or peg-leg interference.

7.5   VSP through the Hold-with-Hope model

Generation of VSP data during a period of commercial acquisition is common in regions where borehole data has previously been drilled. The phase-screen technique allows VSPs to be constructed at an arbitary point within the model and can even create non vertical profiles if desired. This study aims to produce several VSPs for the industrial partners at key areas across the modelled region. A synthetic VSP is modelled at $x = 691700$ across the stacked section shown in figure 7.6 in order to provide a tie-in betwen the different modelling methods. The modelling uses the same source wavelet as the reflection modelling and for simpliciaty the borehole is assumed vertical. The modelling is initially performed with multiples excluded, then three reverberations of multiple are added and the recorded datasets are shown in figure 7.7 (a) and (b) respectively. Specific reflection events can be seen in the plots and the scattering effect of the basalt is noticeable.

It is difficult to draw significant conclusions from the VSP except to say that the down-going primary energy still has significant amplitude when it arrives at the sub-basalt interfaces, and generates measurable reflections at depth. The response within the basalt shows considerable internal reverberations but with a rapid drop off in amplitude. If a borehole was available, then exact local velocities would be determinable and could be used as a ground truth for the reflection seismic studies.
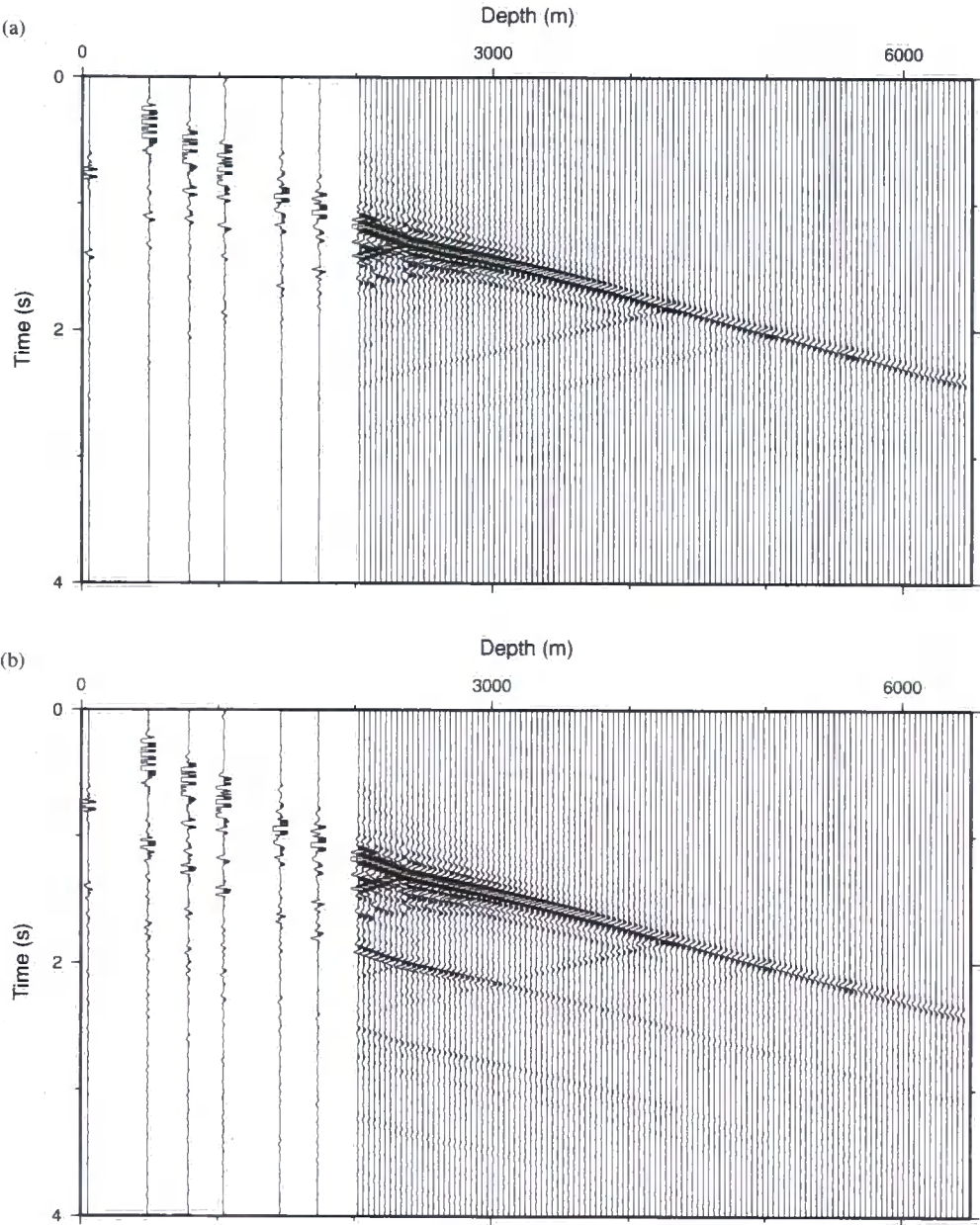
Figure 7.7: *VSP profile through Hold-with-Hope model at* $x = 691700$, $y = 8208690$

7.6 Modelled shots

Figure 7.8 shows a modelled (a) primary only and (b) multiple pass shot from $x = 696300$, $y = 8208690$ to a receiver array with perpendicular offset of 250 m. In both of these shot gathers significant unwanted wraparound energy is highlighted. Extending the 2-D scheme postulated in section 6.11.5 the 3-D shots are originally modelled with a wide (up to 89°) source aperture. These uncorrected gathers contain coherent undesirable energy at both near and far offsets generated as a consequence of the tight lateral modelling extent and also because of the energy emitted from the source.

Figure 7.9 (a) shows the calculated near surface 3-D correction from the top 29 screens (down to top basalt) for the multiple pass dataset, and can be seen to contain high amplitude artificial arrivals since all the plots are clipped at the same amplitude. Figure 7.9 (b) shows the corrected shot prior to interpolation. This method requires a correction at each receiver array for each modelled shot and has necessitated the allocation of a significant amount of run-time. In most projects the reduction in the aperture of the source energy would have been sufficient but this would have limited the extent of F-K space populated by the modelled data and this proved to be a significant issue for the industrial partners meaning this novel approach to removing the near surface wraparound was employed.

A better way to view this problem in 3-D is to repeat the modelling with cross-cutting orthogonal receiver arrays. Figure 7.10 (a) shows the extent of the modelled zone in y with the edge mutes altered slightly to allow additional wraparound energy. These wraparound tails are clearly visible and since the near surface is comprised from a series of flat beds this interference will appear at identical times across the shot gathers with a move-out dependent on both the size of the active model and the velocity of the near surface. Figure 7.10 (b) shows the same shot modelled with the increased active model size and even without optimised edge muting the difference in the wraparound is obvious. The red lines show the position of a receiver swathe from the Hold-with-Hope modelling project and the regions where the unwanted energy occurs can easily be correlated between figures 7.8 (b) and 7.10 (b). Viewing the problem from this additional perspective it becomes clear that the artefacts are primarily a 3-
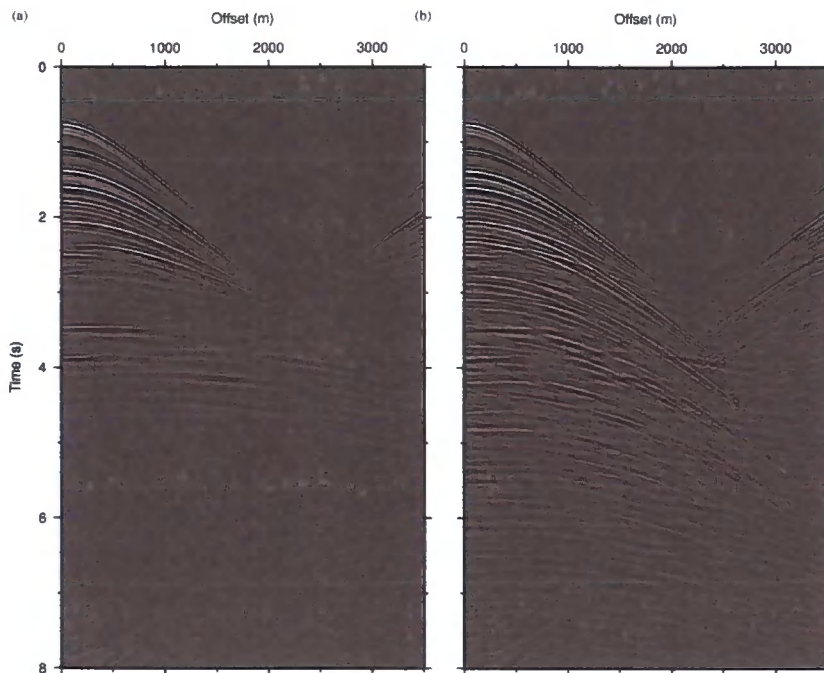
Figure 7.8: *Uncorrected (a) primary only and (b) multiple pass modelled shots from $x = 696300$, $y = 8208690$ within the 3-D Hold-with-Hope volume to an array with 250 m perpendicular offset.*

D issue yet their removal is achieved by the addition of this simple processing procedure.

After the original shot gathers have been modified, the next task is to interpolate the data-set up to its final source spacing. F-X interpolation is performed twice first creating a shot record spaced every $40\ m$ and then filling in the missing shots either side of new data and creating the desired $20\ m$ spacing. Figure 7.11 shows the single pass data where corrected modelled shots are displayed in (a) and (e). The first pass of the interpolation generates the shot gather shown in (c), then the subsequent interpolation produces the shots (b) and (d). There is no noticable degeneration of the wavefield as a consequence of the interpolation and the F-K plots, shown in (f) – (j), reveal that the spectral character of the data is consistent in the modelled and interpolated data.

The same interpolation flow is used for the multiple pass data and an equivalent set of plots is shown in figure 7.12. The conclusions for this data echo those from the primary only data with the limiting gradient in F-K space
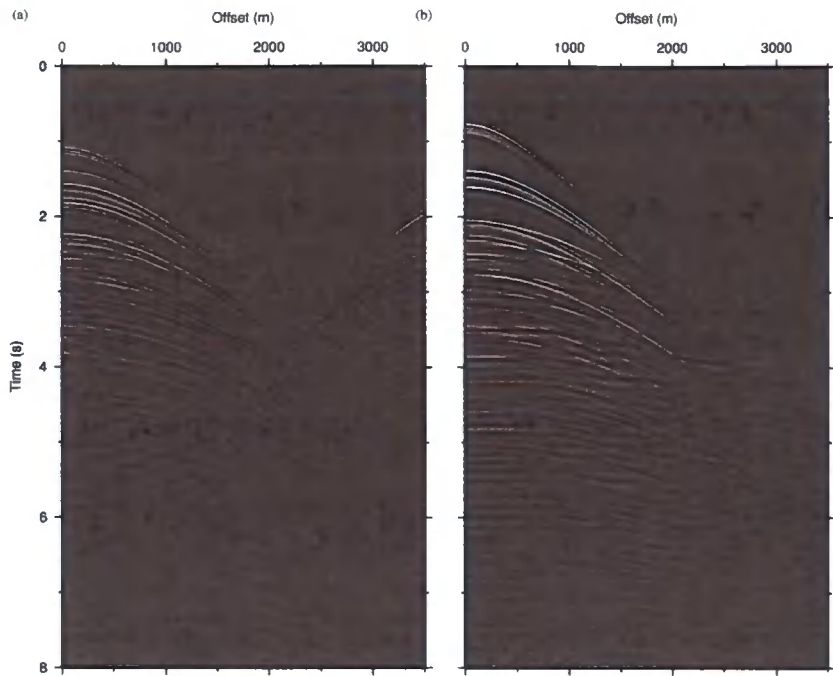
Figure 7.9: *(a) Correction for multiple pass modelled shot and (b) the corrected shot ready for interpolation.*
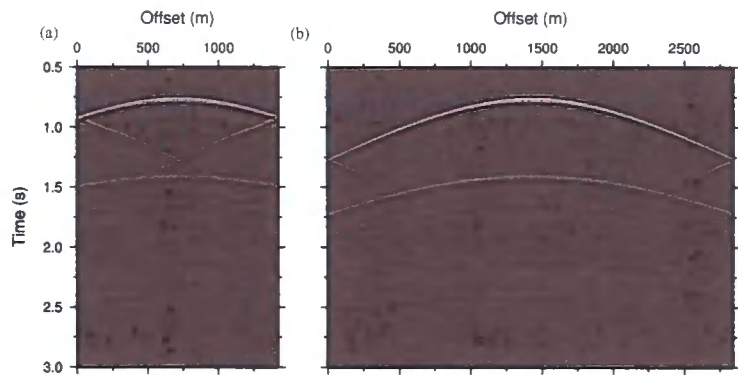
Figure 7.10: *Orthogonal cross cutting receiver arrays for modelled shots from 3-D Hold-with-Hope volume clearly demonstrating the wrap-around issues from the narrow aperture of the model space.*

accounting for the water velocity of $1480 \ ms^{-1}$. Since the data did not contain any frequency specific noise, and noting the fact that the interpolation runs better with a wider spectrum, it was deemed unnecessary to bandpass filter
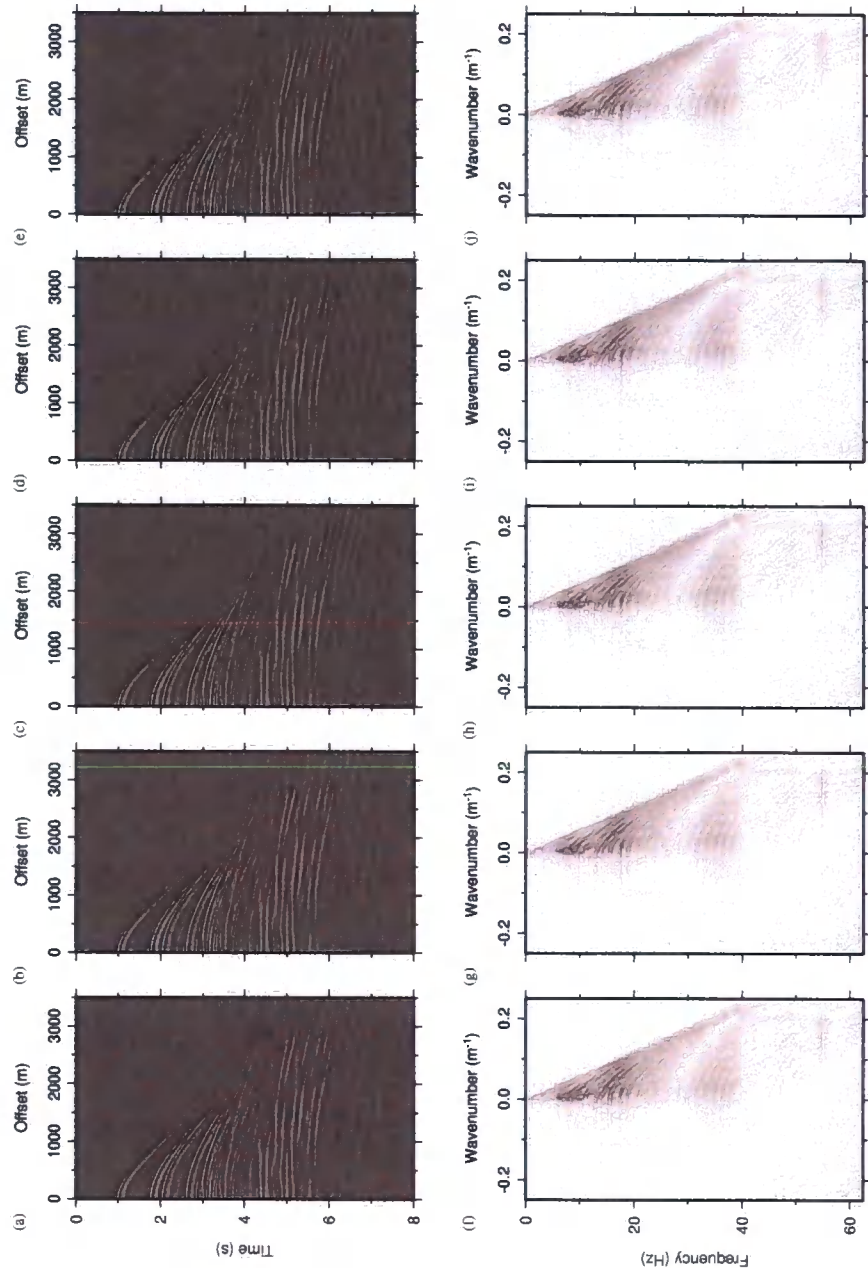
Figure 7.11: *Interpolated primary only shots from 3-D Hold-with-Hope volume where shots (a) and (e) are from $x = 696300$, $y = 8208690$ m and $x = 696380$, $y = 8208690$ m respectively. The receiver array is perpendicularly offset by 250 m and (b), (c) and (d) are the interpolated shots that reduce the final shot spacing to 20 m. (f) – (j) show the respective F-K plots for the shot gathers and can be seen to contain a common frequency content.*
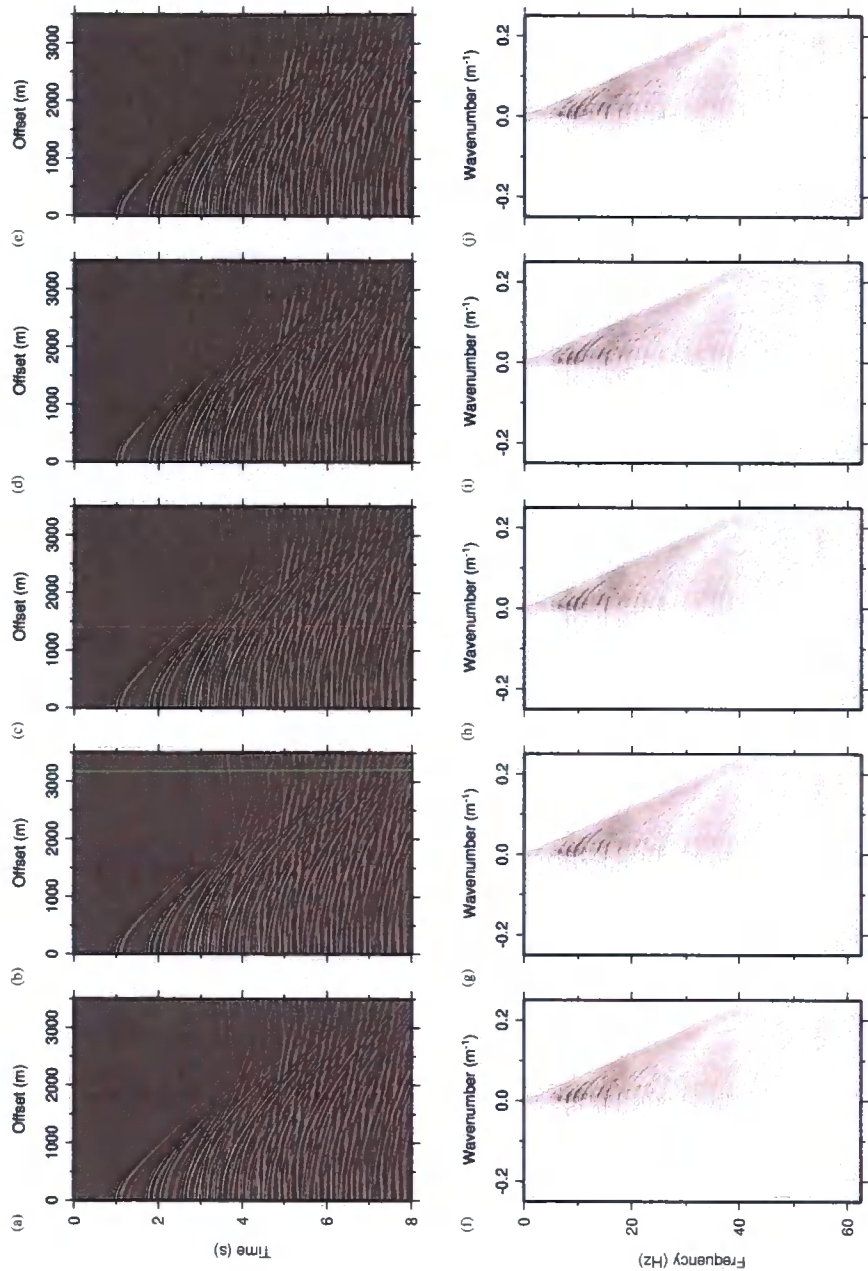
Figure 7.12: *Interpolated multiple pass shots from 3-D Hold-with-Hope volume where shots (a) and (e) are from* $x = 696300$, $y = 8208690$ m *and* $x = 696380$, $y = 8208690$ m *respectively. The receiver array is perpendicularly offset by* 250 m *and (b), (c) and (d) are the interpolated shots that reduce the final shot spacing to* 20 m. *(f) – (j) show the respective F-K plots for the shot gathers and can be seen to contain a common frequency content.*

the data prior to processing. A source deconvolution was attempted in order to remove the bubble pulse, but this study found that the artefacts introduced by this procedure produced a larger amplitude than the bubble. Therefore source deconvolution was not included in the processing flow.

7.7 Velocity picking when the answer is already known

In real industrial acquisition, away from well-constrained borehole locations the velocity function with depth, and therefore time, of the subsurface is rarely known. As such, this study intends to initially treat the Hold-with-Hope data as if it were unconstrained, aiming to pick the stacking velocity functions from semblence plots. Figure 7.13 show semblence analysis for a cdp supergather at x=691500 for the single pass data (left plot) and the multiple pass data (right plot). Since the data is virtually noise free the semblence 'bullseyes' are easy to distinguish and picking a stacking velocity function for the primary data is relatively straight-forward. The white lines display the picked stacking velocities as a function of time.

The high amplitude, high velocity semblence peaks in the near surface are rightly ignored since the cdp stack reveals the application of an agc operator has blown up any remaining wraparound energy giving erroneous slopes that do not correspond to lithology.

The sub-surface velocity structure of the near surface is reasonably easy to determine from the multiple pass data. However, closer inspection reveals that beneath the top basalt, at 2.2 s, the semblence plot is dominated by the effects of the multiple reverberations and little correlation between the semblence maxima and the structure of the Hold-with-Hope volume can be inferred.

The modelling in the Hold-with-Hope project is undertaken from a grid of rock identifiers that point to a table of elastic parameters where the P- and S-wave velocity and the density are stored. Therefore the interval velocity structure as a function of depth is known and application of Dix's equation allows calculation of the RMS stacking velocity structure as a function of time. To ascertain the accuracy of the picked velocity profile, figure 7.13 includes
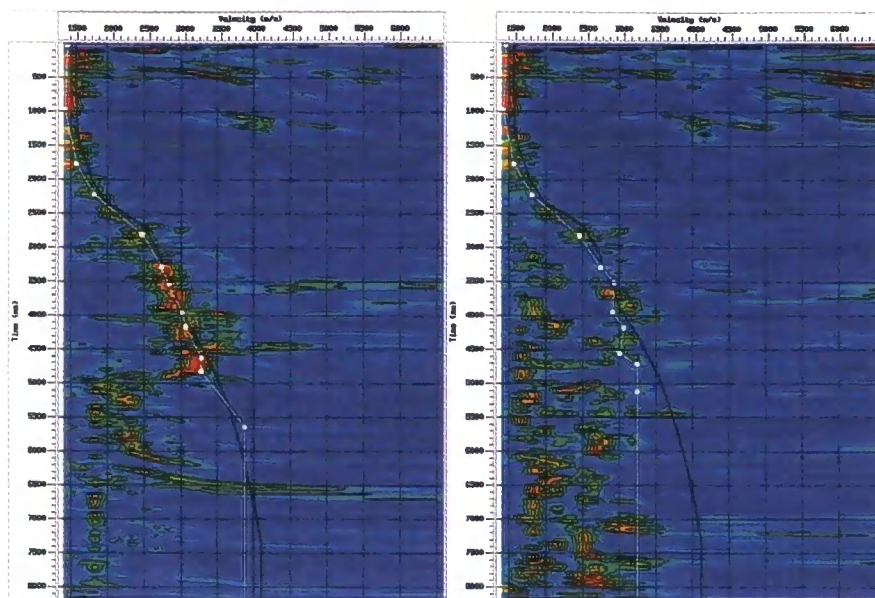
Figure 7.13: *Semblence analysis from primary and multiple pass cdp gathers from the Hold-with-Hope model showing the picked (white) and exact (black) stacking velocity functions.*

the expected velocity profiles (in black) from the Hold-with-Hope model. The overall trend in the velocity profiles reveal a strong correlation, with the true velocity function cross-cutting all the semblence highs.

7.8   Initial stacks

Only simple processing steps have been included in the creation of the stacked data since processing is the job of our industrial sponsors. However due to the lack of random noise in the gathers, the data is unrealistically clear.

Due to the fact that there is no zero offset data (or data from a coincident source-receiver plane) the application of wave equation surface related multiple elimination (SRME) is not possible with the available software as it only has 2-D compatibility. Application of radon transforms to remove multiple energy also proved futile due to the lack of variation in velocity and thickness between the water layer and the top sedimentary unit. As such, the multiple suppression was produced by a near trace mute that, when applied with a well chosen velocity profile, results in the larger offset multiple energy stacking incoherently.

Figures 7.14 and 7.15 show the stacked primary and multiple datasets for a line with subsurface reflection point at $y = 8208595\ m$. The primary only data reveals that the amplitude of reflections from the sub-basalt structure allows imaging if the multiple energy can be significantly reduced. The reflections from the near surface are unsurprisingly coherent in both plots and even some intra-basalt structure can be determined. The multiple data more accurately replicates the expected response of real sub-basalt data with a loss of resolution beneath the basalt for all structure except the sills. The record is dominated by reverberated energy which seems to oscillate in the region between the sea-surface and the base of the basalt.

7.9   Migrated sections

Figure 7.16 shows the Hold-with-Hope velocity model as a function of two-way travel time and position, similar to the stacked synthetic data generated in this chapter. In order to accurately replicate this figure the data necessitates a post-stack migration in order to correctly position the backscattered energy at it's reflection point. Since this study boasts an accurate velocity model a Kirchoff time migration is a suitable method for generating the final stacked section. Surfaces are picked from figure 7.16 in order to enable quantitative comparisons with the data generated from the phase-screen modelling.

The migration algorithm is performed on both the primary only and multiple pass stacked data and since the exact velocity model is utilised the coherence of sub-basalt interfaces should be optimised. Figures 7.17 and 7.18 show the migrated sections with the picked interfaces from the Hold-with-Hope model draped over them. Concentrating initially on the primary only migrated section the conclusions echo those from the unmigrated image displayed in figure 7.14. The supra-basalt reflectors are accurately mapped, the top and base of the basalt can be determined and the sub-basalt structure is dominated by the sill reflections. However coherent structure is visible in the sub-basalt region and realistically replicates the input model. Therefore, it can be concluded that the sub-basalt structure can be accurately imaged if the primary only wavefield can be isolated from the multiple and randomly scattered energy.
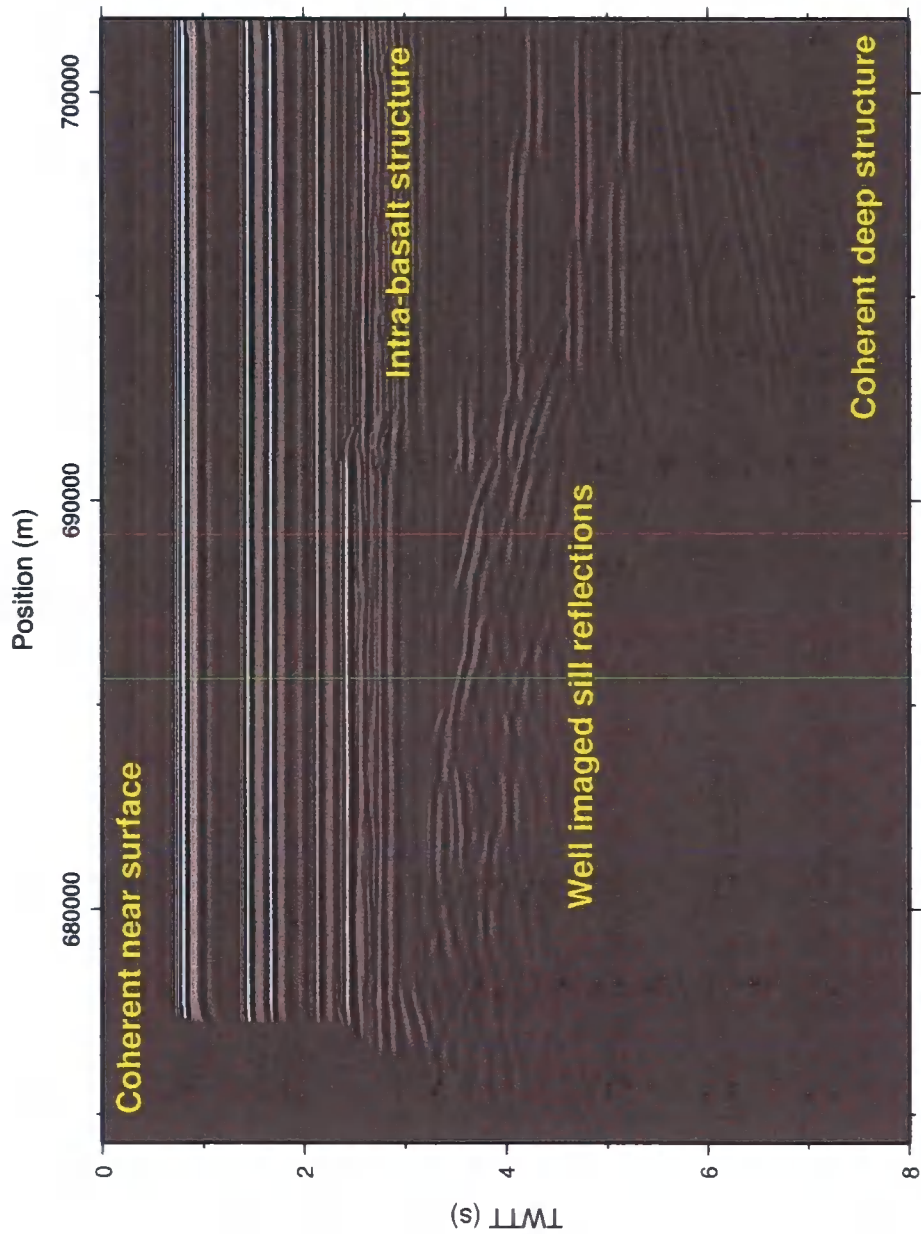
Figure 7.14: *Primary only stack for reflection points along a line at $y = 8208595$ m revealing a significant sub-basalt structure when data is derived without reverberated energy.*
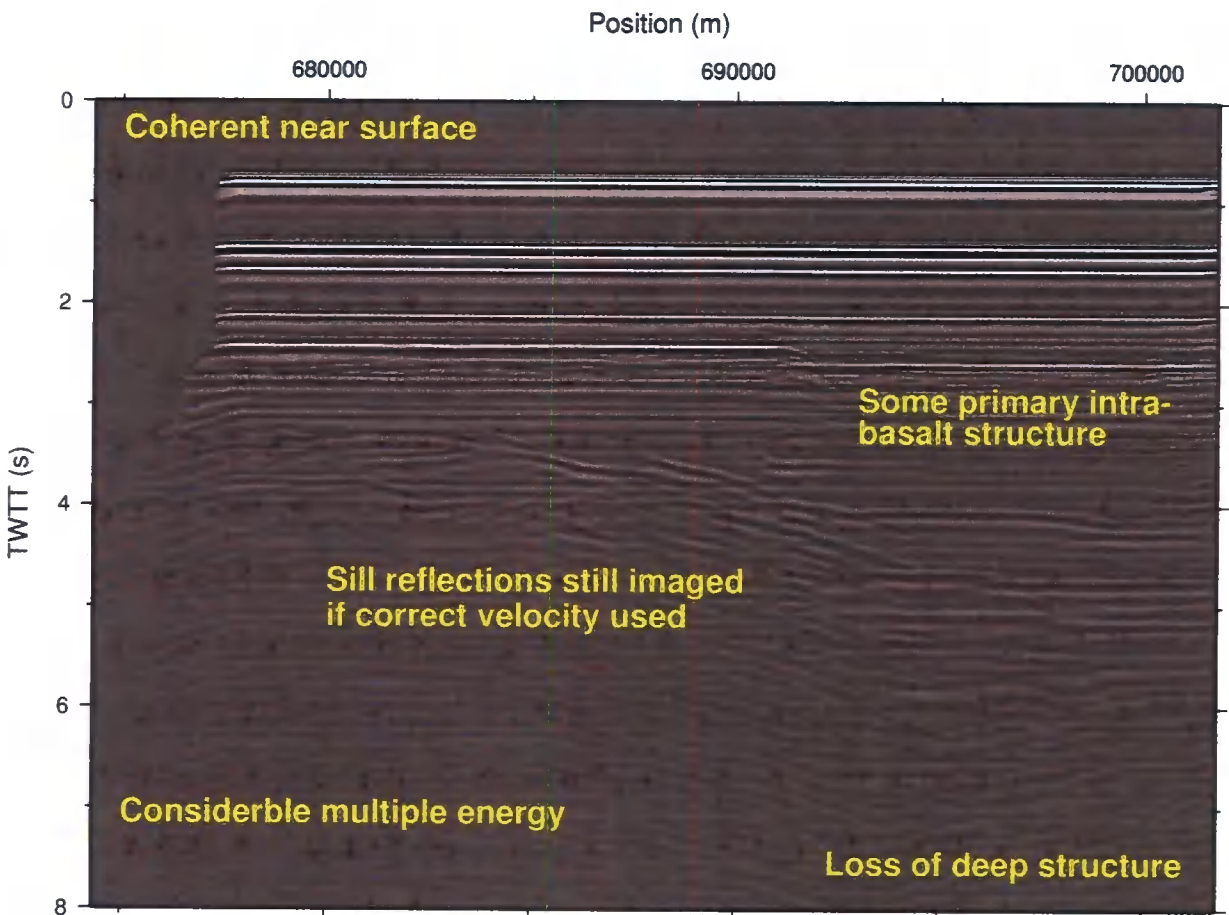
Figure 7.15: *Final stack for reflection points along a line at y = 8208595 m revealing a loss of resolution in the sub-basalt component of the wavefield for all reflections except those due to the sills structure.*
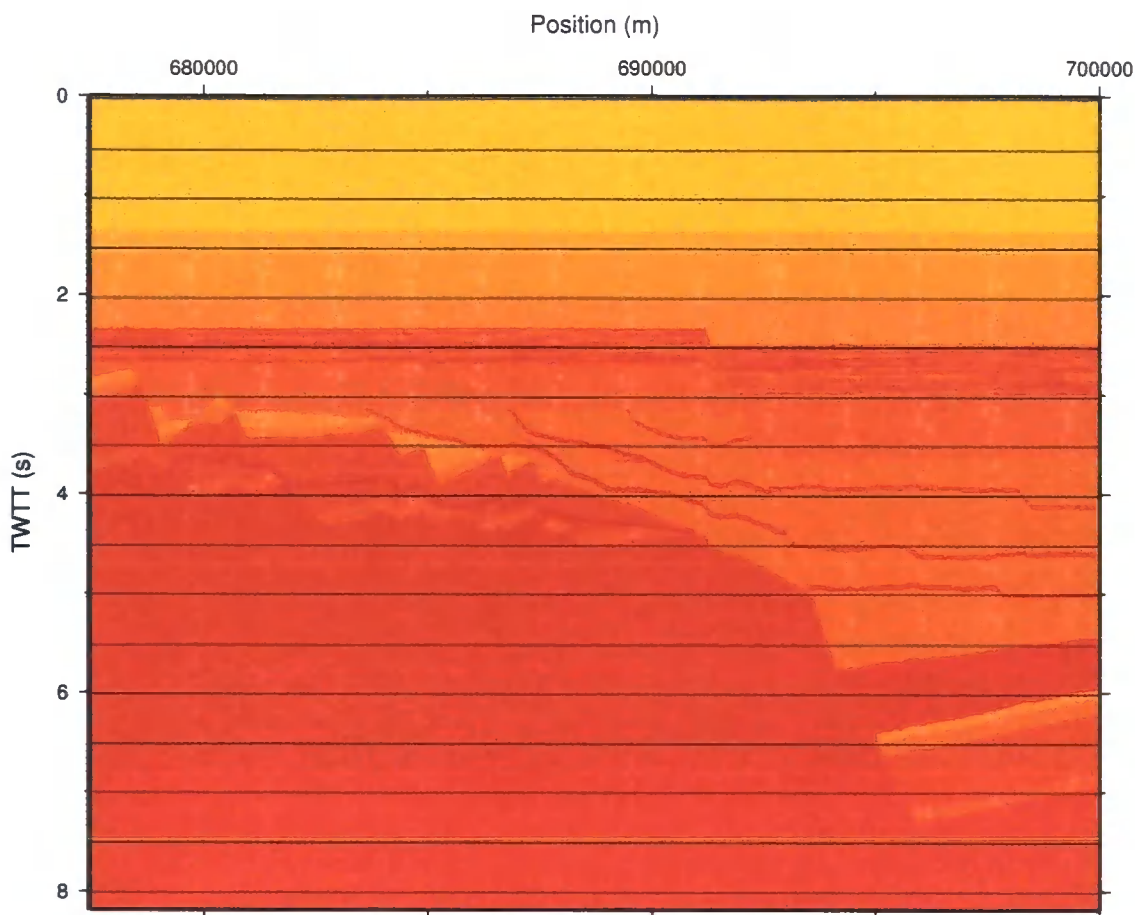
Figure 7.16: *Original Hold-with-Hope velocity model as a function of two-way travel time at* $y = 8208590\ m$

Referring now to figure 7.18, the final migrated stacked section for the multiple pass data after a simple processing flow. Once again the near surface is well constrained and the intra-basalt structure can be inferred down to the base of the basalt. Beneath this the top surface of the Late Cretaceous deep marine mudstones is pickable, but is probably unrealistically flat within the Hold-with-Hope volume. Within this mudstone unit, and the deeper Jurassic mudstone, the intruded sill structure is still the most obvious high amplitude component of the wavefield and displays remarkable continuity in the section. Other than the sills there is some coherent energy but this relates to poorly processed multiple data and not to real sub-basalt structure. It is especially important to draw attention to the sedimentary interfaces in the hanging wall of the Fosdalen fault that were illuminated in the primary only data but are
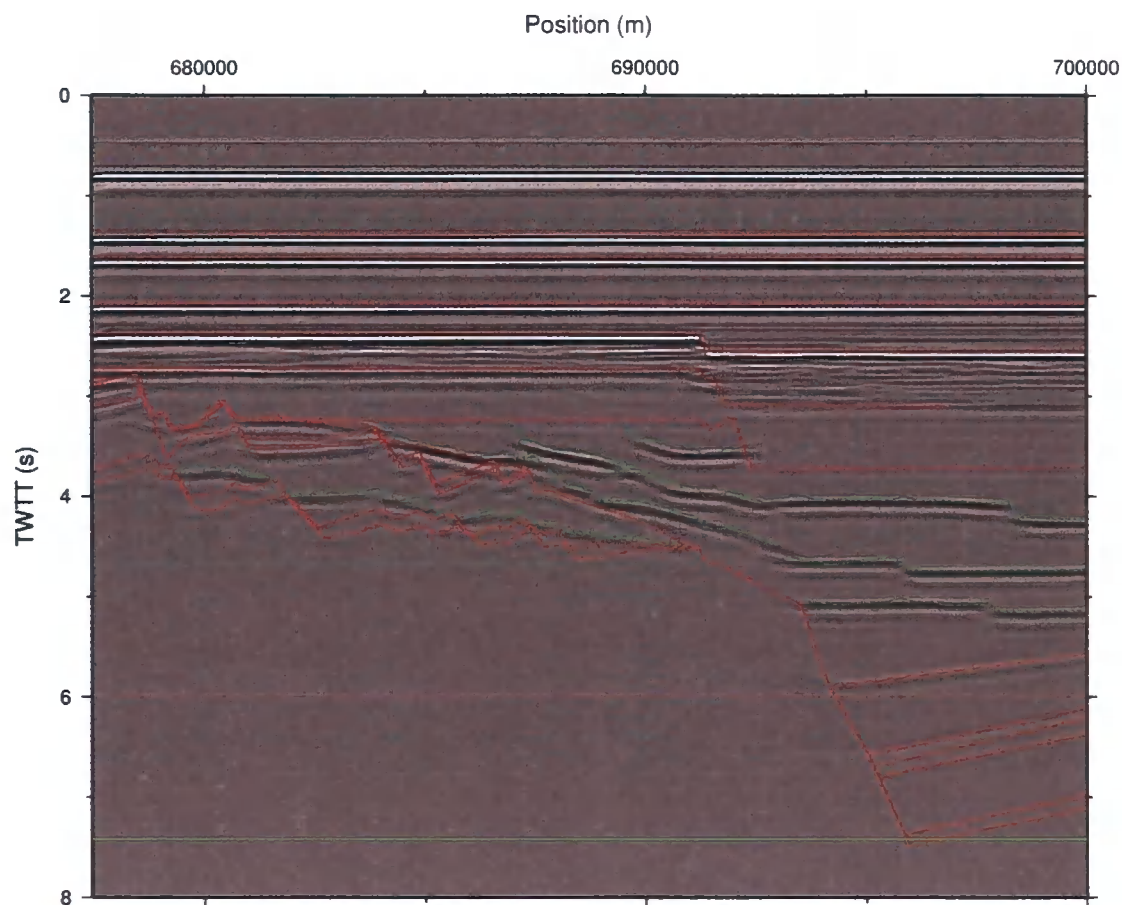
Figure 7.17: *Hold-with-hope primary only migrated stack with original modelled structure overlain.*

obscured within this more realistic stack. In conclusion, the results appear to match those from real seismic acquisition projects targeting sub-basalt structure.

Figure 7.19 shows a geological map from the Mols Bjege region of eastern Greenland. The mapping concentrates on defining the extent of Tertiary basalt and dolerite sills and dykes, the overriding inference is that the sills are formed within the weaker mudstone units. This study has shown that the mapping of sills within the sub-basalt region is an achievable objective with reflection seismics and as such can be used to infer the gross structure of the region. Assuming that continuous, high amplitude sub-basalt reflections are generated
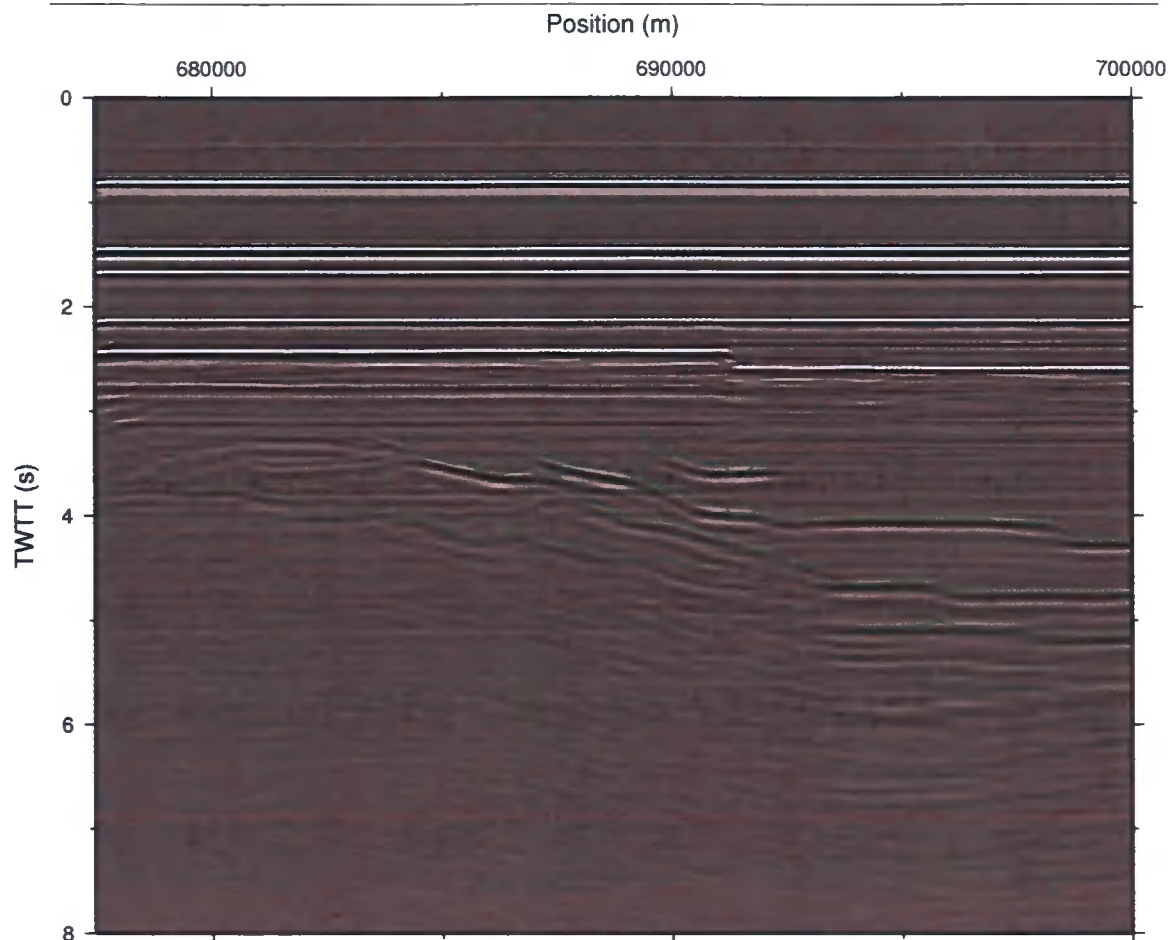
Figure 7.18: *Hold-with-Hope multiple pass migrated stack with original modelled sill structure overlain.*

at the interface betweeen the sedimentary succession and a sill, the surronding region can be reasonably labelled as a mudstone. Since the sills will invariably stay within the mudstone units they can be used to deduce the local structure and can allow the targeting of potential sandstone units where sills are absent. Allied with the gross basement structure derived from gravity modelling, and allowing for some possible coherent wavefield reflected from interfaces within the sedimentary basin the generation of a reasonably accurate gross structural map is achievable. This in turn will point to the preferred location for additional investigation, usually in the form of borehole exploration.
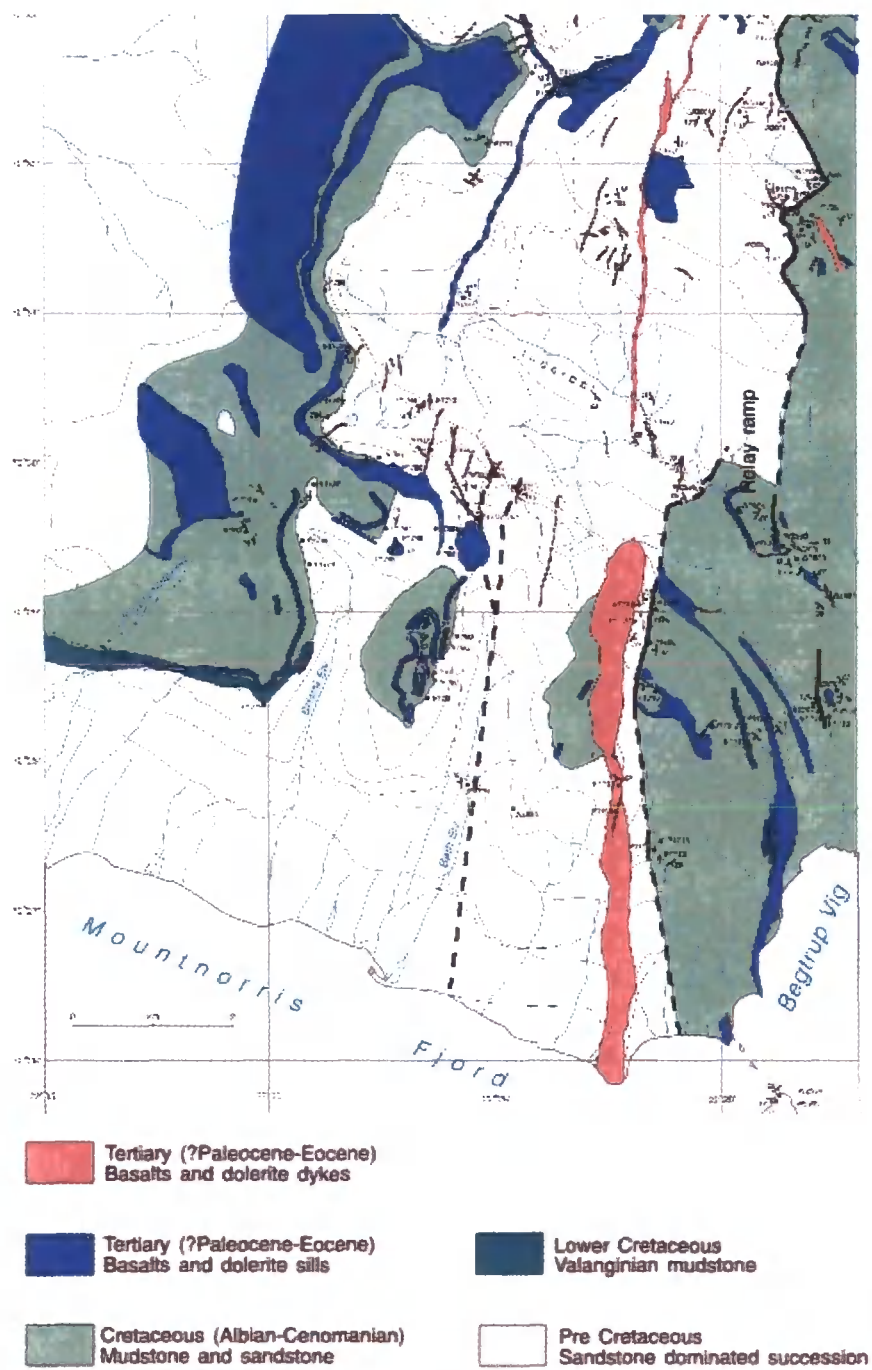
Figure 7.19: *Geological map from Mols Bjerge region of Greenland. The sills can be seen to preferentially form in the Cretaceous mudstone succession, whilst the dykes are preferentially accomodated in the Triassic-Jurassic sandstones giving an indicator as to gross structure (after Price and Whitham, 1993).*

7.10   Computational requirements

The computing for this study was performed on the 135 node Hamilton-1 cluster at Durham University. Utilising up to 35 nodes, each with dual core 2.0 GHz Opteron processors and 4Gb of memory connected by a gigibit network, the swathes were calculated in batch jobs of 10 shots per processor. 30 batch jobs were required to run the entire 301 shot swathe in an average of 6.2 days. The complete Hold-with-Hope 3-D project requires 40 swathes and, allowing for down time and cluster unavailability, 45 weeks were set aside to complete the entire modelling project.

The FFT transform times were the limiting factor in the speed of the computing and for non power of two, well chosen transforms it was expected that a speed approaching ~1500 mflops would be achievable. However since the FFT transforms get larger than the on-chip cache the speed is limited by the memory bus as data must be stored in the main memory.

7.11   Discussion

This section has demonstrated that the generation of large synthetic seismic datasets is a realistic objective for academic institutions. Making use of in-house computing clusters it is possible to produce realistic synthetic data replicating complete acquisition surveys. The seismic data produced in this study has spectral characteristics that match those seen in marine sub-basalt data and the illumination generated is comparable with the real world.

Utilising the narrow angle phase-screen code with an innovative method for removing 3-D wraparound energy a sparsely sampled shot record was generated. Application of a f-x interpolation technique resulted in a shot spacing of 20 m. This study has clearly demonstrated that the data enables accurate velocity analysis down to top basalt but offers a less clear picture beneath this event. However, with simple processing, stacking and migration the intra- and sub-basalt structure can be imaged if the effects of scattering and internal reverberations can be quantified. The migrated final sections have a clarity consistant with the best efforts produced in equivalent deep marine

environments and are suitable for testing the sub-basalt processing algoritms used in the hydrocarbon industry.

This study has also demonstrated that even with synthetic data the contribution from different geophysical datasets is the key to unlocking the mysteries of sub-basalt structure. It has been shown that integrating the effects of numerous small scale density cubes can produce realistic gravity profiles that enable gross structural conclusions to be made about the positioning of the basement. If this data is used in conjunction with conclusions made from the seismic interpretation the major structural trends of the region can be determined.

Chapter 8

Conclusions and further work

8.1 Conclusions

During this thesis the generation of a robust visco-elastic phase-screen code in c++ has been described. The code displays a high level of portability due to its class structure and is based upon the geometrical construction derivation of Wild and Hudson (1998). Following this, the development of the method to include accurate modelling of the propagating wavefield with an aperture up to the critical angle (White and Hobbs, 2007) has been put forward. The removal of the narrow-angle approximation, by splitting the incoming wavefield in the wavenumber domain, has enabled:

1. the partitioning of energy as a function of angle;

2. the capacity to make 3D phase-corrections for the difference between the local and average velocities within a screen.

These additional steps have allowed non-normal raypaths to be modelled accurately. During any development the underlying principles of the phase-screen technique have been adhered to and a rigorous testing procedure has ensured the validity of the enhanced method.

Chapters 4 and 5 demonstrated that the phase-screen method, based upon the geometrical construction, can be used for modelling in anisotropic environments similar to those found in marine sedimentary basins. By recasting anisotropic phase velocities into functions suitable for application within the phase-screen environment, and determining anisotropic energy partitioning solutions, the enhanced phase-screen method modelled the response of a VTI

media. The main challenges associated with this development are encountered when a single screen contains a mixture of both isotropic and anisotropic rock-types (or rocks with a significant range of anisotropy). In these environments the phase-shift propagation must be calculated at intermediate values of δ and ϵ which would produce measurable errors.

A possible solution to this problem is the replacement of the Fourier transforms with wavelet transforms. Here the spatial extent of the data could be altered on a screen-by-screen basis allowing a significant control on lateral variation within the input model.

These developments enable the realistic modelling of real earth subsurfaces which ultimately has benefits for both forward modelling and migration. The code has been tested against a series of problems commonly encountered during seismic acquisition. It has been shown that the code can correctly generate offset dependent source and receiver ghosts, can model in visco-elastic environments, can accurately replicate VSP data and can generate exploding reflector stacks. The enhanced phase-screen method has been tested against seismic gathers generated with the reflectivity method, the ray tracing technique and the acoustic and elastic finite difference modelling schemes with success. The code has also been tested against hydrocarbon traps in the Marmousi2 model to confirm that the AVO signature is successfully replicated. Additionally, the code has been verified in simple anisotropic models against previously published data and has been used to provide an estimate of the errors associated with ignoring anisotropy in sedimentary basins.

The methods described in this thesis may be applicable to other orientations of anisotropy. If the angular and azimuthal variations in velocity can be expressed as a function of horizontal wavenumber and the P-SV waves form a coupled system, then development of a specific phase-screen code is possible. For horizontally transverse isotropic media the challenge would be to calculate and store the multitude of reflection and transmission coefficients, whilst modelling would only be truly accurate in the symmetry planes. Additionally, it can be noted that since only the SV component of the wavefield is accurately modelled during phase-screen forward modelling the development of an exclusive SH-wave propagation system would be trivial.

It is important to point out that the phase-screen technique, even in its enhanced format is still an approximate method based upon a plane wave, planer interface construction that attempts to accurately replicate the solutions generated by exact numerical techniques. The steps neccessary to produce angle dependent solutions are responsible for significant redundancy and there is a genuine need to assess the number of nodes within a model in order to optimise the computational run times.

The phase-screen method is also a suitable tool for modelling in alternative environments. It has been successfully used to model sonar propagation since the lack of numerical dispersion enables the propagation of very high frequencies. Additionally, the author has used the acoustic version of the code to generate synthetic seismic oceanography shot gathers. The 1-D models are produced from temperature and salinity logs derived from XBT data and can be instantly used to generate quality control profiles to compare with the true seismic records. This application is a growing area of interest as it records the movement and change of ocean current patterns that can be used to feed climate change models.

The second half of the project has focused on building and then utilising a sizable elastic 3-D subsurface model to ascertain the feasibility of improving imaging under extrusive basalts. This aspect of the work required undertaking a large scale model building project. This demonstrated how by combining highly detailed mapping projects from well chosen locations, with careful analysis of well-log data and a knowledge of the expected compaction trends in sedimentary basins it was possible to build a complex model from lithological surfaces that accurately imitated current areas of hydrocarbon exploration. Allied to this was the creation of a realistic random basalt, generated with control on the correlation length of individual flows in all three orthogonal directions, similar to the techniques used to generate mantle models. This scheme created statistically accurate basalts which replicated both the velocity variation and the layered flow structure seen within plateau basalts. A novel approach for modelling attenuation within thinly layered media has been postulated. This method was justified for volumes where the sampling is on a scale that necessitates the construction of an equivalent media philosophy.

The phase-screen technique was then used to generate an adroit method for removing the near surface wrap-around energy generated as a consequence of the Fourier modelling method, the limited size of the model grid, and the aperture of the source. This scheme utilises the lateral continuity of the near surface interfaces and by performing additional modelling a wrap-around correction can be determined that results in significantly improved shot gathers. Following this a large scale interpolation project on synthetic data was performed. By interpolating in the common offset domain the entire shot record was used in the interpolation giving a maximum possible aperture whilst avoiding the increased trace separation of the ordinarily used common midpoint domain.

Processing of the data resulted in an unrealistically good solution since random noise is absent from the traces but the conclusions drawn from the modelling are equally applicable to real data. The primary only response revealed that the sub-basalt region was sufficiently illuminated by the wavefield to accurately image the structure. However, once the multiple energy was included the scattering nature of the basalt obscures this stucture and reveals only the presence of intruded sills beneath the basalt. Since the aim for the hydrocarbon industry is still to image the gross structure of the sub-surface in regions comparable to the synthetic Hold-with-Hope volume this mapped sill structure can be used to infer the lithology of the region. Since the sills are almost exclusively encountered in mudstones, a lack of sills in a region of overlying basalt can infer a sandstone unit with hydrocarbon potential. It is these insights that can drive the targeting of boreholes, especially when allied with the general regional structure derived from gravity surveying and any additional geophysical techniques (MT, EM and magnetics) that can better constrain the solution. In conclusion, the best appraoch for generating a sub-basalt structural model is to approach the problem from as many angles as available.

8.2 Further work

Satisfactory steps have been made in the development and application of the phase-screen technique during this study, however, areas for additional development remain:

1. In the unpublished work of Andriatsitohaina (2004) the possibility of using the phase-screen method to model post-critical energy was discussed. In theory, this application is possible, since the determination of complex phase shifts and postcritical energy partitioning equations is trivial. However, the reintroduction of the evanescent energy would only occur in models with a low velocity unit and the storage of this energy as it decays away would put a significant drain on the available memory.

2. The phase-screen method treats all interfaces as if they were planer and occur coincident with a local screen. In order to generate some variability in the position of the interface, and remove the smoothness from the reflected wavefield it would be possible to apply the random phase-shift scheme used in the thin layers Q filter to approximate the rugose nature of subsurface interfaces. Assuming these random phase fluctuations were small, the angular component of the wavefield would still be correct.

3. VTI media have been successfully imaged using the phase-screen method, but application within other anisotropic orientations would be beneficial. Since the phase-screen requires a coupled P-SV system to accuratly model amplitudes it can only generate complete solutions in symmetry planes. Yet, handling travel times in HTI media would be possible by considering the grid orientation with respect to the anisotropy and skewing the grid to replicate the velocity variation of HTI media.

4. The Hold-with-Hope project has demonstrated that the boundary conditions used in the 3-D enhanced phase-screen code require further work. A revised muting system at the edges of the x- and k-space would greatly improve the efficiency of the modelling.

5. It has been demonstrated that the phase-screen code can be used to optimise the acquisition and processing of hydrocarbon exploration (through the Hold-with-Hope project) and this is an area of great potential. Since the phase-screen technique is now capable of greater angular resolution it can be used to generate synthetic surveys, at a fraction of the cost of real acquisition, that offer insights into novel acquisition systems. The

obvious example is to use the enhanced phase-screen code to generate wide angle towed streamer (WATS) data, but the creation of flip-flop and over-under source geometries would also be possible.

6. Since the code runs monochromatically it would be possible to link it to frequency based inversion codes as outlined by Pratt (1999). The speed of the modelling would present significant advatages over the finite difference schemes ordinarily used in these procedures.

7. The ability of the code to determine converted phases could be used in the imaging of long offset data using the method of Baan et al. (2003).

References

K. Aki and P.G. Richards. *Quantitative seismology - Theory and methods*, volume 1. W.H. Freeman, New York, 1980.

T. Alkhalifah. Prestack phase-shift migration of separate offsets. *Geophysics*, 65: 1179–1194, 2000.

J.E. Andriatsitohaina. *Accurate refraction modelling in 3-D complex isotropic media - unpublished*. PhD thesis, Clare Hall College, University of Cambridge, 2004.

D.A. Angus. A one-way wave equation for modelling seismic waveform variations due to elastic heterogeneity. *Geophys. J. Int.*, 162:882–898, 2005.

M.v.d. Baan and J.M. Kendall. Estimating anisotropy parameters and traveltimes in the τ-p domain. *Geophysics*, 67:1076–1086, 2002.

M.v.d. Baan, T. Kerrane, J.M. Kendall, and N. Taylor. Imaging sub-basalt structures using locally converted waves. *First Break*, 21:29–36, 2003.

M.v.d. Baan, J. Wookey, and D. Smit. Stratigraphic filtering and source penetration depth. *Geophys. Prosp.*, 55:679–684, 2007.

A.M. Baig, F.A. Dahlen, and S.-H. Hung. Traveltimes of waves in three-dimensional random media. *Geophys. J. Int.*, 153:467–482, 2003.

G.W. Bear, H.J. Al-Shukri, and A.J. Rudman. Linear inversion of gravity data for 3-d density distributions. *Geophysics*, 60:1354–1364, 1995.

L.K. Bear, T.A. Dickens, and P Traynin. Incorporating non-seismic information for improved positioning with anisotropic psdm. *SEG Technical Program Expanded Abstracts*, 22(1):949–952, 2003.

J.G. Berryman. Long-wave elastic anisotropy in tranversely isotropic media. *Geophysics*, 44:896–917, 1979.

J.P. Blangy. Avo in transversely isotropic media – an overview. *Geophysics*, 59: 775–781, 1994.

B.J. Brennan and F.D. Stacey. Frequency dependence of elasticity of rock - tests of seismic velocity dispersion. *Nature*, 268:220–222, 1977.

A.R. Brown. *Interpretation of 3-dimensionsal seismic data*, volume 1 of *AAPG Memoir 42*. American Association of Petroleum Geology, 1991.

J.N. Brune, G. Mekala, and Y. Zeng. Evidence for anisotropy in the super-thick sedimentary basin, bay of bengal. *Journal of Earth Energy Systems*, 104:L147–L155, 1995.

R. Buckley. Diffraction by a randon phase-changing screen: a numerical experiment. *J. Atmos. Terr. Phys.*, 37:1431–1446, 1975.

J.P. Castagna and M.M. (Eds.) Backus. *Offset-dependent reflectivity - theory and practice of AVO analysis*, volume 8 of *Investigations in geophysics*. SEG, Tulsa, 1993.

C.H. Chapman. Ray theory and its extensions: WKBJ and maslov seismograms. *J. Geophys.*, 58:27–43, 1985.

C.H. Chapman and R. Drummand. Body-wave seismograms in inhomogeneous media using maslov asymptotic theory. *Bull. Seism. Soc. Am.*, 72:S277–S317, 1982.

P. Christie, I. Göllifer, and D. Cowper. Borehole seismic studies of a volcanic succession from the lopra-1/1a borehole in the faroe islands, n.e. atlantic. *Geological Survey of Denmark and Greenland Bulletin*, 9:25–42, 2006.

R.A. Clark, A.J. Carter, P.C. Nevill, and P.M. Benson. Attenuation measurements from surface seismic data - azimuthal variation and time-lapse case studies. In *Expanded abstracts*, pages L–28. EAGE 63rd annual meeting, Amsterdam, 2000.

J.K. Cohen and J.W. Stockwell. Cwp/su: Seismic unix release 37: a free package for seismic research and processing. *Centre for Wave Phenomena, Colorado School of Mines*, 2003.

M. Dablain. The application of high-order differencing to the scaler wave equation. *Geophysics*, 51:54–66, 1986.

P.F. Daley and F. Hron. Reflection and transmission coefficients for transversely isotropic media. *Bull. Seism. Soc. Am.*, 67:661–675, 1977.

P.F. Daley and F. Hron. Reflection and transmission coefficients for seismic waves in ellipsiodally anisotropic media. *Geophysics*, 44:27–38, 1979.

J.T. Etgen and M.J. OBrien. Computational methods for large-scale 3d acoustic finite difference modeling: A tutorial. *Geophysics*, 72 - 5:SM223–SM230, 2007.

J. Falk, E. Tessmer, and D. Gawjeski. Efficient finite-difference modelling of seismic waves using locally adjustable time steps. *Geophys. Prosp.*, 46:603–616, 1998.

M.D. Feit and J.A.Jnr. Fleck. Light propagation in graded-in-dex optical fibers. *Applied Optics*, pages 3990–3998, 1978.

M.D. Fisk and G.D. McCartor. The phase screen method for vector elastic waves. *J. Geophys. Res.*, 96(B4):5985–6010, 1991.

B. Fornberg. The pseudospectral method: Comparisons with finite-differences for the elastic wave equation. *Geophysics*, 52:483–501, 1987.

A. Frankel and R.W. Clayton. Finite difference simulations of seismic scattering: Implications for the propagation of short-period seismic waves in the crust and models of crustal heterogeneity. *J. Geophys. Res.*, 91:6465–6489, 1986.

W.S. French. Two-dimensional and three-dimensional migration of model-experiment reflection profiles. *Geophysics*, 39:265–277, 1974.

L. Frenje. *Scattering of Seismic Waves in Random velocity Models: Finite Difference Simulations*. PhD thesis, Uppsala University, Sweden, 2000.

K. Fuchs. The reflection of spherical waves from transition zones with arbitary depth-dependent elastic moduli and density. *J. Phys. Earth. Special Edition*, 16:27–41, 1968.

K. Fuchs and G. Müller. Computation of synthetic seismograms with reflectivity method and comparison with observations. *Geophys. J.R. Astron. Soc.*, 23: 417–433, 1971.

J.W. Gallagher and P.W. Dromgoole. Exploring below the basalt, offshore faroes: a case history of sub-basalt imaging. *Petroleum Geoscience*, 13:213–225, 2007.

R.B. Gordon and L.A. Davis. Velocity and attenuation of seismic waves in imperfectly elastic rock. *J. Geophys. Res.*, 73:3917–3935, 1968.

M. Graebner. Plane-wave reflection and transmissioncoefficients for a transversely isotropic solid. *Geophysics*, 57:1512–1519, 1992.

C.J. Greenroyd, C. Peirce, M. Rodger, A.B. Watts, and R.W. Hobbs. Crustal structure of the french guiana margin, west equatorial atlantic. *Geophys. J. Int.*, 169:964–987, 2007.

L.T. Ikelle, S.K. Yung, and F. Daube. 2-d random media with ellipsoidal auto-correlation functions. *Geophysics*, 58:1359–1372, 1993.

E.J.W. Jones. *Marine Geophysics*, volume 1. John Wiley and Sons Ltd., Chichester, England, 1999.

P. Kearey, M. Brooks, and I Hill. *An introduction to Geophysical exploration*, volume 3. Blackwell Science Ltd, Oxford, 2002.

K.R. Kelly, R.W. Ward, S. Treital, and R.M. Alford. Synthetic seismograms: A finite difference approach. *Geophysics*, 41:2–27, 1976.

S.R.A. Kelly, A.G. Whitham, M.A. Koraini, and S.P. Price. Lithostratigraphy of the cretaceous (barremian - santonian), hold-with-hope group, north east greenland. *Journal of the Geological Society, London*, 155:993–1008, 1998.

B.L.N. Kennett. *Seismic wave propagation in stratified media*, volume 1. Cambridge University Press, Cambridge, 1983.

C.G. Knott. Reflection and refraction of elastic waves with seismological applications. *Philosophical Magazine*, 1:48–64, 1899.

L.A. Koch and J Haller. Geological map of east greenland 72° - 76° N. Lat. (1:250,000). *Meddelelser om Gronland*, 183:1–26, 1971.

D Komatitsch and J. Tromp. Introduction to the spectral element method for three-dimensional seismic wave propagation. *Geophys. J. Int.*, 139:806–822, 1999.

D.D. Kosloff and E Baysal. Forward modelling by fourier method. *Geophysics*, 47:1402–1412, 1982.

E. Lemers and S.M.M. Carmichael. The paleocene deepwater sandstone play west of shetland. volume 1 of *Petroleum Geology of Northwest Europe*, pages 645–679. Geological Society, London, 1999.

A.R. Levander. Fourth-order finite difference p-sv seismograms. *Geophysics*, 53: 1425–1436, 1988.

F.K. Levin. Seismic velocities ion transversely isotropic media. *Geophysics*, 44: 918–936, 1979.

J. Ludwig, W, J.E. Nafe, and C.L. Drake. *The Sea*, chapter Part1: New concepts in sea floor evolution. Wiley, New York, 1970.

S. Mallick and L.N. Frazer. Practical aspects of reflectivity modeling. *Geophysics*, 52:1355–1364, 1987.

J. Maresh and R.S. White. Seeing through a glass, darkly: strategies for imaging through basalt. *First Break*, 23:27–33, 2005.

J. Maresh, R.S. White, R.W. Hobbs, and J.R. Smallwood. Seismic attenuation of atlantic margin basalts: Observations and modeling. *Geophysics*, 71:B211–B221, 2006.

K.J. Marfurt. Accuracy of finite-difference and finite element modeling of the scaler and elastic wave equations. *Geophysics*, 49:533–549, 1984.

G.S. Martin. *The Marmousi2 model, elastic synthetic data, and an analysis of imaging and AVO in a structurally complex environment.* PhD thesis, Faculty of the Department of Geosciences, University of Houston, 2004.

F. Martini and C.J. Bean. Application of pre-stck wave equation datuming to remove interface scattering in sub-basalt imaging. *First Break*, 20:395–401, 2002a.

F. Martini and C.J. Bean. Interface scattering versus body scattering in sub-basalt imaging and application of pre-stack wave equation datuming. *Geophysics*, 67:1593–1601, 2002b.

F. Martini, R.W. Hobbs, C.J. Bean, and R. Single. A complex 3d volume for sub-basalt imaging. *First Break*, 23:41–51, 2005.

A. A. Mateeva. *Thin horizontal layering as a stratigraphic filter in absorption estimation and seismic deconvolution.* PhD thesis, Centre for Wave Phenomena, Colorado School of Mines, 2003.

D. Muerdter, M. Kelly, and D. Ratcliff. Understanding subsalt illumination through ray-trace modeling, part 2: Dipping salt bodies, salt peaks, and nonreciprocity of subsalt amplitude response. *The Leading Edge*, 20(7):688–697, 2001.

G. Müller. The reflectivity method: a tutorial. *Journal of Geophysics*, 58:153–174, 1985.

J.E. Nafe and C.L. Drake. Variation with depth in shallow and deep water marine sediments of porosity, density and the velocities of compressional and shear waves. *Geophysics*, 22:523–552, 1957.

J.F. Nye. *Physical properties of crystals.* Oxford Press, 1957.

R.F. O'Doherty and N.A. Anstey. Reflections on amplitudes. *Geophys. Prosp.*, 19:430–458, 1971.

I. Opršal and J. Zahradník. Elastic finite-difference method for irregular grids. *Geophysics*, 64:240–250, 1999.

C.S. Pickles and A.G. Whitham. A review of the tertiary evolution of east greenland and its relationship to the opening of the north atlantic. *CASP EGP Report (Unpublished)*, 56:1–104, 1999.

M.M. Popov. A new method of computation of wavefields using gaussian beams. *Wave Motion*, 4:85–97, 1982.

R.G. Pratt. Seismic waveform inversion in the frequency domain, part 1: Theory and verification in a physical scale model. *Geophysics*, 64:888–901, 1999.

William H. Press, William T. Vetterling, Saul A. Teukolsky, and Brian P. Flannery. *Numerical Recipes in C++: the art of scientific computing, 2nd edition*. Cambridge University Press, 2002. ISBN 0-521-75033-4.

J.A. Ratcliffe. Some aspects of diffraction theory and their application to the ionosphere. *Rep. Prop. Phys.*, 19:190–263, 1956.

M. Reshef, D. Kosloff, M Edwards, and C. Hsiung. Three-dimansional acoustic modeling by the fourier method. *Geophysics*, 53:1175–1183, 1988a.

M. Reshef, D. Kosloff, M Edwards, and C. Hsiung. Three-dimansional elastic modeling by the fourier method. *Geophysics*, 53:1184–1193, 1988b.

K.R. Richardson, J.R. Smallwood, R.S. White, Snyderb D.B., and P.K.H. Maguire. Crustal structure beneath the faroe islands and the faroeiceland ridge. *Tectonophysics*, 300:159–180, 1998.

J.O.A Robertsson, J.O. Blanch, and W.W. Symes. Viscoelastic finite-difference modeling. *Geophysics*, 59:1444–1456, 1994.

J.O.A Robertsson and C.H. Chapman. An efficient method for calculating finite-difference seismograms after model alterations. *Geophysics*, 65:907–918, 2000.

J.T. Rutledge and H. Winkler. Attenuation measurements of vertical seismic profile data: leg 104, site 642. *Proceedings of the Ocean Drilling Program, Scientific Results*, 104:965–972, 1989.

M.S. Sams, J.P. Neep, M.H. Worthington, and M.S. King. The measurement of velocity dispersion and frequency-dependent intrinsic attenuation in sedimentary rocks. *Geophysics*, 62:1456–1464, 1997.

M. Schoenberger and F.K. Levin. Apparent attenuation due to intrabed multiples. *Geophysics*, 39:278–291, 1974.

M. Schoenberger and F.K. Levin. Apparent attenuation due to intrabed multiples, ii. *Geophysics*, 43:730–737, 1978.

S. Self, L. Keszthelyi, and Th. Thordarson. The importance of pahoehoe. *Annu. Rev. Earth Planet Sci.*, 26:81–110, 1998.

F. Shaw, M.H. Worthington, R.S. White, M.S. Andersen, U.K. Petersen, and the Seifaba Group. Seismic attenuation in faroe islands basalts. *Geophys. Prosp.*, 56:5–20, 2008.

R.E. Sheriff and L.P. Geldert. *Exploration seismology*. Cambridge University Press, second edition, 1995.

S. Sinclair. Hold with hope 3d gid model - summary. *EGS Sub-basalt Seismic Project Report*, 1:1–23, 2006.

W. Smith. The application of finite element analysis to body wave propagation problems. *Geophys. J. R. Astr. Soc.*, 42:747–768, 1975.

S. Spitz. Seismic trace interpolation in the f-x domain. *Geophysics*, 56:785–794, 1991.

L. Stemmerrik, F.G. Christiansen, S. Piasecki, B. Jordt, C. Marcussen, and H. Nohr-Hansen. Depositional history and petroleum geology of the carboniferous to cretaceous sedimaents in the northern part of east greenland. *Arcic Geology and petroleum Potential. NPF Special Publication*, 2:67–87, 1993.

M. Talwini. Computation with the help of a digital computer of magnetic anomalies caused by bodies of arbitary shape. *Geophysics*, 50:1907–1927, 1985.

F.D. Tappart. *The parabolic approximation method. In: Keller, B. and Papadakis, J.S. (Eds.) Lecture Notes in Physics 70: Wave propagation and Underwater acoustics*, chapter 5. Springer-Verlag, 1977.

L. Thomsen. Weak anisotropy. *Geophysics*, 51:1954–1966, 1986.

L. Thomsen. *Weak anisotropic reflections: in Castagna, J.P. and Backus, M.M. (Eds.)*, volume 8 of *Investigations in Geophysics*, pages 103–111. Society of Exploration Geophysicists, 1998.

K. Thomson. Volcanic features of the north rockall trough: application of visualisation techniques on 3d seismic reflection data. *Bull Volcanol*, 67:116–128, 2005.

I. Trinks and R.W. Hobbs. Gravity modelling based on small cells. In *Expanded abstracts*, page 347. EAGE 67th annual meeting, 2005.

I. Tsvankin. P-wave signatures and notation for transversely isotropic media: An overview. *Geophysics*, 61:467–483, 1996.

I. Tsvankin and L. Thomsen. Nonhyperbolic moveout in anisotropic media. *Geophysics*, 59:1290–1304, 1994.

University of Calgary. Crewes zoeppritz explorer 2.0, 2005. Available: http://www.crewes.org/ResearchLinks/ExplorerPrograms/ZE/ZEcrewes.

B.G.J. Upton, C.H. Emeleus, D. Rex, and M. Thirlwall. Early tertiary magmatism in ne greenland. *Journal of the Geological Society of London*, 152:959–964, 1995.

V. Červený, I.A. Molotkov, and I. Pšenčik. *Ray method in seismology*. Univerzita Karlova, 1977.

R. Versteeg. The marmousi experience: Velocity model determination on a synthetic complex data set. *The Leading Edge*, 13:927–936, 1994.

W.W. Wepfer and N.I. Christensen. Compressional wave attenuation in oceanic basalts. *J. Geophys. Res.*, 95:17431–17439, 1990.

J.C. White. *Extension of a forward modelling phase-screen code for AVO analysis in both isotropic and anisotropic media: Development and applications.* PhD thesis, Durham University, England, 2008.

J.C. White and R.W. Hobbs. Extension of forward modeling phase-screen code in isotropic and anisotropic media up to critical angle. *Geophysics*, 72:SM107–SM114, 2007.

J.E. White. Computed waveforms in transversely isotropic media. *Geophysics*, 47:771–783, 1982.

J.E. White. *Underground sound: Application of seismic waves*, volume 18 of *Methods in Geochemistry and Geophysics*. Elsevier, 1983.

A.G. Whitham and C.S. Pickles. Cretaceous paaeogeographies for east greenland between 68° and 77° N. *CASP EGS Report (unpublished)*, 68:1–114, 2000.

A.J. Wild, R.W. Hobbs, and L. Frenje. Modelling complex media: an introduction to the phase-screen method. *Physics of the Earth and Planetary Interiors*, 120:219–225, 2000.

A.J. Wild and J.A. Hudson. A geometrical approach to the elastic complex screen. *J. Geophys. Res.*, 103:707–725, 1998.

J. Wright. The effects of transverse isotropy on reflection amplitude vs offset. *Geophysics*, 52:564–567, 1987.

R.-S. Wu. *The perturbation method for elastic wave scattering in Seismic wave scattering and attenuation*, volume 131 of *Pure Apll. Geophys.*, pages 603–637. 1989.

R.-S. Wu. Wide-angle elastic wave one-way propagation in heterogeneous media and an elastic complex-screen method. *J. Geophys. Res.*, 95:751–766, 1994.

R.-S. Wu and Aki. Introduction: seismic wave scattering in three-dimensionally heterogeneous earth. *Pure and Applied Geophysics*, 128:1–6, 1988.

R.-S. Wu and L.J. Huang. *Reflected wave modeling in heterogeneous acoustic media using the De Wolf approximation in Mathematical methods in Geophysical imaging III*, pages 176–186. 1995.

X.-B. Xie and R.-S. Wu. A complex-screen method for modeling elastic wave reflections. In *Expanded abstracts*, pages 1269–1272. SEG 65th annual meeting, 1995.

J. Yang. Numerical and physical modeling of p-s converted waves in vti media. Master's thesis, University of Calgary, Canada, 2003.

J. Zhu and L.R. Lines. Comparison of kirchhoff and reverse-time migration methods with applications to prestack depth imaging of complex structures. *Geophysics*, 63:1166–1176, 1998.

K. Zoeppritz. Über reflexion and durchgang seismischer wellen durrch unstetigkeitsflachen: Gottinger nachrichten. *Über Erdbebenwellen*, VII B:66–84, 1919.

Appendix

A Well log examples

In order to populate the Hold-with-Hope volume with accurate elastic rock types well logs from the north east European margin were studied. The supra-basalt succession was primarily based upon well 214/4-1 and the relevant sections relating to the Breydon and Oligo-plio-pleisto- sands are shown in the following sections. Also displayed is the section of well log 206/4-1 relating to the Valanginian deep marine conglomerates and sands which display an anomalously fast velocity from the sonic log.

A.1   Breydon sands - log 214/4-1
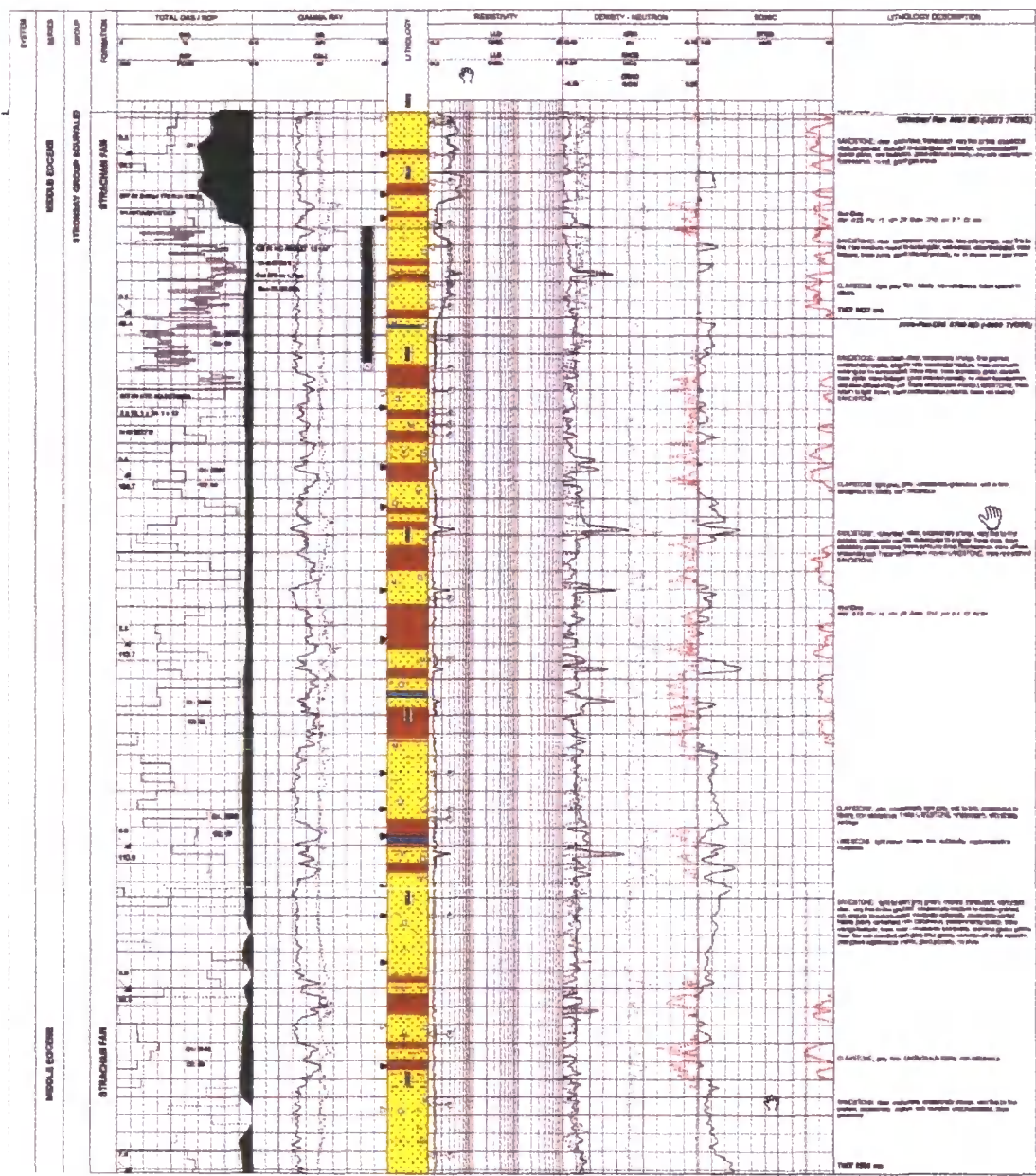
Figure A.1: *Well log record 214/4-1 for Breydon sands used to generate the elastic parameters for the supra-basalt section of the Hold-with-Hope model.*

A.2   Oligo-plio-pleisto- sands - log 214/4-1
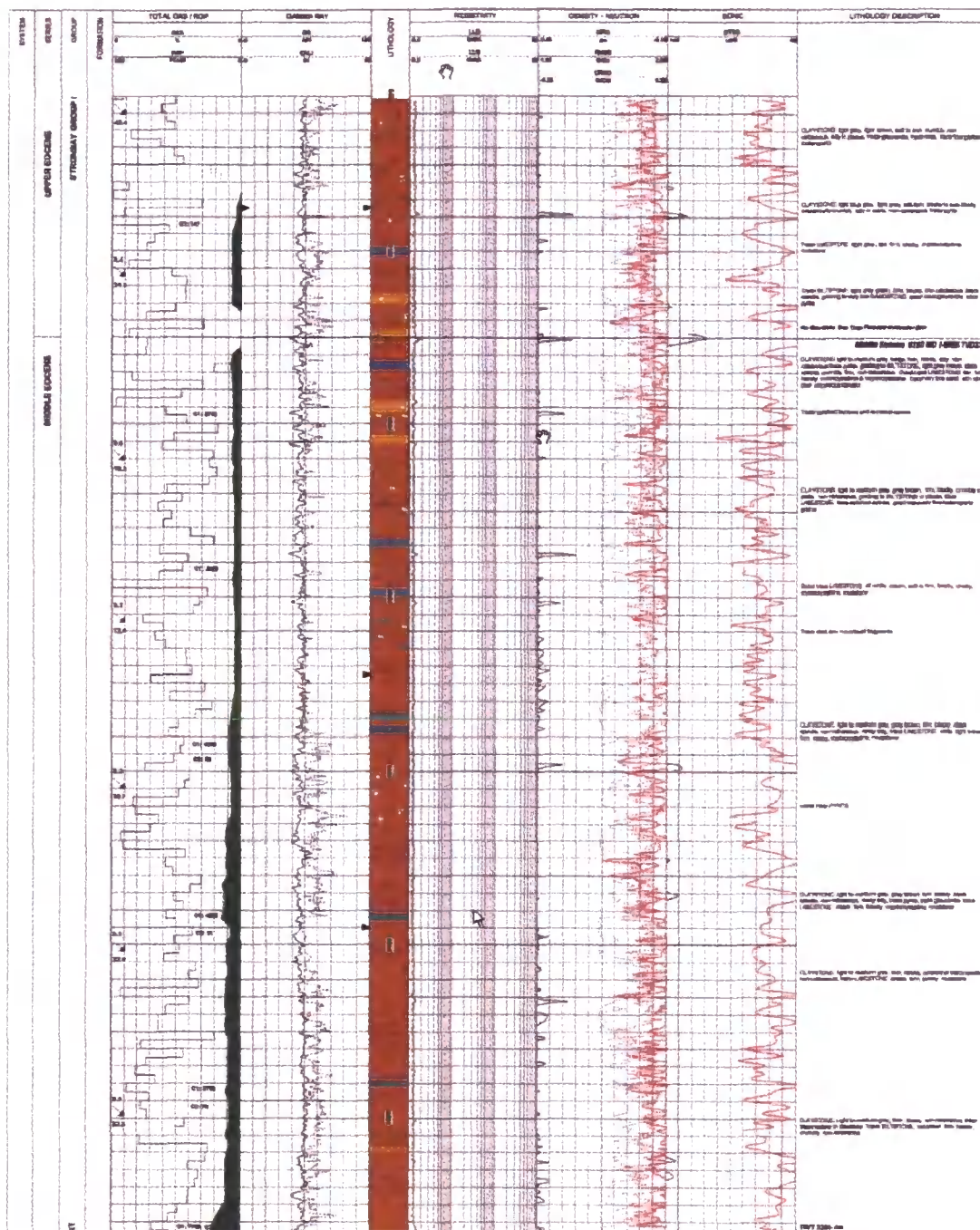
Figure A.2: *Well log record 214/4-1 for Oligo-plio-pleisto sands used to generate the elastic parameters for the supra-basalt section of the Hold-with-Hope model.*

A.3 Oligo-plio-pleisto- sands - log 214/4-1
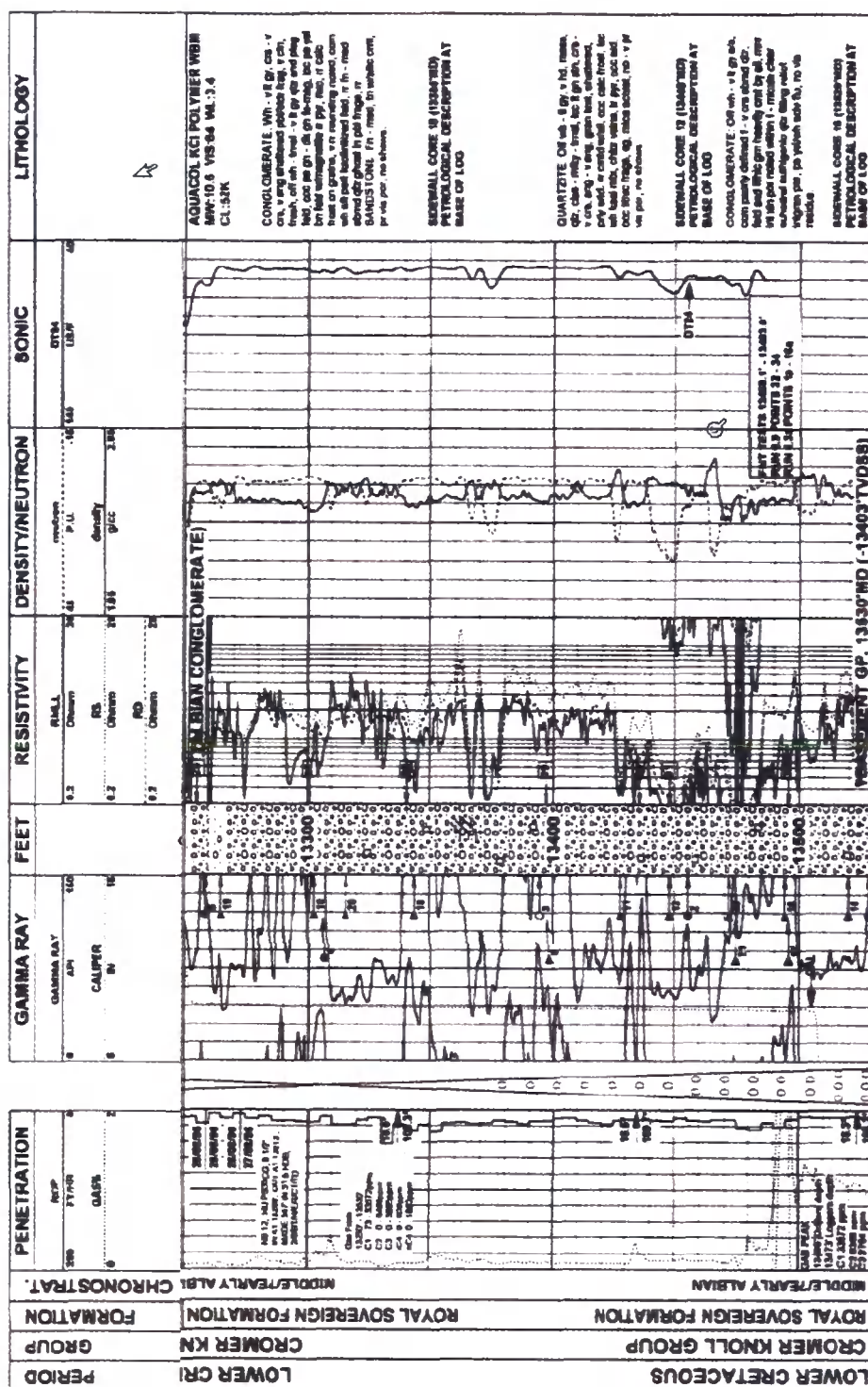
Figure A.3: *Well log record 206/4-1 for Valanginian deep marine conglomerates and sands used to generate the elastic parameters for the relevent section of the Hold-with-Hope model.*

B   Random volume building code

```
#include <iostream>
#include <fstream>
#include <cstdlib>
#include <cmath>
#include <ctime>
#include <new>
#include "/local/white/scratch/include/fftw3.h"
using namespace std;

// This program uses the Fast Fourier Transform package FFTW3
// This package was written and developed by Matteo Frigo and Steven G Johnson
// FFTW3 is available under a GNU General Public License, Free Software Foundation
// www.fftw.org
// YOU MUST FIRST INSTALL FFTW3 BEFORE COMPILING THIS CODE

/*
This program creates a random 3D velocity distribution by creating a von Karman
power spectrum in the wavenumber domain applying a random phase and transform-
ing to the spatial domain.
The model space is specified in terms of three correlation lengths ax, ay, az and the std
dev, σ.
The model produces a Gaussian velocity distribution with zero mean which can then
be scaled for your purposes.
White (2008) provides details of how to convert this to a log-normal velocity distribu-
tion.

This code is available to all but please reference the author, James C White, in any
publications that arise from this work.

The input file for this code is an ascii list of numbers: no. of nodes in x, no. of nodes
in y, no. of nodes in z, grid spacing, correlation length in x, correlation length in y,
correlation length in z, standard deviation and Hurst number.

The output is a 4 column ascii list: x, y, z, value

Compile this code with:
      c++ -o FinalRandomBuild.exe FinalRandomBuild.c -L/../lib -lfftw3 -lm
where the -L points to the fftw3 library files

Run this code with:
      ./FinalModelBuild.exe ParamFile
where the param file is the file containing the required parameters
*/

double pi=3.1415926536;
typedef double complx[2];
```

```
class ModelParams {

public:
    int xsize, ysize, zsize; // size of box
    int zsizecomp; // and the size of z in wavenumber domain, only need half
    int gridspacing; // the grid spacing in x, y and z
    double var; // the variance
    double ax, ay, az; // scale lengths in x, y and z
    double mean; // the mean of the distribution
    double xx, yy; // the Hurst numbers
    double gamma_sol, gamma_sol2; // solutions to the Gamma function
    ifstream in;
    ModelParams(char *argv[]);
};

ModelParams::ModelParams(char *argv[]) {

    in.open(argv[1], ios::in); // open the file specified in the execution
    cout << "\nThe model parameters are being read from " << argv[1] << "\n\n";
    in >> xsize >> ysize >> zsize >> gridspacing >> ax >> ay >> az >> var >>
        xx;
    yy=xx+3/2;
    var=var*var;
    zsizecomp=int(zsize/2+1);
}

class Gamma {

    int j;
public:
    double y,x,tmp,ser;
    double GammaCalc(double xx);
};

double Gamma::GammaCalc(double xx) { // calcualte gamma func for Hurst number

    y=x=xx;
    double cof[6]={76.18009172947146, -86.50532032941677, 24.01409824083091,
        -1.231739572450155, 0.1208650973866179e-2, -0.5395239384953e-5};
    tmp=x+5.5;
    tmp-=(x+0.5)*log(tmp);
    ser=1.000000000190015;
    for (j=0;j<6;j++) {

        ser += cof[j]/++y;
    }
    return -tmp+log(2.5066282746310005*ser/x);
}
```

```
class KVals {

    int x, y, z; // loop counters
    int posx, posy, posz;
    int max_val;
public:
    double *kxgrd;
    double *kygrd;
    double *kzgrd;
    fftw_complex *randgrd;
    double *realrandgrd;
    KVals(ModelParams &MP);
};

KVals::KVals(ModelParams &MP) {
// allocate the dynamic memory for the required arrays, and then calcualte the kx, ky
and kz values of the grid in wavenumber domain

    try {

        kxgrd=new double[MP.xsize];
    } catch (bad_alloc xa) {

        cout << "Can't allocate kxgrd\n";
    }
    try {

        kygrd=new double[MP.ysize];
    } catch (bad_alloc xa) {

        cout << "Can't allocate kygrd\n";
    }
    try {

        kzgrd=new double[MP.zsizecomp];
    } catch (bad_alloc xa) {

        cout << "Can't allocate kzgrd\n";
    }
    try {

        randgrd=new fftw_complex[MP.xsize*MP.ysize*MP.zsizecomp];
    } catch (bad_alloc xa) {

        cout << "Can't allocate randgrd\n";
    }
    try {

        realrandgrd=new double[MP.xsize*MP.ysize*MP.zsize];
```

```
} catch (bad_alloc xa) {

    cout << "Can't allocate real_randgrid\n";
}
for (x=0; x<MP.xsize; x++) {

    posx=((x+(MP.xsize/2-1))%MP.xsize)-(MP.xsize/2-1); // calculate the position
in wavenumber domain
    kxgrd[x]=2.0*pi*((double)posx)/((MP.xsize)*MP.gridspacing); // now in real
distance ^-1
}
for (y=0; y<MP.ysize; y++) {

    posy=((y+(MP.ysize/2-1))%MP.ysize)-(MP.ysize/2-1); // calculate the position
in wavenumber domain
    kygrd[y]=2.0*pi*((double)posy)/((MP.ysize)*MP.gridspacing); // now in real
distance ^-1
}
for (z=0; z<MP.zsizecomp; z++) {

    posz=((z+(MP.zsize/2-1))
    kzgrd[z]=2.0*pi*((double)posz)/((MP.zsize)*MP.gridspacing); // now in real
distance ^-1
}
}

class Grid {

    double a, ak;
    int x, y, z;
    double phase, amp;
    fftw_plan k_x_3D;
    ofstream box, profile_power, profile_x, profile_y, profile_z;
public:
    Grid(ModelParams &MP, KVals &KV, double yy);
};

Grid::Grid(ModelParams &MP, KVals &KV, double yy) {

    srand((unsigned)time(0));
    a=sqrt(MP.ax*MP.ax+MP.ay*MP.ay+MP.az*MP.az);
    profile_x.open("profile_along_x.lst");
    profile_y.open("profile_along_y.lst");
    profile_z.open("profile_along_z.lst");
    box.open("RandomBox.lst");
    for (x=0; x¡MP.xsize; x++) {

        for (y=0; y<MP.ysize; y++) {
```

```
        for (z=0; z<MP.zsizecomp; z++) {

                ak=KV.kxgrd[x]*KV.kxgrd[x]*MP.ax*MP.ax+KV.kygrd[y]*KV.kygrd[y]*
                        MP.ay*MP.ay+KV.kzgrd[z]*KV.kzgrd[z]*MP.az*MP.az;
                amp=(MP.var*pow((2*sqrt(pi)*a),3)*MP.gamma_sol2/
                        (MP.gamma_sol*pow(1+ak,yy)));
                amp=sqrt(amp);
                if (x==0 && y==0 && z==0) amp=0.0; // for a zero mean
                phase=2*pi*(double(rand()))/(double(RAND_MAX));
                KV.randgrd[z+MP.zsizecomp*(y+MP.ysize*x)][0]=amp*cos(phase);
                KV.randgrd[z+MP.zsizecomp*(y+MP.ysize*x)][1]=amp*sin(phase);
            }
        }
    }
    k_x_3D=fftw_plan_dft_c2r_3d(MP.xsize, MP.ysize, MP.zsize, KV.randgrd,
        KV.realrandgrd, FFTW_ESTIMATE);
    fftw_execute(k_x_3D);
    fftw_destroy_plan(k_x_3D);
    for (x=0; x¡MP.xsize; x++) {

        for (y=0; y¡MP.ysize; y++) {

            for (z=0; z¡MP.zsize; z++) {

                KV.realrandgrd[z+MP.zsize*(y+MP.ysize*x)]/=
                    (MP.xsize*MP.ysize*MP.zsize);
                box << x*MP.gridspacing << " " << y*MP.gridspacing << " "
                    << z*MP.gridspacing << " " <<
                    KV.realrandgrd[z+MP.zsize*(y+MP.ysize*x)] << endl;
                if (y==10) profile_x << x*MP.gridspacing << " " << z*MP.gridspacing
                    << " " << KV.realrandgrd[z+MP.zsize*(y+MP.ysize*x)] << endl;
                if (x==10) profile_y << y*MP.gridspacing << " " << z*MP.gridspacing
                    << " " << KV.realrandgrd[z+MP.zsize*(y+MP.ysize*x)] << endl;
                if (z==10) profile_z << x*MP.gridspacing << " " << y*MP.gridspacing
                    << " " << KV.realrandgrd[z+MP.zsize*(y+MP.ysize*x)] << endl;
            }
        }
    }
    box.close();
    profile_x.close();
    profile_y.close();
    profile_z.close();
}

int main(int argc, char *argv[]) {

    ModelParams MP(argv);
    KVals KV(MP);
    Gamma gamma;
```

```
MP.gamma_sol=gamma.GammaCalc(MP.xx);
MP.gamma_sol=exp(MP.gamma_sol);
MP.gamma_sol2=gamma.GammaCalc(MP.yy);
MP.gamma_sol2=exp(MP.gamma_sol2);
Grid Gd(MP, KV, MP.yy);
return 0;
}
```

C Phase-screen manual

PSWhiteVer9.0 Phase-screen manual
J.C. White
Department of Earth Sciences, Durham University, Science Labs, Durham. DH1 3LE

Ownership
James C White owns the IPR for this code. It may be used by academic users with his permission for non-commercial work. In cases where publication arises from this research, the work of the author must be acknowledged:

White, J.C. and Hobbs, R.W., 2007, Extension of forward modelling phase-screen code for AVO analysis in isotropic and anisotropic media up to critical angle: Geophysics, 72, SM107–SM114.

Phase-screen theory
Elastic phase-screen theory was developed by Wu (1994), then Wild and Hudson (1998) published a geometrical derivation that was not only easier to comprehend but could also be considered physically. Both approaches produced the same set of governing equations limited to small-angle propagation through weak-scattering perturbations. The technique works by dividing the model space into a series of screens perpendicular to the primary direction of propagation and shifting the wavefields through the model a screen at a time. At each screen the energy is flipped from the spatial domain to the wavefield domain and back again. Propagation is undertaken in the wavenumber domain whilst the spatial domain is used to correct the phase locally and the correctly partition energy at interfaces.

This version of the code expands the method to critical angle by improving the small-angle phase correction and transforming the wavefield as a function of angle so exact reflection and transmission coefficients can be applied. It also offers the opportunity to model simple anisotropic rocktypes (those which display vertically transverse isotropy).

Since the code relies upon Fourier methods it must suppress energy at the edges of the model space in order to avoid the introduction of wrap-around energy. The degree of suppression is user controlled and should be carefully monitored during computation.

Computational requirements
The code is compact and whilst running relies upon grabbing the dynamic memory it needs. The code will run best if the total size of the code and the allocated memory is less than the RAM on the machine. Permissions must also ensure that the code can read the input files and write the output files to the hard disk. Unless specified in the input file paths the outputs will write to the current directory

The code is written in c++ and requires the standard libraries called in the primary script. The discrete Fourier transforms are calculated using the third party software FFTW. This can be downloaded from the web at www.fftw.org and must be installed prior to compilation of the phase-screen code. PSWhiteVer9.0 compiles with fftw-3.1.2 and all current versions of the third release. It is incompatible with earlier versions and as such MPI can not be implemented with this version.

How the code works

The code works by constructing a 1-, 2- or 3-D grid of rock types. The lateral spacing is constant, and is set in the input file, but the vertical spacing is controlled by the screen position and can be varied with depth. As such, screen concentration can be increased in regions of complexity. The input velocity file is a list of integers representing the rock type at each grid position. In the rock parameters file V_P, V_S, ρ, $1/Q_P$, $1/Q_S$, δ and ϵ are provided for each rock type. Each line in the file starts with the rock type integer identifier starting with rock type zero.

The model input file, described below, consists of 6 lines of model space parameters followed by a screen specific line for each screen.

The code should be compiled with:

```
c++ -o PSWhiteVer9.0.exe PSWhiteVer9.0.c -L/../lib -lfftw3 -lm -O3
```

where the -L points to the fftw3 library files and ensuring the fftw files are in the specified directory. Then to run the code:

```
./PSWhiteVer9.0.exe model_param_file
```

There will be a check file created which will reproduce the input file if everything has been read correctly, and the log file will offer clues if the code runs unsuccessfully. Serious errors will be written directly to the screen.

The code automatically reformats both the single and multiple pass data (if required) into sgl.sgy and mul.sgy files which are ready to be read by SeismicUnix (IEEE numbers). A simple command line to view the data would look like:

```
segyread tape=outputmul.sgy conv=0 | suximage
```

Model parameter file

The first six lines (five lines of model information and a separator line) relate to the entire model, lines seven and beyond are screen specific and one is required for every screen.

Line 1

This line provides the input file names and root name for the output files.

Parameter	Information	Data type
velocity file	input velocity grid	binary
rock property file	rock properties	ascii
output root name	output files prefix	

the output files generated will be (with the output root prefix) a .log file, a .check file, raw multiplexed .sgl and .mul data and converted .sgl.sgy and .mul.sgy files

Line 2

This line provides the primary model data

Parameter	Information	Data type
modsizex1	number of samples in x direction	int
modsizex2	number of samples in y direction	int
no_screens	total number of screens	int
max_no_rocks	number of rock types	int
modminx1	origin of model in x direction (m)	double
modminx2	origin of model in y direction (m)	double
d1	sample spacing in x direction (m)	double
d2	sample spacing in y direction (m)	double

Line 3

This line provides the run specific details

Parameter	Information	Data type
nf	number of frequencies (calculated as $3 \times f_{max} \times dt \times nt$ for a ricker wavelet and $f_{max} \times dt \times nt$ for a given source wavelet	int
nt	number of time samples in output traces	int
dt	time sample interval	double
actmodsizex	actual model size in x (m)	double
actmodsizey	actual model size in y (m)	double
over	padding factor for model to avoid wrap around. best to stick to 1.0 as memory requirement gets excessively large	double
tdecay	to prevent wrap around imposes a exponential decay on time axis. Good for long period multiple but can blow up noise. 0.0 is no decay, 1.0 is $e^{2\pi}$ decay	double
decayfunc	wavenumber decay mute between % of Nyquist chosen later. If positive use Gaussian taper, if negative use cosine taper, if zero use linear taper. 0.01 to 0.1 advised	double
model_mode	0 for pre stack normal reflection modelling. 1 for VSP modelling. 2 for a post stack exploding reflector modelling	int
backscatt	0 is no backscatter calculated. 1 to calculate backscatter	int
no_mult	number of free surface and peg-leg multiples to calculate	int
sgl_or_mul	0 - output just the single pass data 1 - just the multiple data 2 - both single and multiple pass data	int
basalt	additional basalt Q filtering 0 - no additional basalt filtering 1 - allow additional basalt filtering	int
zoep	0 - single screen transforms 1 - split wavefield transforms	
basaltlimit	minimum rock code for additional basalt Q filtering only if basalt==1	int
Q_bas_ filtername	name of ascii file containing Q wavelet. sample rate must be equal to dt and first line must contain an integer detailing the number of points sampled. only if basalt==1	char
slope	include local slope in RT calculations 0 - no, 1 - yes only if zoep==1	int

Line 3 continued

This line provides the run specific details

Parameter	Information	Data type
anisotropy	include anisotropy in propagation and RT calculation 0 - no, 1 - yes only if zoep==1	int
weight_type	how to split the wavefield prior to RT calculation 0 - node-by-node 1 - split into gaussians only if zoep==1	int
gaussians_total_x	number of gaussians subsets in 1st direction. only if weight_type==1	int
gaussians_total_y	number of gaussians subsets in 2nd direction. only if weight_type==1	int
diag	diagnostics level 0-3	int
qf	Q filter 0 - zero phase Q filter if required 1 - causal Q filter	int
filtername	name of Q wavelet ascii file with known phase characteristics sample rate must be equal to dt	char

The actual model size can be lass than the full model volume. This can rapidly increase run time and if an inappropriate size is chosen for a particular set-up an error message will appear on screen.

Line 4

This line provides the source specific details

Parameter	Information	Data type
st	source type	int
	1 plane p-wave displacement	
	2 plane s-wave displacement	
	3 point p-wave displacement	
	4 point p-wave forced 2-D	
	5 point p-wave forced 1-D	
	6 point p-wave displacement	
	7 point s-wave forced 2-D	
	8 point s-wave forced 1-D	
source_screen	screen number at required source depth	int
no_shots	number of shots to model	int
	(use 1 for exploding reflector simulation)	
ki[0]	angle between plane and 1st direction (degrees)	double
	only if plane wave source	
ki[1]	angle between plane and 2nd direction (degrees)	double
	only if plane wave source	
source_decay_ begin_x	angle to start point source taper in x (degrees)	double
	only if point source	
source_decay_ begin_y	angle to start point source taper in y (degrees)	double
	only if point source	
source_decay_ end_x	angle to end point source taper in x (degrees)	double
	only if point source	
source_decay_ end_y	angle to end point source taper in y (degrees)	double
	only if point source	
source_x1	absolute position of source in x	double
source_x2	absolute position of source in y	double
sourceinc_x1	source increment in x (m)	double
	only if no_shots>1	
sourceinc_x2	source increment in y (m)	double
	only if no_shots>1	
fmin	minimum peak frequeny for Ricker wavelet (Hz)	double
	only if st>0	
fmax	maximum peak frequeny for Ricker wavelet (Hz)	double
	only if st>0	

<u>*Line 4 continued*</u>
This line provides the run specific details

Parameter	Information	Data type
sourcename	file name for source wavelet smapled at same time as modelling (dt) first line gives number of samples then additional lines give wavelet amplitude with time only if st<0	char
soudepth	depth to force angular source ghost (m) only if source_screen=0	double
recdepth	depth to force angular receiver ghost (m) only if source_screen=0	double

Line 5

This line provides receiver speciific details

Parameter	Information	Data type
rectype	receiver type	int
	1 - single comp displacement	
	3 - three comp displacement	
	11 and 13 - as above but velocity	
	21 and 23 - as above but pressure	
	31 and 33 - as above but acceleration	
recloc	receiver position	int
	0 - wrt to model grid	
	1 - wrt to source position	
recscreen	screen number at receiver depth	int
recs	number of receivers in each array	int
	For a VSP recs=no_screens	
recx1	position of first receiver in x1	double
recx2	position of first receiver in x2	double
recinc_x1	receiver spacing in x1	double
recinc_x2	receiver spacing in x2	double
no_recarrays	numbers of arrays deployed	int
recarrayoff1	array spacing in x1	double
recarrayoff2	array spacing in x2	double
recazmuth	VSP angle wrt northings (degrees)	double
recdip	VSP angle between vertical and well bore (degrees)	double

Line 6

Seperator flag - 99999

If this flag is not read in correctly (due to an incorrect number of arguments) during a modelling run then an error message will be written to screen.

Lines 7+

Every screen requires a separate line of arguments:

Parameter	Information	Data type
1	screen depth (m)	double
2	% of critical angle to begin p-wave taper in wavenumber domain for average layer velocity	double
3	% of critical angle to begin s-wave taper in wavenumber domain for average layer velocity	double
4	p-wave critical angle scale factor, normally 1.0, allows post critical energy to be passed	double
5	s-wave critical angle scale factor, normally 1.0, allows post critical energy to be passed	double
6 - 13	control switches for forward propagation Tpp, Rpp, Tps, Rps, Tss, Rss, Tsp, Rsp 0 - set to 0.0 1 - pass entire wavefield 2 - apply RT coefficeints	int
14 - 17	master control switches for forward propagation 0 - do not compute this energy mode 1 - compute this energy mode	int
18 - 25	control switches for backward propagation	int
26 - 29	master control switches for backward propagation	int
30	width in samples of absorbing boundary at edge of model in 1st direction	int
31	width in samples of absorbing boundary at edge of model in 2nd direction	int
32	type of taper to apply at boundary +ive - gaussian filter -ive - cosine taper 0 - linear taper	double

The control switches make it possible to run models acoustically as well as elastically.

Model velocity file

The velocity model is stored as a binary file with each data node represented by an unsigned character byte. These bytes are read with the fastest variation in the 2nd direction, then the primary lateral direction with the depth varying most slowly.

Rock property file

This file details the elastic properties for the codes assigned in the model velocity file. The file contains max_no_rocks lines and each line will contain:

the rock code number, p-wave velocity (ms^{-1}), s-wave velocity (ms^{-1}), density (kgm^{-3}), $1/Q_p$, $1/Q_s$, δ and ϵ.